



HAL
open science

Forçage volumique basé sur une méthode de type reconstruction pour un modèle de fermeture algébrique hybride RANS/LES

Jeremie Janin

► **To cite this version:**

Jeremie Janin. Forçage volumique basé sur une méthode de type reconstruction pour un modèle de fermeture algébrique hybride RANS/LES. Mécanique des fluides [physics.class-ph]. Aix-Marseille Université, 2023. Français. NNT: 2023AIXM0011 . tel-04432681

HAL Id: tel-04432681

<https://irsn.hal.science/tel-04432681>

Submitted on 1 Feb 2024

HAL is a multi-disciplinary open access archive for the deposit and dissemination of scientific research documents, whether they are published or not. The documents may come from teaching and research institutions in France or abroad, or from public or private research centers.

L'archive ouverte pluridisciplinaire **HAL**, est destinée au dépôt et à la diffusion de documents scientifiques de niveau recherche, publiés ou non, émanant des établissements d'enseignement et de recherche français ou étrangers, des laboratoires publics ou privés.

THÈSE DE DOCTORAT

Soutenue à Aix-Marseille Université
par

Jérémie JANIN

Volume forcing method based on a reconstruction-like
procedure for a hybrid RANS/LES algebraic closure model

Forçage volumique basé sur une méthode de type
reconstruction pour un modèle de fermeture algébrique hybride
RANS/LES

Discipline

Sciences Pour l'Ingénieur

Spécialité

Mécanique et physique des fluides

École doctorale

ED353

Laboratoire/Partenaires de recherche

Institut de Radioprotection et de Sécurité Nucléaire
(IRSN)

Laboratoire de Mécanique, Modélisation et Procédés Propres, M2P2, UMR 7340

Composition du jury

Lars DAVIDSON Rapporteur
Chalmers University of Technology

Rémi MANCEAU Rapporteur
Université de Pau, CNRS

Paola CINNELLA Présidente
Sorbonne université

Benoît de Laage de Meux Examineur
EDF R&D, Chatou

Christophe FRIESS Co-encadrant
Aix-Marseille Université

Fabien DUVAL Co-encadrant
IRSN, Cadarache

Pierre SAGAUT Directeur de thèse
Aix-Marseille Université

I, undersigned, Jeremie Janin, hereby declare that the work presented in this manuscript is my own work, carried out under the scientific direction of Pierre Sagaut, Christophe Friess and Fabien Duval, in accordance with the principles of honesty, integrity and responsibility inherent to the research mission. The research work and the writing of this manuscript have been carried out in compliance with both the french national charter for Research Integrity and the Aix-Marseille University charter on the fight against plagiarism.

This work has not been submitted previously either in this country or in another country in the same or in a similar version to any other examination body.

Marseille 07/11/2022

Jérémie
JANIN

Signature numérique
de Jérémie JANIN
Date : 2022.11.07
10:30:49 +01'00'



Cette œuvre est mise à disposition selon les termes de la [Licence Creative Commons Attribution - Pas d'Utilisation Commerciale - Pas de Modification 4.0 International](https://creativecommons.org/licenses/by-nc-nd/4.0/).

Résumé

L'étude des écoulements turbulents intéresse un grand nombre de domaines pour des problématiques de sûreté dans des situations aussi bien naturelles qu'industrielles. Dans le cadre des études de sûreté menées par l'Institut de Radioprotection et de Sûreté Nucléaire (IRSN), une problématique importante concerne le risque de déflagration dans les locaux où une source d'hydrogène est présente ainsi que dans l'enceinte de confinement lors d'un accident de fusion du cœur d'un réacteur nucléaire. Dans ces situations, le mélange turbulent des différentes espèces gazeuses joue un rôle déterminant sur les niveaux de concentration et donc sur le risque d'inflammation et d'explosion.

L'objectif de cette thèse s'inscrit dans un contexte plus général d'amélioration des prévisions des modèles de turbulence pour l'ensemble des applications de la plateforme CALIF³S développée à l'IRSN (dispersion, déflagration, incendie, transport de polluant, ...). Il s'agit en particulier de poursuivre les développements menés pour les méthodes hybrides RANS/LES. Ces approches ont vocation à conduire à de meilleures prédictions comparativement aux modèles RANS pour un coût de calcul inférieur à celui des approches LES. L'essentiel du travail de thèse s'articule autour du développement d'une méthode de forçage volumique et de sa mise en œuvre dans un contexte hybride pour différents types d'écoulements (turbulence homogène, écoulements cisailés, ...) afin de décrire le plus correctement possible les zones de transition RANS/LES. Ces zones où le rapport entre énergie cinétique turbulente résolue et modélisée varie fortement, correspondent typiquement à la zone en aval du cône inertiel d'un jet ou à la zone de proche paroi.

La méthode de forçage volumique développée dans ce travail s'appuie sur l'enrichissement des échelles résolues de la turbulence. Dans les équations du mouvement résolu, cette approche d'enrichissement des échelles résolues revient à ajouter une vitesse synthétique à la vitesse résolue et à introduire des termes supplémentaires dits de forçage. Seuls les termes identifiés comme principalement responsables de la production d'énergie cinétique turbulente sont retenus. Dans le cadre des modèles hybrides RANS/LES, une équation de transport de l'énergie de sous-filtre est résolue. Afin d'assurer la conservation de l'énergie cinétique turbulente, la production synthétique, échue aux termes de forçage et permettant une augmentation de l'énergie cinétique turbulent résolue, est soustraite de l'équation de transport de l'énergie de sous-filtre.

La vitesse synthétique utilisée dans ce travail est basée sur la méthode Random Fourier Modes (RFM). La méthode RFM assure la construction d'un signal synthétique

homogène et isotrope. La vitesse synthétique est paramétrée à partir de grandeurs statistiques cibles telles que l'énergie cinétique turbulente et l'échelle de longueur intégrale. L'amplitude du signal synthétique est déterminée à partir d'un modèle de spectre d'énergie. Ce dernier peut être sélectionné en fonction de la physique étudiée.

La méthode d'enrichissement des échelles résolues proposée a dans un premier temps été mise en œuvre avec succès pour l'entretien d'une turbulence homogène isotrope. Dans le cas d'une turbulence homogène, la méthode s'apparente à un forçage linéaire des équations du mouvement pour la vitesse résolue. Un contrôle dynamique permet de diriger rapidement l'énergie turbulente vers un niveau cible. Dans un deuxième temps, l'intérêt et les potentialités de la technique de forçage ont été illustrés sur des simulations hybrides RANS/LES d'un jet plan représentatif d'une bouche de soufflage d'un local ventilé. Enfin, cette technique a été mise en œuvre sur des configurations d'écoulement du programme expérimental CARDAMOMETTE mené à l'IRSN, notamment afin de caractériser l'aérodynamique d'un local ventilé. Les résultats démontrent clairement la validité et les potentialités de l'approche proposée.

Mots clés : Mécanique des fluides, Turbulence, Forçage volumique, Enrichissement, Hybride RANS/LES, CARDAMOMETTE

Abstract

The study of turbulent flows is of interest in a large number of fields for safety issues in natural and industrial situations. In the context of safety studies conducted by the Institut de Radioprotection et de Sûreté Nucléaire (IRSN), an important issue concerns the risk of deflagration in premises where a source of hydrogen is present as well as in the containment during a core meltdown accident. In these situations, the turbulent mixing of the various gaseous species plays a determining role in the concentration levels and thus in the risk of ignition and explosion.

The objective of this thesis is to improve the predictions of turbulence models for all applications of the CALIF³S platform developed at IRSN (dispersion, deflagration, fire, pollutant transport,...) In particular, it is a question of continuing the developments carried out for the hybrid RANS/LES approaches. These approaches are intended to lead to better predictions compared to RANS models for a lower computational cost than LES approaches.. The main part of the thesis work is based on the development of a volume forcing method and its implementation in a hybrid context for different types of flows (homogeneous turbulence, sheared flows, ...) in order to describe as correctly as possible the RANS/LES transition zones. These zones where the ratio between resolved and modeled turbulent kinetic energy varies strongly, typically correspond to the zone downstream of the inertial cone of a jet or to the near wall zone.

The volume forcing method developed in this work is based on the enrichment of the resolved scales of turbulence. In the resolved momentum equations, this approach amounts to adding a synthetic velocity to the solved velocity and to introducing additional terms called forcing terms. Only the terms identified as mainly responsible for the production of turbulent kinetic energy are retained. In the framework of hybrid RANS/LES models, a subfilter energy transport equation is solved. In order to ensure the conservation of the turbulent kinetic energy, the synthetic production, which is due to the forcing terms and allows an increase of the solved turbulent kinetic energy, is subtracted from the subfilter energy transport equation.

The synthetic velocity used in this work is based on the Random Fourier Modes (RFM) method. It corresponds to a superimposition of Fourier modes randomly drawn on a half-sphere in Fourier space. The RFM method ensures the construction of a homogeneous and isotropic synthetic signal. The synthetic velocity is parameterized from target statistical quantities such as turbulent energy and integral length scale. The amplitude of the synthetic signal is determined from an energy spectrum model. The latter can be selected according to the physics under study.

The proposed resolved scale enrichment method was first successfully implemented for the maintenance of isotropic homogeneous turbulence. In the case of homogeneous turbulence, the method is similar to a linear forcing of the equations of motion for the resolved velocity. A dynamic control allows to quickly direct the turbulent energy towards a target level. In a second step, the interest and the potentialities of the forcing technique were illustrated on hybrid RANS/LES simulations of a plane jet representative of a ventilated room's air outlet. Finally, this technique has been implemented on flow configurations of the CARDAMOMETTE experimental program conducted at IRSN, in particular in order to characterize the aeraulics of a ventilated room. The simulation results show the viability and potential of the proposed forcing approach.

Keywords: Fluid mechanics, Turbulence, Forcing method, Enrichment, Hybrid RANS/LES, CARDAMOMETTE

*We are so busy watching out for what's just ahead of us
that we don't take time to enjoy where we are*
- Bill Watterson

À mes parents

Acknowledgements

First, I would like to express my gratitude to my supervisory team: Fabien Duval, Christophe Friess and Pierre Sagaut.

I want to start by thanking Fabien Duval, engineer/researcher at IRSN, without whom this thesis would not have been successful. His attentiveness and availability put me at ease and helped me move forward by providing me with a good working environment. His scientific skills allowed us to advance as planned on the project. I am grateful for all of his trips to Marseille and for his constant encouragement throughout our work which was a huge help.

I want to express my gratitude to Christophe Friess, associate professor at Aix-Marseille University, for helping me to achieve this thesis. I also want to thank him for his time, for all our scientific discussions and his repeated advice, as well as for being patient with me while I was sharing crazy ideas.

A special thanks goes to Pierre Sagaut, Professor at Aix-Marseille University, for ensuring the scientific direction of this thesis. His knowledge and experience has consistently served as a reliable source of guidance that has helped me develop my research. I particularly enjoyed our morning discussions on the history of the literature of turbulence.

Much appreciation to all three of you for your social and scientific skills.

Furthermore, a special thanks goes to the members of the jury, Lars Davindson, Rémi Manceau, Paola Cinnella and Benoît de Laage de Meux, for accepting to review my work and for the scientific discussions that followed.

At this point, I want to express my gratitude to the M2P2 lab for having me in their facility. I owe Michel Pognant a sincere debt of gratitude for saving me from challenging computer problems. Thanks to the administrative team, Sophie Baudin, Sadia Bouchikh and Marine Monterastelli for their help and their proactiveness. I also want to express my gratitude to Elena Rosue for all the chances she gives PhD students to promote science outside of the lab. Big thanks to my M2P2 co-workers for all the good moments! Thank you Isabelle, Jérémie, Félix, Alexandre, Yves and Hippolyte for all the laughs and debates in the office. I am also thrilled to have met outstanding scientists and friends José Luis, the boss of Marseille-Cassis (for now ...), Gabriel and Tom from the office next door. The same is true of all the people from "la cave", Thibault, Clara, Thomas, Xenia, Saïd, Gauthier, Hiseek. My thanks also go to Julien with whom this thesis journey has begun. In a nutshell, thank you all for all the

scientific and personal conversations, that proved to be a great help when wrapping up my thesis.

I would now like to thank the members of the LIE. Thanks to Jean claude Latché for his scientific advice (and also for the good hiking spots in the Pyrenees). Thanks to Fabrice Babik for his technical support. I would also like to thank Frédéric Cousin, Philippe March and Joëlle Fleurot for their review of journal and conference papers. I am also glad to have met some great people among the LIE doctoral students. Thank you Aubin, Bassem, Safir and Uday for all the days spent working from home. We were successful in forming a solid remote team, caféoooo ;).

I have probably forgotten some of them but I would like to thank everyone who has helped and supported me over the last three years.

On a more personal level, I would like to thank Kévin, my good friend and first roommate in Marseille. Thank you for allowing me to work in the best conditions, the change of room made all the difference! Then, I had the chance to meet and live with some lovely folks, Baptiste and Carla. I appreciate you getting my mind off the math so I could go enjoy Marseille. I would also like to thank Martin for his friendship and his welcome in Aix-en-Provence.

Much appreciation to Les Palois for coming to the defense and making this last weekend in Marseille unforgettable. Chouchou, Sophie, Quentin, Younes, Hélo, Julien, Arthur, Clara, Antho, Kimkey, Charlotte and Béré thank you for the last three years, you have been an incredible support day in day out.

A big thank you to my oldest friends, Aurélien, Alice, Louis and Robin for being presents in the most challenging moments.

There are no words to say how thankful I am to my parents for all their support throughout my studies and life. I truly appreciated that Philippe and Dominique came to my defense. A huge thank you to my sister, Orianne, who read the thesis to correct spelling mistakes! Thank you to Marion and Denis for their constant support since Hamburg and to Anaëlle and Xavier for their support and their welcome in Paris! I would like to thank Florence and his family for their welcome in Erlangen, which was the beginning of this amazing journey. I can't end this paragraph without mentioning Emmanuel and Léonore, my favorite team from Sweden.

Finally, I want to thank Giverny for her love, encouragement, and everything she has done for me.

Contents

Contents	13
List of Figures	15
List of Tables	19
Nomenclature	20
1 Introduction	22
1.1 Importance of turbulence modeling in safety studies	23
1.2 Turbulence modeling	24
1.2.1 Definitions	27
1.2.2 Reynolds Average Navier-Stokes Simulation	28
1.2.3 Large Eddy Simulation	35
1.2.4 Hybrid RANS/LES methods	40
1.3 Objectives and outline	47
2 Forcing method for homogeneous isotropic turbulence	49
2.1 State of the art	50
2.1.1 Forcing in spectral space	50
2.1.2 Forcing in physical space	51
2.2 Forcing based on a reconstruction-like method	52
2.2.1 Reconstruction method	55
2.2.2 Synthetic velocity	56
2.2.3 Kinetic energy monitoring	61
2.3 Forcing to sustain homogeneous isotropic turbulence	64
2.3.1 Numerical set up	65
2.3.2 Constant frequency	66
2.3.3 Influence of grid resolution	71
2.3.4 Towards more realistic frequencies	72
2.3.5 Consideration of anisotropy	74
2.4 Towards a self-adaptive forcing : Decaying isotropic turbulence	78
2.4.1 Balance of turbulent kinetic energy	78
2.4.2 Results	81
2.5 Conclusion	86
3 Forcing shear flows	88

3.1	Feature of the forcing in non-homogeneous turbulence	89
3.1.1	Divergence-free property	89
3.1.2	Target properties	90
3.1.3	Formulation of the reconstruction method	91
3.2	Planar jet	92
3.2.1	Problem description	93
3.2.2	Statistical properties of the synthetic velocity	96
3.2.3	Turbulent inlet condition and forcing	98
3.2.4	Mimicking a zonal method	101
3.2.5	Interest of the forcing for VLES	108
3.3	Conclusion	114
4	Evaluation of E-DES with forcing for flows in ventilated room	116
4.1	The CARDAMOMETTE experimental program	117
4.1.1	Objectives	117
4.1.2	Description of the facility	118
4.2	Numerical simulations of the air transfer jet	119
4.2.1	Numerical set-up	119
4.2.2	Inlet precursor simulations	119
4.2.3	Air transfer jet simulation results	124
4.3	Conclusion	131
	Conclusions and perspectives	141
	Bibliography	142
	APPENDICES	154
A	Synthetic velocity	154
A.1	Isotropy	154
A.2	Statistical homogeneity	155
A.3	Moments of the synthetic velocity	156
B	Hybridization of a RANS model	158
B.1	Overview	158
B.2	EAHSM $k-\omega$ model	158
B.3	Enforcing near-wall RANS mode using elliptic blending	159

List of Figures

1.1	Example of a geometrical singularity: the backward facing step.	46
1.2	Thesis overview. Blue text: name of chapter, italic text: objective	48
2.1	Wave vector geometry of the n^{th} Fourier mode.	56
2.2	Two-time correlation functions of the synthetic velocity.	60
2.3	Selective forcing scheme.	62
2.4	Comparison between the two forcing techniques. Time evolution of the energy and spectra.	67
2.5	Mean longitudinal correlation functions.	68
2.6	Time evolution of the longitudinal length scale for three different prescribed integral length scales $L_{ }$. (a) Prescribed Passot-Pouquet energy spectrum, (b) prescribed von Kármán-Pao energy spectrum.	68
2.7	Mean longitudinal $f(r)$ and transverse $g(r)$ correlation functions.	70
2.8	Two-time correlation function.	70
2.9	Comparison between four grid resolutions.	72
2.10	Comparison between a prescribed PP or VKP spectrum.	73
2.11	Wave vector geometry of the n^{th} Fourier mode.	75
2.12	Selective forcing at low wavenumbers: comparison between the isotropic and anisotropic.	77
2.13	Time evolution of the turbulent kinetic energy compared with the analytical decay	82
2.14	Time evolution of the subgrid turbulent kinetic energy.	83
2.15	Forcing applied to the DIT case with a prescribed VKCS energy spectrum.	84
2.16	Time evolution of (a) the dissipation and (b) the target and resolved kinetic energy ratio. Plain and dashed lines correspond respectively to the target and resolved turbulent kinetic energy ratios.	85
2.17	Energy spectra for the forcing applied to the DIT.	85
3.1	Plane jet scheme	93
3.2	Turbulent kinetic energy mapping for a slice taken at $0.5L_z$. (a) RANS computation, (b) updating synthetic velocity PP, c) updating synthetic velocity VKP	97
3.3	Turbulent kinetic energy mapping for a slice taken at $0.5L_z$. Updating synthetic velocity (a) with space dependent frequency, (b) with space independant frequency.	98
3.4	Color map of the synthetic production term near the jet inlet region.	99

3.5	(a) Axial evolution of the mean velocity at the center of the jet U_c . Comparison between the forcing method, the Turbulent IC simulation and the DNS results and LES results, (b) Axial evolution of the turbulent kinetic energy. Comparison between the forcing method, the Turbulent IC simulation, the RANS computation and the DNS results.	100
3.6	Radial profiles in the self-similar region at $x = 11d_j$. (a) Streamwise velocity fluctuations U_{rms} , (b) Normalwise velocity fluctuations V_{rms}	100
3.7	Instantaneous snapshot of the velocity magnitude. The black plain line delimits the upstream RANS domain from the downstream E-DES at the axial position $x = 30d_j$. Dashed and dotted lines represent schematically the delimitation for zonal cases $x = 6d_j$ and $x = 11d_j$	101
3.8	(a) Axial evolution of the jet half width defined by Eq. 3.5. Comparison between the forcing method, Turbulent IC and RANS simulations, (b) Axial evolution of the mean velocity excess defined by Eq. 3.6.	102
3.9	Axial evolution of the turbulent kinetic energy for the three different zonal computations. (a) total turbulent kinetic energy, (b) $x_T = 6d_j$ case, (c) $x_T = 11d_j$ case and (d) $x_T = 30d_j$ case.	103
3.10	RANS mode enforced for $x < 6d_j$. Radial profiles in the self-similarity region compared with the Turbulent IC simulation at $x = 40d_j$. (a) Mean streamwise velocity, (b) Streamwise velocity fluctuations U_{rms} , (c) Normalwise velocity fluctuations V_{rms} and (d) Spanwise velocity fluctuations W_{rms}	104
3.11	RANS mode enforced for $x < 11d_j$. Radial profiles in the self-similarity region compared to the Turbulent IC simulation at $x = 40d_j$. (a) Mean streamwise velocity, (b) Streamwise velocity fluctuations U_{rms} , (c) Normalwise velocity fluctuations V_{rms} and (d) Spanwise velocity fluctuations W_{rms}	105
3.12	RANS mode enforced for $x < 30d_j$. Radial profiles in the self-similarity region compared to the Turbulent IC simulation at $x = 40d_j$. (a) Mean streamwise velocity, (b) Streamwise velocity fluctuations U_{rms} , (c) Normalwise velocity fluctuations V_{rms} and (d) Spanwise velocity fluctuations W_{rms}	106
3.13	Map color of the synthetic production. The domain ranges from $x = 0$ to $x = 40d_j$. (a) $x = 6d_j$ case, (b) $x = 11d_j$ case and (c) $x = 30d_j$ case.	107
3.14	Comparison between the Forcing and the Turbulent IC simulation on the Coarse8 mesh grid and also compared to the Turbulent IC simulation on the reference grid. (a) Growth of the jet half-width, (b) Decay of the streamwise mean velocity excess.	109
3.15	Comparison between the Forcing and the Turbulent IC simulation on the Coarse8 mesh grid and also compared to the Turbulent IC simulation on the reference grid. (a) Total turbulent kinetic energy, (b) distribution of the total energy between the resolved part k_r and the sub grid part k_s	109

3.16	Comparison between the Forcing and the Turbulent IC simulation on the Coarse8 mesh grid and also compared to the Turbulent IC simulation on the reference grid. Mean longitudinal velocity profiles (a) Forcing, (b) Turbulent IC - Coarse8 and longitudinal Reynolds stress profiles (c) Forcing, (d) Turbulent IC - Coarse8.	111
3.17	Comparison between the Forcing and the Turbulent IC simulation on the Coarse20 mesh grid and also compared to the Turbulent IC simulation on the reference grid. (a) Growth of the jet half-width, (b) decay of the streamwise mean velocity excess.	112
3.18	Comparison between the Forcing and the Turbulent IC simulation on the Coarse20 mesh grid and also compared to the Turbulent IC simulation on the reference grid. (a) total turbulent kinetic energy, (b) distribution of the total energy between the resolved part k_r and the sub grid part k_s	112
3.19	Comparison between the Forcing and the Turbulent IC simulation on the Coarse20 mesh grid and also compared to the Turbulent IC simulation on the reference grid. Mean longitudinal velocity profiles (a) Forcing, (b) Turbulent IC - Coarse20 and longitudinal Reynolds stress profiles (c) Forcing, (d) Turbulent IC - Coarse20.	113
4.1	General view of the CARDAMOMETTE facility at IRSN Saclay	117
4.2	Sketch of the CARDAMOMETTE facility	118
4.3	Square duct flow: mean streamwise velocity (left) and secondary motion (right) along the corner bisector	121
4.4	Square duct flow: mean streamwise dimensionless vorticity $\bar{\omega}_z h / W_b$ for DNS (top left), EARSM (top right), LES (bottom left) and EAHSM (bottom right)	122
4.5	Square duct flow: turbulent kinetic energy along the corner bisector (left) and average along the streamwise direction of the target, r_k , and observed, r_k^{obs} , kinetic energy ratio (right)	123
4.6	Rectangular duct flow: mean streamwise velocity along the vertical (left) and horizontal (right) cut planes at the center of the duct	124
4.7	Rectangular duct flow: mean streamwise rms velocity along the vertical (left) and horizontal (right) cut planes at the center of the duct	125
4.8	Perspective view of vertical and horizontal cut planes (top) and side view of the vertical cut plane (bottom) of the meshing composed of 3.415 million hexahedral cells	127
4.9	Vertical cut plane passing through the middle of the vents $x = 0.85$ of the dimensionless mean (left) and rms (right) streamwise velocities for LES, SST, and EARSM (from top to bottom) models.	128
4.10	Vertical cut plane passing through the middle of the vents $x = 0.85$ of the dimensionless mean (left) and rms (right) streamwise velocities for LES, EAHSM, EAHSM-F and EAHSM-FZ (from top to bottom) models.	129

4.11	Mean streamwise velocity profiles in the vertical plane at $z = 0.05, 0.15$ and 0.2 m (top) and $z = 0.3, 0.4, 0.5$ and 0.6 m (bottom)	132
4.12	Rms velocity profiles in the vertical plane at $z = 0.05, 0.15$ and 0.2 m (top) and $z = 0.3, 0.4, 0.5$ and 0.6 m (bottom)	133
4.13	Rms velocity profiles in the vertical plane at $z = 0.05, 0.15$ and 0.2 m (top) and $z = 0.3, 0.4, 0.5$ and 0.6 m (bottom)	134
4.14	Mean streamwise velocity profiles in the horizontal plane at $z = 0.05, 0.15$ and 0.2 m (top) and $z = 0.3, 0.4, 0.5$ and 0.6 m (bottom)	135
4.15	Rms velocity profiles in the horizontal plane at $z = 0.05, 0.15$ and 0.2 m (top) and $z = 0.3, 0.4, 0.5$ and 0.6 m (bottom)	136
4.16	Mean streamwise velocity profiles in the vertical (top) and horizontal (bottom) plane at $z = 0.8, 1, 1.2, 1.4$ and 1.6 m	137
4.17	Statistical (temporal) average of the energy ratio in the vertical plane corresponding to EAHSM (top) EAHSM-F (middle) and EAHSM-FZ (bottom) model predictions	138
.1	Wave vector geometry of the n^{th} Fourier mode.	154

List of Tables

1.1	Summary table of velocity notations	27
1.2	Constants of the one equation model	40
2.1	Overview of introduced forcing techniques. $\langle \cdot \rangle$ and $\tilde{\cdot}$ represent respectively a temporal and spatial filter. $\hat{\cdot}$ represents a double spatial filter, where the second filter is explicit. T denotes the turn-over time scale.	53
2.2	Probability density functions of random variable	58
2.3	Summary table of study parameters	66
3.1	Turbulent inflow conditions for the planar jet. SL stands for Shear Layer.	95
3.2	Grid first domain - structured mesh	95
3.3	Grid second domain - structured mesh	96
3.4	Numerical parameters	96
3.5	Summary of the resulting coefficients K1, K2, C1 and C2 for the region $[10d_j; 16d_j]$	99
3.6	Summary of the resulting coefficients K1, K2, C1 and C2 for the region $[50d_j; 65d_j]$	102
3.7	Computations on the Coarse8 grid. Summary of the resulting coefficients K1, K2, C1 and C2 for the region $x \in [50d_j; 65d_j]$	110
3.8	Computations on the Coarse20 grid. Summary of the resulting coefficients K1, K2, C1 and C2 for the region $x \in [50d_j; 65d_j]$	110
4.1	RANS, LES and hybrid RANS/LES modes used for the calculations	120
4.2	Square duct parameters and simulation results	121
4.3	Air transfer jet simulation parameters	126
4.4	Cost of the calculations for RANS, LES-coarse and hybrid simulations on the same mesh employing 3.25 million cells. The time step and the mesh distribution corresponds respectively to 0.002 s and 200 cores for LES and hybrid simulations whereas, for RANS simulations, these correspond to 0.02 s and 36 cores.	130

Nomenclature

Latin characters

a_{ij}	Anisotropy tensor normalized	
D	Diffusion	$[m^2.s^{-3}]$
D_{ij}	Diffusion tensor	
d_j	Diameter of jet inlet	$[m]$
D_h	Hydraulic diameter	$[m]$
f_i^*	Instantaneous force	$[m^2.s^{-2}]$
F_i^*	Mean force	$[m^2.s^{-2}]$
\tilde{F}_i	Filtered force	$[m^2.s^{-2}]$
f_i''	Filtered force	$[m^2.s^{-2}]$
I	Turbulent intensity	
J_k	Turbulent diffusion term	$[m^2.s^{-3}]$
J_e	Turbulent diffusion term	$[m^2.s^{-4}]$
k	Total turbulent kinetic energy	$[m^2.s^{-2}]$
k^\dagger	Targeted total turbulent kinetic energy	$[m^2.s^{-2}]$
k_r	Resolved turbulent kinetic energy	$[m^2.s^{-2}]$
k_r^\dagger	Targeted resolved turbulent kinetic energy	$[m^2.s^{-2}]$
k_s	Subgrid turbulent kinetic energy	$[m^2.s^{-2}]$
k_m	Mean subgrid turbulent kinetic energy	$[m^2.s^{-2}]$
$k_{synthetic}$	Synthetic kinetic energy	$[m^2.s^{-2}]$
L_t	Integral length scale	$[m]$
$L_{ }$	Longitudinal length scale	$[m]$
L_e	Energetic eddies integral length scale	$[m]$
L_η	Kolmogorov integral length scale	$[m]$
p^*	Instantaneous pressure	$[N.m^{-2}]$
\tilde{p}	Resolved pressure	$[N.m^{-2}]$
p''	Subgrid pressure	$[N.m^{-2}]$
P	Production term	$[m^2.s^{-3}]$
P_s	Subgrid production term	$[m^2.s^{-3}]$
$p_{synthetic}$	Synthetic production term	$[m^2.s^{-3}]$
P_k	Subgrid synthetic production term	$[m^2.s^{-3}]$
P_e	Subgrid synthetic dissipation term	$[m^2.s^{-4}]$
P_{ij}	Production tensor	$[m^2.s^{-3}]$
R_{ij}	Reynolds stress tensor	$[m^2.s^{-2}]$

r_k	Kinetic energy ratio	
$r_k^{observed}$	Observed kinetic energy ratio	
S_{ij}	Normalized mean strain tensor	
\tilde{S}_{ij}	Resolved mean strain tensor	$[s^{-1}]$
T	Turn over time scale	$[s]$
T_0	Convective time	$[s]$
u_i^*	Instantaneous velocity	$[m.s^{-1}]$
U_i	Mean velocity	$[m.s^{-1}]$
\tilde{U}_i	Resolved velocity	$[m.s^{-1}]$
\tilde{u}_i	Fluctuating resolved velocity	$[m.s^{-1}]$
u_i''	Subgrid velocity	$[m.s^{-1}]$
u_i	Fluctuating velocity	$[m.s^{-1}]$
u_i^s	Synthetic velocity	$[m.s^{-1}]$

Greek characters

ϵ	Total dissipation	$[m^2.s^{-3}]$
ϵ_r	Resolved dissipation	$[m^2.s^{-3}]$
ϵ_m	Mean resolved dissipation	$[m^2.s^{-3}]$
ϵ_s	Subgrid dissipation	$[m^2.s^{-3}]$
ϵ_{SGS}	Estimation of the subgrid dissipation	$[m^2.s^{-3}]$
Δ	Mesh size	$[m]$
δ_{ij}	Kronecker symbol	
κ	Wavenumber	$[m^{-1}]$
κ_{cut}	Cutoff wavenumber	$[m^{-1}]$
ν	Kinematic viscosity	$[m^2.s^{-1}]$
ν_t	Turbulent viscosity	$[m^2.s^{-1}]$
Π_{ij}	Redistribution tensor	$[m^2.s^{-3}]$
ρ	density	$[kg.m^{-3}]$
τ_{ij}	Subgrid stress tensor	$[s^{-1}]$
ω	Frequency	$[s^{-1}]$
Ω_{ij}	Normalized mean rotation tensor	

Non-dimensional numbers

Re	Reynolds number
Re_t	Turbulent Reynolds number
Re_b	Bulk Reynolds number
Re_τ	Friction Reynolds number
S_t	Turbulent Strouhal number

1. Introduction

Table of contents

1.1	Importance of turbulence modeling in safety studies	23
1.2	Turbulence modeling	24
1.2.1	Definitions	27
1.2.2	Reynolds Average Navier-Stokes Simulation	28
1.2.2.1	First order models	28
1.2.2.2	Reynolds stress models	32
1.2.2.3	Explicit algebraic Reynolds stress models	33
1.2.3	Large Eddy Simulation	35
1.2.3.1	Algebraic viscosity models	37
1.2.3.2	Transport equation models - Deardorff	38
1.2.4	Hybrid RANS/LES methods	40
1.2.4.1	Zonal approaches	41
1.2.4.2	Seamless approaches	42
1.2.4.3	Importance of forcing	45
1.3	Objectives and outline	47

This first chapter aims at highlighting the interest of volume forcing methods for hybrid RANS/LES methods. The first part of this chapter recalls the need for IRSN to rely on CFD tools. In the context of IRSN investigations, the quality of the data provided by these CFD tools is particularly dependent on turbulence modeling. The presentation of the various approaches for modeling turbulence takes up the second part of this chapter and thus allows for the opportunity to emphasize the value of volume forcing. In the final section, the thesis's goal and sub-goals are outlined.

1.1. Importance of turbulence modeling in safety studies

Safety studies Many safety studies carried out at the Institut de Recherche et de Sûreté Nucléaire (IRSN) involve turbulence phenomena. Safety issues of interest include for instance *(i)* the formation of an explosive atmosphere (ATEX) in the case of a release of flammable species within either a ventilated room or within the containment vessel during a severe accident, *(ii)* the transport and the deposition of aerosols in ventilation networks and *(iii)* atmospheric dispersion related to the discharge from chimneys.

The case *(i)* of a release of flammable species within a ventilated room or within the containment vessel during a severe accident is of great interest. As an illustration, on March 11th, 2011, an earthquake followed by a tsunami caused the nuclear accident at the Fukushima Daiichi nuclear power plant. Three of the nuclear reactor cores melted down and several spent fuel pool unit lost their cooling system resulting in some fuel damage in storage ponds. Several explosions followed due to the accumulation of hydrogen in the upper part of the reactor buildings which resulted from the competition between buoyancy and turbulent mixing. Hydrogen was formed by oxidation of the zirconium alloys and enters the reactor building via uncontrolled leakage paths.

Moving to the deposition of aerosols in ventilation networks *(ii)*, depending on the duct geometry and on the characteristic size of aerosols, turbulence will be a significant factor. Aerosols produced by a nuclear power plant are released into the environment after passing through ventilation networks and air filters during operation or during an accident phase. These air ducts have different geometries including for example 90° bends (Breuer, Baytekin, and Matida 2006). Predicting the aerosol deposition in this kind of arrangement is crucial. This may affect the effectiveness or clogging of air filters.

Finally, in the case of atmospheric dispersion *(iii)*, gaseous species that are discharged through chimneys might spread over an urban area. Atmospheric dispersion may significantly be influenced in this case by building layout. Building layouts, for instance, may result in recirculation areas. Consequently, it is crucial to have a thorough grasp of the turbulence mechanisms at play (Tominaga and Stathopoulos 2013).

Modeling strategies Safety studies are conducted following various approaches depending on the complexity and on the background of the studied case. These approaches are based on experimental measurements and physical models starting from integral models to more sophisticated numerical tools. Focusing on the ATEX issue mentioned above, one distinguish typically three types of physical modeling approaches together with experimental data employing either real materials (hydrogen, ...) or surrogates (helium, ...). The three main physical modeling approaches correspond to:

- i) instantaneous dilution assumption (see for instance Taveau 2011),
- ii) lumped parameter approach that consists roughly in modeling the situation of interest using sub-domains described by mean quantities (concentration, ...) in which different integral models apply,
- iii) Computational Fluids Dynamic (CFD) approaches.

Depending on the situation, typically the characteristics of the ventilated room (geometry, admission and extraction locations, ...), the instantaneous dilution approach may fail to predict the ATEX related risk (Taveau 2011). In the same way, the lumped parameter approach may lead to poor predictions in situations where integral models are no longer valid (*e.g* strong stratification, highly geometrical dependent turbulent eddies). In such situations, CFD numerical tools are expected to provide more reliable results.

Key point: turbulence modeling According to the degree of mixing in the containment vessel, the release and dispersion of hydrogen lead to a distribution of hydrogen with a strong stratification (Bentaib, Meynet, and Bleyer 2015). This stratification may result in regions where the gas flammability limits are exceeded. In such cases, numerical tools that presuppose a homogeneous mixing (*i.e.* lumped parameter approach) of the gaseous species considered are inadequate. IRSN is therefore turning to CFD tools to obtain physical quantities (velocity, pressure, temperature, ...) at each location in space and time. The turbulent mixing of the different gaseous species plays a determining role on the concentration levels of hydrogen and thus on the risk of ignition and explosion of the gaseous mixture. Moreover, the prediction of the severity of deflagrations requires a sufficiently precise evaluation of the turbulent kinetic energy level to quantitatively predict the flame propagation velocities and the corresponding overpressures. As a result, the accuracy of the CFD simulation will be greatly influenced by the turbulence model's reliability in simulating the phenomena that are at play (shear, buoyancy, ...).

Emphasis of this work This work focuses on improving the predictions of turbulence models for all applications of the CALIF³S platform developed at IRSN. In particular, this thesis is part of the development of the P²REMICS (Partially PRE-Mixed Combustion Solver) which is an in-house CFD software. This CFD software is a component of IRSN's plan for carrying out studies on gas dispersion and explosions/deflagrations.

1.2. Turbulence modeling

There are essentially three types of approaches to numerical simulation of turbulence :

1. Introduction – 1.2. Turbulence modeling

- i) Direct Numerical Simulation (DNS) consists in solving the Navier-Stokes equations without any modeling. In this case, all length scales (characteristic length scale of eddies) and time scales (characteristic turnover time scale of eddies) are solved. Typically, the range of length scales of eddies is bounded in the upper part by the geometry of the studied flow (diameter of the ventilation duct, dimensions of the room, ...) and in the lower part by the Kolmogorov scale where the viscous dissipation takes place,
- ii) On the other hand, the RANS approach for *Reynolds-Averaged Navier-Stokes* adopts a purely statistical point of view and consists in modeling all the characteristic scales of the turbulence. The local instantaneous quantities (velocity, pressure, ...) are decomposed into an average and fluctuating part according to the Reynolds decomposition, for example for the velocity $u_i^* = U_i + u_i$. The application of this statistical averaging operator and the Reynolds decomposition leads to the RANS equations for the mean flow which can be solved based on a modeling of the $\overline{u_i u_j}$ correlations called Reynolds tensions,
- iii) Finally, the Large Eddy Simulation (LES), can be seen schematically as an intermediate approach consisting in solving in a "direct" way the large scales of the flow, whose characteristics depend on the considered flow (anisotropy due to the geometry, ...), and modeling the small ones which have a more universal character. While the so-called filtered Navier-Stokes equations for the resolved velocity \tilde{u}_i are formally similar to the RANS equations, they are very different in nature and allow to access like the DNS to many statistical properties of the resolved field on the basis of a modeling of the $\overline{u_i u_j} - \tilde{u}_i \tilde{u}_j$ terms called subgrid¹ stresses.

These three approaches proceed schematically in different cuttings of the turbulent energy spectrum. This energy spectrum, obtained by Fourier transform of the velocity signal, is represented on a range of wave numbers (in the case of the spatial spectrum) or frequencies (in the case of the temporal spectrum). It usually comprises three distinct zones. The first region corresponds to the production zone which contains the most energetic structures generated by the mean flow (shear, ...) up to a maximum of energy which occurs for $\kappa \simeq 2\pi/L_t$ where L_t is the integral length scale. The second zone corresponds to the so-called inertial zone, more or less extended according to the Reynolds number, with a constant slope $\kappa^{-5/3}$, where the turbulent kinetic energy schematically cascades mainly from large structures to smaller ones. Finally, the last zone corresponds to the viscous dissipation zone. Thus, one distinguishes schematically three types of description :

- i) In the case of a DNS, the entire set of wave numbers is resolved,
- ii) On the contrary, a RANS method proposes a modeling on the whole range of wave numbers. However, depending on the studied flow, RANS or URANS (for

1. and sometimes, *subfilter*

Unsteady Reynolds-Averaged Navier-Stokes) methods are able to describe a small part of the energy spectrum for low wavenumbers (or frequencies),

- iii) Finally, LES results from the application of a low-pass filter where the wavenumbers higher than a cutoff wavenumber κ_{cut} correspond to the subfilter scales for which a modeling must be proposed.

These methods have different purposes and are potentially complementary. Typically, DNS provides predictive results in the absence of modeling on many statistical properties of the flow (turbulent kinetic energy, spatio-temporal correlations, ...) but on the other hand the numerical cost is very important. Indeed, the number of meshes required to perform a direct numerical simulation is of the order of $Re_t^{9/4}$, where Re_t represents the turbulent Reynolds number. This makes it difficult to use it for the release and dispersion of explosive gases since flows studied generally have very large Reynolds numbers (of the order of 10^4 - 10^5). This would require running a simulation on billions of points, which is eventually possible, but of little interest due to the large number of cases studied. More crucially, the time constants for gas dispersion are on the order of many hours. This necessitates running simulations with very extensive computation duration. Consequently, DNS are restricted in practice to a very limited flow cases that represent a particular flow situation at a lower Reynolds number (impinging region, beginning of jet spreading, ...) to provide detailed data for the development and the validation of RANS and LES approaches.

On the other hand, a RANS approach has an affordable computational cost in many cases of interest. However, its intrinsic empiricism may lead to poorly predictive results in some situations. Most of usual RANS models have been calibrated to give good results for the mean field through the calculation of a turbulent eddy viscosity. The latter is estimated from a turbulent kinetic energy and a characterise length scale. These two variables together allow for the accurate determination of eddy viscosity, but when viewed separately, they may yield inaccurate results. Another flaw in these models is that they accurately predict the jet half-width evolution for a planar jet but not for a round jet (Launder, Morse, Rodi, et al. 1972). Nevertheless, developments on RANS-type models with advanced Reynolds stresses modelling (second-order or algebraic modeling) are still underway and offer promising interesting perspectives.

In contrast to these models, which sometimes have to be used on a case-by-case bases, it seems interesting to use LES models. The LES approach is schematically situated between DNS and RANS approaches. It allows to capture the unsteadiness of the flow over a wide range of frequencies and is considered as a reliable method on fine enough meshes. This approach provides predictive results for the assessment of turbulent kinetic energy levels in the case of the round and planar jet. However, when studying flows with walls such as a jet in a ventilated room, this approach has the disadvantage of having a huge numerical cost. This is one of the motivations for the development of hybrid RANS/LES approaches. The idea of being able to model the near-wall region using a RANS approach and the large scale vortices far from the wall

using a LES approach is appealing. After introducing RANS and LES methodologies, the remainder of this chapter discusses these so-called hybrid methods.

1.2.1. Definitions

This section follows the overview proposed by Chaouat and Schiestel 2009 who produced a very clear summary of RANS and LES methodologies with a focus on hybrid methods. It is important to remember the initial equations that define the temporal and spatial evolution of an incompressible flow before introducing the various models of turbulence. Under the assumptions of a Newtonian fluid and an incompressible flow, the Navier-Stokes equations employed to describe the temporal and spatial evolution of the flow read:

$$\frac{\partial u_i^*}{\partial x_i} = 0 \quad (1.1)$$

$$\frac{\partial u_i^*}{\partial t} + \frac{\partial u_i^* u_j^*}{\partial x_j} = -\frac{1}{\rho} \frac{\partial p^*}{\partial x_i} + \nu \frac{\partial^2 u_i^*}{\partial x_j \partial x_j} + f_i^* \quad (1.2)$$

in which u_i^* , p^* and f_i^* represent instantaneous quantities which are respectively the velocity, pressure and an external force. The physical parameters of the considered fluid are defined by the density and the cinematic viscosity.

For the sake of clarity, notations of the various velocities (mean, fluctuating, ...) are recalled in Tab. 1.1, resulting in the following relationship:

$$u_i^* = \tilde{U}_i + u_i'' = U_i + \tilde{u}_i + u_i'' = U_i + u_i \quad (1.3)$$

Notation	Name
u_i^*	Instantaneous velocity
$U_i = \overline{u_i^*}$	Mean velocity
$\tilde{U}_i = \langle u_i^* \rangle$	Resolved velocity
$\tilde{u}_i = \tilde{U}_i - U_i$	Fluctuating resolved velocity
u_i''	Subgrid velocity
u_i	Fluctuating velocity
p^*	Instantaneous pressure
\tilde{p}	Fluctuating resolved pressure
p''	Subgrid pressure

Table 1.1. – Summary table of velocity notations

1.2.2. Reynolds Average Navier-Stokes Simulation

Introducing the Reynolds decomposition of an instantaneous variable $A^*(\mathbf{x}, t)$ (O. Reynolds 1895):

$$A^*(\mathbf{x}, t) = A(\mathbf{x}, t) + a(\mathbf{x}, t) \quad (1.4)$$

in which $a(\mathbf{x}, t)$ is the fluctuating part and $A(\mathbf{x}, t)$ the statistical mean defined as:

$$\overline{A^*(\mathbf{x}, t)} = \lim_{R \rightarrow +\infty} \frac{1}{R} \sum_{i=1}^R A_i^*(\mathbf{x}, t) \quad (1.5)$$

where $A_i^*(\mathbf{x}, t)$ represents one realization and R is the number of realization. The overbar denotes therefore a statistical-averaged quantity. The main properties of the Reynolds operator are:

- i) preservation of constants $\overline{C} = C$,
- ii) additivity $\overline{A^* + B^*} = \overline{A^*} + \overline{B^*}$,
- iii) idempotence $\overline{\overline{A^*}} = \overline{A^*}$,
- iv) commutivity with differential operators $\overline{\frac{\partial A^*}{\partial t}} = \frac{\partial \overline{A^*}}{\partial t}$.

In RANS computations, the ensemble average introduced in Eq. 1.5 is often reduced to a time average using an ergodic assumption. In this case, the variable is averaged over a certain period that must be larger than the turn over time scale T . The latter being a characteristic period that can be interpreted as the length of time it takes for the biggest vortex structures to fully rotate.

Applying Reynolds's averaging operator on the Navier-Stokes equations (Eq. 1.1 and Eq. 1.2), the Reynolds-averaged transport equations governing the flow read:

$$\frac{\partial U_i}{\partial x_i} = 0 \quad (1.6)$$

$$\frac{\partial U_i}{\partial t} + \frac{\partial U_i U_j}{\partial x_j} = -\frac{1}{\rho} \frac{\partial \overline{p^*}}{\partial x_i} + \nu \frac{\partial^2 U_i}{\partial x_j \partial x_j} + F_i - \frac{\partial \overline{u_i u_j}}{\partial x_j} \quad (1.7)$$

The last term of the right hand side of Eq. 1.7 is commonly referred to as the Reynolds stress tensor. It is unknown, and therefore has to be modeled to close the system of equations.

1.2.2.1. First order models

First order model are based on Boussinesq's hypothesis, which relates the momentum turbulent fluxes to the mean velocity gradients as:

1. Introduction – 1.2. Turbulence modeling

$$\overline{u_i u_j} = -\nu_t \left(\frac{\partial U_i}{\partial x_j} + \frac{\partial U_j}{\partial x_i} \right) + \frac{2}{3} k \delta_{ij} \quad (1.8)$$

through the use of an eddy viscosity ν_t , that remains to be specified. k is the turbulent kinetic energy $k = \frac{1}{2} \overline{u_i u_i}$. The eddy diffusivity is generally built as the product of a velocity scale and a length scale. These scales have then to be estimated either from the mean flow behavior through algebraic relations, or by solving additional transport equations. Typically, the former corresponds to mixing length models while the latter corresponds to two-equations models.

The $k - \epsilon$ model The main model employed in this work is the two equations $k - \epsilon$ model developed at first by Jones and Launder 1972. In this case, the eddy viscosity is expressed as:

$$\nu_t = C_\mu \frac{k^2}{\epsilon} \quad (1.9)$$

and the transport equation for turbulent kinetic energy k and the dissipation rate ϵ read:

$$\frac{\partial k}{\partial t} + \frac{\partial U_j k}{\partial x_j} = P - \epsilon + J_k \quad (1.10)$$

$$\frac{\partial \epsilon}{\partial t} + \frac{\partial U_j \epsilon}{\partial x_j} = \frac{\epsilon}{k} (C_{\epsilon 1} P - C_{\epsilon 2} \epsilon) + J_\epsilon \quad (1.11)$$

in which P is the production term and $C_{\epsilon 1}$ and $C_{\epsilon 2}$ are constants. It is worth noticing that the k -equation (Eq. 1.10) is exact. Although one can derive the exact form of the ϵ equation, it contains many higher order correlations and the equation is very complex. Therefore, several authors (Harlow and Nakayama 1968 and Hanjalic 1970) chose to go towards a model analog to the k -equation: Convection = Production - Destruction + Diffusion. For both transport equations, unknown correlations have to be modelled based on known quantities U_i , k and ϵ . The turbulent diffusion terms J_k and J_ϵ are expressed with a gradient hypothesis:

$$J_k = \frac{\partial}{\partial x_j} \left[\left(\nu + \frac{\nu_t}{\sigma_k} \right) \frac{\partial k}{\partial x_j} \right] \quad (1.12)$$

$$J_\epsilon = \frac{\partial}{\partial x_j} \left[\left(\nu + \frac{\nu_t}{\sigma_\epsilon} \right) \frac{\partial \epsilon}{\partial x_j} \right] \quad (1.13)$$

The production term reads:

$$P = -\overline{u_i u_j} \frac{\partial U_i}{\partial x_j} = 2\nu_t S_{ij} S_{ij} \quad (1.14)$$

This is now a closed system of equations which can be solved numerically. The constants that have been introduced (C_μ , $C_{\epsilon 1}$, $C_{\epsilon 2}$, σ_k and σ_ϵ) are determined from experience or DNS computation. For example, the constant C_μ is determined from flows in local equilibrium ($P \sim \epsilon$). The constant $C_{\epsilon 2}$ is determined from a grid turbulence experiment (isotropic turbulence). After optimization and careful evaluation with further experiments (mixing layer, jets, ...) the set of constants for the $k - \epsilon$ turbulence model is as follows:

$$C_\mu = 0.09, \quad C_{\epsilon 1} = 1.44, \quad C_{\epsilon 2} = 1.92, \quad \sigma_k = 1, \quad \sigma_\epsilon = 1.3 \quad (1.15)$$

As mentioned previously, these constants have to be changed in some situations such as axisymmetric jet ($C_{\epsilon 2}, C_\mu$), when P and ϵ differ strongly from each other, or for small turbulent Reynolds number ($0 < Re_t < 10$).

The $k - \omega$ model Alternative models have been developed to overcome some of the shortcomings of the $k - \epsilon$ model. One such model is the $k - \omega$ model. Similar to the $k - \epsilon$ model, the first transported variable is the turbulent kinetic energy, k . The second transported variable is the specific dissipation rate. It was initially proposed by Wilcox 1988. Its major shortcoming is its sensitivity to freestream boundary conditions for free shear flows. This motivated the development of Menter's Baseline (BSL) $k - \omega$ model of F. R. Menter 1992 which consists in a blending of:

- Wilcox's $k - \omega$ model in the inner region (nearest to the wall),
- the $k - \epsilon$ model, however transformed in some equivalent $k - \omega$ through the change of variable $\omega = \epsilon / (\beta^* k)$

The function F_1 is designed to take a value of one in the near wall region (activating the original $k - \omega$ model) and zero away from the wall, usually in the outer wake region. F_1 is written as:

$$F_1 = \tanh(ar g_1^4) \quad (1.16)$$

with

$$ar g_1 = \min \left(\max \left(\frac{\sqrt{k}}{\beta^* \omega y}, \frac{500\nu}{y^2 \omega} \right); \frac{4\rho\sigma_{\omega 2} k}{CD_{k\omega} y^2} \right) \quad (1.17)$$

The first term in Eq. 1.17 corresponds to the ratio of turbulent length scale, L_t to the shortest distance to the wall, y . The second argument provides a lower limit for the function F_1 ensuring that this function does not go to zero in the viscous sublayer. The third argument is an additional safeguard against the "degenerate" solution of the original $k - \omega$ model with small freestream values for ω in free shear flows where the inclusion of a lower limit for ω is impossible F. R. Menter 1993.

The original $k - \omega$ model is multiplied by F_1 and the transformed model by the function $1 - F_1$. The model constants are given through the equation

$$\phi = F_1 \phi_1 + (1 - F_1) \phi_2 \quad (1.18)$$

where, ϕ_1 represents any constant in the original model, ϕ_2 represents its counterpart

constant in the transformed model and ϕ is the corresponding constant in the new model. This method gives rise to Menter's BSL model:

$$\frac{dk}{dt} = P - \beta^* \omega k + \frac{\partial}{\partial x_j} \left[(v + \sigma_k v_t) \frac{\partial k}{\partial x_j} \right] \quad (1.19)$$

$$\frac{d\omega}{dt} = \gamma \frac{\omega}{k} P - \beta \omega^2 + \frac{\partial}{\partial x_j} \left[(v + \sigma_\omega v_t) \frac{\partial \omega}{\partial x_j} \right] + \underbrace{2(1 - F_1) \sigma_{\omega_2} \frac{1}{\omega} \frac{\partial k}{\partial x_j} \frac{\partial \omega}{\partial x_j}}_{CD_{k\omega}} \quad (1.20)$$

with the model constants

$$\sigma_{k_1} = 0.4968, \quad \sigma_{\omega_1} = 0.5, \quad \beta_1 = 0.075, \quad \beta^* = 0.09, \quad \gamma_1 = 0.55 \quad (1.21)$$

It is worth paying attention to the *cross-derivative* term $CD_{k\omega}$ arising from the use of a $k - \epsilon$ branch in Menter's baseline $k - \omega$ model

$$CD_{k\omega} = \max \left(2\sigma_{\omega_2} \frac{1}{\omega} \frac{\partial k}{\partial x_j} \frac{\partial \omega}{\partial x_j}, CD_{k\omega, \min} \right) \quad (1.22)$$

$CD_{k\omega}$ is the positive portion of the cross-diffusion term present in the transformed ϵ equation. Menter has used 10^{-20} as the value for $CD_{k\omega, \min}$. Later, Hellsten 1998 stated that the choice of such a small value for $CD_{k\omega, \min}$ may lead to a bad numerical behavior of the turbulence model and can introduce undesirable rise of the blending function F_1 back to a value of 1 around the outer edge of the boundary layer. To obtain a better behavior, Hellsten made $CD_{k\omega, \min}$ proportional to the maximum value of the cross-diffusion term in each grid-block instead of the maximum value of the whole flow field. This maximum value is then multiplied by a factor of 10^{-8} to obtain a proper value for $CD_{k\omega, \min}$.

The production term P in Eqs. 1.19-1.20 is specified by Eq. 1.14. To prescribe the eddy viscosity, further concerns need to be accounted for, such as separation in flows with strong adverse pressure gradient. In such flows, linear eddy viscosity models tend to overpredict the main turbulent shear stress. Thus, F. Menter 1994 in his Shear Stress Transport (SST) formulation, introduces an upper bound for the principal shear-stresses. The SST model is similar to the BSL model except for a limiter introduced in the SST formulation. The SST limiter is suitable only for wall-bounded flows, *i.e.*, for high values of S . But in case of free shear flows, the SST limitation has to be switched off. Similar to F_1 , a blending function F_2 is used in the SST model. F_2 is given by:

$$F_2 = \tanh(\text{arg} g_2^2) \quad (1.23)$$

with,

$$\text{arg} g_2 = \max \left(\frac{2\sqrt{k}}{\beta^* \omega y}; \frac{500\nu}{y^2 \omega} \right) \quad (1.24)$$

with ν_t given as:

$$\nu_t = \frac{a_1 k}{\max(a_1 \omega; F_2 S)} \quad (1.25)$$

with $a_1 = 0.31$.

1.2.2.2. Reynolds stress models

On the other hand, transport equations for turbulent fluxes form the basis of second order or differential Reynolds-stress models. These equations are obtained by multiplying the transport equation of the velocity fluctuations u_i (resp. u_j) by u_j (resp. u_i), summing the arising equations, and then averaging the result. The resulting transport equations read:

$$\frac{\partial \overline{u_i u_j}}{\partial t} + \frac{\partial U_k \overline{u_i u_j}}{\partial x_k} - D_{ij} = P_{ij} + \Pi_{ij} - \epsilon_{ij} \quad (1.26)$$

where D_{ij} , P_{ij} , Π_{ij} and ϵ_{ij} refer respectively to diffusion, production, pressure redistribution and dissipation of the Reynolds stresses. The production term reads

$$P_{ij} = -\overline{u_i u_k} \frac{\partial U_j}{\partial x_k} - \overline{u_j u_k} \frac{\partial U_i}{\partial x_k} \quad (1.27)$$

The dissipation rate tensor is assumed to be isotropic and thus reads

$$\epsilon_{ij} = \frac{2}{3} \epsilon \delta_{ij} \quad (1.28)$$

The pressure redistribution term is expressed following the model proposed by Rotta 1951 for the slow pressure strain and Launder, Reece, and Rodi 1975 for the rapid part

$$\begin{aligned} \Pi_{ij} = & -c_1 \frac{\epsilon}{k} \left(\overline{u_i u_j} - \frac{2}{3} k \delta_{ij} \right) - \frac{c_2 + 8}{1} \left(P_{ij} - \frac{2}{3} P_{kk} \delta_{ij} \right) \\ & - \frac{30c_2 - 2}{55} k \left(\frac{\partial U_i}{\partial x_j} + \frac{\partial U_j}{\partial x_i} \right) - \frac{8c_2 - 2}{11} \left(-\overline{u_i u_j} \frac{\partial U_k}{\partial x_j} - \overline{u_j u_k} \frac{\partial U_i}{\partial x_j} - \frac{1}{3} P_{kk} \right) \end{aligned} \quad (1.29)$$

where c_1 and c_2 are constants that remain to be specified. The transport equation for the turbulent kinetic energy k is obtained by taking half the trace of Eq. 1.26 and can be written as

$$\frac{dk}{dt} - D = P - \epsilon \quad (1.30)$$

where the production term given by Eq. 1.14, is recovered:

$$P = \frac{1}{2} P_{ii} = -\overline{u_i u_j} \frac{\partial U_i}{\partial x_j} \quad (1.31)$$

More physics is present in second order models, but modeling third order moments and solving four extra differential equations (compared to two equations models) are

required.

1.2.2.3. Explicit algebraic Reynolds stress models

Algebraic models are based on the weak-equilibrium assumption, which asserts that the advection and diffusion of the dimensionless Reynolds-stress anisotropy tensor can be omitted. This means that the first step is to formulate the transport equations for the Reynolds stresses in terms of the dimensionless anisotropy tensor denoted by

$$a_{ij} = \frac{\overline{u_i u_j}}{k} - \frac{2}{3} \delta_{ij} \quad (1.32)$$

The weak-equilibrium assumption consists of two equations:

$$\frac{da_{ij}}{dt} = 0 \quad (\text{anisotropy equilibrium}) \quad (1.33)$$

$$\frac{D_{ij}}{D} = \frac{\overline{u_i u_j}}{k} \quad (\text{alignment between diffusion and anisotropy}) \quad (1.34)$$

The transport equation for the dimensionless anisotropy tensor reads

$$\frac{da_{ij}}{dt} = \frac{1}{k} \frac{d\overline{u_i u_j}}{dt} - \frac{\overline{u_i u_j}}{k} \frac{dk}{dt} \quad (1.35)$$

Then, from Eqs. 1.26, 1.30 and 1.35, the previous equation can be written as

$$\frac{da_{ij}}{dt} - \frac{1}{k} \left(D_{ij} - \frac{\overline{u_i u_j}}{k} D \right) = \frac{1}{k} \left(P_{ij} + \Pi_{ij} - \frac{2}{3} \epsilon \delta_{ij} - \frac{\overline{u_i u_j}}{k} (P - \epsilon) \right) \quad (1.36)$$

Using the weak-equilibrium assumption, the left-hand side of the previous equation is removed and the resulting algebraic equations read

$$\frac{\overline{u_i u_j}}{k} (P - \epsilon) = P_{ij} + \Pi_{ij} - \frac{2}{3} \epsilon \delta_{ij} \quad (1.37)$$

This equation can be written in terms of a_{ij} , S_{ij} and Ω_{ij} where S_{ij} and Ω_{ij} denote respectively the mean strain and the mean rotation tensor normalized with the turbulent time scale $T = k/\epsilon$

$$S_{ij} = \frac{T}{2} \left(\frac{\partial U_i}{\partial x_j} + \frac{\partial U_j}{\partial x_i} \right), \quad \Omega_{ij} = \frac{T}{2} \left(\frac{\partial U_i}{\partial x_j} - \frac{\partial U_j}{\partial x_i} \right) \quad (1.38)$$

Inserting a_{ij} , S_{ij} and Ω_{ij} in the definition of the production and redistribution terms leads to the following expressions

$$\frac{P_{ij}}{\epsilon} = -\frac{4}{3} S_{ij} - (a_{ik} S_{kj} + S_{ik} a_{kj}) + a_{ik} \Omega_{kj} - \Omega_{ik} a_{kj} \quad (1.39)$$

$$\begin{aligned} \frac{\Pi_{ij}}{\epsilon} = & -c_1 a_{ij} + \frac{4}{5} S_{ij} + \frac{9c_2 + 6}{11} \left(a_{ik} S_{kj} + S_{ik} a_{kj} - \frac{2}{3} a_{km} S_{mk} \delta_{ij} \right) \\ & + \frac{7c_2 - 10}{11} (a_{ik} \Omega_{kj} - \Omega_{ik} a_{kj}) \end{aligned} \quad (1.40)$$

As a result, the algebraic equation for the Reynolds stress anisotropy tensor reads

$$\begin{aligned} \left(c_1 - 1 + \frac{P}{\epsilon} \right) a_{ij} = & -\frac{8}{15} S_{ij} + \frac{7c_2 + 1}{11} (a_{ik} \Omega_{kj} - \Omega_{ik} a_{kj}) \\ & - \frac{5 - 9c_2}{11} \left(a_{ik} S_{kj} + S_{ik} a_{kj} - \frac{2}{3} a_{km} S_{mk} \delta_{ij} \right) \end{aligned} \quad (1.41)$$

According to Wallin and Johansson 2000, the value of c_2 close to $5/9$ recommended by several studies enables to disregard the last term in the right hand side of Eq. 1.41 and substantially simplifies the algebraic equation. Adopting this value results in the Reynolds stress anisotropy tensor with the following implicit but streamlined algebraic relation.

$$N a_{ij} = c_1 S_{ij} + (a_{ik} \Omega_{kj} - \Omega_{ik} a_{kj}) \quad (1.42)$$

where $c_1 = 6/5$ and N is a function of a_{ij} that reads

$$\begin{aligned} N = & \frac{9}{4} \left(c_1 - 1 + \frac{P}{\epsilon} \right) \\ = & \frac{9}{4} (c_1 - 1 - a_{km} S_{km}) \end{aligned} \quad (1.43)$$

Assuming that the coefficient N is known up front, the process for solving the implicit equation for a_{ij} follows. The Cayley-Hamilton theorem can be used to solve the resulting linear equation. The nonlinear equation for N must then be solved as the last step. Introducing $\mathbf{s} \equiv c_1 \mathbf{S}/N$ and $\mathbf{o} \equiv \mathbf{\Omega}/N$, the implicit relation, Eq. 1.42, is first rewritten as

$$\mathbf{a} = -\mathbf{s} + (\mathbf{a}\mathbf{o} - \mathbf{o}\mathbf{a}) \quad (1.44)$$

Following the direct procedure suggested by Grigoriev and Lazeroms 2016, the first step consists of formulating the dimensionless Reynolds-stresses anisotropy tensor in terms of the dimensionless mean strain tensor S_{ij} and the dimensionless mean rotation Ω_{ij} . The procedure for two-dimensional mean flows is presented hereafter. The procedure remains the same for three-dimensional mean flows.

The first step to derive an algebraic equation for the dimensionless Reynolds-stress anisotropy tensor is to write the first recursive usage of the implicit relation, Eq. 1.44, which results in

$$\mathbf{a} = -\mathbf{s} + (\mathbf{s}\mathbf{o} - \mathbf{o}\mathbf{s}) + (\mathbf{a}\mathbf{o}^2 + \mathbf{o}^2\mathbf{a} - 2\mathbf{o}\mathbf{a}\mathbf{o}) \quad (1.45)$$

Recalling that the Cayley-Hamilton theorem for a two-dimensional traceless tensor

states the following

$$\mathbf{c}^2 = \frac{1}{2} II_c \mathbf{I}, \quad II_c = \text{Tr}\{\mathbf{c}^2\} \quad (1.46)$$

one can use it to represent the last term in the right hand side of Eq. 1.45. Substituting $\mathbf{c} = \mathbf{a} + \mathbf{o}$ into Eq. 1.46 leads to

$$\mathbf{a}\mathbf{o} + \mathbf{o}\mathbf{a} = \text{Tr}\{\mathbf{a}\mathbf{o}\} \mathbf{I} \quad (1.47)$$

As \mathbf{a} is symmetric and \mathbf{o} is antisymmetric, the right hand side of Eq. 1.47 is zero and this allows to get

$$\mathbf{a}\mathbf{o}^2 + \mathbf{o}^2\mathbf{a} = -2\mathbf{o}\mathbf{a}\mathbf{o} \quad (1.48)$$

Finally, substituting $\mathbf{c} = \mathbf{o}$ into Eq. 1.46 and multiplying by \mathbf{a} leads to

$$\mathbf{a}\mathbf{o}^2 + \mathbf{o}^2\mathbf{a} = II_o \mathbf{a} \quad (1.49)$$

The resulting algebraic relation is as follows:

$$(1 - 2II_o) \mathbf{a} = -\mathbf{s} + (\mathbf{s}\mathbf{o} - \mathbf{o}\mathbf{s}) \quad (1.50)$$

The resulting expression is formally equivalent to the common expression presented by Wallin and Johansson given by substituting $\mathbf{s} \equiv c_1 \mathbf{S}/N$ and $\mathbf{o} \equiv \mathbf{\Omega}/N$:

$$a_{ij} = \beta_1 S_{ij} + \beta_4 (S_{ik} \Omega_{kj} - \Omega_{ik} S_{kj}) \quad (1.51)$$

with

$$\beta_1 = -\frac{c_1 N}{N^2 - 2II_\Omega}, \quad \beta_4 = -\frac{c_1}{N^2 - 2II_\Omega} \quad (1.52)$$

Including the solution for a_{ij} given by Eq. 1.51 in the definition of N , the nonlinear equation for N can then be obtained. The resulting equation reads

$$N^3 - c'_1 N^2 - N \left(\frac{9}{4} c_1 II_S + 2II_\Omega \right) + 2c'_1 II_\Omega = 0 \quad (1.53)$$

1.2.3. Large Eddy Simulation

Large Eddy Simulation consists in applying a filter to the Navier-Stokes equations (Eq. 1.1 and Eq. 1.2). This filtering operation can be seen schematically as a way to partition the energy spectrum. As mentioned before, the purpose of this approach is to solve the large scales of the flow that strongly depends on the geometrical configuration and to model the small scales which are supposed to be universal and isotropic. In this way, Large Eddy Simulation allows to obtain more detailed information on the considered turbulent flow compared to RANS computation such as minimum or maximum events of physical quantities.

In Large Eddy Simulation, the mathematical operator that is used is a low pass

convolution filter (Sagaut 2004). This allows to resolve a part of the turbulence scales while the other part is filtered. The filtering operation is different from the Reynolds operator and does not have the same properties. Nonetheless, we make the same assumptions in practice:

- i) preservation of constants $\langle C \rangle = C$,
- ii) additivity $\langle A^* + B^* \rangle = \langle A^* \rangle + \langle B^* \rangle$,
- iii) idempotence (hypothesis) $\langle \tilde{A} \rangle = \tilde{A}$,
- iv) commutivity with differential operators (hypothesis) $\langle \frac{\partial A^*}{\partial t} \rangle \sim \frac{\partial \langle A^* \rangle}{\partial t}$.

Filtering the Navier-Stokes equations, one obtains the continuity and momentum equations for the filtered velocity that read:

$$\frac{\partial \tilde{U}_i}{\partial x_i} = 0 \quad (1.54)$$

$$\frac{\partial \tilde{U}_i}{\partial t} + \frac{\partial \langle u_i^* u_j^* \rangle}{\partial x_j} = -\frac{1}{\rho} \frac{\partial \langle p^* \rangle}{\partial x_i} + \nu \frac{\partial^2 \tilde{U}_i}{\partial x_j \partial x_j} - \tilde{F}_i \quad (1.55)$$

with

$$\langle u_i^* u_j^* \rangle = \langle \tilde{U}_i \tilde{U}_j \rangle + \langle \tilde{U}_i u_j'' \rangle + \langle u_i'' \tilde{U}_j \rangle + \langle u_i'' u_j'' \rangle \quad (1.56)$$

Eq. (1.56) can be rewritten as:

$$\langle u_i^* u_j^* \rangle = \underbrace{\langle \tilde{U}_i \tilde{U}_j \rangle - \tilde{U}_i \tilde{U}_j}_{L_{ij}} + \tilde{U}_i \tilde{U}_j + \underbrace{\langle \tilde{U}_i u_j'' \rangle + \langle u_i'' \tilde{U}_j \rangle}_{C_{ij}} + \underbrace{\langle u_i'' u_j'' \rangle}_{R_{ij}} \quad (1.57)$$

The subgrid (or subfilter) stress tensor is then defined as :

$$\tau_{ij} = \langle u_i^* u_j^* \rangle - \tilde{U}_i \tilde{U}_j = L_{ij} + C_{ij} + R_{ij} \quad (1.58)$$

This triple decomposition, also called Leonard decomposition, highlights three mechanisms:

- i) The interaction between the large structures of the flow (L_{ij}),
- ii) Cross-correlations between small and large scales (C_{ij}),
- iii) Interaction at small scales (R_{ij}).

It is important to note that in the case of an idempotent filter and with the decorrelation assumption (zero correlation between small and large scales $C_{ij} = 0$), the subgrid stresses read:

$$\tau_{ij} = R_{ij} = \langle u_i'' u_j'' \rangle \quad (1.59)$$

In the general case, the filtered momentum equations are written as follows:

$$\frac{\partial \tilde{U}_i}{\partial t} + \tilde{U}_j \frac{\partial \tilde{U}_i}{\partial x_j} = -\frac{1}{\rho} \frac{\partial \langle p^* \rangle}{\partial x_i} + \nu \frac{\partial^2 \tilde{U}_i}{\partial x_j \partial x_j} - \frac{\partial \tau_{ij}}{\partial x_j} + \tilde{F}_i \quad (1.60)$$

In a similar way to the RANS model, under Boussinesq's assumption, the subgrid stress tensor is modeled as:

$$\tau_{ij} = -2\nu_t \left(\frac{\partial \tilde{U}_i}{\partial x_j} + \frac{\partial \tilde{U}_j}{\partial x_i} \right) + \frac{2}{3} k \delta_{ij} \quad (1.61)$$

The way to prescribe the subgrid viscosity ν_t leads to various LES models.

Before presenting the subgrid models, it is necessary to introduce the transport equation of the mean subgrid turbulent kinetic energy $k_m = \bar{k}_s = \overline{\langle u_i'' u_i'' \rangle} / 2$. For sake of clarity, not all equations are developed. The resolved fluctuating velocity (\tilde{u}_i) transport equation, which is obtained by subtracting the mean velocity (U_i) transport equation from the resolved velocity (\tilde{U}_i) transport equation, is multiplied by the subgrid velocity u_i'' and taking the overall average, we get:

$$\begin{aligned} \frac{\partial \bar{k}_s}{\partial t} + \frac{\partial \bar{k}_s U_j}{\partial x_j} = & -\frac{1}{\rho} \frac{\partial \overline{\langle u_i'' p'' \rangle}}{\partial x_i} + \frac{\partial \left[-\frac{1}{2} \overline{\langle u_i'' u_i'' u_j'' \rangle} + \nu \frac{\partial \bar{k}_s}{\partial x_j} - \bar{k}_s \tilde{u}_j \right]}{\partial x_j} \\ & - \nu \overline{\left\langle \frac{\partial u_i''}{\partial x_j} \frac{\partial u_i''}{\partial x_j} \right\rangle} - \overline{\langle \tau_{ij} \frac{\partial u_i''}{\partial x_j} \rangle} - \overline{\langle u_i'' u_j'' \rangle} \frac{\partial U_i}{\partial x_j} - \overline{\langle u_i'' u_j'' \rangle} \frac{\partial \tilde{u}_i}{\partial x_j} \end{aligned} \quad (1.62)$$

The resolved turbulent kinetic energy is defined by:

$$k_r = \frac{1}{2} \overline{\tilde{u}_i \tilde{u}_i} \quad (1.63)$$

Its transport equation can be derived, performing similar algebra as for \bar{k}_s :

$$\begin{aligned} \frac{\partial k_r}{\partial t} + \frac{\partial k_r U_j}{\partial x_j} = & -\frac{1}{\rho} \frac{\partial \overline{\tilde{u}_i \tilde{p}}}{\partial x_i} + \frac{\partial \left[-\frac{1}{2} \overline{\tilde{u}_i \tilde{u}_i \tilde{u}_j} + \nu \frac{\partial k_r}{\partial x_j} - \tilde{u}_i \tau_{ij} \right]}{\partial x_j} + \overline{\tau_{ij} \frac{\partial \tilde{u}_i}{\partial x_j}} \\ & - \nu \overline{\frac{\partial \tilde{u}_i}{\partial x_j} \frac{\partial \tilde{u}_i}{\partial x_j}} - \overline{\tilde{u}_i \tilde{u}_j} \frac{\partial U_i}{\partial x_j} \end{aligned} \quad (1.64)$$

It is possible to recover the total turbulent energy ($k = k_r + \bar{k}_s$) transport equation by summing equations (1.62) and (1.64).

1.2.3.1. Algebraic viscosity models

This section is limited to a presentation of the Smagorinsky model, because it corresponds to an asymptotic behavior of turbulence models. The Smagorinsky

model prescribes subgrid viscosity by analogy with mixing length models:

$$\nu_t = l_s^2 \underbrace{\sqrt{2\tilde{S}_{ij}\tilde{S}_{ij}}}_{\tilde{S}} \quad (1.65)$$

in which l_s is a characteristic length scale and

$$\tilde{S}_{ij} = \frac{1}{2} \left(\frac{\partial \tilde{U}_i}{\partial x_j} + \frac{\partial \tilde{U}_j}{\partial x_i} \right) \quad (1.66)$$

In the case where the cut-off scale $\kappa_c = \pi/\Delta$ is in the inertial zone of the spectrum, the characteristic time is expressed as Hinze 1975:

$$\overline{\tilde{S}^2} = 2 \int_0^{\kappa_c} \kappa^2 E(\kappa) d\kappa = 2 \int_0^{\kappa_c} C_k \epsilon^{2/3} \kappa^{1/3} d\kappa = \frac{3}{2} C_k \tilde{\epsilon}^{2/3} \left(\frac{\pi}{\Delta} \right)^{4/3} \quad (1.67)$$

The average dissipation rate is written as:

$$\tilde{\epsilon} = C_s^2 \Delta^2 \overline{\tilde{S}^2}^{3/2}, \text{ with } C_s^2 = \frac{1}{\pi} \left(\frac{2}{3C_k} \right)^{3/4} \approx 0.173 \quad (1.68)$$

The transfer of energy between the resolved part and the subgrid part is done through the following production term:

$$\overline{P''} = -\overline{\tau_{ij} \frac{\partial \tilde{U}_i}{\partial x_j}} = \overline{2\nu_t S_{ij} S_{ij}} \approx \nu_t \overline{\tilde{S}^2} \quad (1.69)$$

Applying the equilibrium hypothesis that stipulates that production is equal to the destruction term

$$C_s^2 \Delta^2 \overline{\tilde{S}^2}^{3/2} = \nu_t \overline{\tilde{S}^2} \quad (1.70)$$

With the use of the approximation $\overline{\tilde{S}^2}^{3/2} \approx \overline{\tilde{S}}^3$, ν_t reads:

$$\nu_t = C_s^2 \Delta^2 \overline{\tilde{S}} \quad (1.71)$$

And by using Eq. 1.65, one can identify:

$$l_s = C_s \Delta \quad (1.72)$$

1.2.3.2. Transport equation models - Deardorff

In a similar fashion to the RANS approach, there have been other models put forth for which additional transport equations need to be solved. When coarser meshes are employed, these models are attractive because more physics may be taken into account. The one-equation turbulence model of Deardorff 1980 is introduced here.

1. Introduction – 1.2. Turbulence modeling

The mean subgrid turbulent kinetic energy (\bar{k}_s) is related to the energy spectrum by the following relation:

$$\bar{k}_s = \int_{\kappa_c}^{\infty} E(\kappa) d\kappa = \int_{\kappa_c}^{\infty} C_k \epsilon^{2/3} k^{-5/3} d\kappa = \frac{3}{2} C_k \epsilon^{2/3} \left(\frac{\Delta}{\pi} \right)^{2/3} \quad (1.73)$$

The dissipation rate is expressed as

$$\epsilon = \frac{\bar{k}_s^{3/2}}{C_d \Delta}, \quad \text{with} \quad C_d = \frac{1}{\pi} \left(\frac{3C_k}{2} \right)^{3/2} \approx 1.074 \quad (1.74)$$

According to Heisenberg's hypothesis, the turbulent kinematic viscosity is given by Hinze 1975:

$$\bar{\nu}_t = \alpha \int_{\kappa_c}^{\infty} \sqrt{\frac{E(\kappa)}{\kappa^3}} d\kappa \quad (1.75)$$

Which gives using the Kolmogorov energy spectrum model:

$$\bar{\nu}_t = \alpha \int_{\kappa_c}^{\infty} C_k \epsilon^{1/3} \kappa^{-7/3} d\kappa = \frac{3}{4} \alpha C_k \epsilon^{1/3} \left(\frac{\Delta}{\pi} \right)^{4/3} \quad (1.76)$$

Introducing the dissipation rate (Eq. 1.74) in the above equation and switching back to an instantaneous formulation (Sagaut 2004), one gets:

$$\nu_t = \frac{3}{4} \alpha C_k \left(\frac{\Delta}{\pi} \right)^{4/3} \frac{k_s^{1/2}}{(C_d \Delta)^{1/3}} = C_\mu \Delta k_s^{1/2}, \quad \text{with} \quad C_\mu = \frac{3}{4} \alpha C_k \left(\frac{1}{\pi^4 C_d} \right)^{1/3} \quad (1.77)$$

in which $\alpha \sim 0.5$. This constant was predicted as $\alpha = 0.438$ by the Test Field Model (TFM) and as $\alpha = 0.441$ by the Eddy Damped Quasi-Normal Markovian (EDQNM) theory (Aupoix and Cousteix 1982). The one-equation models therefore intend to solve a transport equation for the subgrid energy k_s (Eq 1.62). In this equation, two terms need to be modeled:

- i) the dissipation term which is modeled by Eq. 1.74,
- ii) the pressure diffusion associated with the turbulent diffusion modeled by a gradient hypothesis (Kolmogorov-Prandtl equation):

$$-\frac{\partial \frac{1}{\rho} \langle u_j'' p'' \rangle + \frac{1}{2} \langle u_i'' u_i'' u_j'' \rangle}{\partial x_j} = C_2 \frac{\partial \left(\Delta \sqrt{k_s} \frac{\partial k_s}{\partial x_j} \right)}{\partial x_j} \quad (1.78)$$

The subgrid energy transport equation that is solved numerically is written as:

$$\frac{\partial k_s}{\partial t} + \tilde{U}_j \frac{\partial k_s}{\partial x_j} = \underbrace{\nu_t \tilde{S}^2}_{\text{I}} + \underbrace{\frac{\partial}{\partial x_j} \left[\left(\nu + \frac{\nu_t}{\sigma_k} \right) \frac{\partial k_s}{\partial x_j} \right]}_{\text{II}} - \underbrace{\frac{k_s^{3/2}}{C_d \Delta}}_{\text{III}} + \underbrace{\langle u_i'' f_i'' \rangle}_{\text{IV}} \quad (1.79)$$

The usual physical contributions can be found in the above equation:

I - Production,

II - Diffusion,

III - Dissipation,

IV - Energy given by the subgrid part of the external force (further discussed in Chapter 2).

The constants of the Deardoff model (C_d, C_μ, C_2) can be expressed with respect to the Smagorinsky constant (C_s). By matching the viscosity of the two models and their respective production term, we get:

$$C_s^2 \Delta^2 \tilde{S} = C_\mu \Delta k_s^{1/2} \quad ; \quad C_s^2 \Delta^2 \tilde{S}^3 = \frac{k_s^{3/2}}{C_d \Delta} \quad (1.80)$$

This results in:

$$C_s = C_\mu^{3/4} C_d^{1/4} \quad (1.81)$$

Based on the Direct-Interaction (DI) approximation, Yoshizawa and Horiuti 1985 proposed the following set of constant:

$$C_\mu = 0.05, \quad C_d = 1, \quad \sigma_k = 1 \quad (1.82)$$

As an indication, Table 1.2 displays different values of constants of the one equation model that can be found in the literature.

Authors	α	C_μ	C_d	σ_k	Applications
Yoshizawa and Horiuti 1985	0.322	0.05	1.0	1.0	Rectangular channel
V. K. Chakravarthy and Menon 2000	0.474	0.067	1.074	1.0	Premixed flames
Sone and Menon 2003	0.474	0.067	1.074	1.0	Fuel-air mixing
Taghinia and Rahman 2018 (RAST)	-	Dynamic	0.67 - 1.	1.0	Round impinging jet
TFM (Aupoix and Cousteix 1982)	0.438	0.0687	0.0969	1.0	-
EDQNM (Aupoix and Cousteix 1982)	0.441	0.0692	0.0969	1.0	-

Table 1.2. – Constants of the one equation model

1.2.4. Hybrid RANS/LES methods

Hybrid RANS/LES methods aim at combining the advantages of both RANS and LES turbulence approaches in a single simulation. For example, this can be very useful

for wall-bounded flows. While the near-wall region is treated as RANS, the region far from the walls is treated as LES. This allows to considerably reduce the computational cost and at the same time to keep a detailed description of the turbulence in the flow. Besides, there are certain interesting setups where one may choose to solve part of the flow in RANS and the other part (the area of interest) in LES using a finer mesh (Hamba 2001, Hamba 2003, Davidson and Peng 2003, Temmerman, Haziabdic, Leschziner, et al. 2005, Jaffrézic and Breuer 2008 and Schmidt and Breuer 2014). As both approaches are founded on the Boussinesq hypothesis, this unification of the two approaches is made possible. Indeed, the Reynolds and subgrid stress tensor are written in a very similar way (Eq. 1.8 and Eq. 1.61). The first one makes use of the flow's mean velocity, while the second one makes use of the flow's filtered velocity. The RANS operator can be conceptualized as the limit of LES with all scales filtered². In this way, the two approaches can be unified. The concept of hybrid RANS/LES methods has also strong roots in the multiple-scale models (Hanjalic, Launder, and Schiestel 1980 and Schiestel 1987) which is based on a spectral splitting of the energy spectrum.

Two main types of hybrid methods are to be distinguished, namely zonal and seamless approaches. The zonal approach divides the computational domain a priori, and in each of the two regions, two separate turbulence models are applied. Non-zonal (or seamless) methods, in contrast, use a single set of equations over the whole computational domain, and the transition is made as part of the computation through an appropriate parameter (*i.e.* parameter based on the mesh size). Following Chaouat 2017, zonal and non-zonal techniques are further explained in this section. The hybrid model that is used in the present project is then presented.

1.2.4.1. Zonal approaches

In zonal hybrid RANS/LES approaches, the computational domain is divided into sub-domains, that are described either in RANS or in LES. The main challenge is the coupling between RANS and LES regions (Hamba 2003, Davidson and Peng 2003, Temmerman, Haziabdic, Leschziner, et al. 2005, Batten, Golberg, and S. Chakravarthy 2004, Tessicini, Temmerman, and Leschziner 2006 and Hamba 2009). The physical quantities (velocity, pressure, ...) must be averaged in order to go from LES to RANS. Conversely, to go from RANS to LES, turbulent fluctuations must be injected to enrich the average signal from the RANS region. Many efforts have been made to introduce and enhance the signal quality introduced at the practical boundary circumstances. For more information on synthetic injection methods, the reader is referred to articles on the subject (Shur, P. R. Spalart, Strelets, et al. 2014, Wu 2017 and Dhamankar, Blaisdell, and Lyrintzi 2018). One drawback of this approach is its high dependency in the RANS/LES repartition of the subdomains, and how the RANS/LES interfaces

2. However, since the RANS operator is generally a temporal average, it is more rigorous to interpret it as the limit of *temporal* LES (TLES) with all scales filtered. This issue has been discussed e.g. in Fadaï-Ghotbi, Christophe Friess, Rémi Manceau, T. B. Gatski, et al. 2010

(effective boundary conditions) are handled. For instance, the determination of a priori RANS and LES regions can be quite challenging for complex geometries, such as a ventilated room with obstacles.

1.2.4.2. Seamless approaches

Contrary to zonal approaches, seamless techniques consider a continuous transition between RANS and LES. The other main feature of seamless approaches is that they use the same set of equations (momentum and turbulence model) over the whole computational domain, except that their physical meaning is not the same everywhere. This smooth transition is allowed by a suitable modification of the turbulence model. This modification is performed by considering a transition criterion, basically a comparison between RANS-like (scales obtained by the turbulence model) and LES (filter size). The most famous seamless technique is Detached Eddy Simulation (DES, Philippe R Spalart 1997).

This section focuses on the so-called Equivalent DES method (E-DES), which seeks a compromise between:

- i) Detached Eddy Simulation (DES), robust but rather empirical,
- ii) Partially Integrated Transport Model (PITM), provided with strong theoretical justification,

and is presented hereafter, along with DES and PITM. The link between the two aforementioned methods is made using the so-called *H-equivalence* proposed by C. Friess, R. Manceau, and T. Gatski 2015. The *H-equivalence* stipulates that two hybrid approaches based on the same closure model, but using a different method of control of the energy partition, yield similar low-order statistics of the resolved velocity fields, provided that they yield the same level of modeled turbulent kinetic energy. In their work, C. Friess, R. Manceau, and T. Gatski 2015 proposed to bridge two seamless hybrid RANS/LES techniques, namely the DES and PITM models. In hybrid context, similarly as in RANS, the eddy viscosity can be expressed as:

$$\nu_t = C_\mu \frac{k_s^2}{\epsilon_s} \quad (1.83)$$

in which $C_\mu = 0.09$ is a calibrated constant coefficient and k_s and ϵ_s are respectively the subgrid turbulent kinetic energy and the subgrid dissipation.

Detached Eddy Simulation The two subgrid equations of the DES model read:

$$\frac{\partial k_s}{\partial t} + \frac{\partial \tilde{U}_j k_s}{\partial x_j} = P_s + J_k - F_{DES} \epsilon_s \quad (1.84)$$

$$\frac{\partial \epsilon_s}{\partial t} + \frac{\partial \tilde{U}_j \epsilon_s}{\partial x_j} = C_1 \frac{\epsilon_s}{k_s} P_s + J_\epsilon - C_2 \frac{\epsilon_s^2}{k_s} \quad (1.85)$$

where P_s is the production term, which represents the energy transfer between the resolved and subgrid parts in LES mode and the classical production term in RANS mode, as defined by Eq. 1.14. J_s and J_ϵ are diffusion terms and C_1 and C_2 are constant coefficients. Finally, the function F_{DES} writes as:

$$F_{DES} = \max\left(1, \frac{k_s^{3/2}}{\epsilon_s L_{DES}}\right) \quad (1.86)$$

in which $L_{DES} = C_{DES}\Delta$ with C_{DES} a constant coefficient and Δ the mesh size. By defining the local (instantaneous) subgrid length scale $L_s = k_s^{3/2}/\epsilon_s$, it is clear that the F_{DES} function is a comparison between the subgrid length scale and a length scale corresponding to the mesh size.

- i) When $L_s < L_{DES}$ it means that the local length scale is smaller than the length scale attributed to the mesh size and thus, the mesh is not refined enough to capture fluctuations. In this case the model behaves like the classic $k - \epsilon$ model (RANS mode),
- i) When $L_s > L_{DES}$, the dissipation term is expressed as for the one equation model: $k_s^{3/2}/L_{DES}$, and does not depend on the subgrid dissipation (LES mode). Nevertheless, the subgrid dissipation is still at play in the production term through the eddy viscosity.

Partially Integrated Transport Model PITM is elegant since it takes its roots in the theory of spectral turbulence. Working in spectral space, some authors have provided a theory that allows to split the turbulent energy spectrum into several subranges, leading to partial spectral integration models (Schiestel and Dejoan 2005, Chaouat and Schiestel 2005 and Chaouat and Schiestel 2007). PITM can be used both for a eddy viscosity model and for a second-moment closure. The example of an eddy viscosity subfilter model is shown (Chaouat 2017):

$$\frac{\partial k_s}{\partial t} + \frac{\tilde{U}_j k_s}{\partial x_j} = P_s + J_k - \epsilon_s \quad (1.87)$$

$$\frac{\partial \epsilon_s}{\partial t} + \frac{\partial \tilde{U}_j \epsilon_s}{\partial x_j} = C_{\epsilon 1} \frac{\epsilon_s}{k_s} P_s + J_\epsilon - C_{\epsilon 2}^* \frac{\epsilon_s^2}{k_s} \quad (1.88)$$

in which $C_{\epsilon 2}^*$ is a variable defined by:

$$C_{\epsilon 2}^* = C_{\epsilon 1} + r_k (C_{\epsilon 2} - C_{\epsilon 1}) \quad (1.89)$$

where r_k is the target turbulent kinetic energy ratio. This ratio is function of an energy spectrum. The simplest way would be to use a Kolmogorov energy spectrum which

gives the following expression:

$$r_k = \frac{k_s}{k} = \frac{1}{k} \int_{\kappa_{cut}}^{\infty} C_k \epsilon^{2/3} \kappa^{-5/3} d\kappa = \frac{3}{2} C_k (\kappa_{cut} L_t)^{-2/3} \quad (1.90)$$

This formulation cannot be used as is since the limit at $\kappa_{cut} = 0$ is not defined. To circumvent this issue, a limiter can be applied:

$$r_k = \min \left[1, \frac{3}{2} C_k (\kappa_{cut} L_t)^{-2/3} \right] \quad (1.91)$$

Schiestel and Dejoan 2005 proposed another empirical formulation to avoid this inconsistency:

$$r_k = \frac{1}{1 + \frac{2}{3C_k} (\kappa_{cut} L_t)^{2/3}} \quad (1.92)$$

With this formulation, both the limit when $\kappa_{cut} \rightarrow 0$ ($r_k \rightarrow 1$) and when $\kappa_{cut} \rightarrow \infty$ ($r_k \rightarrow 0$) are satisfied. But this formulation is highly empirical and has led Chaouat and Schiestel 2007 to derive a new energy spectrum inspired from a von Kármán-like spectrum:

$$E_{VKCS}(\kappa) = \frac{2}{3} \beta k L_e \frac{(\kappa L_e)^2}{[1 + \beta (\kappa L_e)^3]^{11/9}} \quad (1.93)$$

The difficulty when deriving an energy spectrum is that there are three main constraints: *i*) the integral over the whole spectral range has to be equal to the turbulent kinetic energy, *ii*) the limiting behavior of the spectrum has to tend towards the Kolmogorov scaling-law "-5/3" and with the correct Kolmogorov constant C_k and finally *iii*) the definition of the integral length scale (2.27) should be used to find the coefficient α_L , $L_e = \alpha_L L_{||}$.

Unfortunately, meeting all these constraints is not feasible. For example, the von Kármán-Pao presented before agrees with points *i*) and *ii*) but even though the spectrum has an inertial subrange with a $-5/3$ slope, the constant of the energy spectrum model $C_{VKP} \sim 0.8$ does not match the Kolmogorov constant $C_k \sim 1.5$. As a result, this spectrum cannot be used to evaluate the amount of energy that is found at small scales. With this in mind, Chaouat and Schiestel 2007 proposed an energy spectrum model that meets requirements *i*) and *ii*). This spectrum was developed both to satisfy Kolmogorov's law and also allows to have a spectral description at large scales ($E(\kappa) \sim \kappa^2$). However, the coefficient α_L is set to one as $L_e = L_t$ because the definition of the longitudinal integral length scale can not be met. This energy spectrum is valid on the entire range of wavenumber and gives the right limiting behavior (when $\kappa_{cut} \rightarrow 0$, $r_k \rightarrow 1$ and when $\kappa_{cut} \rightarrow \infty$, $r_k \rightarrow 0$) for the associated kinetic energy ratio:

$$r_k = [1 + \beta (L_t \kappa_{cut})^3]^{-2/9} \quad (1.94)$$

and the coefficient $\beta = \left(\frac{2}{3C_k} \right)^{9/2}$ is found by taking the limit $\lim_{\kappa \rightarrow +\infty} E(\kappa)$.

Bridging DES and PITM : "Equivalent" DES (E-DES) C. Friess, R. Manceau, and T. Gatski 2015 performed a perturbation analysis between RANS and an arbitrary LES state, in order to establish a relation between F_{DES} and r_k in the spirit of *H-equivalence*. The resulting E-DES model is expressed as:

$$\frac{\partial k_s}{\partial t} + \frac{\tilde{U}_j k_s}{\partial x_j} = P_s + J_k - F_{E-DES} \epsilon_s \quad (1.95)$$

$$\frac{\partial \epsilon_s}{\partial t} + \frac{\partial \tilde{U}_j \epsilon_s}{\partial x_j} = C_1 \frac{\epsilon_s}{k_s} P_s + J_\epsilon - C_2 \frac{\epsilon_s^2}{k_s} \quad (1.96)$$

with

$$F_{E-DES} = \max\left(1, \frac{k_s^{3/2}}{\epsilon_s L_{E-DES}}\right) ; \quad L_{E-DES} = \frac{r_k^{3/2} L_t}{\Psi(r_k)} \quad (1.97)$$

In order to express the function Ψ , C. Friess, R. Manceau, and T. Gatski 2015 applied the *H-equivalence* according to three assumptions such as turbulence in equilibrium layer or inhomogeneous turbulence. In this work, the most general form of the function Ψ is chosen:

$$\Psi(r_k) = 1 + \frac{C_2 - C_1}{C_1} (1 - r^{C_1/C_2}) \quad (1.98)$$

"Equivalent" DES has been further improved, e.g. with the H-TLES (R. Manceau 2018; Duffal, De Laage de Meux, and R. Manceau 2022). This is an active research topic and Duffal, De Laage de Meux, and R. Manceau 2022 recently suggested interesting changes to the E-DES procedure, specifically by altering the dissipation. They also introduced an estimation of r_k in terms of frequency (instead of wavenumber) spectrum.

1.2.4.3. Importance of forcing

It is worth recalling that in the absence of natural instability mechanisms, such as a strong shear associated with a geometrical singularity (cf. figure 1.1), DNS, LES or hybrid RANS/LES methods tend to underestimate the level of turbulence or eventually, this underestimation leads in some cases to a laminar solution, *i.e.* free of any fluctuations.

Usually this is circumvented by introducing fluctuations through boundary or initial conditions. Another possibility consists in introducing fluctuations by using a volume forcing of the equations of motion. For instance, when the region of interest is distant from boundaries, fluctuations that have been superimposed on the mean velocity field at the inlet boundary condition might be quickly dissipated due to coarse meshes and would not be convected to the region of interest. This contrasts with a volume forcing approach that enables the injection of fluctuations close to any region of interest (De Nayer, Schmidt, Wood, et al. 2018).

In the context of hybrid RANS/LES approaches, volume forcing methods are attrac-

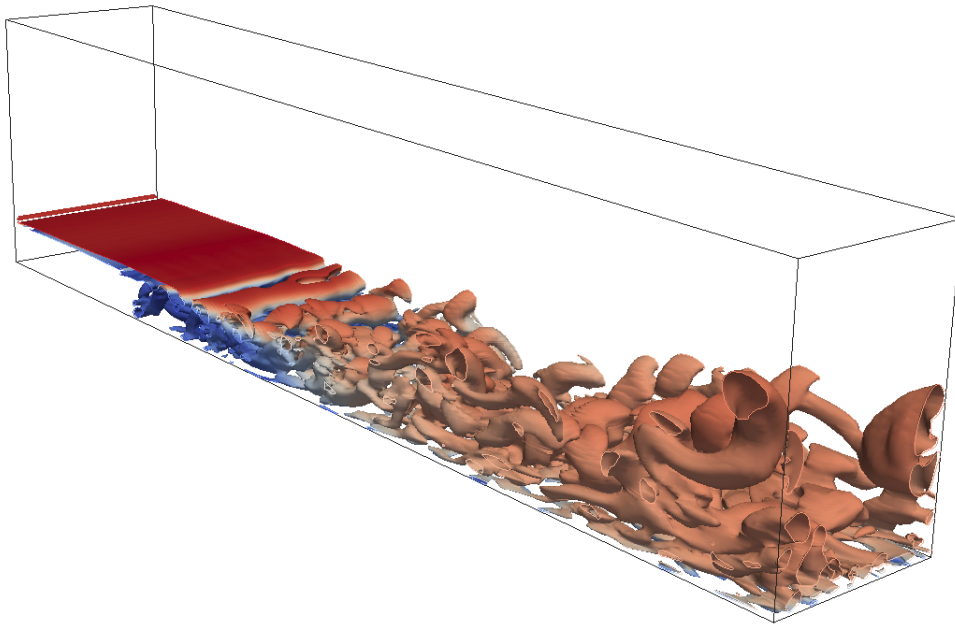


Figure 1.1. – Example of a geometrical singularity: the backward facing step³. Iso-surfaces of the Q criterion are represented and colored by the average velocity.

tive to generate fluctuations in transition regions (*i.e.* switching from RANS to LES regions). A volume forcing method should ideally fulfill the following requirements:

- i) The generated fluctuations should be consistent with some of the most important turbulent properties of the considered flow such as the integral length scale (through spatial correlations) or the Reynolds stress levels. One should also consider temporal correlations, along with third and fourth order correlations of the velocity signal.
- ii) The injected velocity fluctuations should be divergence-free in order to avoid the appearance of spurious pressure modes,
- iii) It should not alter the mean flow,
- iv) It should be independent of the geometry,
- v) It should be self-adaptive meaning that it should be automatically activated in any region of interest.

Gathering all these criteria would, in principle, allow to treat the transition region properly. In the rest of the present work, effort is put in meeting as many of these criteria as possible, even though in practice it remains difficult.

3. I gratefully thank Thibaut ROSSI for performing the simulation and transferring the data to me.

1.3. Objectives and outline

As mentioned before, IRSN relies partly on CFD simulations to address some safety concerns for which simplified approaches prove to be unreliable (hydrogen distribution, atmospheric dispersion, ...). The ability to perform calculations that produce reliable results is crucial and a cornerstone is in the modelling of turbulence. In practice, most of the situations of interest remain difficult to access using LES approaches and hybrid RANS/LES approaches appear as an interesting and promising alternative approach. In this frame, RANS/LES transitions require a particular attention.

The goal of this thesis is the development of a volume forcing method and its implementation in a hybrid context for different types of flows (homogeneous turbulence, shear flows, ...) in order to describe as correctly as possible the RANS/LES transition regions. This study has been separated into three sub-goals, as shown in Fig. 1.2:

- i) The first sub-goal of this thesis is to propose a forcing method to sustain homogeneous isotropic turbulence. Chapter 2 is therefore dedicated to the development of the forcing method. Forcing techniques, based on Lundgren 2003 approach, in homogeneous isotropic turbulence face two main challenges: recovering a proper integral length scale and monitoring efficiently the turbulent kinetic energy. The method developed in this chapter aims at addressing these two issues. Finally, the goal is to demonstrate how effective this forcing method is, in combination with the hybrid E-DES method.
- ii) The second sub-goal is to adapt the forcing method developed in Chap 2 to non-homogeneous turbulence. This involves performing hybrid RANS/LES simulations of a planar jet, that mimic the air inflow of a ventilated premise, to show the potential and interest of the forcing technique. The case of the plane jet is presented, and the corresponding forcing method is described in Chapter 3. The synthetic velocity is first incremented in time by itself (without solving the Navier-Stokes equations) to check the quality of the statistics in a non-homogeneous framework. Then, the reconstruction approach is applied to the planar jet.
- iii) Finally, in Chapter 4, the aeraulics of a ventilated room is prescribed using E-DES with the reconstruction-like procedure, associated with an explicit algebraic subfilter closure. Results are compared with experimental data that comes from the experimental program CARDAMOMETTE conducted at IRSN. This is a challenging configuration since wall effects have to be taken into account.

In order to assess the forcing method on relatively simple configurations, incompressible flows of Newtonian fluids are considered. Furthermore, no temperature change is considered in this work. Because thermal effect are not relevant in this situation, no additional equations are required to solve Navier-Stokes equations. Buoyancy effects are also not taken into account either. This choice is made to test the forcing method in a simplified framework.

Forcing method for hybrid RANS/LES method

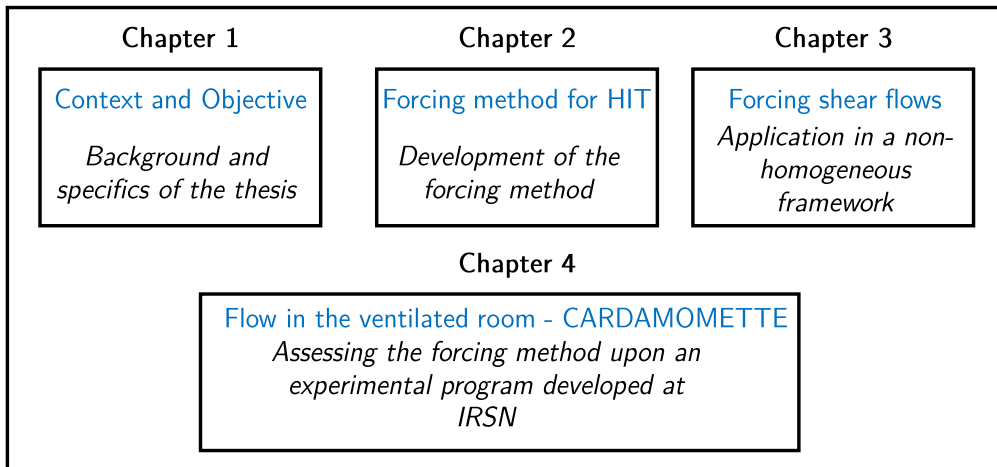


Figure 1.2. – Thesis overview. Blue text: name of chapter, italic text: objective

In this work, simulation results are obtained using the in-house CALIF³S software. Time discretization is carried out by using a fractional step algorithm that consists in a pressure correction method. Space discretization is performed by using a staggered finite volume scheme for which scalar unknowns are located at cell centers while the velocity is located at cell faces. Most of the simulations use a centered second-order spatial discretization of both convective and diffusive fluxes together with the semi-implicit Crank-Nicolson time scheme. The corresponding numerical scheme is discretely kinetic energy conserving (Boyer, Dardalhon, Lapuerta, et al. 2014).

2. Forcing method for homogeneous isotropic turbulence

Table of contents

2.1	State of the art	50
2.1.1	Forcing in spectral space	50
2.1.2	Forcing in physical space	51
2.2	Forcing based on a reconstruction-like method	52
2.2.1	Reconstruction method	55
2.2.2	Synthetic velocity	56
2.2.2.1	Formulation	56
2.2.2.2	Spectral density spectrum	60
2.2.3	Kinetic energy monitoring	61
2.2.3.1	Modulation coefficient	63
2.2.3.2	Selective forcing	63
2.3	Forcing to sustain homogeneous isotropic turbulence	64
2.3.1	Numerical set up	65
2.3.2	Constant frequency	66
2.3.2.1	Deterministic frequency	66
2.3.2.2	Stochastic frequency	69
2.3.3	Influence of grid resolution	71
2.3.4	Towards more realistic frequencies	72
2.3.5	Consideration of anisotropy	74
2.4	Towards a self-adaptive forcing : Decaying isotropic turbulence	78
2.4.1	Balance of turbulent kinetic energy	78
2.4.2	Results	81
2.4.2.1	Validation of E-DES	81
2.4.2.2	Forcing in E-DES	82
2.5	Conclusion	86

This chapter is devoted to the development of a forcing method based on a reconstruction-like for Large Eddy Simulation and hybrid RANS/LES approaches. After the presentation of the synthetic velocity employed in this work, the forcing method is described and used to force isotropic homogeneous turbulence. The forcing method is then adjusted to work with hybrid RANS/LES approaches. Finally, hybrid method with forcing is used to simulate the decay of homogeneous isotropic turbulence.

2.1. State of the art

Forcing techniques generally consist in adding a force to the Navier-Stokes equations. There are essentially two types of forcing depending on the technique used to solve the Navier-Stokes equations. One can either solve the Navier-Stokes equation in spectral space or in physical space. On one hand, spectral codes allow to have attractive computational cost but cannot be easily applied to all geometries. On the other hand, numerical codes implemented in the physical space can be applied to all geometries. Forcing in spectral space (Eswaran and Pope 1988; Alvelius 1999) is generally restricted to a limited range of wavenumbers, located towards low wavenumbers. This is motivated by the need to enrich only large-scale structures, without explicitly modifying the inertial region of the energy spectrum. In the case of a resolution in physical space, the forcing is generally performed on the whole range of wavenumbers (Spille-Kohoff and Kaltenbach 2001; Lundgren 2003).

2.1.1. Forcing in spectral space

First, the focus is on forcing methods in spectral space because the forcing method that has been developed in this work, which is implemented in the physical space, is based on properties of forcing methods in the spectral space. Forcing methods in spectral space were the first form of forcing historically. This is because resolving the Navier-Stokes equations in spectrum space enables the use of more effective methods, like the fast Fourier transform, which lowers the computational cost. The velocity, which is one of the unknowns of the Navier-Stokes equations, is therefore expressed using a Fourier transformation of the velocity in physical space. This method gives better prediction for spatial derivatives compared to finite-difference methods (Mansour, Moin, W. C. Reynolds, et al. 1979; Gottlieb and Orszag 1977). This kind of methods is often called pseudo-spectral since the derivatives are estimated in spectral space but the product between the velocity and its derivative is computed in physical space.

The first forcing in spectral space to sustain isotropic homogeneous turbulence in a $N^3 = 32^3$ triply periodic box was proposed by Siggia and Patterson 1978. The primary purpose of sustaining isotropic homogeneous turbulence was to study the intermittency effect and to provide some answers for the field of turbulence modeling. Siggia and Patterson 1978 proposed two ways to force the computation. As in Chasnov 1991, the first approach was to freeze the first shell of wavenumbers at their initial values which allows to keep a constant kinetic energy at low wavenumbers. The second idea proposed by Siggia and Patterson 1978 consists in adding a linear forcing term to momentum equations which is only active at low wavenumbers, in practice $2 < \kappa < 4$ with κ representing the wavenumber. In this case the forcing term is multiplied by a constant to match a desired dissipation rate. This method was then successfully applied by Siggia 1981 to a mesh $N^3 = 64^3$. R. M. Kerr 1984 also performed the same kind of simulation on $N^3 = 128^3$ grid points still with the aim of examining small-scale

2. Forcing method for homogeneous isotropic turbulence – 2.1. State of the art

structures.

Additional methods have also been developed to maintain a constant dissipation rate by means of a dynamic constant which allows to keep either the dissipation rate of the computation (Jiménez, Wray, Saffman, et al. 1993, Ishihara and Kaneda 2002, Mosheni, Kosovic, Shkoller, et al. 2003 and Lamorgese, Cauhey, and Pope 2005) or a prescribed dissipation rate (Goshal, Lund, Moin, et al. 1995 and Carati, Ghosal, and Moin 1995). Then, in the methods for conserving a constant turbulent kinetic energy at the low wavenumber range, Sullivan, Mahalingam, and R. Kerr 1994 evaluated the turbulent kinetic energy lost at each time step ($k(t + dt) - k(t)$) in the wavenumber range $\kappa < \kappa_f$ to inject it at low wavenumbers by means of a multiplicative factor. With a somewhat similar idea, Seror, Sagaut, Bailly, et al. 2001 achieved to keep the turbulent kinetic energy constant by injecting the energy lost at each time step into the wavenumber range $1 \leq \kappa \leq 5$. Wang, Chen, Brasseur, et al. 1996 proposed a method which is consistent with the Kolmogorov "-5/3" scaling law further to keep the turbulent kinetic energy constant at the low wavenumber range. Chen and Shan 1988 and Mosheni, Kosovic, Shkoller, et al. 2003 used this method respectively to investigate Kolmogorov's theory by performing high-resolution computations at $N^3 = 512^3$ and to show the capabilities of the Lagrangian averaged Navier-Stokes equations for turbulence calculations.

In order to study small-scale structures, it is also important to ensure that the forcing scheme employed don't alter these small scales. It was shown by Eswaran and Pope 1988 that forcing the low wavenumber range does not influence results at the high wavenumbers. This is an important point to keep in mind that will be emphasised when presenting the features of the proposed forcing method. The method of Eswaran and Pope 1988 is based on a stochastic process that gives proper turbulent kinetic energy and time correlation. Alvelius 1999 introduced a forcing scheme developed in the Craya-Herning frame of reference and presented results of sustained isotropic and anisotropic turbulence.

Important point to remember about forcing methods in spectral space is that the turbulent kinetic energy added to the system is localized at low wavenumber range in order not to disturb the inertial zone of the energy spectrum. The choice of this range can be discussed. Most of the CFD codes to solve engineering problems are developed in physical space which is also the case of the CALIF³S-P²REMICS software developed at IRSN. Consequently, in this thesis the goal is to develop a new forcing method in physical space.

2.1.2. Forcing in physical space

The forcing method described in the following section has been developed in physical space. For forcing methods in physical space, in the context of large-scale simulation methods, the filtered equations of motion are modified by the addition of a

2. Forcing method for homogeneous isotropic turbulence – 2.2. Forcing based on a reconstruction-like method

forcing term noted f_i :

$$\frac{\partial \tilde{U}_i}{\partial t} + \tilde{U}_j \frac{\partial \tilde{U}_i}{\partial x_j} = -\frac{1}{\rho} \frac{\partial \langle p^* \rangle}{\partial x_i} + \nu \frac{\partial^2 \tilde{U}_i}{\partial x_j \partial x_j} - \frac{\partial \tau_{ij}}{\partial x_j} + \tilde{F}_i \quad (2.1)$$

The forcing techniques studied in this chapter are based on the linear forcing method proposed by Lundgren 2003 which is an efficient way to sustain isotropic turbulence. Analysis of the turbulent kinetic energy budget shows that the term leading to turbulent production comes from $u'_j \partial_j \bar{u}_i$ (where $\bar{\cdot}$ stands for the ensemble average) in the transport equation for the fluctuating velocity component u'_i . This term vanishes for homogeneous isotropic flows, which motivated Lundgren to produce his “linearly forced isotropic turbulence” method in physical space by adding a forcing term proportional to the velocity. This method has two well-known shortcomings when applied to sustain isotropic homogeneous turbulence in a triply periodic box:

- (i) it generates important oscillations of the turbulent kinetic energy,
- (ii) the resulting integral length scale $L_{||}$, defined as $L_{||} = U_{rms}^3 / \epsilon$, depends on the domain size L_{box} , in practice $L_{||} \sim 0.2 L_{box}$.

Rosales and Meneveau 2005 pointed out these two limitations by performing several DNS simulations in a triply periodic box with a mesh from $N^3 = 128^3$ to $N^3 = 330^3$. As for forcing method in spectral space, it is common to perform simulations on a triply periodic box of size L_{box} in isotropic homogeneous turbulence. However, recent improvements allow to circumvent these shortcomings by:

- (i) introducing a modulation coefficient based on the turbulent kinetic energy or dissipation budget, that greatly reduces oscillations and substantially shortens the initial transient phase (Carroll and Blanquart 2013; Bassenne, Urzay, Park, et al. 2016),
- (ii) employing filters that ensure a nearly unconstrained integral length scale which is independent of the domain size (De Laage de Meux, Audebert, R. Manceau, et al. 2015; Palmore Jr. and Desjardins 2018).

In most instances, the two aforementioned limitations are tackled separately, focusing on the control of either turbulent kinetic energy or integral length scale as noted in Table 2.1.

2.2. Forcing based on a reconstruction-like method

In the present work, an alternative approach is investigated that consists in introducing synthetic velocity fluctuations through a linear-like forcing technique approach. Following a reconstruction approach (Sagaut 2004), a homogeneous isotropic Gaussian synthetic turbulent velocity field is built and introduced in the Navier-Stokes equations. In other words, synthetic velocity fluctuations are added to the resolved

2. Forcing method for homogeneous isotropic turbulence – 2.2. Forcing based on a reconstruction-like method

Source	Forcing term \tilde{F}_i	Remarks
Lundgren (2003)	$A\tilde{u}_i$	Constrained $L_{ } \sim 19\%L_{box}$. Long transition to statistically stationary state $\sim 20T$
Carroll & Blanquart (2013)	$A\frac{k_r^\dagger}{k_r}\tilde{u}_i$	Constrained $L_{ } \sim 19\%L_{box}$. Short transition to statistically stationary state $\sim 8T$
Mallouppas <i>et al.</i> (2013)	$\frac{\sqrt{k_r^\dagger} - \sqrt{k_r}}{\delta t \sqrt{k_r^\dagger}} u_i^s$	Very short transition to statistically stationary state $< T$
De Laage de Meux <i>et al.</i> (2015)	$A_{ij}(\tilde{u}_j - \hat{\tilde{u}}_j) + B_i$	Unconstrained $L_{ }$. Short transition to statistically stationary state $\sim T$. Appropriate for anisotropic flows
Bassenne <i>et al.</i> (2016)	$\frac{\epsilon - G[k_r - k_r^\dagger]/T}{2k_r} \tilde{u}_i$	Constrained $L_{ } \sim 19\%L_{box}$. Very short transition to statistically stationary state $< T$
Schmidt & Breuer (2017)	$\frac{\langle u_i^s \rangle}{T}$	Unconstrained $L_{ }$. Prescribed two-point and two-time correlations are matched
Palmore Jr. & Desjardins (2018)	$A\frac{k_r^\dagger}{k_r}\hat{\tilde{u}}_i$	Unconstrained $L_{ }$. Short transition to statistically stationary state $\sim T$

Table 2.1. – Overview of introduced forcing techniques. $\langle \cdot \rangle$ and $\tilde{\cdot}$ represent respectively a temporal and spatial filter. $\hat{\cdot}$ represents a double spatial filter, where the second filter is explicit. T denotes the turn-over time scale.

velocity field promoting turbulence within the simulation. This is in line with the work of Schmidt and Breuer 2017a. They proposed to add a synthetic source term to the Navier-Stokes equations. In their work, this source term is expressed as the ratio between a synthetic velocity and a turn-over time scale. The synthetic velocity field is frozen, *i.e.* time independent, and is based on a digital filter approach (Klein, Sadiki, and Janicka 2003b). The parameters of the digital filter procedure are randomly chosen at each time step and to obtain the targeted two-time correlations, the synthetic velocity field is filtered. Their work was then taken over by De Nayer, Schmidt, Wood, *et al.* 2018 to improve prediction for a practical LES case.

In this work, an inverse Fourier approach is used to build the synthetic velocity field. This methodology, based on the work of Kraichnan 1970, basically consists in writing the velocity field in the Fourier space and then summing different Fourier modes over a shell. The generated velocity field needs an energy spectrum model as input. Consequently, one has to specify a total kinetic energy as well as an integral length

2. Forcing method for homogeneous isotropic turbulence – 2.2. Forcing based on a reconstruction-like method

scale to set up the prescribed energy spectrum. Statistical properties such as two-point and two-time correlation functions depend strongly on the energy spectrum function. This suggests that the prescribed spectrum must be as close as possible to the considered physics. A careful choice of other variables (wave number, phase, ...) allows to ensure homogeneity and isotropy, along with a divergence-free field.

This frozen synthetic velocity field is well suited and mainly used to initialize simulations. Based on the work of Kraichnan 1970, Fung, Hunt, Malik, et al. 1992 provided an unfrozen synthetic velocity field, *i.e.* time dependent, introducing a prescribed time frequency which remains to be specified. Following Bailly, Lafon, and Candel 1995, one way is to prescribe a constant time frequency for all Fourier modes. More physics can be added to the model by means of *straining* or *sweeping* hypothesis. Time frequencies are driven by two distinct mechanisms, depending on whether large scales or small scales are considered. Favier, F. Godeferd, and Cambon 2010 highlighted the transition between *straining* and *sweeping* hypotheses. They validated that large scales follow the *straining* hypothesis while small scales verify the *sweeping* hypothesis. The *straining* hypothesis states that large scale frequencies only depend on size and energy of the larger eddies ($\omega_n = \sqrt{E(\kappa)\kappa^3}$), whereas the *sweeping* hypothesis stipulates that small scales are advected by larger ones ($\omega_n = U_{rms}\kappa$). As described by Favier, F. Godeferd, and Cambon 2010, using a random frequency that obeys a Gaussian distribution smoothens the two-time synthetic velocity correlations. In the next section, we show the impact of a random frequency on two-time velocity correlations.

In addition to recovering the prescribed length scale and the two-time correlations, the control of the resolved turbulent kinetic energy is of significant importance. An efficient way for controlling the turbulent kinetic energy is to use a PI controller to trigger second order moments towards a targeted value as in the work of Spille-Kohoff and Kaltenbach 2001. Since their pioneer work, the method has been improved in particular by Laraufie, Deck, and Sagaut 2011. An other way is to introduce a modulation coefficient based on the turbulent kinetic energy budget (Carroll and Blanquart 2013; Bassenne, Urzay, Park, et al. 2016). For instance, Carroll and Blanquart 2013 proposed a modified version of Lundgren’s linear forcing method Lundgren 2003 by multiplying the forcing term by the control coefficient k_r^\dagger/k_r as shown in Table 2.1. This control aims at driving the kinetic energy k_r towards the targeted one k_r^\dagger . This has the effect of reducing both oscillations of the turbulent kinetic energy and the initial transient phase. Finding a modulation coefficient when applying a forcing based on the resolved velocity field is well suited but becomes challenging when adding a forcing based on synthetic velocity fluctuations to the Navier-Stokes equations. In this instance, Mallouppas, George, and Wachem 2013 proposed an approach that consists in multiplying the forcing term by the coefficient $(\sqrt{k_r^\dagger} - \sqrt{k_r})/\delta t\sqrt{k_r^\dagger}$, where δt is the computational time step. In the present work, two novel strategies for monitoring the turbulent kinetic energy are proposed.

2. Forcing method for homogeneous isotropic turbulence – 2.2. Forcing based on a reconstruction-like method

- i) A modulation coefficient is proposed based on the kinetic energy budget with an estimate of the production of turbulent kinetic energy related to the forcing method,
- ii) A control that mimics spectral forcing techniques is developed. The aim of this method is to control the resolved kinetic energy by summing a specific number of Fourier modes, *i.e.* injecting a specific amount of kinetic energy.

The proposed approach is tested upon homogeneous and isotropic turbulence (HIT), the starting point of today's approach to benchmark and investigate a forcing method's characteristics.

2.2.1. Reconstruction method

The proposed forcing technique developed in this work consists in introducing velocity fluctuations in the filtered Navier-Stokes equations following a reconstruction approach (Sagaut 2004). This approach consists roughly in substituting the resolved velocity by the sum of the resolved velocity and a synthetic component u_i^s . This operation, that can be seen as $\tilde{U}_i \rightarrow \tilde{U}_i + u_i^s = \tilde{U}_i^*$ (the reconstruction of the pressure term is not taken into account), leads to new terms in the filtered Navier-Stokes equations:

$$\frac{\partial \tilde{U}_i^*}{\partial t} + \frac{\partial \tilde{U}_i^* \tilde{U}_j^*}{\partial x_j} = -\frac{1}{\rho} \frac{\partial \langle p^* \rangle}{\partial x_i} + \nu \frac{\partial^2 \tilde{U}_i^*}{\partial x_j \partial x_j} - \frac{\partial \tau_{ij}}{\partial x_j} \quad (2.2)$$

We assume here that all these new terms can be neglected at least for homogeneous isotropic turbulence except for the unsteady term, leading to the following forcing:

$$\frac{\partial \tilde{U}_i}{\partial t} + \tilde{U}_j \frac{\partial \tilde{U}_i}{\partial x_j} = -\frac{1}{\rho} \frac{\partial \langle p^* \rangle}{\partial x_i} + \nu \frac{\partial^2 \tilde{U}_i}{\partial x_j \partial x_j} - \frac{\partial \tau_{ij}}{\partial x_j} - \frac{\partial u_i^s}{\partial t} \quad (2.3)$$

in which \tilde{u}_i , $\langle p^* \rangle$, ν and τ_{ij} are respectively the resolved velocity, the resolved pressure, the kinematic viscosity, and the subgrid tensor. This approach is formally equivalent to the method proposed by Schmidt and Breuer 2017a in which the last term on the right hand side of Eq.(2.3) plays the role of the forcing term. In their approach, the synthetic velocity is frozen, *i.e.* time independent. In order to recover the two-time correlations, a relaxation time based on Taylor's hypothesis is used instead of the temporal derivative. Then the synthetic velocity field is preliminary filtered by a temporal exponential moving average before being injected into the computation. The resulting forcing writes as the ratio of a filtered stochastic synthetic velocity \hat{u}_i^s , prescribed randomly at each time step, by a specified characteristic turbulent time scale. The forcing term is therefore expressed in a similar way as in the linear forcing approach (Lundgren 2003; Rosales and Meneveau 2005; Carroll and Blanquart 2013;

2. Forcing method for homogeneous isotropic turbulence – 2.2. Forcing based on a reconstruction-like method

Bassenne, Urzay, Park, et al. 2016):

$$\frac{\partial \tilde{U}_i}{\partial t} + \tilde{U}_j \frac{\partial \tilde{U}_i}{\partial x_j} = -\frac{1}{\rho} \frac{\partial \langle p^* \rangle}{\partial x_i} + \nu \frac{\partial^2 \tilde{U}_i}{\partial x_j \partial x_j} - \frac{\partial \tau_{ij}}{\partial x_j} + \frac{\hat{u}_i^s}{T} \quad (2.4)$$

The present approach uses an unfrozen synthetic velocity field through the introduction of a stochastic time frequency. More details are given in Sec. 2.2.2.

2.2.2. Synthetic velocity

Several possibilities exist for the choice of the synthetic signal u_i^s . From white noise to DNS velocity fields, there is a wide range of choices depending on the quality and complexity of the signal. Here, regarding this synthetic signal we have the following specifications:

- i) zero mean and prescribed turbulent kinetic energy,
- ii) prescribed energy spectrum,
- iii) provides accurate space and time correlations.

The goal is to inject a maximum of physics into the computation without having an overly complex signal.

2.2.2.1. Formulation

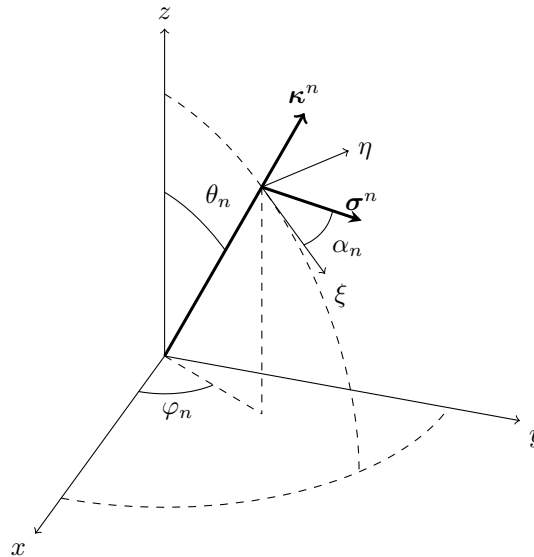


Figure 2.1. – Wave vector geometry of the n^{th} Fourier mode.

2. Forcing method for homogeneous isotropic turbulence – 2.2. Forcing based on a reconstruction-like method

The synthetic velocity used in this work originates from the work of Kraichnan 1970 which has been later extended by Fung, Hunt, Malik, et al. 1992, providing an unfrozen synthetic velocity field. The method is recalled hereafter. The starting point of this approach is the inverse Fourier transform representation of the velocity field:

$$\mathbf{u}^s(\mathbf{x}, t) = \int_{-\infty}^{\infty} \int_{-\infty}^{\infty} [\hat{u}(\boldsymbol{\kappa}, \omega) e^{i\psi(\boldsymbol{\kappa}, \omega)} \boldsymbol{\sigma}(\boldsymbol{\kappa}, \omega)] e^{i(\boldsymbol{\kappa} \cdot \mathbf{x} + \omega t)} d\boldsymbol{\kappa} d\omega \quad (2.5)$$

Considering only one frequency for each wavelength, the integral in Eq. (2.5) is then discretized in a sum of N random Fourier modes:

$$\mathbf{u}^s(\mathbf{x}, t) = \sum_{n=-\infty}^{\infty} \hat{u}_n \boldsymbol{\sigma}^n e^{i(\boldsymbol{\kappa}^n \cdot \mathbf{x} + \psi_n + \omega_n t)} \quad (2.6)$$

The right hand-side of this equation can be split into two parts as:

$$\mathbf{u}^s(\mathbf{x}, t) = \sum_{n < 0} \hat{u}_n \boldsymbol{\sigma}^n e^{i(\boldsymbol{\kappa}^n \cdot \mathbf{x} + \psi_n + \omega_n t)} + \sum_{n > 0} \hat{u}_n \boldsymbol{\sigma}^n e^{i(\boldsymbol{\kappa}^n \cdot \mathbf{x} + \psi_n + \omega_n t)} \quad (2.7)$$

leading to

$$\mathbf{u}^s(\mathbf{x}, t) = \sum_{n > 0} \hat{u}_n \boldsymbol{\sigma}^n \left(e^{i(\boldsymbol{\kappa}^n \cdot \mathbf{x} + \psi_n + \omega_n t)} + e^{-i(\boldsymbol{\kappa}^n \cdot \mathbf{x} + \psi_n + \omega_n t)} \right) \quad (2.8)$$

finally using Euler formula, the synthetic velocity is discretized in N random Fourier modes on a half-spherical spectral space:

$$\mathbf{u}^s(\mathbf{x}, t) = 2 \sum_{n=1}^N \hat{u}_n \cos(\boldsymbol{\kappa}^n \cdot \mathbf{x} + \psi_n + \omega_n t) \boldsymbol{\sigma}^n \quad (2.9)$$

where \hat{u}_n , ψ_n , $\boldsymbol{\sigma}^n$ and ω_n correspond respectively to the amplitude, the phase, the direction and the time frequency of the n^{th} Fourier mode related to the wave vector $\boldsymbol{\kappa}^n$. The wave vector $\boldsymbol{\kappa}^n$ is randomly chosen on a half spherical shell with radius $\kappa_n = |\boldsymbol{\kappa}^n|$ to ensure statistical isotropy. Using spherical coordinates $(\kappa_n, \phi_n, \theta_n)$, as shown in Fig. 2.1, its components are calculated as:

$$\kappa_1^n = \kappa_n \sin(\theta_n) \cos(\phi_n) \quad (2.10)$$

$$\kappa_2^n = \kappa_n \sin(\theta_n) \sin(\phi_n) \quad (2.11)$$

$$\kappa_3^n = \kappa_n \cos(\theta_n) \quad (2.12)$$

where θ_n , $0 \leq \theta_n \leq \pi$ and ϕ_n , $0 \leq \phi_n \leq \pi$ are random angles defined for the n^{th} mode. Requiring that the probability of a randomly selected direction of a wave vector is the same for all dS on the half shell of the sphere whose radius is κ_n , leads to (see

2. Forcing method for homogeneous isotropic turbulence – 2.2. Forcing based on a reconstruction-like method

Pdf	Interval
$P(\varphi_n) = 1/\pi$	$0 \leq \varphi_n \leq \pi$
$P(\theta_n) = \sin(\theta_n)/2$	$0 \leq \theta_n \leq \pi$
$P(\alpha_n) = 1/(2\pi)$	$0 \leq \alpha_n \leq 2\pi$
$P(\psi_n) = 1/(2\pi)$	$0 \leq \psi_n \leq 2\pi$

Table 2.2. – Probability density functions of random variable

Appendix A.1):

$$p(\kappa_n) d\kappa_n = \frac{dS}{2\pi\kappa_n^2} \quad (2.13)$$

$$p(\theta_n) d\theta_n p(\varphi_n) d\varphi_n = \frac{\kappa_n d\theta_n \kappa_n \sin(\theta_n) d\varphi_n}{2\pi\kappa_n^2} \quad (2.14)$$

The divergence-free condition $\nabla \cdot \mathbf{u}^s = 0$ implies that $\boldsymbol{\kappa}^n$ is orthogonal to $\boldsymbol{\sigma}^n$. As a result, the unit vector $\boldsymbol{\sigma}^n$ is given by:

$$\sigma_1^n = \cos(\varphi_n) \cos(\theta_n) \cos(\alpha_n) - \sin(\varphi_n) \sin(\alpha_n) \quad (2.15)$$

$$\sigma_2^n = \sin(\varphi_n) \cos(\theta_n) \cos(\alpha_n) + \cos(\varphi_n) \sin(\alpha_n) \quad (2.16)$$

$$\sigma_3^n = -\sin(\theta_n) \cos(\alpha_n) \quad (2.17)$$

Despite the synthetic velocity being divergence-free at the continuous level, Saad, Cline, Stoll, et al. 2017 have shown that this is not always the case at the discrete level. In their work, they proposed a method to guarantee a divergence-free synthetic signal at the discrete level. To guarantee a free-divergence synthetic velocity much work has been put forward over the past years and references exist on the subject such as the work of Poletto, Craft, and Revell 2013 and Patruno and Ricci 2018. In this work, no attempt is made to ensure a free-divergence synthetic signal and this is left for future prospects.

The phase ψ_n is randomly chosen to satisfy spatial homogeneity (see Appendix A.2). The probability density functions for the parameters φ_n , θ_n , α_n and ψ_n are given in Table 2.2. Besides, the amplitude is written as $\hat{u}_n = \sqrt{E(\kappa_n)\delta\kappa_n}$, where $E(\kappa)$ is a prescribed energy spectrum and $\delta\kappa_n$ denotes the wave number step of the n^{th} mode in the interval $[\kappa_1, \kappa_N]$. For a logarithmic discretization, κ_n and $\delta\kappa_n$ are simply given by:

$$\delta\kappa_n = \frac{\log(\kappa_N) - \log(\kappa_1)}{N}, \quad \kappa_n = e^{(\log(\kappa_1) + n\delta\kappa_n)} \quad (2.18)$$

This allows a better discretization in the lower wave number range corresponding to the larger energy-containing eddies rather than a linear discretization (Béchara, Bailly, and Lafon 1994 and Flohr and Vassilicos 2000). Using statistical properties of

2. Forcing method for homogeneous isotropic turbulence – 2.2. Forcing based on a reconstruction-like method

the prescribed probability density functions, the synthetic kinetic energy is defined as:

$$k_{synthetic} = \sum_{n=1}^N \hat{u}_n^2 = \int_0^{\kappa_{cut}} E(\kappa) d\kappa \quad (2.19)$$

in which κ_{cut} is the cut off number. Similarly, one can show (Bailly, Lafon, and Candel 1995) that moments of the synthetic velocity verify a Gaussian distribution with zero mean and variance equal to $\overline{u_i^s u_j^s} = \frac{2}{3} k_{synthetic} \delta_{ij}$ where the over bar represents a statistical averaging (see Appendix A.3). The frequency ω_n is defined as:

$$\omega_n = \sqrt{\frac{\pi}{2}} \frac{\lambda_n}{T} = \lambda_n \check{\omega}_n \quad (2.20)$$

in which T corresponds to the prescribed turn-over time scale and λ is a normal random variable which can be set to be deterministic, *i.e.* $\lambda \sim \mathcal{N}(\lambda_m, \lambda_\sigma = 0)$ or stochastic, *i.e.* $\lambda \sim \mathcal{N}(\lambda_m, \lambda_\sigma > 0)$ ¹. The turn-over time scale T is mode-independent and therefore its corresponding frequency $\omega = \check{\omega}_n$ is referred to as constant frequency.

Rather than using a deterministic value for λ , the use of a Gaussian distribution plays a crucial role in recovering two-time correlations of the synthetic velocity u_i^s . Indeed, a stochastic value for λ prevents strong oscillations on the behavior of the two-time correlation function (Favier, F. Godeferd, and Cambon 2010).

When looking at the two-time correlation function, and considering the frequency $\omega_n = \lambda_n \omega$, one gets:

$$\mathcal{R}(\tau) = \frac{\overline{u_1^s(t) u_1^s(t+\tau)}}{\overline{u_1^s u_1^s}} = \frac{1}{k_{synthetic}} \sum_{n=1}^N \hat{u}_n^2 \overline{\cos(\lambda_n \omega \tau)} \quad (2.21)$$

where τ is the separation time. By using the central limit theorem and by ensuring in practice that $N > 30$, Eq. (2.21) becomes:

$$\mathcal{R}(\tau) \xrightarrow{N \rightarrow +\infty} \frac{1}{k_{synthetic}} \sum_{n=1}^N \hat{u}_n^2 \exp\left(-\frac{1}{2}(\lambda_m^2 + \lambda_\sigma^2)\omega^2 \tau^2\right) \quad (2.22)$$

In order not to alter the correlation function, one needs to ensure that $(\lambda_m^2 + \lambda_\sigma^2) = 1$. In addition, as explained by Favier, F. Godeferd, and Cambon 2010, the condition $\lambda_\sigma > \lambda_m$ must be satisfied to avoid negative loops as depicted in Fig. 2.2. The two following Gaussian distributions are assessed in this study:

$$\lambda \sim \begin{cases} \mathcal{N}(\lambda_m = 1, \lambda_\sigma = 0) & \text{deterministic} \\ \mathcal{N}(\lambda_m = 0.6, \lambda_\sigma = 0.8) & \text{stochastic} \end{cases} \quad (2.23)$$

1. λ_m corresponds to the mean and λ_σ to the standard deviation

2. Forcing method for homogeneous isotropic turbulence – 2.2. Forcing based on a reconstruction-like method

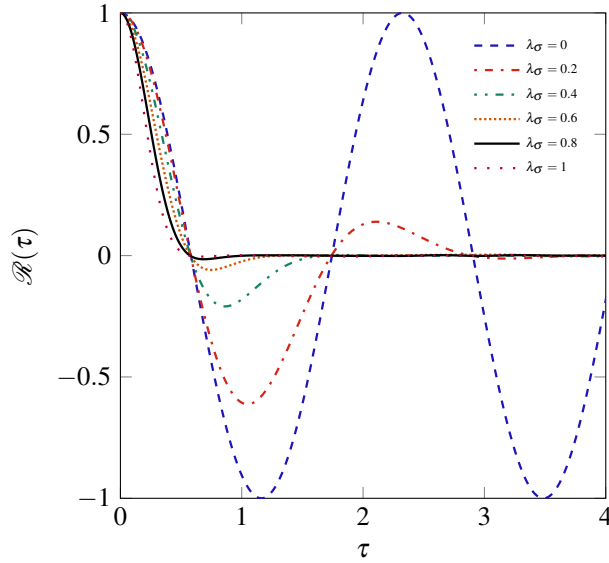


Figure 2.2. – Two-time correlation functions of the synthetic velocity u_i^s for different Gaussian distributions $\lambda \sim \mathcal{N}(\lambda_m = 0.6, \lambda_\sigma)$. Calculated from Eq 2.21.

The $\sqrt{\frac{\pi}{2}}$ factor in the definition of the frequency ω Eq. (2.20) allows to theoretically recover the prescribed turn-over time scale T . Indeed, the turn-over time scale is defined as the integration of the two-time correlation function. Integrating Eq. (2.22) from zero to infinity leads to the recovery of a factor $\frac{\pi}{2}$ in the numerator which is a classical Gaussian integration result. Indeed, without this coefficient the turn-over time scale would be increased.

2.2.2.2. Spectral density spectrum

As mentioned before, the spectral density spectrum has to be prescribed. Two different spectrum models are used to sustain homogeneous isotropic turbulence:

- i) The Passot-Pouquet (PP) energy spectrum which provides a description of the largest scales that reads as:

$$E_{PP}(\kappa) = \alpha_e k L_e (\kappa L_e)^4 \exp\{-2(\kappa L_e)^2\} \quad (2.24)$$

where L_e is the wavelength associated with κ_e responsible for the most energetic eddies. In other words, $E(\kappa)$ reaches its peak at $\kappa = \kappa_e$. This spectrum only represents large eddies while the inertial range is omitted, thus a coarse grid is sufficient to recover all wave numbers containing energy. L_e is related to the integral length scale $L_{||}$ as:

$$L_e = \alpha_L L_{||} \quad (2.25)$$

2. Forcing method for homogeneous isotropic turbulence – 2.2. Forcing based on a reconstruction-like method

The coefficient α_e is calibrated so that the integration of Eq. 2.24 gives the total turbulent kinetic energy and therefore found from the definition of the kinetic energy:

$$k = \int_0^{\infty} E(\kappa) d\kappa \quad (2.26)$$

α_L is recovered from the definition of the integral length scale for an isotropic homogeneous turbulence:

$$L_{||} = \frac{3\pi}{4k} \int_0^{\infty} \frac{E(\kappa)}{\kappa} d\kappa \quad (2.27)$$

Therefore, one obtains:

$$\alpha_e = \frac{32}{3} \sqrt{\frac{2}{\pi}} \approx 8.511, \quad \alpha_L = \frac{1}{\sqrt{2\pi}} \approx 0.3989 \quad (2.28)$$

- ii) The von Kármán-Pao (VKP) energy spectrum model which gives a description of the largest scales as well as the smallest ones given by:

$$E_{VKP}(\kappa) = \frac{2}{3} \alpha_e k L_e \frac{(\kappa L_e)^4}{[(\kappa L_e)^2 + 1]^{17/6}} \exp\{-2(\kappa L_\eta)^2\} \quad (2.29)$$

where L_η represents the Kolmogorov scale, *i.e.* the most dissipative eddies:

$$L_\eta = \left(\frac{\nu^3}{\epsilon} \right)^{(1/4)} \quad (2.30)$$

This spectrum is in agreement with Kolmogorov's "-5/3" power-law and therefore reproduces the inertial subrange. The maximum occurs at $\sqrt{12/5} \kappa_e$. As seen previously, the coefficients α_E and α_L are determined respectively by definitions of kinetic energy (Eq. (2.26)) and integral length scale (Eq. (2.27)). For integration, the exponential part of the spectrum is neglected since for small values of κL_η , $f_\eta = \exp\{-2(\kappa L_\eta)^2\}$ tends to unity (Lafitte, Le Garrec, Bailly, et al. 2014). As a result one gets

$$\alpha_e = \frac{55}{9\sqrt{\pi}} \frac{\Gamma(5/6)}{\Gamma(1/3)} \approx 1.453, \quad \alpha_L = \frac{\Gamma(1/3)}{\sqrt{\pi}\Gamma(5/6)} \approx 1.339 \quad (2.31)$$

Here, note that coefficients α_L and α_e are approximated by numerical integration. This allows to ensure a proper kinetic energy k and integral length scale $L_{||}$.

2.2.3. Kinetic energy monitoring

The resolved kinetic energy k_r has to be controlled to ensure that it reaches the target filtered kinetic energy k_r^\dagger . In the following, two strategies for monitoring the

2. Forcing method for homogeneous isotropic turbulence – 2.2. Forcing based on a reconstruction-like method

resolved kinetic energy are presented, both based on the turbulent kinetic energy budget that reads in homogeneous turbulence:

$$\frac{\partial k_r}{\partial t} = -\epsilon - u_i \frac{\partial u_i^s}{\partial t} \quad (2.32)$$

in which u_i , k_r and ϵ represent respectively the large scale velocity fluctuation, the resolved turbulent kinetic energy and the total dissipation which is the sum of the resolved and the sub-grid scale (SGS) dissipation $\epsilon = \epsilon_r + \epsilon_{SGS}$.

The first technique makes use of a modulation coefficient that is set so that the synthetic production balances out the target dissipation. In the second approach, the synthetic velocity is computed over a set of predetermined modes using a selective forcing technique that attempts to mimic spectral space forcing. It should be recalled that the synthetic velocity is parameterized by the target total turbulent kinetic energy and the target integral length scale through the formulation for the energy spectrum. Here, the target resolved turbulent kinetic energy is directly linked to the target total kinetic energy k^\dagger and the subgrid turbulent kinetic energy leading to the definition of the ratio $r = k_s^\dagger / k^\dagger = k_s^\dagger / (k_r^\dagger + k_s^\dagger)$. This ratio is estimated using the formulation of the considered energy spectrum model.

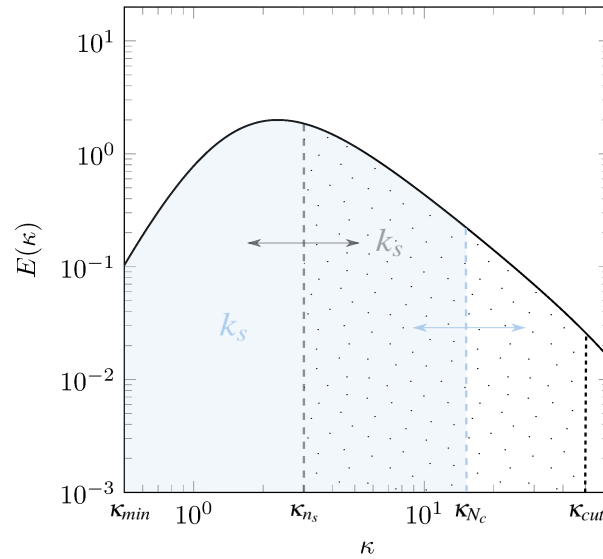


Figure 2.3. – Selective forcing scheme. Blue area: forcing starts from the lowest wave number κ_{min} to the time depending wave number κ_{Nc} . Dotted area: Forcing starts from the time depending wave number κ_{ns} to the cut off wave number κ_{cut} .

2. Forcing method for homogeneous isotropic turbulence – 2.2. Forcing based on a reconstruction-like method

2.2.3.1. Modulation coefficient

Adding a modulation coefficient A to the forcing term in the momentum equations Eq. (2.3) leads to rewrite Eq. (2.32) as:

$$\frac{\partial k_r}{\partial t} = -\epsilon - A \overline{\tilde{u}_i \frac{\partial u_i^s}{\partial t}} \quad (2.33)$$

The synthetic production term $P^{synthetic} = -\overline{\tilde{u}_i \frac{\partial u_i^s}{\partial t}}$ can be written as:

$$P^{synthetic} = -\omega \overline{\left[\tilde{u}_i \frac{1}{\omega} \frac{\partial u_i^s}{\partial t} \right]} = \frac{\beta}{\omega} \overline{\left(\frac{\partial u_i^s}{\partial t} \right)^2} \quad (2.34)$$

where β is a scalar. In practice, the estimation of β is somewhat challenging, thus it is empirically set to the value 0.5. Using the expression for the synthetic velocity in Eq. (2.9), we obtain:

$$P^{synthetic} = 2\beta\omega \sum_{n=1}^N \hat{u}_n^2 \lambda_n^2 \quad (2.35)$$

Hence, when the statistically steady state is reached, the right-hand side of the kinetic energy budget Eq. (2.33) is cancelled and this allows the coefficient to be expressed as:

$$A = \frac{\epsilon^\dagger}{2\beta\omega \sum_{n=1}^N \hat{u}_n^2 \lambda_n^2} \quad (2.36)$$

in which ϵ^\dagger corresponds to the target total dissipation. In the case of a deterministic λ , Eq. (2.36) simplifies to:

$$A = \frac{\epsilon^\dagger}{2\beta\omega k_{synthetic}} \quad (2.37)$$

This is very similar to Lundgren's approach (Lundgren 2003) but with the resolved kinetic energy replaced by the synthetic kinetic energy $k_{synthetic}$ in the resulting forcing term. It is worth noticing that this modulation coefficient method acts as a passive control device. Moreover, it is strongly dependent on the value of the coefficient β . A better performance can be achieved with an active control method, as presented in the following section.

2.2.3.2. Selective forcing

With the present method, the amount of energy to be injected into the simulation is quantified through first principle considerations. At each time step, enough energy must be injected to (i) compensate dissipation and (ii) drive the computed resolved turbulent kinetic energy k_r towards its target value k_r^\dagger . As a result, one can split the

2. Forcing method for homogeneous isotropic turbulence – 2.3. Forcing to sustain homogeneous isotropic turbulence

production term $P^{synthetic}$ induced by the synthetic velocity into a compensation of the dissipation P^{sd} and a dynamic control part P^{sc} . This approach naturally leads to the selective forcing because $P^{synthetic}/\omega$ is a sum of discretized energies which can easily be adjusted to the kinetic energy that has to be injected, mimicking spectral space forcing.

In order to determine the amount of energy to be injected, Eq. (2.32) is integrating between t and $t + \delta t$:

$$k_r(t + \delta t) - k_r(t) = -\epsilon(t)\delta t + (P^{sd}(t) + P^{sc}(t))\delta t \quad (2.38)$$

where δt is an arbitrarily short time scale, e.g. the computational time step. As postulated, the production term P^{sd} must balance the total dissipation and is then equal to the target dissipation when the statistical stationary regime is reached. Since the production term P^{sd} balances the target dissipation and requiring that the resolved kinetic energy reaches the targeted kinetic energy k_r^\dagger , the control part can be expressed as:

$$P^{sc}(t) = \frac{k_r^\dagger - k_r(t)}{\delta t} \quad (2.39)$$

By expressing $P^{synthetic} = P^{sd} + P^{sc}$ with Eq. (2.35) and using Eq. (2.39), the amount of energy to be injected writes:

$$\sum_{n_s}^{N_c} \hat{u}_n^2 \lambda_n^2 = \frac{\epsilon^\dagger}{2\beta\omega} + \frac{k_r^\dagger - k_r(t)}{2\beta\delta t\omega} \quad (2.40)$$

in which $n_s \in [1 : N]$ and $N_c \in [1 : N]$ are the lower and upper limit Fourier modes that satisfy Eq. (2.40). A specific wave number range can be selected by either summing upwards starting from the lowest wave number considered or downwards starting from the cut off wave number as illustrated in Fig. 2.3, *i.e.* this forcing may be performed either at large or small scales. Typically, when $n_s = 1$ and $N_c \ll N(\kappa_{cut})$ this mimics spectral space forcing at low wave numbers. In any case, the kinetic energy injected into the simulation must meet the condition defined by Eq. (2.40).

2.3. Forcing to sustain homogeneous isotropic turbulence

In this section, the reconstruction-like method is employed to sustain isotropic homogeneous turbulence. Working in the framework of homogeneous isotropic turbulence enables using existing analytical results as energy spectrum models, two-point and two-time correlations functions. Naturally, the energy spectrum model needs to be in accordance with the physics since it drives the correlation functions. The following desired specifications have been imposed:

2. Forcing method for homogeneous isotropic turbulence – 2.3. Forcing to sustain homogeneous isotropic turbulence

- i) monitoring of the turbulent kinetic energy,
- ii) recovering physical energy spectrum,
- iii) recovering physical space and time correlations.

As for the forcing methods presented before, it is necessary to be able to reach a target energy as well as the steady state as quickly as possible. It is also important to recover an energy spectrum that is in agreement with the Kolmogorov "-5/3" scaling law. The proposed method must also overcome the limitations of Lundgren's forcing method and thus, the resulting longitudinal lengthscale has to be consistent with the prescribed one.

In this section, we test the robustness and the efficiency of the proposed approach upon homogeneous isotropic turbulence (HIT). Two strategies relating to the constant frequency ω of the synthetic velocity are investigated: (i) using a deterministic value for all modes, (ii) varying randomly from one mode to another following a Gaussian distribution. The reader is referred to Eq. (2.23) for the two Gaussian distributions used in this work. Then, we investigate the influence of grid resolution on important features of turbulence. The last part of this section provides an insight of the versatility of the proposed methodology by testing a more realistic frequency.

2.3.1. Numerical set up

The proposed approach is assessed by performing large-eddy simulations of a sustained homogeneous isotropic turbulence at $Re_\lambda = 90$ in a triply periodic box of size $L_{box} = 2\pi$. This case has been chosen considering previous investigation of linear forcing such as Carroll and Blanquart 2013, Rosales and Meneveau 2005, and Bassenne, Urzay, Park, et al. 2016 among others. The same procedure as in Sec. 2.2.2 is used for initialization with $N = 200$ modes. The same number of mode is used for the synthetic forcing. Simulation results are obtained using the open-source generic CFD solver library CALIF³S introduced in Sec. 1.3. Here, the time step is fixed according to the CFL based on the prescribed root mean square (rms) velocity and the mesh size to be 0.1.

The numerical results are obtained with the dynamic Smagorinsky subgrid-scale model (Germano, Piomelli, Moin, et al. 1991) and a mesh containing $N^3 = 128^3$ grid points. The density is fixed to $\rho = 1.2 \text{ kg.m}^{-3}$ and the viscosity is equal to $\nu = 0.005 \text{ m}^2 \text{ s}^{-1}$. The grid resolution is such that $\kappa_{max} L_\eta = 0.46$, meaning that eddies with a size above six times the Kolmogorov scale are resolved. The target total dissipation is defined as $\epsilon^\dagger = U_{rms}^3 / L_{||}$ where $U_{rms} = \sqrt{2/3 k^\dagger}$ is the root mean square velocity. Besides the studied length scale $L_{||} = 13\% L_{box}$, two different length scales are tested in this study. The corresponding simulation parameters are summarized in Table 2.3. For the following results, all the statistic quantities considered (spectrum, two-point and two-time correlation) are averaged over at least 100 saves during 70 times the turn-over time scale T (Eq. (2.41)) for each case.

2. Forcing method for homogeneous isotropic turbulence – 2.3. Forcing to sustain homogeneous isotropic turbulence

Parameters	Unity	$L_{ } = 0.5m$	$L_{ } = 0.8m$	$L_{ } = 1.19m$
$L_{ }/L_{box}$	-	8%	13%	19%
Re_{λ}	-	71	90	110
k	$m^2.s^{-2}$	17.1	17.1	17.1
ϵ^{\dagger}	$m^2.s^{-3}$	77.2	48.2	32.3
ν	$m^2.s^{-1}$	0.005	0.005	0.005
ρ	$kg.m^{-3}$	1.2	1.2	1.2
$\kappa_{max}L_{\eta}$	-	0.41	0.46	0.50

Table 2.3. – Summary table of study parameters

2.3.2. Constant frequency

As mentioned previously, the present approach is studied using a constant turn-over time scale T defined as:

$$T = \frac{k^{\dagger}}{\epsilon^{\dagger}} \quad (2.41)$$

A comparison is made between a forcing with the modulation coefficient A and the proposed selective forcing starting from low wave numbers $\kappa_{min} = 0.01\kappa_e$. The consequences of the spectrum choice are shown hereafter by looking separately at the two proposed distributions of λ , the deterministic and stochastic one.

2.3.2.1. Deterministic frequency

In this section, the influence of a deterministic λ as referred in Eq. (2.23) is investigated. Fig. 2.4a shows the time evolution of the resolved kinetic energy. The corresponding energy spectra, averaged over the period of time $t \in [8T : 80T]$, are depicted in Fig. 2.4b. In the first place, it is worth noting that spectra have all a very similar inertial subrange. The main observed differences take place at large scales. In this area both spectra resulting from simulations with modulation coefficient lack energy, when compared to selective forcing cases. The behavior of the forced PP spectrum with modulation coefficient needs particular attention. First, the maximum occurs nearly at the same wave number k_e as the analytical PP spectrum. However, it is observed that an inertial subrange is recovered whereas none are prescribed. This desirable outcome is due to the nonlinearities of the Navier-Stokes equations. Both spectra resulting from the selective forcing are characterized by a small break near the beginning of the inertial subrange. The "-5/3" slope is also recovered for both prescribed spectra. These results suggest that regardless of the imposed spectrum resulting spectra tends towards a more physical behavior, well described in this case of HIT by the VKP spectrum.

As shown in Fig. 2.4a, the proposed forcing with the modulation coefficient drives the resolved kinetic energy towards different stationary values depending on the prescribed energy spectrum. More energy is recovered when using a PP energy spectrum

2. Forcing method for homogeneous isotropic turbulence – 2.3. Forcing to sustain homogeneous isotropic turbulence

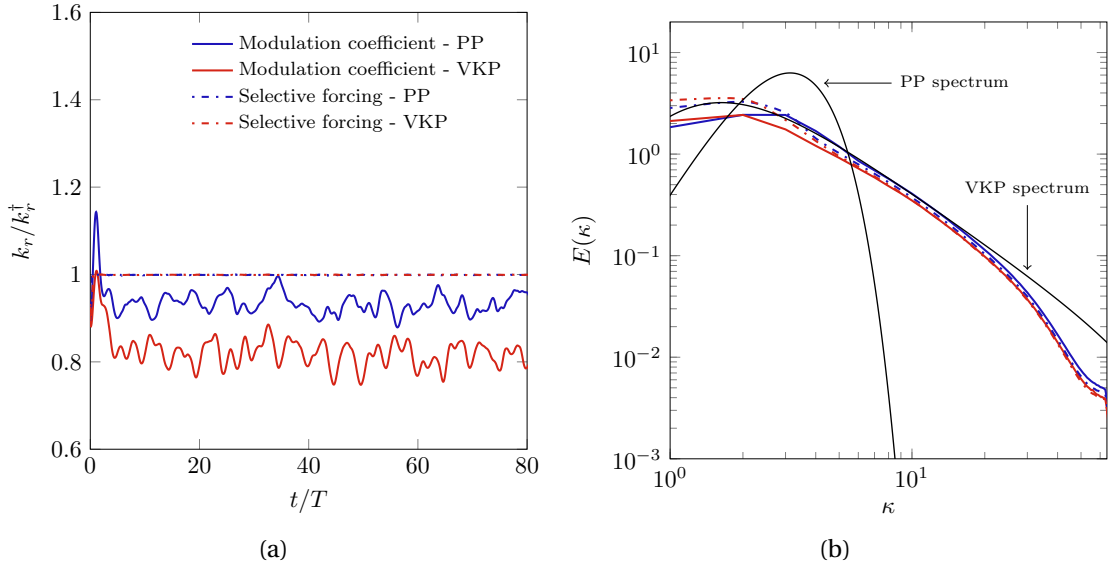


Figure 2.4. – Comparison between the two forcing techniques: modulation coefficient A and selective forcing. Results are presented for the two studied energy spectrum: Passot-Pouquet (PP) and von Kármán-Pao (VKP) energy spectrum. (a) Time evolution of the resolved kinetic energy and (b) mean energy spectra averaged over the period of time $t \in [8T : 80T]$. Plain lines depict the analytical energy spectra.

rather than with VKP energy spectrum. This may be due to confinement effect regarding the VKP spectrum. The empirical choice of β leads to underestimate the resolved kinetic energy by 5% in the "Modulation coefficient - PP" case. For a prescribed VKP energy spectrum, the primary loss of kinetic energy due to confinement effect along with the rough approximation of β , leads to an under-estimate by 20% of the resolved kinetic energy. In contrast to the modulation coefficient, the selective forcing drives the resolved kinetic energy towards its target value for both prescribed energy spectra. This approach also removes oscillations in the turbulent kinetic energy curve and shortens the transient time. These results are suitable to recover better statistical properties which could be taken only after one turn-over time scale T .

The longitudinal correlation functions are shown in Fig. 2.5a and Fig. 2.5b respectively for a prescribed PP and VKP energy spectrum. Two-point correlation functions are highly dependent on the energy spectrum model. In HIT, an analytic relationship between the energy spectrum and the longitudinal correlation function can be derived Hinze 1975; Sagaut and Cambon 2018 and is expressed as:

$$U_{rms}^2 f(r, t) = 2 \int_0^\infty \left(\frac{\sin \kappa r}{\kappa^3 r^3} - \frac{\cos \kappa r}{\kappa^2 r^2} \right) E(\kappa, t) d\kappa \quad (2.42)$$

in which r represents the space separation. This relation is used to plot the analytical

2. Forcing method for homogeneous isotropic turbulence – 2.3. Forcing to sustain homogeneous isotropic turbulence

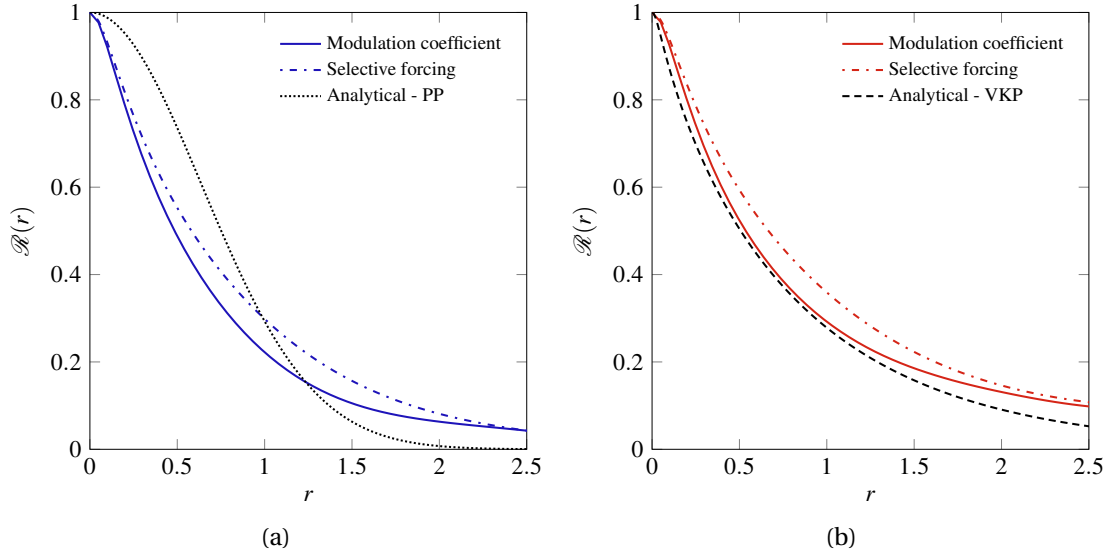


Figure 2.5. – Mean longitudinal correlation functions taken over the three directions and averaged over the period of time $t \in [8T : 80T]$. Left: prescribed Passot-Pouquet (PP) energy spectrum. Right: prescribed von Kármán-Pao (VKP) energy spectrum.

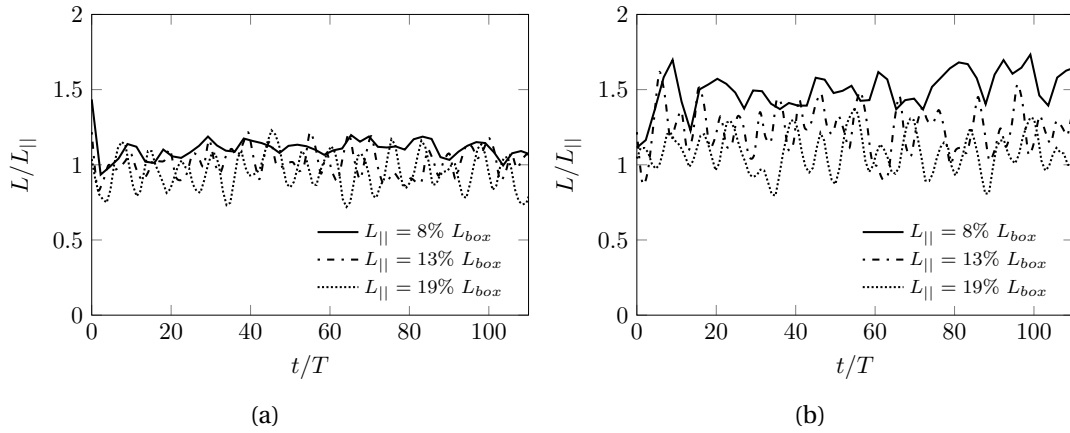


Figure 2.6. – Time evolution of the longitudinal length scale for three different prescribed integral length scales $L_{||}$. (a) Prescribed Passot-Pouquet energy spectrum, (b) prescribed von Kármán-Pao energy spectrum.

PP and VKP correlation functions. All the resulting correlation functions appear to tend towards the analytical two-point correlation function calculated with a VKP spectrum. This result is in agreement with the obtained spectra since the resulting spectra match well the analytical VKP spectrum. In detail, when imposing a PP spectrum with the modulation coefficient (Fig. 2.5a), the resulting spatial correlations tend to follow the

2. Forcing method for homogeneous isotropic turbulence – 2.3. Forcing to sustain homogeneous isotropic turbulence

VKP longitudinal function for small distance separations r . The deviation between $0.5m$ and $2.5m$ may be attributed to the different descriptions of large scales between the corresponding spectra as shown in Fig. 2.4b. The two-point correlation function from the simulation with the modulation coefficient and a prescribed VKP spectrum follows similar trends as the analytical one. The spread between the origin and $1.5m$ is about 6%. For both prescribed spectra, the selective forcing approach entails a shift towards higher correlation values comparing to modulation coefficient simulations.

To show that the resulting length scales are independent of the domain size, two different length scales $L_{||} = 8\%L_{box}$ and $L_{||} = 19\%L_{box}$ are tested in addition to the studied length scale $L_{||} = 13\%L_{box}$. Simulation parameters are given in Table 2.3. Fig. 2.6a and Fig. 2.6b represent the time evolution of the longitudinal length scale for these three cases using the selective forcing approach. This result highlights that the resulting length scales are independent of the domain size, sidestepping the main shortcoming of Lundgren’s method (Lundgren 2003). Nevertheless, for both prescribed spectra, reducing the prescribed length scale leads to an increase of the resulting length scale, particularly significant for prescribed VKP spectra (Fig. 2.6b). Finally, the transverse integral scale is approximately equal to half the longitudinal integral scale complying with HIT conditions. This result is highlighted in Fig. 2.7 in which longitudinal $f(r)$ and transverse $g(r)$ correlation functions are plotted for the studied case and a prescribed VKP spectrum. The analytical function $f(r)$ is given by Eq. (2.42) and a similar expression can be obtained for $g(r)$ (Hinze 1975; Sagaut and Cambon 2018). In the present case, the ratio between the resulting longitudinal and transverse integral scales is about 2.1.

The proposed approach allows to recover length scales that are independent of the domain size. For all cases, the choice of the spectrum seems to affect only large scale while the inertial subrange is recovered. The choice of the β coefficient is significant for modulation coefficient simulations and leads to an under-estimate of the resolved kinetic energy, magnified by confinement effect in the case of a prescribed VKP spectrum. In contrast, the selective forcing approach allows to recover the targeted kinetic energy within a short period of time and with a much less oscillating behavior, thereby removing the effects of the β approximation. However, this method leads to an overestimate of longitudinal integral scales, especially in the case of a prescribed VKP spectrum. Finally, the resulting two-time correlation functions, not shown in this section, have an oscillating behavior which is highly non-physical. The next section focuses exclusively on the selective forcing approach and a stochastic frequency is introduced to damp oscillations of the two-time correlation function.

2.3.2.2. Stochastic frequency

The stochastic part of Eq. (2.23) is used for the Gaussian distribution of λ . Fig. 2.8 shows the two-time correlation functions comparing the deterministic cases with the stochastic ones for the selective forcing approach. The analytical two-time correlations

2. Forcing method for homogeneous isotropic turbulence – 2.3. Forcing to sustain homogeneous isotropic turbulence

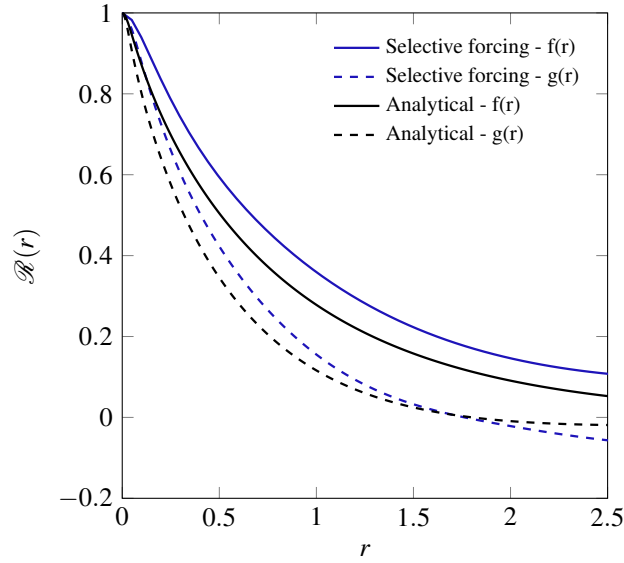


Figure 2.7. – Mean longitudinal $f(r)$ and transverse $g(r)$ correlation functions taken over the three directions and averaged over the period of time $t \in [8T : 80T]$ for the selective forcing with a prescribed VKP spectrum.

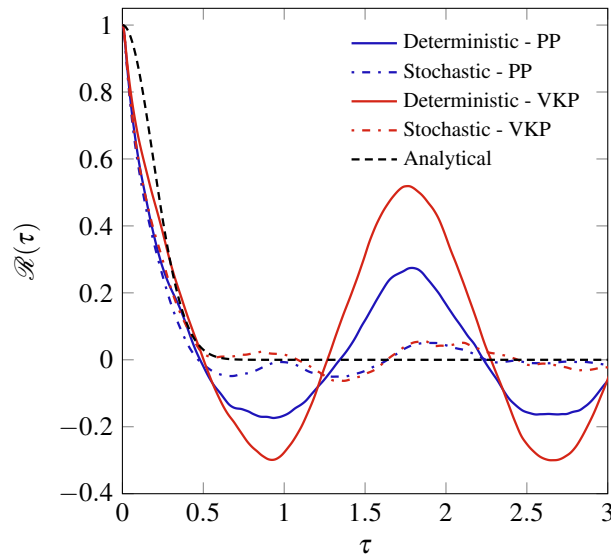


Figure 2.8. – Two-time correlation function comparison between a deterministic frequency and a stochastic frequency using the selective forcing approach for the two prescribed energy spectra: Passot-Pouquet (PP) and von Kármán-Pao (VKP) energy spectra.

expressed in Eq. (2.22) are similar considering either a PP or VKP energy spectrum, thus only the two-time correlations corresponding to a prescribed PP spectrum are plotted in Fig. 2.8. It is recalled here that imposing a deterministic frequency means

2. Forcing method for homogeneous isotropic turbulence – 2.3. Forcing to sustain homogeneous isotropic turbulence

introducing a non-physical behavior into the computation via the synthetic velocity, *i.e.* strong oscillations of the theoretical two-time correlation function as shown in Fig. 2.2. For deterministic cases, this effect is tempered, reducing by a factor five for a prescribed PP spectrum and a factor two for a prescribed VKP spectrum oscillations amplitude of the resulting two-time correlations. For small time separation τ the two-time correlation functions follow the same trends for both prescribed energy spectra. Given a stochastic frequency it is noticeable that oscillations are drastically reduced. Correlation functions are also very similar before vanishing. This confirms that the randomness of the frequency aims only at suppressing oscillations. The fact that small oscillations are still present may be due to the limited number of modes. Indeed, increasing the mode number theoretically leads to better statistics and smooth the two-time correlations related to the synthetic velocity. Simulations with $N = 1000$ modes were performed without any significant improvement (not shown here). Nonetheless, the CPU cost increases drastically when using large number of modes. Therefore, a compromise has to be found between CPU time issues and the layout of the two-time correlation function.

Applying a stochastic frequency to the synthetic velocity gives the desired effect, *i.e.* prevents from oscillations of two-time correlations. However, one needs to ensure that statistical properties such as energy spectrum and two-point correlations remain unchanged. This is done by carrying out a benchmark between the deterministic and the stochastic cases using the selective forcing. The results are not shown here because only minor differences have been observed between the two cases regarding energy spectra and two-point correlation functions. As expected and shown by Eq. (2.40), the use of a stochastic frequency modifies the amount of energy injected at each wavelength. Naturally, this slightly affects the energy containing part of the resulting spectra, *i.e.* large scales. Therefore, the two-point correlations are altered but with minor modifications.

2.3.3. Influence of grid resolution

In this section, the selective forcing is assessed at various grid resolutions. This sensitivity study is performed by examining some of the well-known most important features occurring in the inertial subrange of HIT. In order to ensure a clearly defined inertial subrange, we consider the case of an inviscid flow. The same numerical parameters as before are used except for the subgrid model. A Smagorinsky subgrid model is employed with a Smagorinsky constant $C_s = 0.148$ (Sagaut 2004). Simulations are performed for three additional grid resolutions $N^3 = 64^3, N^3 = 96^3$ and $N^3 = 192^3$ besides the studied grid resolution $N^3 = 128^3$.

Among important features, we examine energy spectra and two-point correlations that are plotted respectively in Fig. 2.9a and Fig. 2.9b. Energy spectra are in good agreement with Kolmogorov's " $-5/3$ " power-law for all grid resolutions. The results show that the inertial subrange remains almost not affected by the selective forcing.

2. Forcing method for homogeneous isotropic turbulence – 2.3. Forcing to sustain homogeneous isotropic turbulence

Fig. 2.9b emphasizes a grid convergence of the two-point correlation functions for small distance separations, for values below $0.5m$. In this region, a similar trend between the four meshes can be drawn, which can be related to the very similar inertial subranges recovered for all spectra. As a remark, discrepancies observed in the two-point correlations at larger r values may come from energy spectra variations observed at low wave numbers in Fig. 2.9a. A thorough investigation of the influence of grid resolution is beyond the scope of this work. However, it established that two main features of HIT are preserved.

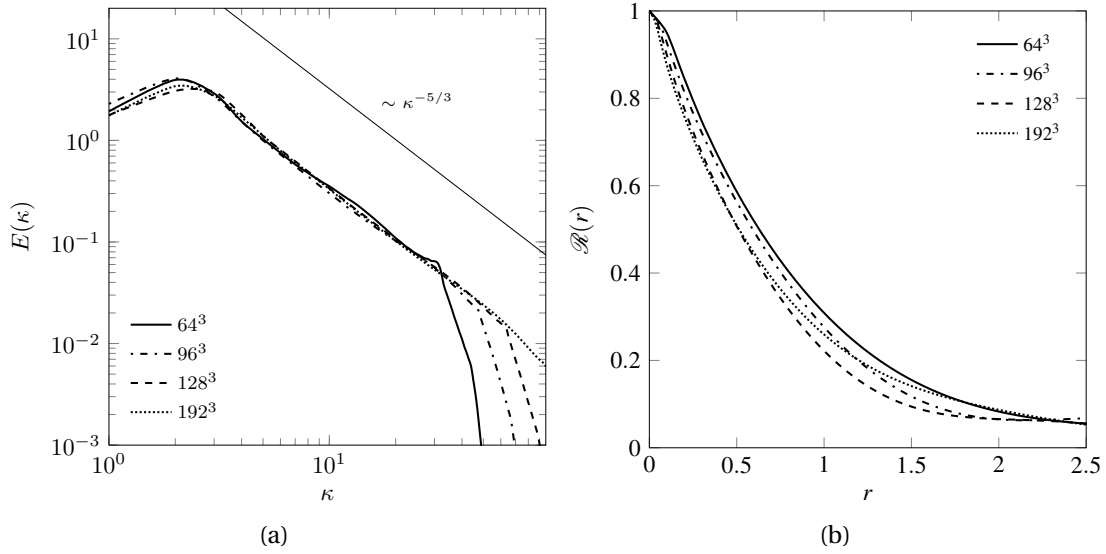


Figure 2.9. – Comparison between four grid resolutions $N^3 = 64^3$, $N^3 = 96^3$, $N^3 = 128^3$ and $N^3 = 192^3$ for the selective case with a prescribed PP spectrum and a stochastic frequency in the framework of an inviscid flow. a) Energy spectra, b) two-point correlation functions

2.3.4. Towards more realistic frequencies

The reconstruction approach coupled with the inverse Fourier method allows some degrees of freedom on the physics that is injected into the computation. The spectrum model as well as the frequency formulation have to be specified and can therefore be adjusted to the physical problem of interest.

As mentioned above, the *straining* hypothesis assumes that large scale frequencies only depend on eddy's size and energy. This aspect is spurring us to apply the *straining* hypothesis when forcing at low wave numbers, *i.e.* at large scales. Then, in this section, a frequency following the *straining* hypothesis is assessed. The frequency ω_n reads as:

$$\omega_n = \lambda_n \sqrt{\kappa_n^3 E(\kappa_n)} \quad (2.43)$$

2. Forcing method for homogeneous isotropic turbulence – 2.3. Forcing to sustain homogeneous isotropic turbulence

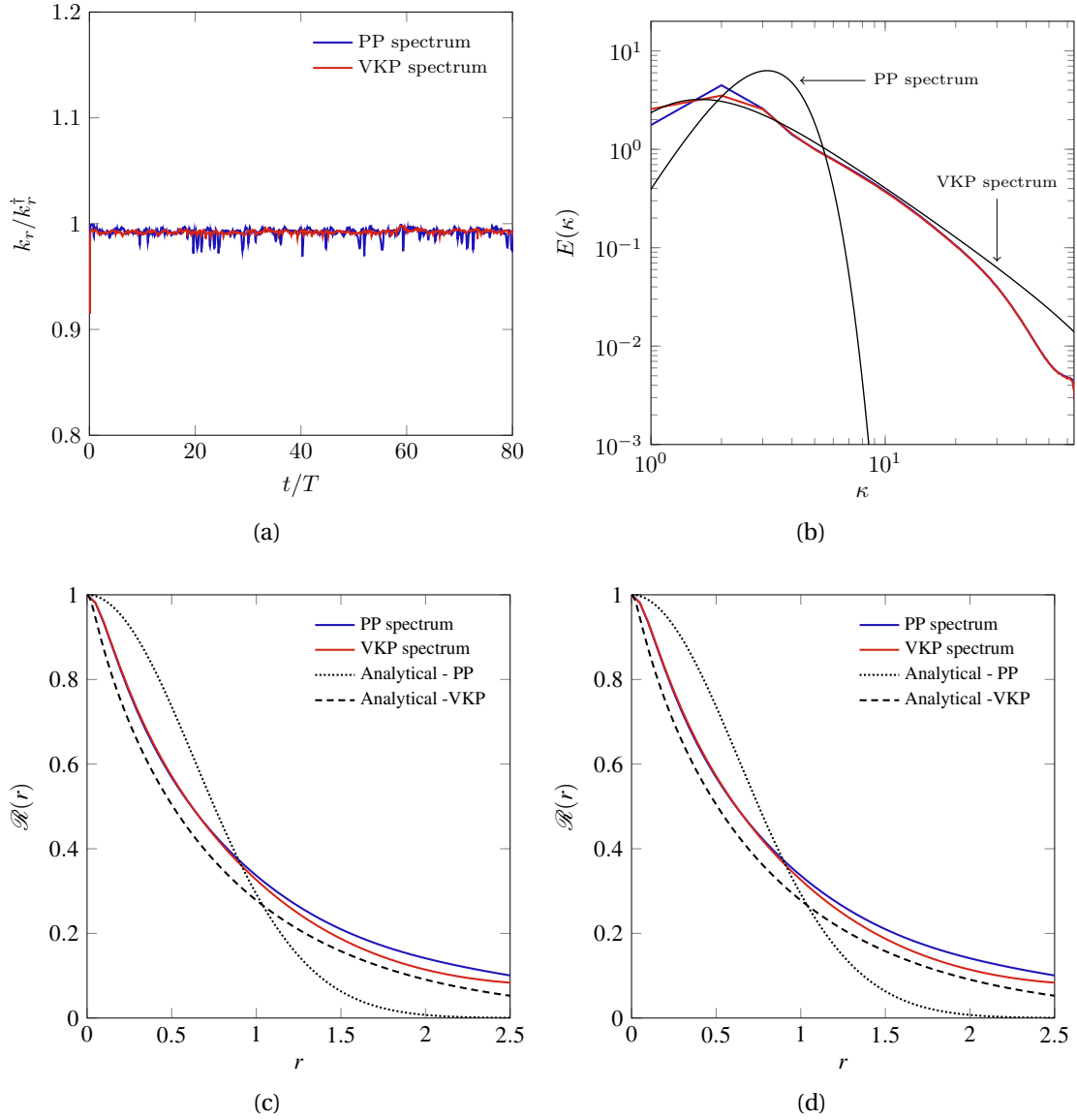


Figure 2.10. – Comparison between a prescribed PP or VKP spectrum for a selective forcing at low wave numbers with a stochastic *straining* frequency. (a) Time evolution of the kinetic energy, (b) energy spectra, (c) two-point correlation functions and (d) two-time correlation functions.

This frequency formulation is also tested upon HIT in a 2π -triple periodic box, using the same physical and numerical parameters as in 2.3.1. The random variable λ follows the same as before Gaussian distribution $\lambda \sim \mathcal{N}(0.6, 0.8)$. Considering a mode-dependent frequency, Eq. (2.40) must be modified. The turn-over time scale T defined by Eq. (2.41) is introduced to express the production term $P^{synthetic}$ from

2. Forcing method for homogeneous isotropic turbulence – 2.3. Forcing to sustain homogeneous isotropic turbulence

Eq. (2.34). This leads to the following condition:

$$\sum_{n_s}^{N_c} \hat{u}_n^2 \omega_n^2 = \frac{\epsilon^\dagger}{2\beta T} + \frac{(k_r^\dagger - k_r(t))}{2\beta T \delta t} \quad (2.44)$$

in which the coefficient β is still set to 0.5. Fig. 2.10a shows the time evolution of the resolved kinetic energy. For both prescribed spectra the target value is reached but one can notice that more oscillations of the resolved kinetic energy are observed with a prescribed PP spectrum than with a prescribed VKP spectrum. As shown in Fig. 2.10b the two spectra present a very similar inertial subrange. At large scales, the maximum of energy is unsurprisingly reached by the prescribed PP spectrum simulation. As expected by the resulting spectrum shape, the outgoing two-point correlation functions are in close agreement. The deviation from the analytical correlation function is about 13% compared to a 26% discrepancy with a constant frequency. This indicates that prescribing a more realistic frequency also influences statistical properties such as spectra and two-point correlations.

The two-time correlation functions are depicted in Fig. 2.10d. Besides the small oscillations on their behavior, the two-time correlations are in good agreement with the analytical two-time correlation functions.

2.3.5. Consideration of anisotropy

In most common flows, turbulence is inhomogeneous and anisotropic, especially near walls. It is therefore interesting to assess the capabilities of the forcing, first, on the case of an anisotropic homogeneous turbulence. There exist mathematical tools to obtain an anisotropic resulting Reynolds tensor, using for example a Cholesky decomposition. In this case the synthetic velocity writes as:

$$u_j^{s,aniso}(x_j, t) = \frac{3b_{ij}}{2k_r^\dagger} u_j^s(x_j, t) \quad (2.45)$$

with

$$b_{ij} = \begin{pmatrix} \sqrt{R_{11}^r} & 0 & 0 \\ R_{21}^r/a_{11} & \sqrt{R_{22}^r - a_{21}^2} & 0 \\ R_{31}^r/a_{11} & (R_{32}^r - a_{21}a_{31})/a_{22} & \sqrt{R_{33}^r - a_{31}^2 - a_{32}^2} \end{pmatrix} \quad (2.46)$$

in which R_{ij}^r are the resolved targeted turbulent stresses. It can be noted that the procedure still consists in generating isotropic synthetic velocity fields and then applying anisotropic coefficients to it. This means that the selective forcing can still be applied but as previously only the resolved turbulent kinetic energy can be controlled and thus, no individual control of a specific component of the Reynolds stresses is feasible. A specific control of U_{rms} , V_{rms} and W_{rms} may be conceivable by switching the used energy spectra for an anisotropic energy spectrum.

2. Forcing method for homogeneous isotropic turbulence – 2.3. Forcing to sustain homogeneous isotropic turbulence

The aim here is to show how the behavior of the method when applying a Cholesky decomposition. Regarding the anisotropy, it is common to represent it on the invariant map of the anisotropy tensor defined as:

$$a_{ij} = \frac{\overline{u_i u_j}}{k} - \frac{2}{3} \delta_{ij} \quad (2.47)$$

The first invariant ($I = \text{tr}(a_{ij})$) of this tensor is equal to zero and therefore Lumley and Newman 1977 used the non-zero second and third invariant

$$II = \frac{a_{ij} a_{ji}}{2} = A_1^2 + A_1 A_2 + A_2^2 \quad (2.48)$$

$$III = \frac{a_{ij} a_{jn} a_{ni}}{3} = -A_1 A_2 (A_1 + A_2) \quad (2.49)$$

to plot, Figure 2.11, the so-called Lumley triangle (Choi and Lumley 2001, Banerjee, Krahl, Durst, et al. 2007 and Emory and Iaccarino 2014). A_i are the eigenvalues of the anisotropy tensor. The key point here is that all the anisotropy can be represented

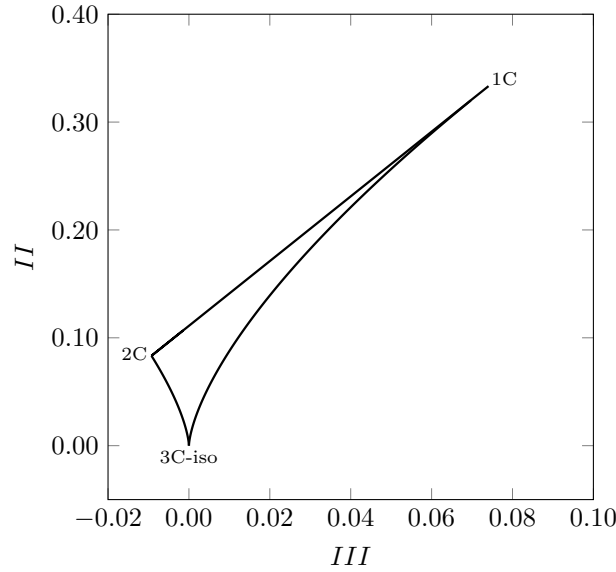


Figure 2.11. – Wave vector geometry of the n^{th} Fourier mode.

inside Lumley's triangle. Emory and Iaccarino 2014 provided clear explanation of the different kind of anisotropy. To summarize, the first limited point "1C" corresponds to a turbulence which exists only along one direction that is also called a cigar-shaped turbulence. This point is determined by the eigenvalue $A_i = \left[\frac{2}{3}, \frac{-1}{3}, \frac{-1}{3} \right]$. The limited point "2C" corresponds to a turbulence which exists in two directions and is also known as pancake-like turbulence. This point is determined by the eigenvalue $A_i = \left[\frac{1}{6}, \frac{1}{6}, \frac{-1}{3} \right]$. Finally, the limited point "3C" represents isotropic turbulence for which the eigenvalue of the anisotropic tensor are equal to zero.

2. Forcing method for homogeneous isotropic turbulence – 2.3. Forcing to sustain homogeneous isotropic turbulence

De Laage de Meux, Audebert, R. Manceau, et al. 2015 performed three cases of anisotropy, choosing one case where the three components are non-zero and two limit cases "1C" and "2C" of anisotropy. Here, the choice is made to focus on the limited state "1C" which is represented by the Reynolds tensor:

$$R_{ij}^r = k_r^\dagger \begin{pmatrix} 1.96 & 0 & 0 \\ 0 & 0.02 & 0 \\ 0 & 0 & 0.02 \end{pmatrix} \quad (2.50)$$

The two weak components are not set strictly to zero to avoid nonphysical behavior such as to obtain fluctuations time independent as explained by De Laage de Meux, Audebert, R. Manceau, et al. 2015. Furthermore, the motivation here is not to have a division by zero during the Cholesky decomposition.

The same numerical setups are employed as for the isotropic case. The synthetic velocity is built here with a PP spectrum. The integral length scale is set up to $L_{||} = 13\%L_{box}$ and the stochastic straining frequency with the same random variable λ as before (Eq. 2.23) is used. The control of the turbulent kinetic energy is performed from Eq. 2.44. The results are compared to the previous case, *i.e.* the prescribed PP energy spectrum case with the straining hypothesis.

Fig. 2.12a displays the time evolution of the resolved turbulent kinetic energy. The level of resolved turbulent kinetic energy in the anisotropic case is similar to that of isotropic cases. The same magnitude of oscillation of the temporal evolution of the resolved turbulent kinetic energy is also observed. Regarding the repartition of energy between the three components, Fig. 2.12b, it is observed that the first component does not reach the prescribed level $U_{rms}^2/k_r \sim 1.96$. However, there is a clear distinction between the two weak components (V_{rms} and W_{rms}) and the strong component U_{rms} . It seems that the Cholesky decomposition does not allow to reach the desired level of anisotropy. This is mainly due to the fact that the method does not provide a control of each component of the anisotropy tensor like what is done in De Laage de Meux, Audebert, R. Manceau, et al. 2015.

Energy spectra are displayed in Fig. 2.12c for the two cases and compared to the analytical VKP energy spectrum. The two resulting spectra exhibit similar behavior. This is in contrast to the results presented by De Laage de Meux, Audebert, R. Manceau, et al. 2015 which show that the spectra tend to be steeper in anisotropic cases. Finally, the two-point correlation functions are shown in Fig. 2.12d. For the anisotropic case the two-point correlations are displayed for each direction and compared to the correlation function of the isotropic case which is an average over the three directions (as it was done in previous sections). It clearly appears that the two-point correlations of the first component of the velocity in the x direction are higher compared to the two other components. This means that the integral length scale is higher in the x direction which was an expected result ($L_1 = \int R_{11}^1 dr = \int \overline{u(x)u(x+r)} dr > L_2 = \int \overline{v(y)v(y+r)} dr = L_3$).

2. Forcing method for homogeneous isotropic turbulence – 2.3. Forcing to sustain homogeneous isotropic turbulence

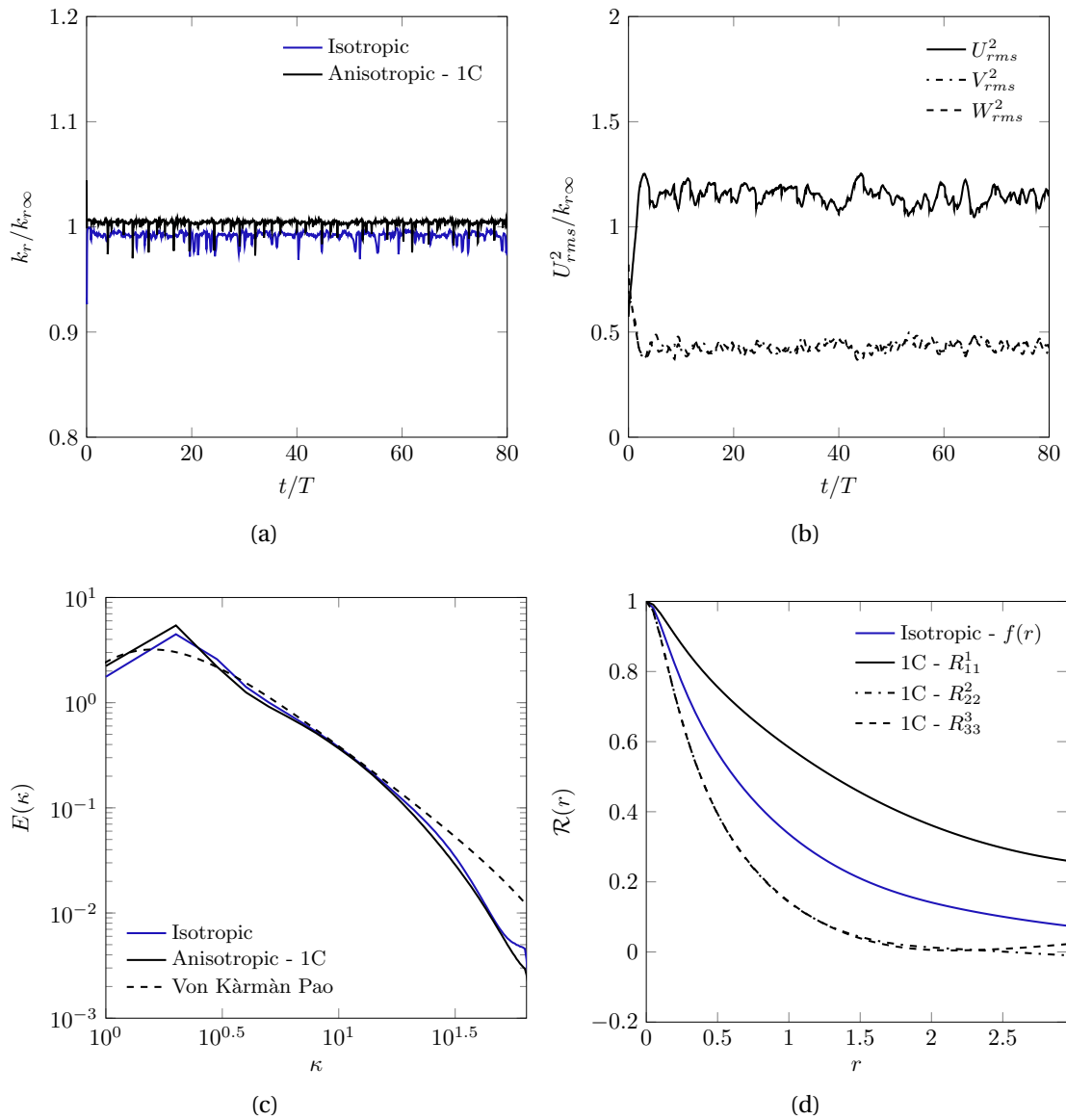


Figure 2.12. – Selective forcing at low wavenumbers: comparison between the isotropic and anisotropic "1C" with, for both computation a prescribed, a prescribed PP energy spectrum. (a) Time evolution of the kinetic energy, (b) Time evolution of the rms velocity, (c) energy spectra and (d) two-point correlation functions.

As a result, it is feasible to recover an anisotropic turbulence but without any control on it. The Cholesky decomposition clearly affects the resulting Reynolds components without affecting the total turbulent kinetic energy. As the method is not built to inject more turbulent kinetic energy than there is under the energy spectrum, the method is not designed to inject negative Reynolds stresses to reach a desired level.

2.4. Towards a self-adaptive forcing : Decaying isotropic turbulence

In the previous section, the proposed method has been shown to be effective in sustaining a homogeneous isotropic turbulence. This forcing can be used as is to study turbulence properties at small scales as well as, for example in particle-laden flows. A significant advantage of this approach is its versatility. For instance, the spectrum model is problem dependent and hence can be adjusted. The time frequency also needs to be specified and can therefore be adapted depending on whether the forcing takes place at high or low wave numbers. The use of a more realistic frequency as the straining assumption seems well suited for the forcing of homogeneous isotropic turbulence and also improves the resulting two-point correlations. Moreover, this approach is relatively adaptable to anisotropic homogeneous turbulence by the use of a Cholesky decomposition.

The idea is now to use the forcing method, not to sustain an homogeneous isotropic turbulence, but to perform a readjustment of the turbulent kinetic energy repartition between the resolved and subgrid parts. The concept is the following: for a given total turbulent kinetic energy, the starting point is a situation where there is an excess of subgrid kinetic energy, *i.e.* a lack of resolved turbulent kinetic energy compared to what the mesh could actually allow to resolve. For example, considering an hybrid RANS/LES simulation with injection of fluctuations at the interface, in the transition region between the upstream RANS domain and the downstream LES domain the subgrid kinetic energy would be in excess since the turbulence needs a certain distance to develop. The focus is now on computation domain for which the mesh size is not enough to resolve entirely the energy spectrum or not at all (RANS) and thus, LES with Smagorinsky subgrid-scale is not anymore a usable turbulence model. Consequently, we move from a dynamic Smagorinsky subgrid-scale model to the Equivalent-Detached Eddy Simulation model developed by C. Friess, R. Manceau, and T. Gatski 2015. In addition to that, this choice is motivated by the fact that we later want to perform simulations on meshes that are not refined enough to perform a LES and for which hybrid models, such as the E-DES model, perform better.

The first case of interest here is the decaying isotropic turbulence. Simulations are still performed in homogeneous isotropic turbulence, thus the reconstruction remains unchanged, *i.e.* only the unsteady term of the Navier-Stokes equation is affected by the reconstruction procedure. We first present the E-DES model and then the results for a decaying isotropic turbulence.

2.4.1. Balance of turbulent kinetic energy

The goal is to keep the total turbulent kinetic energy budget unchanged. The two equations that are at stake are the resolved turbulent kinetic energy budget and the transport equation of the mean subgrid turbulent kinetic energy, that is the ensemble

2. Forcing method for homogeneous isotropic turbulence – 2.4. Towards a self-adaptive forcing : Decaying isotropic turbulence

averaged Eq. (1.95). Considering isotropic homogeneous turbulence and the forcing production $P^{synthetic}$, the resolved turbulent kinetic energy budget writes as (Eq. (2.32) with $\epsilon_{SGS} \rightarrow P_m$):

$$\frac{\partial k_r}{\partial t} = -\epsilon_r - P_m + P^{synthetic} \quad (2.51)$$

and the mean subgrid turbulent kinetic energy budget writes as:

$$\frac{\partial k_m}{\partial t} = P_m - \overline{F_{E-DES}\epsilon_s} - P_k \quad (2.52)$$

with $P_m = \overline{P_s}$, $k_m = \overline{k_s}$ and $\epsilon_m = \overline{\epsilon_s}$. The production term that must be established in order to maintain the energy balance is denoted by the symbol P_k . The transport equation of the total turbulent kinetic energy ($k = k_r + k_m$) is found by adding Eq. (2.52) and Eq. (2.51):

$$\frac{\partial k}{\partial t} = -\epsilon_r - \overline{F_{E-DES}\epsilon_s} + P^{synthetic} - P_k \quad (2.53)$$

In decaying isotropic turbulence and for E-DES, the time evolution of the turbulent kinetic energy should be as:

$$\frac{\partial k}{\partial t} = -\epsilon_r - \overline{F_{E-DES}\epsilon_s} \quad (2.54)$$

Expressing the last term of the right hand side of previous equation and using the hypothesis that $\overline{k_s^{3/2}} \approx k_m^{3/2}$:

$$\frac{\partial k}{\partial t} = -\epsilon_r - \frac{k_m^{3/2}}{L_{E-DES}} \quad (2.55)$$

Here, the preceding equation is developed to highlight how the subgrid model behaves.

$$\frac{\partial k}{\partial t} = -\epsilon_r - \Psi(r_k) \frac{k_m^{3/2}}{r_k^{3/2} L_t} \quad (2.56)$$

For now, let's ignore the resolved dissipation and concentrate on the dissipation term.

$$\frac{\partial k}{\partial t} = -\Psi(r_k) \frac{k_m^{3/2}}{r_k^{3/2} k^{3/2}} \epsilon_m = -\Psi(r_k) \left(\frac{r_k^{observed}}{r_k} \right)^{3/2} \epsilon_m \quad (2.57)$$

in which $r_k^{observed} = k_m/k$ is the observed energy ratio. It appears that the ratio between the observed ratio and the target ratio drives the dissipation rate of the subgrid kinetic energy. For example, in the case where the observed ratio is higher than the target ratio (excess of subgrid energy compared to what the mesh could resolve), the model tends to dissipate the subgrid energy to tend towards the target ratio. Therefore, still in this case, the model allows to decrease the subgrid energy but no mechanism allows to inject this energy to the resolved motion: this is where the selective forcing comes into play.

2. Forcing method for homogeneous isotropic turbulence – 2.4. Towards a self-adaptive forcing : Decaying isotropic turbulence

Two options are possible at this stage: *i*) the subgrid energy lost at each time step is reinjected into the resolved motion. This would mean adding a coefficient in front of the synthetic velocity to reach the desired production term. The second option *ii*) is to use the selective forcing as is and to delay the decay of the subgrid kinetic energy in the case production terms from the reconstruction are not sufficient to balance the right hand side of Eq. (2.57). The second option is chosen for the rest of this study. The right hand side of Eq. 2.53 should therefore be equal to the target dissipation as:

$$-\epsilon_r - \frac{k_m^{3/2}}{L_{E-DES}} + P^{synthetic} - P_k = -\epsilon_r - \frac{(k_m^\dagger)^{3/2}}{L_{E-DES}} \quad (2.58)$$

The term P_k can then be deduced:

$$P_k = P^{synthetic} + \frac{(k_m^\dagger)^{3/2}}{L_{E-DES}} - \frac{k_m^{3/2}}{L_{E-DES}} \quad (2.59)$$

where k_m^\dagger is the target subgrid turbulent kinetic energy derived from the target ratio. This can be seen as a comparison between what the subgrid model naturally dissipates and the production of energy that is added to the resolved motion. In a transition region, where there is not enough resolved turbulent kinetic energy compared to what the calculation could resolve (*e.g.* RANS to LES region), the forcing is activated to rebalance the energy but the total energy decreases as expected. In other words, the forcing is activated and $P_k \neq 0$ when $r_k^{observed} > r_k$ and the forcing is not activated and $P_k = 0$ when $r_k^{observed} < r_k$: the method is self-adaptive.

While there is clear evidence to modify the subgrid kinetic energy transport equation based on the total kinetic energy budget, the question arises for the transport equation of the dissipation. Here, we follow the usual methodology that consists in modifying the transport equation for the dissipation following heuristically arguments. More precisely, two formulations are assess here, the first one keeps the subgrid transport equation unchanged while the second one includes an additional term proportional to the synthetic production term:

$$\frac{\partial \epsilon_m}{\partial t} = \frac{\epsilon_m}{k_m} (C_{\epsilon 1} P_m - C_{\epsilon 2} \epsilon - C_{f\epsilon} P_\epsilon) \quad (2.60)$$

in which $P_\epsilon = P^{synthetic}$. Here, the coefficient $C_{f\epsilon}$ is set to be equal to $r_k^{observed}$ and thus depends on time. This choice has been made after several attempts on the decaying isotropic turbulence case and is completely empirical.

The previous developments were made on average quantities. There are two options:

- i) as in the development of some turbulence models, moving from average quantities to instantaneous quantities,

2. Forcing method for homogeneous isotropic turbulence – 2.4. Towards a self-adaptive forcing : Decaying isotropic turbulence

ii) using mean quantities.

Here, the choice has been made to use the mean part of the synthetic production. It must be kept in mind that this average quantity is affected by the choice of the temporal filters used for the averaging process.

2.4.2. Results

Decaying homogeneous isotropic turbulence is one of the simplest turbulent cases. For example, it is used to assess the behavior of LES turbulence models. The most widely used published experimental data for grid turbulence provided by Comte-Bellot and Corrsin 1971 are used as reference data. These data were measured at three different distances $tU_0/M = 42, 98$ and 171 from a grid with mesh size $M = 50.8\text{mm}$ and a mean speed near the grid $U_0 = 10\text{m}\cdot\text{s}^{-1}$. At these locations, the Taylor Reynolds numbers Re_λ are $71.6, 65.3$ and 60.7 . This can be recast for the simulation in terms of time advancement $t_0 = 0$, $t_1 = 56M/U_0$ and $t_2 = 129M/U_0$ by applying Taylor's hypothesis. Numerical simulations are performed in a triply periodic box $[0, L]^3$ with $L = \pi/6$. This length is much larger than the integral length scale in order to avoid spurious effects of periodic boundary conditions. The initial velocity field is provided by a synthetic field defined according to the data measured at the first downstream position.

First, the E-DES model is assessed compared to other well-known models such as the dynamic smagorinsky model and the DES model. Then, the objective is to start from a RANS solution and to take advantage of the forcing to rebalance the resolved and subgrid turbulent kinetic energies.

2.4.2.1. Validation of E-DES

As preliminary step, the behavior of the E-DES approach on the DIT case is illustrated. This computation is then compared to results with the previous dynamic Smagorinsky approach. In all cases, the resolved velocity field is prescribed according to the Random Fourier Method (RFM) that provides a synthetic turbulent velocity field enforcing the von Kármán-Pao energy spectrum model (Eq. 2.29). For simulations for which the subgrid transport equations are solved, a precursor computation can be performed to initialize values of the considered subgrid quantities. In this precursor simulation, the resolved velocity field is frozen and the subgrid transport equations converge towards a stationary state. No tremendous change (Fig 2.13a) was observed between computations with or without initialization of subgrid fields. The major difference is at $t = 0$ since the two simulations do not start with the same turbulent kinetic energy. The resolved turbulent kinetic energy being the same for both simulations, the discrepancy comes from different values of the subgrid energy.

Here, computations that start with the desired level of energy are needed to compare directly with RANS computations. This is the reason why it has been chosen to

2. Forcing method for homogeneous isotropic turbulence – 2.4. Towards a self-adaptive forcing : Decaying isotropic turbulence

benchmark our results with the computation without precursor simulation. Fig. 2.13b shows the time of evolution of the turbulent kinetic energy between the DES and E-DES models. The two models give similar results on the DIT case. Given that the evolution of the subgrid energy is nearly the same for both models (Fig. 2.14), it appears that the two models provide roughly the same energy distribution.

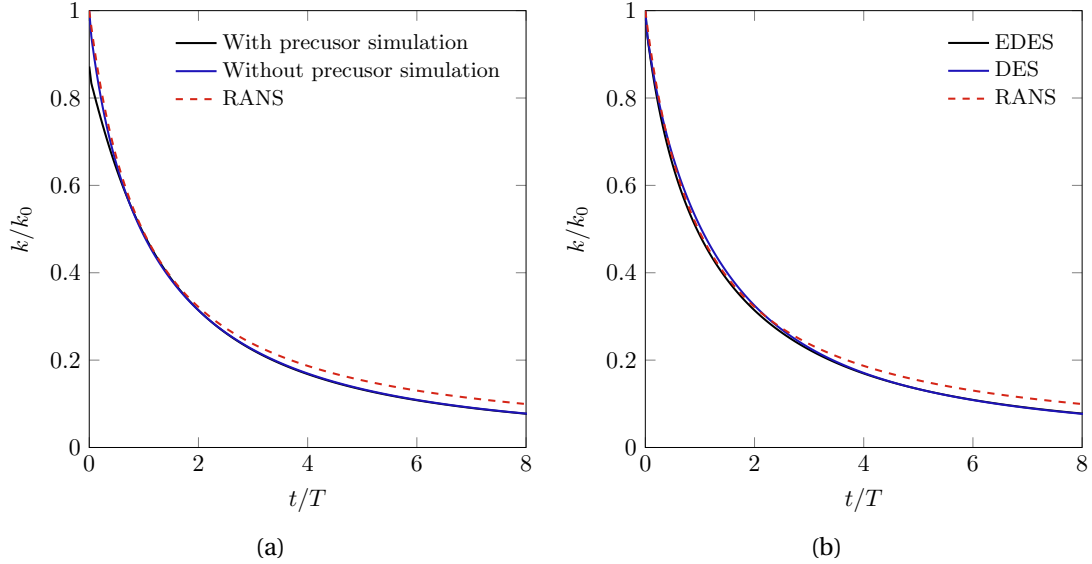


Figure 2.13. – Time evolution of the turbulent kinetic energy compared with the analytical decay (RANS equations). a) Comparison between the DIT case with or without a precursor simulation to initialize the subgrid fields. b) Comparison between the DES and E-DES models.

2.4.2.2. Forcing in E-DES

In order to assess the forcing method, another simulation is performed with a differently initialized setup. The goal is to keep the same total turbulent kinetic energy but with a different distribution of kinetic energy between the resolved and the subgrid parts. The forcing is then employed to restore the kinetic energy distribution which is defined by the integral quantities of the computation and the grid size. Here, we assess the forcing approach in the limiting case that consists in starting from a "RANS state" meaning that the entire turbulent kinetic energy is found in the subgrid part ($k_r(t=0) = 0$). The VKCS energy spectrum model is used to be consistent between the calculation of the energy ratio r_k and the forcing.

Fig. 2.15a shows the time evolution of the total turbulent kinetic energy for four different cases: the first case with the term P_k in the transport equation of the subgrid energy, the second case with both P_k and P_ϵ added respectively to the subgrid energy and subgrid dissipation equations. This two cases are compared to the case with

2. Forcing method for homogeneous isotropic turbulence – 2.4. Towards a self-adaptive forcing : Decaying isotropic turbulence

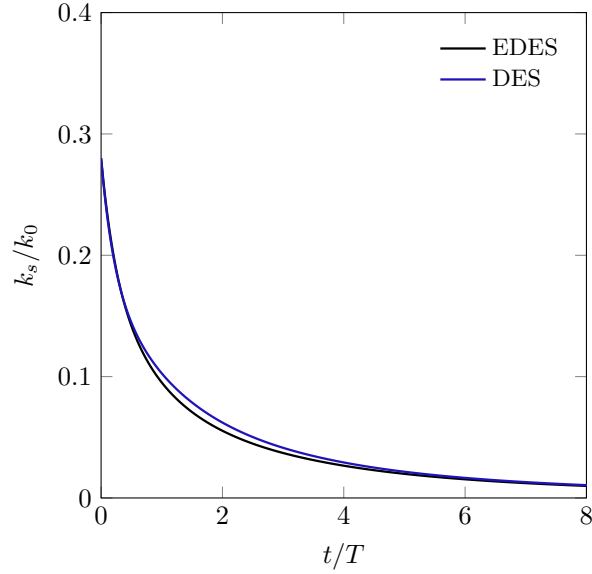


Figure 2.14. – Time evolution of the subgrid turbulent kinetic energy. Comparison between the DES and E-DES model.

a proper initialization. In this plot, the case without forcing is also presented to better assess the contribution of forcing. It can be seen that the case P_k & P_ϵ agrees well with the reference solution. The case with only the term in the subgrid energy transport equation agrees well with the reference solution for about one turn-over time scale but a discrepancy is observed with the reference solution for $t/T > 1$. The case without forcing shows the mechanism that is at play when using the E-DES model and highlighted in Sec. 2.4.1. Indeed, focusing on Eq. 2.57: in this situation $r_k^{observed} > r_k$ and therefore the dissipation is more important than the expected dissipation $\Psi(r_k)\epsilon_m$, and this results in a steeper slope of the total turbulent kinetic energy.

This result is emphasised in Fig. 2.15c which displays the time evolution of the subgrid kinetic energy. The curve for the case without forcing is the same as in Fig. 2.15a since there is no resolved part of the turbulent kinetic in this case. Therefore, it is interesting to note that the slopes are less steep in both studied cases. That means that the computation starts with a production term P_k that is negative. In other words, the synthetic production is not enough, at the beginning of the computation, to balance the "natural" dissipation of the E-DES model.

The discrepancy between the two studied cases on the total turbulent kinetic energy can be understood by Fig. 2.15b and Fig. 2.15d. Indeed, Fig. 2.15b presents the time evolution of the resolved turbulent kinetic energy and it is seen that for the case P_k the energy does not reach the same level as for the case P_k & P_ϵ . This is in line with Fig. 2.15d that shows the time evolution of the synthetic energy. The x-axis has been divided by two since the synthetic energy is zero up to 8 turn-over time scale. Here, it

2. Forcing method for homogeneous isotropic turbulence – 2.4. Towards a self-adaptive forcing : Decaying isotropic turbulence

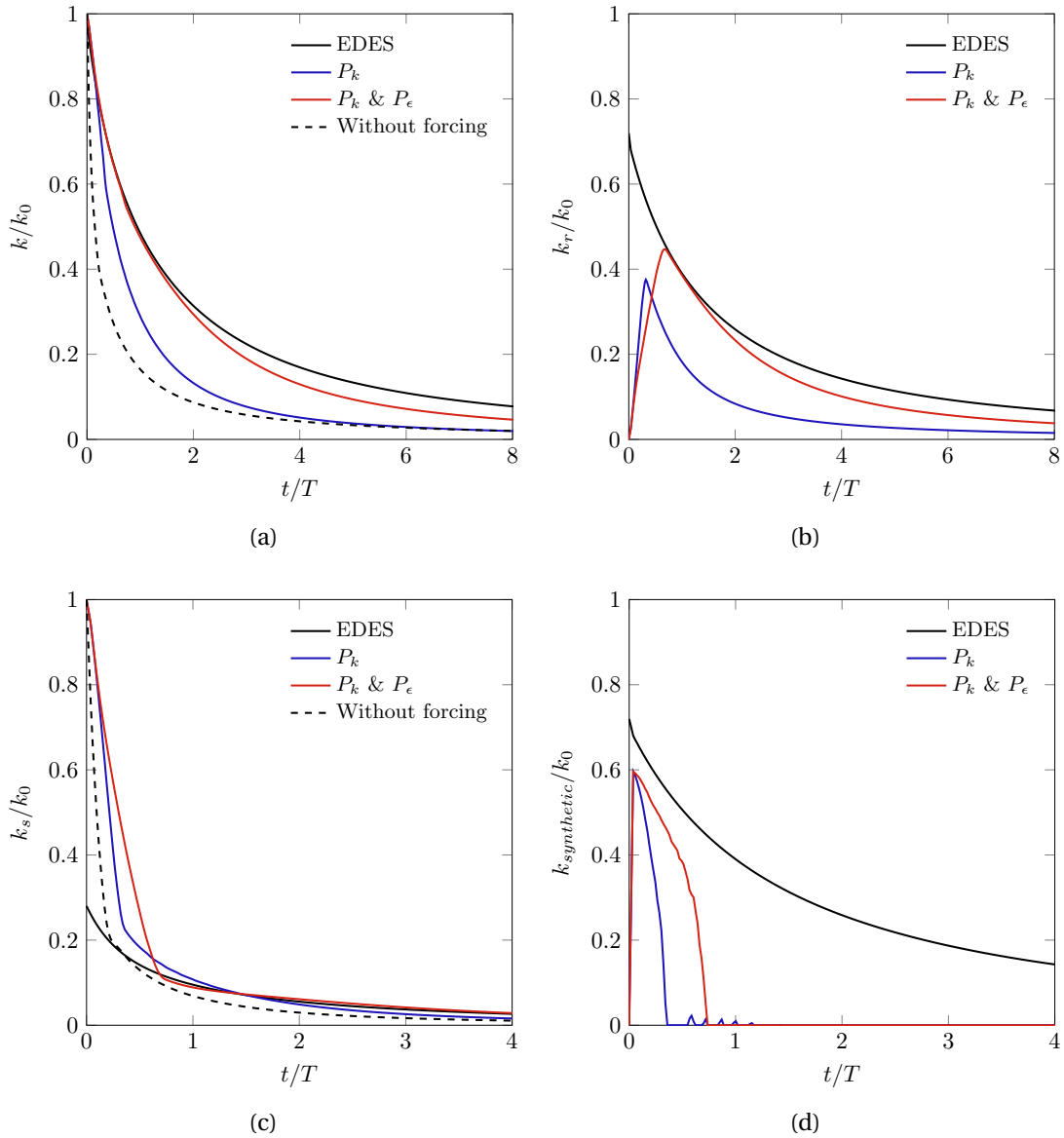


Figure 2.15. – Forcing applied to the DIT case with a prescribed VKCS energy spectrum. (a) Time evolution of the kinetic energy, (b) Time evolution of the resolved kinetic energy, (c) Time evolution of the subgrid kinetic energy and (d) Time evolution of the synthetic kinetic energy.

is observed that in the case $P_k \& P_\epsilon$, the forcing stops around $0.7T$ while in the case P_k the forcing stops around $0.4T$.

What really helps to explain the difference between the two studied cases on the total turbulent kinetic energy is Fig. 2.16b which shows the time evolution of the target and resolved turbulent kinetic energy ratio. In this plot, the resolved energy ratio

2. Forcing method for homogeneous isotropic turbulence – 2.4. Towards a self-adaptive forcing : Decaying isotropic turbulence

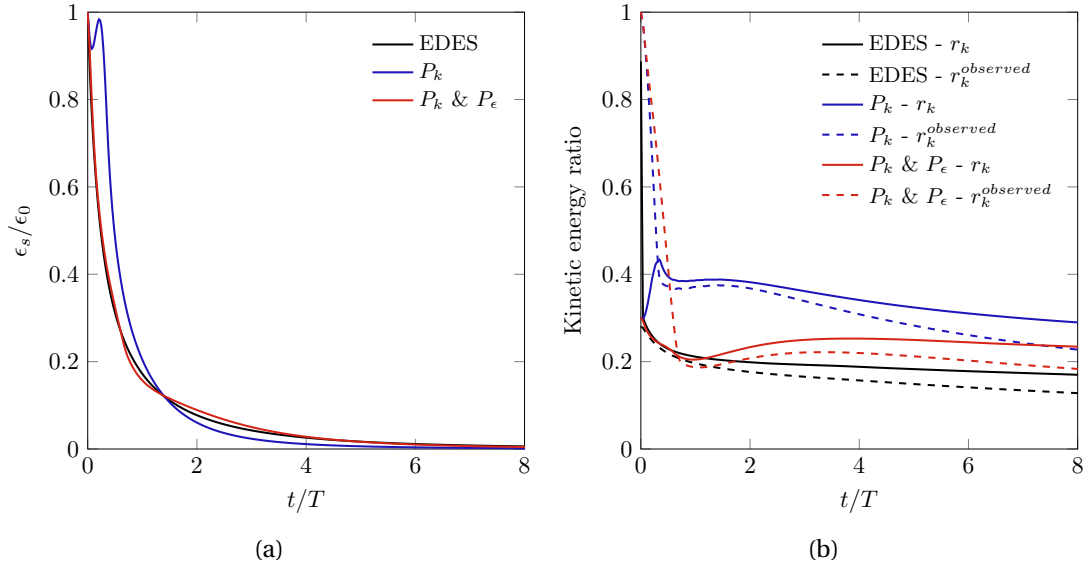


Figure 2.16. – Time evolution of (a) the dissipation and (b) the target and resolved kinetic energy ratio. Plain and dashed lines correspond respectively to the target and resolved turbulent kinetic energy ratios.

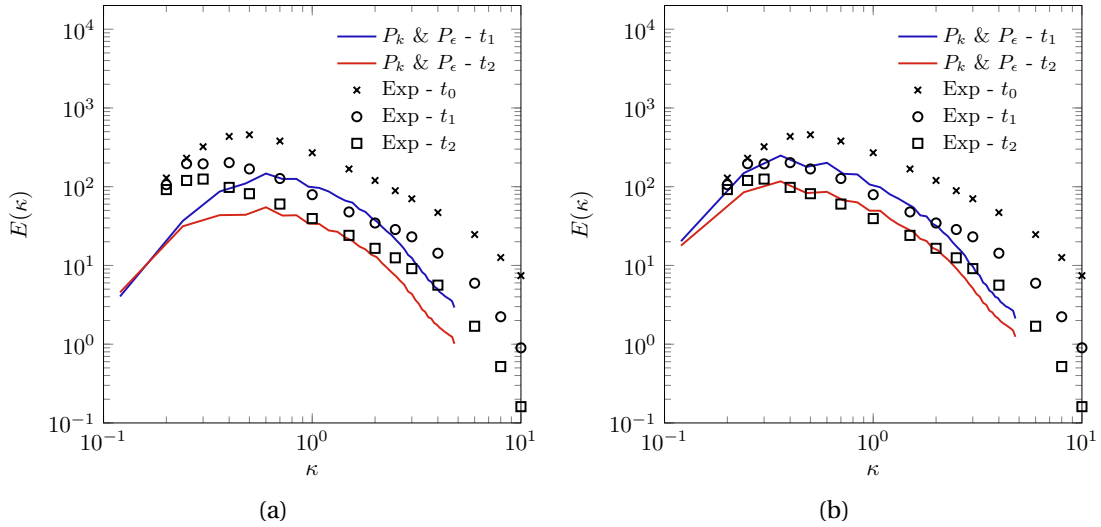


Figure 2.17. – Energy spectra for the forcing applied to the DIT. (a) prescribed VKCS energy spectrum, (b) VKP energy spectrum

starts from $r_k^{observed} = 1$ as expected (corresponding to the RANS state). Then, the two observed ratios decrease until they reach the target ratios. This is exactly what was expected from the proposed self-adaptive forcing since if $r_k < r_k^{observed}$ then $k_r^\dagger < k_r$ and so the right hand side of Eq.2.44 can become negative, hence no more energy is

2. Forcing method for homogeneous isotropic turbulence – 2.5. Conclusion

injected into the computation. The points of intersection between the curves r_k and $r_k^{observed}$ thus correspond to the moment where k_s cancels in Fig. 2.15d. Oscillations observed on the curve of the case P_k in Fig. 2.15d show the balance between the term that compensates the dissipation and the control term in Eq. 2.44. Now focusing on the target ratio of the P_k case, it can be noted that there is an increase while the forcing is activated. This increase can be directly linked to the increase observed on the dissipation in Fig. 2.16a. Indeed, an increase in dissipation leads to a decrease in the integral length scale and thus to an increase in the target ratio. For the case P_k & P_ϵ the subgrid dissipation strictly decreases which results in a target ratio that tends to the target ratio of the E-DES with proper initialisation case, at least while the forcing is activated. Afterwards, when the forcing is no longer activated, it appears that the ratios no longer converge as if the system were reacting to the forcing.

Fig. 2.17a shows the turbulent kinetic energy spectrum at t_1 and t_2 . The spectrum at t_0 is not shown here since it contains no energy. The two spectra match well the reference data at the high wavenumbers but a large mismatch appears at the large scales. These discrepancies can be explain by the form of the prescribed energy spectrum. Indeed, Fig. 2.17b displays the energy spectrum for a computation with a VKP prescribed spectrum. The reader is reminded here that the VKP energy spectrum was built for homogeneous isotropic turbulence. In this case, the resulting spectrum matches well with the experimental results at both the high and low wavenumbers.

2.5. Conclusion

On homogeneous isotropic turbulence, a new forcing technique for eddy-resolving simulations has been developed and evaluated. Based on a reconstruction strategy, the suggested forcing technique seeks to perturb the resolved velocity field with a synthetic velocity field. Overall, the forcing is relevant to sustain isotropic turbulence and allows to perform a smooth balance between the subgrid and resolved turbulent kinetic energies for the DIT case.

The inverse Fourier approach is the foundation for this synthetic velocity. It is necessary to specify an energy spectrum with integral length scale and total kinetic energy as its parameters.

Two approaches have been put forth for controlling resolved kinetic energy: one based on a modulation coefficient and the other based on a first-principles analysis that permits dynamic control. The second option proves to be more effective since it enables quick and precise convergence of the resolved kinetic energy to the desired value. Moreover, by recovering an unrestricted integral length scale, the suggested method gets beyond the major shortcoming of linear forcing approaches. Additionally, by dampening oscillations in their behavior, the introduction of a stochastic frequency enables the recovery of more realistic two-time correlation functions.

2. Forcing method for homogeneous isotropic turbulence – 2.5. Conclusion

This method's adaptability is a significant benefit. For instance, the spectrum model is problem dependent and hence can be adjusted. The time frequency also needs to be specified and can therefore be adapted according on whether the forcing occurs at high or low wave numbers. The forcing of homogeneous isotropic turbulence appears to be well suited for the use of a more realistic frequency as the *straining* assumption, which also enhances the resulting two-point correlations. It was shown that this approach is easily adaptable to anisotropic homogeneous turbulence by the use of a Cholesky decomposition. Unfortunately, the Reynolds tensions cannot be driven one by one, as in the work of De Laage de Meux, Audebert, R. Manceau, et al. [2015](#), so it is not possible to reach all the desired anisotropy levels.

The DIT box is used to derive the full forcing model with a 2-equations hybrid RANS-LES subgrid model (E-EDES). This model includes an additional term in each subgrid equation. The term added to the subgrid energy transport equation is based on an assumption of total energy conservation. The term added to the transport equation for subgrid dissipation is based on an empirical argument.

3. Forcing shear flows

Table of contents

3.1	Feature of the forcing in non-homogeneous turbulence	89
3.1.1	Divergence-free property	89
3.1.2	Target properties	90
3.1.3	Formulation of the reconstruction method	91
3.2	Planar jet	92
3.2.1	Problem description	93
3.2.2	Statistical properties of the synthetic velocity	96
3.2.3	Turbulent inlet condition and forcing	98
3.2.4	Mimicking a zonal method	101
3.2.5	Interest of the forcing for VLES	108
3.3	Conclusion	114

In this chapter, the forcing method is tested upon non-homogeneous turbulent flows. Although the forcing is established in the framework of homogeneous isotropic turbulence, this framework is still quite limited and far from having any interesting industrial applications. When dealing with non-homogeneous turbulence, it is possible to employ the forcing method presented in the preceding chapter. However, this requires some careful changes. Here, modifications due to inhomogeneous turbulence are highlighted. The new formulation of the forcing is then assessed upon planar jet flow. This test case is of particular interest, since it mimics, however in a simplified way, the air inlet of the ventilated room of the experimental program CARDAMOMETTE, presented and discussed in further details in Chap. 4.

3.1. Feature of the forcing in non-homogeneous turbulence

In the framework of non-homogeneous turbulent flows with non-zero mean velocity, the synthetic velocity expressed by Eq. 2.9 can be rewritten as follows:

$$\mathbf{u}^s(\mathbf{x}, t) = 2 \sum_{n=1}^N \hat{u}_n(\mathbf{x}) \cos(\boldsymbol{\kappa}^n \cdot (\mathbf{x} - \mathbf{U}_b t) + \psi_n + \omega_n t) \boldsymbol{\sigma}^n \quad (3.1)$$

In comparison with Eq. 2.9, two changes have been made in the above equation: the addition of the bulk velocity U_b , which symbolizes the convection movement of the turbulent structures downstream of the flow (Bailly and Juvé 1999), and the spatial dependency of the amplitude $\hat{u}_n(\mathbf{x})$. The quantities in the cosine must be space-independent in order to maintain the spatio-temporal characteristics (synthetic turbulent kinetic energy, two-point and two-time correlation function, ...) of the constructed synthetic signal. Indeed, all the algebraic operations performed in Appendix A.2 require the quantities in the argument of the cosine term to be independent of the position. In order to provide a given amount of energy to various cells, it is crucial to have an amplitude that is space dependent. This entails a major change to the synthetic signal's divergence-free property, which will be discussed in the following section.

3.1.1. Divergence-free property

The divergence-free property of the synthetic signal is lost in non-homogeneous turbulence. For a homogeneous isotropic turbulence, the solenoidality $\nabla \cdot \mathbf{u}^s = 0$ implies that $\boldsymbol{\kappa}^n$ is orthogonal to $\boldsymbol{\sigma}^n$. Here, the divergence of the synthetic velocity reads

$$\begin{aligned} \nabla \cdot \mathbf{u}^s &= 2 \sum_{n=1}^N \hat{u}_n(\mathbf{x}) \cos(\boldsymbol{\kappa}^n \cdot (\mathbf{x} - \mathbf{U}_b t) + \psi_n + \omega_n t) \boldsymbol{\sigma}^n \cdot \boldsymbol{\kappa}^n \\ &+ 2 \sum_{n=1}^N \cos(\boldsymbol{\kappa}^n \cdot (\mathbf{x} - \mathbf{U}_b t) + \psi_n + \omega_n t) \boldsymbol{\sigma}^n \cdot \nabla \hat{u}_n(\mathbf{x}) \end{aligned} \quad (3.2)$$

while the first term on the right hand side of Eq. 3.2 cancels, there remains a non-zero term which results in a non-zero divergence of the synthetic signal. A workaround would be to subtract this term from the momentum conservation equations to ensure a free-divergence synthetic source term. However, in the present work, the choice is made not to subtract this term. The study of the influence of this term is part of the perspectives of this work.

3. Forcing shear flows – 3.1. Feature of the forcing in non-homogeneous turbulence

3.1.2. Target properties

As seen in the previous chapter, the forcing method needs target quantities. A turbulent kinetic energy and a length scale must be provided as input data. These statistical quantities could come from either a precursor simulation as in Pamier, Weiss, Garnier, et al. 2009 or from the RANS upstream domain as in De Laage de Meux, Audebert, R. Manceau, et al. 2015. For the latter, the forcing is applied to a channel flow, whose target energy distribution is assumed not to vary in the streamwise direction. Therefore, the use of values from the RANS upstream domain as targets, appears relevant. However, in non-homogeneous turbulence flows, the turbulent kinetic energy can significantly vary in the streamwise direction. For this reason, another approach is proposed here, which consists in deriving the target quantities from a prescribed kinetic energy ratio between resolved and subgrid scales as introduced in Sec 2.2.3. Furthermore, a strong assumption is made here, that the total turbulent kinetic energy is preserved in transition regions. This being assumed, merely a rebalancing between the subgrid and resolved kinetic energy needs to be carried out.

In homogeneous isotropic turbulence, the target quantities are the same over the whole computational domain. As a consequence, setting the parameters (frequency, spectrum model, limits of the spectrum, ...) of the synthetic signal, is straightforward. However, in non-homogeneous turbulent flows, these parameters must be chosen carefully. The parameters of the synthetic velocity must be determined during the initialisation phase and be enforced at each cell and time step:

- i) κ_{min} and κ_{max} must be set at $t = 0$. For κ_{max} , the maximum cutoff wave number over the cells is taken, $\max(\kappa_{max}, \kappa_{cut})$. This can lead to forcing wavelengths larger than the local cutoff. However, in this case, the extra-amount of synthetic energy will be dissipated naturally by the computation. Considering the minimum wave number κ_{min} , the same formulation as in the previous chapter is used, $\min(\kappa_{min}, 0.01\kappa_e)$ with κ_e being a function of the integral length scale. To ensure that the correct wavelength range is forced for all cells, one needs to estimate the maximum integral length scale of the considered flow. This can be done for instance with a precursor computation. For example, in the case of the planar jet, the maximum length scale (used to establish k_{min}) allowed is determined from a geometric criterion such as $L_t^{max}=0.25L_x$. Although not ideal, this kind of geometry-dependent criterion works well in the case of the jet,
- ii) The bulk velocity must be set before the computation and has to be space independent,
- iii) The frequency ω_n has to be determined prior to the computation. For instance, using a sweeping frequency $\omega_n = U_{rms}\kappa$, one needs to determine U_{rms} . This can be done using a prescribed turbulent intensity $I = U_{rms}/U_b$ and a chosen bulk velocity U_b ,
- iv) The choice of the energy spectrum model: the VKCS spectrum model is imposed here for the same reason as computations in DIT (consistency between the

3. Forcing shear flows – 3.1. Feature of the forcing in non-homogeneous turbulence

energy ratio and the forcing).

- v) it is recalled here that the target resolved turbulent kinetic energy is determined from the energy ratio as: $k_r^\dagger = k(1 - r_k)$.
- vi) the same control method, as in the previous chapter, of the resolved turbulent kinetic is employed (Eq. 2.44). For the plane jet case, the forcing is therefore set up as follows:

$$\left\{ \begin{array}{ll} \text{Forcing activated, } P_k \neq 0, & P_\epsilon = 0 \quad \text{if } r_k < r_k^{observed} \\ \text{Forcing disabled, } P_k = 0, & P_\epsilon = 0 \quad \text{otherwise} \end{array} \right.$$

3.1.3. Formulation of the reconstruction method

Following developments made in Sec. 2.2.1, the reconstruction procedure consists in adding a fluctuating part, that corresponds here to a synthetic velocity, to the resolved velocity. This operation introduces additional terms into the filtered Navier-Stokes equations. Usually, as in the previous chapter, only the unsteady term is retained (Schmidt and Breuer 2017b) requiring, at least formally, that turbulence is statistically homogeneous. However, the flow of interest here involves shear flow turbulence and this calls to retain a convective term related to the reconstruction procedure. We follow the motivations of Lundgren 2003 regarding the physical meaning of his linear forcing and we also retain here the term proportional to the resolved velocity gradient. Similar developments have been followed using either an unsteady forcing term (Schmidt and Breuer 2017b) or a forcing term proportional to the velocity gradient (Davidson and Billson 2006, Zhang 2021). Here, both contributions are retained with the proposed reconstruction approach and the resulting filtered Navier-Stokes equations read:

$$\frac{\partial \tilde{U}_i}{\partial t} + \tilde{U}_j \frac{\partial \tilde{U}_i}{\partial x_j} = -\frac{1}{\rho} \frac{\partial \langle p^* \rangle}{\partial x_i} + \nu \frac{\partial^2 \tilde{U}_i}{\partial x_j \partial x_j} - \frac{\partial \tau_{ij}}{\partial x_j} - \frac{\partial u_i^s}{\partial t} - u_j^s \frac{\partial \tilde{U}_i}{\partial x_j} \quad (3.3)$$

The production term is then expressed as:

$$p^{synthetic} = -\overline{\tilde{u}_i \frac{\partial u_i^s}{\partial t}} - \overline{\tilde{u}_i u_j^s \frac{\partial \tilde{U}_i}{\partial x_j}} \quad (3.4)$$

The former version of the forcing, developed in homogeneous isotropic turbulence, had no influence on the mean velocity evolution since the ensemble average of the synthetic velocity is null. Here, with the reconstruction of the convective term, a non-zero term arises in the transport equation of the mean velocity (ensemble average of Eq. 3.3): $-\overline{u_j^s \frac{\partial \tilde{U}_i}{\partial x_j}}$. In the present work, this term is not subtracted from momentum equations. The focus is primarily set on fluctuating velocities.

3.2. Planar jet

In this section, the forcing is applied to the case of the planar jet which is representative of the CARDAMOMETTE ventilated room (see Chap. 4 for further details). Spatially evolving turbulent planar jets have been widely studied either through DNS or LES computations. Le Ribault, Sarkar, and S. Stanley 1999 performed a LES study to compare turbulence subgrid models at $Re = 3000$ and $Re = 30000$. This Reynolds number is based on the velocity U_j and the jet diameter d_j . S. A. Stanley, Sarkar, and Mellado 2002 provided an extensive DNS study of the planar jet at $Re = 3000$ with passive scalar. Klein, Sadiki, and Janicka 2003a and Klein, Sadiki, and Janicka 2003c focused on the turbulent inlet condition as well as the influence of the Reynolds number on the results by varying the Reynolds number from $Re = 1000$ to $Re = 6000$ using DNS. The authors highlighted that the axial evolution of the mean streamwise velocity as well as the turbulent kinetic energy strongly depend on the integral length scale imposed at the inflow. The length of the potential core decreases as the length scale imposed at the inlet increases. Silva, Lopes, and Raman 2015 assessed various LES subgrid turbulence models at $Re = 6000$ by comparing their results with DNS results. Bisoi, Das, Roy, et al. 2017 performed a LES study of the planar jet without turbulent inlet condition at the inlet, focusing their interest on the laminar-turbulent transition. Some useful data are also available in the work of Armengol, Vicquelin, Coussement, et al. 2019 and Cascioli, Buckingham, Keijers, et al. 2020 whom performed DNS and LES of a heated planar jet. The work of Li, Anand, Hassan, et al. 2019 and Liu, Dong, and Lai 2019, which focuses on a parallel planar jet, has also been used to recover the turbulent data imposed at the inlet. Finally, a recent DNS with 1.3 billion grid points has been performed by Engelmann, Klein, and Kempf 2021 at $Re = 10000$.

When studying the planar jet, two average quantities are of particular interest: the axial evolution of the mean axial velocity (U_c) and the jet half width ($\delta_{0.5}$) evolution. The jet half-width is defined in this study as the distance between the jet centerline and the location equivalent to half of the centerline velocity excess. In order to assess the quality of a computation with references, coefficients of the following linear functions are usually compared (S. A. Stanley, Sarkar, and Mellado 2002):

$$\frac{\delta_{0.5}}{d_j} = K_1 \left(\frac{x}{d_j} + K_2 \right) \quad (3.5)$$

$$\left(\frac{\Delta U_j}{\Delta U_c} \right)^2 = C_1 \left(\frac{x}{d_j} + C_2 \right) \quad (3.6)$$

in which, ΔU_j and ΔU_c represent respectively the inlet velocity excess and the local center line velocity excess, meaning that the velocity of the co-flow is subtracted to the two aforementioned center line velocities. These coefficients are calculated over a certain distance within the self-similar region.

3.2.1. Problem description

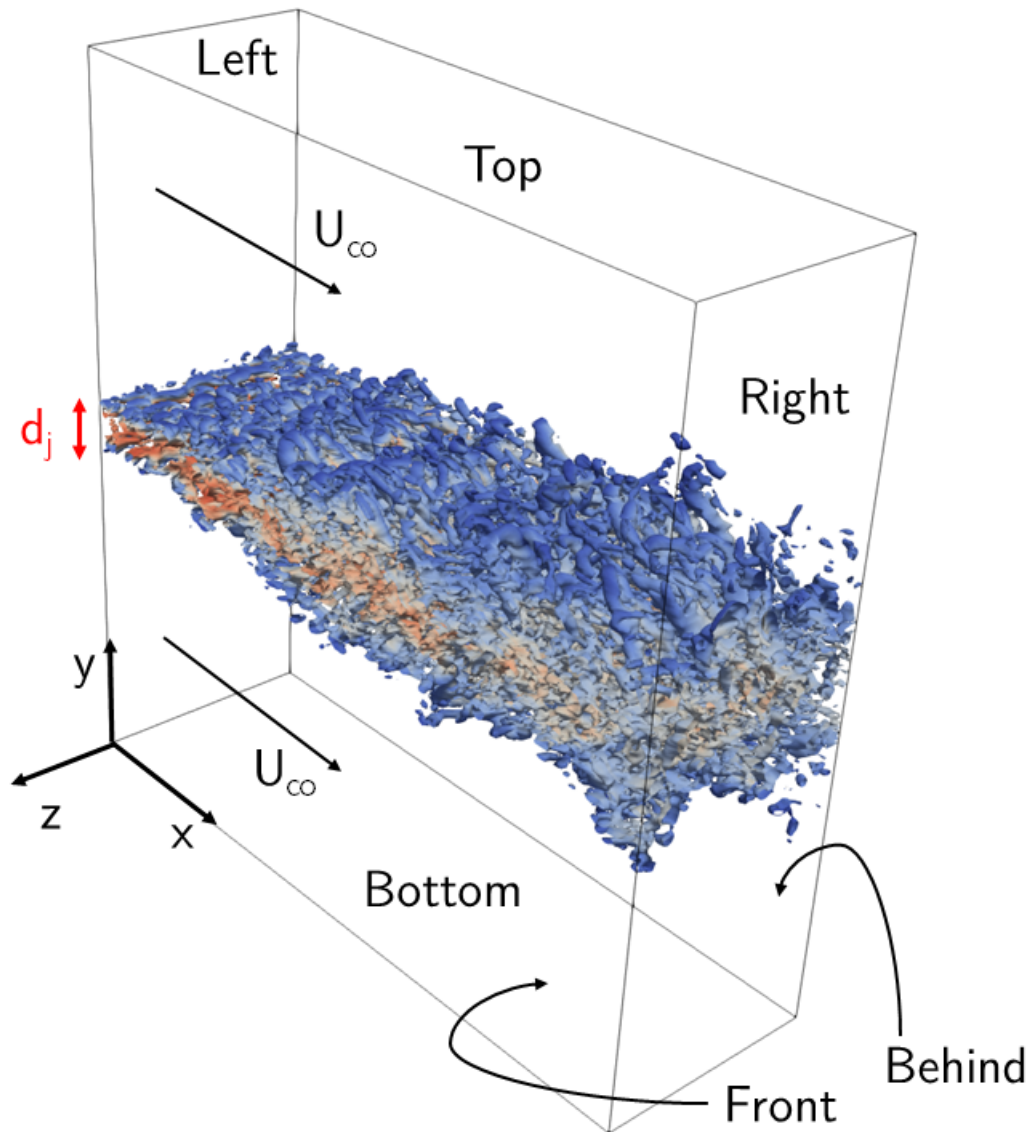


Figure 3.1. – Plane jet scheme

In order to study the planar jet, two different domain sizes have been used:

- i) The first domain size corresponds to that of Engelmann, Klein, and Kempf 2021: $[0; L_x] \times [0; L_y] \times [0; L_z]$ with $L_x = 20d_j$, $L_y = 20d_j$ and $L_z = 6.4d_j$. This domain size is used to show the capability of the synthetic velocity to reproduce the turbulent kinetic energy of a precursor RANS calculation. This domain is also used to show the differences between a computation with turbulent inlet condition and a computation with the forcing method.

- ii) The second domain size is an extended form of the first domain: $[0; L_x]x[0; L_y]x[0; L_z]$ with $L_x = 80d_j$, $L_y = 60d_j$ and $L_z = 9.6d_j$. This extended domain allows us to assess the capability of the forcing method by mimicking a zonal method. Indeed, to assess the overall effect of the reconstruction procedure, the RANS mode (*i.e.* $r_k = 1$) is enforced over an area downstream the nozzle, with three different lengths : $6d_j$, $11d_j$ and $30d_j$, while r_k keeps its original formulation (Eq. 1.94) downstream black dashed lines reported in Fig. 3.7.

The governing equations of this flow are the mass and momentum balances equations (\mathbf{u}, p). The turbulence is treated with either RANS $k - \epsilon$ model or E-DES model. For all the following computations, the considered fluid is air with density $\rho = 1.2 \text{ kg} \cdot \text{m}^{-3}$ and molecular viscosity $\mu = 1.810^{-5} \text{ kg} \cdot \text{m}^{-1} \cdot \text{s}^{-1}$.

In the existing literature, a wide range of turbulent inlet conditions are employed and are refereed in Tab. 3.1. The different initials and boundary conditions, used in this work, will now be detailed. For the initial condition, the fluid is at rest ($\mathbf{u}(\mathbf{x}, 0), p(\mathbf{x}, 0) = 0$). For boundary conditions, periodic conditions are used in the z -spanwise direction. An outlet-like condition that allows a control of the kinetic energy is imposed at the outlet that corresponds to the right, top and bottom boundaries as illustrated on Fig. 3.1. For the inflow condition, the prescribed mean axial velocity profile is an hyperbolic tangent:

$$U(x = 0, y, z) = \frac{U_j + U_{co}}{2} + \frac{U_j - U_{co}}{2} \tanh\left(\frac{-|y - 0.5L_y| + r_j}{2\theta}\right) \quad (3.7)$$

in which the co-flow velocity is $U_{co} = 9\%U_j$, $r_j = 0.5d_j$ and $\theta = d_j/20$ represents respectively the velocity of the co-currant , the radius and the initial momentum thickness.

For computations with turbulent inflow condition (Turbulence IC), a fluctuating component is superimposed at the inlet as $\mathbf{u}^*(x = 0, y, z) = U(x = 0, y, z) + \mathbf{u}$. This fluctuating part of the inlet velocity is generated with the RFM (see Chap.2) method. The same number of mode as in the previous chapter is used $N = 200$. The bulk velocity is defined as $U_b = 0.5 * (U_j + U_{co})$. An isotropic Reynolds tensor is prescribed with

$$U_{rms} = 0.1(U_j - U_{co}) \exp\left[-a\left(\frac{|y - 0.5L_y| - r_j}{d_j}\right)^2\right] \quad (3.8)$$

in which $a = -4 \ln\left(\frac{9.24 \times 10^{-3}}{0.1}\right)$. This allows a peak of turbulent kinetic energy at the shear layer location and to have a turbulent intensity of 0.019 at the center line (S. A. Stanley, Sarkar, and Mellado 2002). From this, the turbulent kinetic is imposed by $k = 1.5U_{rms}$. The prescribed integral length scale is $L_t = 0.4d_j$ as in Klein, Sadiki, and Janicka 2003a. Inflow conditions are a key parameter considering their influence on the near field. While the mean velocity profiles is mainly an hyperbolic tangent in the literature, input parameters for the velocity fluctuations vary a lot (see Tab. 3.1).

3. Forcing shear flows – 3.2. Planar jet

Authors	Turbulent intensity	Length scale	Method	Profile
S. A. Stanley, Sarkar, and Mel-lado 2002	10%	$L_t = 1.515d_j$ ($St = 0.033$)	RFM	Peaks in the SL
Le Ribault, Sarkar, and S. Stanley 1999	10%	-	RFM	Peaks in the SL
Klein, Sadiki, and Janicka 2003a	2%	$L_t^{(x)} = 0.4d_j,$ $L_t^{(y)} = L_t^{(z)} = 0.125d_j$	Digital Filtering	Top hat
Pantano 2004	4%	-	RFM	Peaks in the SL
Silva, Lopes, and Raman 2015	-	-	Numerical noise	Peaks in the SL
Bisoi, Das, Roy, et al. 2017	-	-	-	-
Armengol, Vic-quelin, Cousse-ment, et al. 2019	5%	$L_t = 0.5d_j$	RFM	Top hat
Huang, Wang, and Xu 2020	-	$S_t = 0.3$	TFD	-

Table 3.1. – Turbulent inflow conditions for the planar jet. SL stands for Shear Layer.

Following the work of Le Ribault, Sarkar, and S. Stanley [1999](#), the same kind of grids as in their work have been used. In the streamwise x direction, the mesh is stretched from $x = d_j$ to $x = 2d_j$ with the respective mesh sizes $\Delta_x = 0.1d_j$ and $0.25d_j$. In the normalwise y direction, the mesh is constant for $L_y/2 - d_j/2 < y < L_y/2 + d_j$. From these bounds, $L_y/2 \pm d_j/2$, the mesh is stretched over $4.25d_j$ in both ways and finally the mesh is constant from $0.25d_j/L_y - 0.25d_j$ to boundaries. In the case of the large domain, the mesh size is stretched from the position of boundaries of the small domain to the boundaries of the large domain. The mesh size is set to be equal to d_j at boundaries. In the spanwise z direction, the mesh size is constant and is equal to $0.25d_j$. The mesh sizes for both employed domains are displayed in Tab. [3.2](#) and Tab. [3.3](#).

Number of cells	311 168
Δ_x	$[0.1d_j, 0.25d_j]$
Δ_y	$[0.0667d_j, 0.25d_j]$
Δ_z	$[0.25d_j]$

Table 3.2. – Grid first domain - structured mesh

Number of cells	3 938 624
Δ_x	$[0.1d_j, 0.25d_j]$
Δ_y	$[0.0667d_j, 0.25d_j, d_j]$
Δ_z	$[0.25d_j]$

Table 3.3. – Grid second domain - structured mesh

The numerical parameters are recalled in Tab. 3.4. It should be mentioned here that a restart is performed at $5T_0$. This restart allows for faster convergence, by removing the transient phase of the computed statistics and therefore statistics are averaged over a period of time of $15T_0$. The statistics have also been spatially averaged along the homogeneous spanwise direction.

Final time	$20T_0$ with $T_0 = L_x/U_c$ and $U_c = (U_j + U_{co})/2$
Time step	$\Delta t_{CFL} = 0.5 \min(\Delta_y)/U_j$
Time integration	Crank-Nicolson scheme
Convective scheme	centered

Table 3.4. – Numerical parameters

3.2.2. Statistical properties of the synthetic velocity

In order to illustrate the capabilities of the synthetic velocity to reproduce the turbulent kinetic energy field, simulations without solving the Navier-Stokes equations are first proposed. In these simulations, the synthetic velocity is updated over time and statistics are computed. This is similar to the work of Lafitte, Le Garrec, Bailly, et al. 2014. The targeted properties come from a RANS precursor simulation. The $k-\epsilon$ turbulence model is used to provide the targeted quantities such as k_m and ϵ_m which are needed to build the synthetic velocity.

At first, the frequency-free synthetic velocity ($\omega_n = 0s^{-1}$) is updated. Two computations are performed with either a PP or VKP energy spectrum model. Fig. 3.2 represents the turbulent kinetic energy for a slice taken at $0.5L_z$. The resulting turbulent kinetic energy from the RANS computation is displayed in Fig. 3.2a. Fig. 3.2b and Fig. 3.2c display respectively the synthetic kinetic energy for a PP and a VKP energy spectrum model. By comparing with the results of the RANS simulation, the turbulent energy field is well reconstructed in the case of the PP spectrum while an underestimation of the turbulent energy appears in the case of the VKP spectrum. This underestimation can be explained by the VKP spectrum's mesh size dependence, which causes the reconstructed energy to correlate with a resolved energy instead of a total energy.

Secondly, the synthetic velocity is unfrozen ($\omega_n \neq 0$) and is written as in Eq. 3.1. To highlight the importance of having a space independent frequency as explained by Batten, Golberg, and S. Chakravarthy 2004 and Lafitte, Le Garrec, Bailly, et al. 2014, two computations are performed:

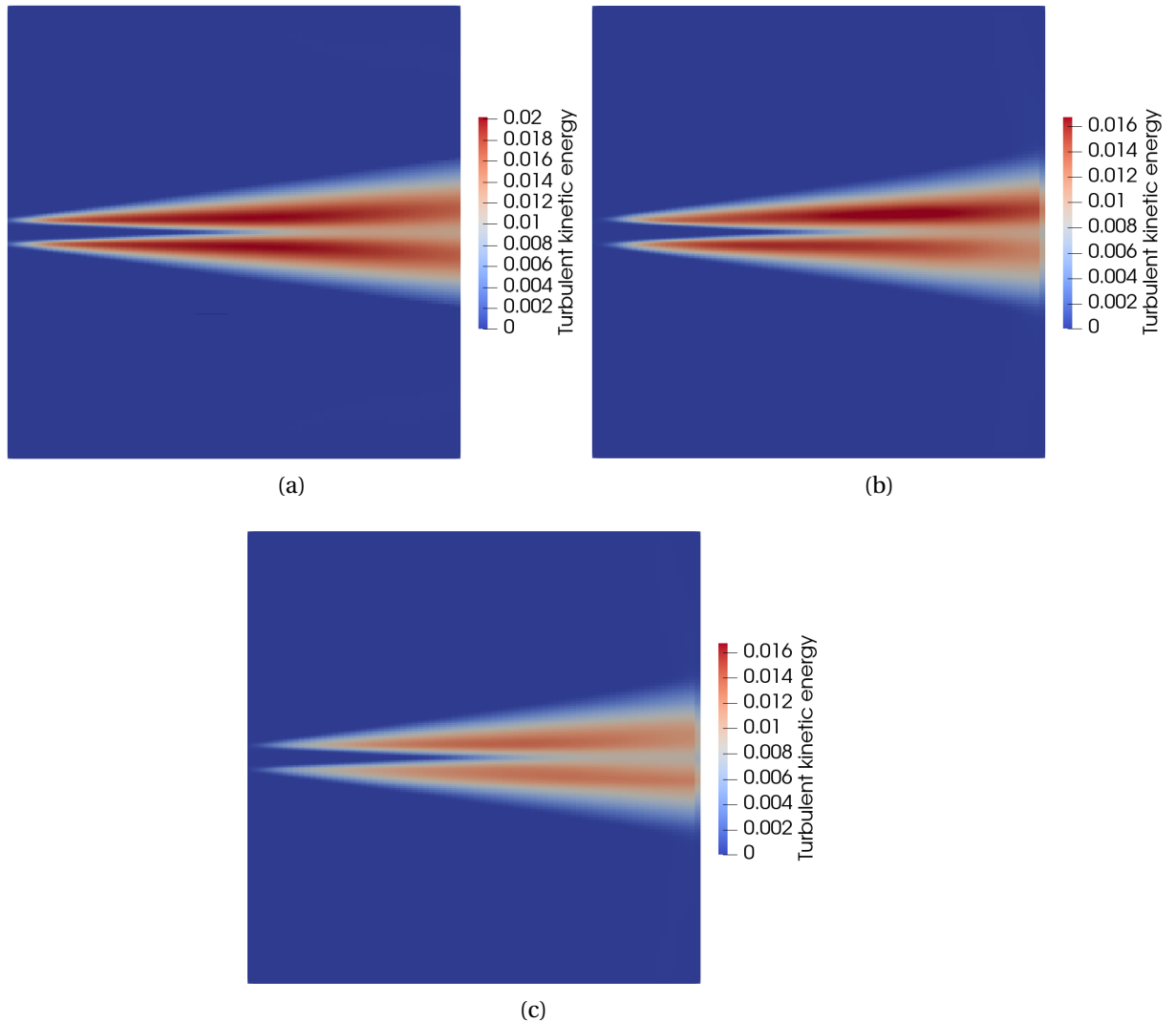


Figure 3.2. – Turbulent kinetic energy mapping for a slice taken at $0.5L_z$. (a) RANS computation, (b) updating synthetic velocity PP, (c) updating synthetic velocity VKP.

- i) straining frequency $\omega_n = \sqrt{E(\kappa)\kappa^3}$ with $E(\kappa)$ a function of space,
- ii) constant sweeping $\omega_n = U_{rms}\kappa$ with $U_{rms} = 0.1U_b$ representing a turbulent intensity of 10%.

Fig. 3.3a displays the color map of the turbulent kinetic energy for the space dependent straining frequency. It appears clearly that the reconstructed energy field is influenced by the space dependent frequency. It is as if the energy was shifted in the direction of the flow, losing intensity in the first part of the computational domain. On the other hand, when using a constant frequency (Fig. 3.3b), the energy field is recovered. Comparing Fig. 3.3b and Fig. 3.2c, the use of the sweeping frequency allows

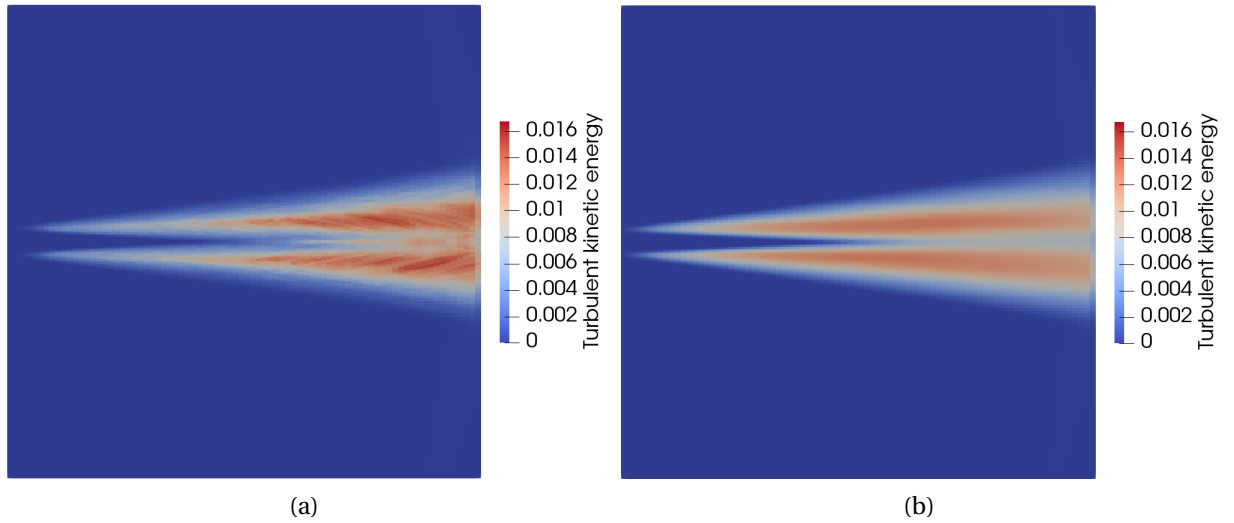


Figure 3.3. – Turbulent kinetic energy mapping for a slice taken at $0.5L_z$. Updating synthetic velocity (a) with space dependent frequency, (b) with space independent frequency.

to recover a higher level of synthetic turbulent energy.

3.2.3. Turbulent inlet condition and forcing

Here, the goal is to show that using turbulent inlet condition (Turbulent IC) is almost equivalent to using the reconstruction method. Indeed, the forcing method primarily affects the jet's entrance, acting as a means of introducing turbulent fluctuations at the boundary (see Fig. 3.4). It is worth noting that no production term is added to the subgrid dissipation transport equation for the following computations. Although this method has proven to be effective in the case of DIT, some computations have diverged in the case of the planar jet. Therefore, only the production term (Eq. 2.59) in the transport equation of k_s is kept to ensure conservation of the total turbulent kinetic energy.

Fig. 3.5a displays the axial evolution of the streamwise mean velocity U_c . It can be seen that there is no difference between the Turbulence IC and computation using the reconstruction procedure. As shown in Tab. 3.5, the coefficient of the slope C_1 , which appears in Eq. 3.6, compares well with references. As mentioned before, the length of the potential core depends on the imposed integral length scale at the boundary condition, which explains the differences with the reference ($L_t = 1.515d_j$ used by S. A. Stanley, Sarkar, and Mellado 2002 and $L_t = 0.4d_j$ used for the Turbulent IC computation). It is interesting to note that the same length of the potential core is recovered for both Turbulent IC and Forcing computations. In Tab. 3.5, the coefficient K_1 (Eq. 3.5), that represents the linear growth of the jet-half width is also presented.

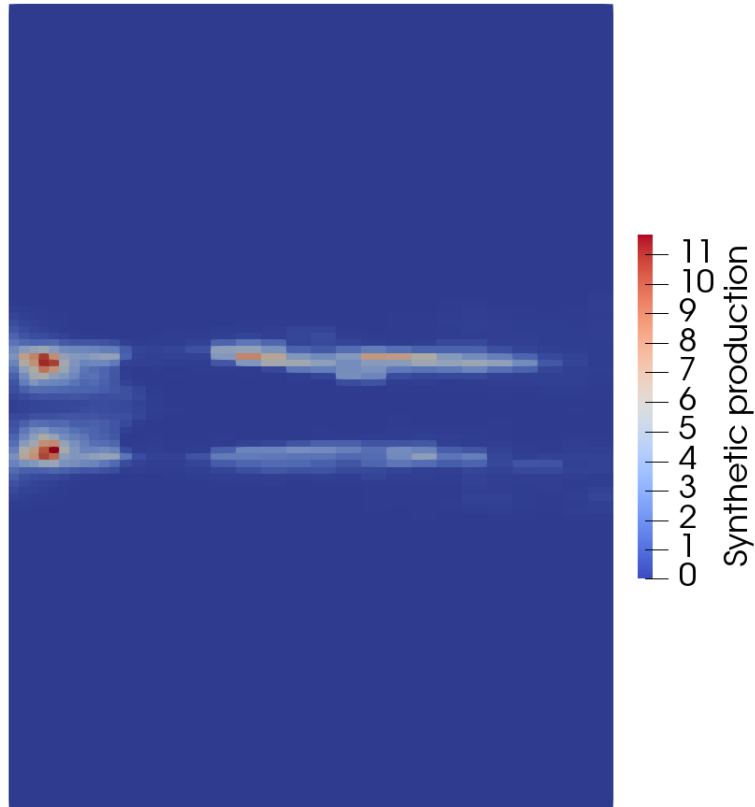


Figure 3.4. – Color map of the synthetic production term near the jet inlet region.

Results are in good agreements with references.

Simulations	K1	K2	C1	C2
Forcing	0.086	0.67	0.19	-0.986
Turbulent IC	0.091	0.17	0.206	-1.71
RANS	0.082	2.16	0.168	0.273
S. A. Stanley, Sarkar, and Mellado 2002	0.092	2.63	0.201	1.23

Table 3.5. – Summary of the resulting coefficients K1, K2, C1 and C2 for the region $[10d_j; 16d_j]$.

Fig. 3.5b shows the axial evolution of the turbulent kinetic energy. Comparing Turbulent IC and Forcing computations, there is a difference of less than 15% between the two curves in the self-similar region ($x_j > 11d_j$). Even though there is a discrepancy at the peak of turbulent kinetic energy between results and the DNS computation, the level of turbulent kinetic energy matches the reference in the self-similar region.

Normal profiles of U_{rms} and V_{rms} in the self-similar region ($x = 11d_j$) are displayed respectively in Fig. 3.6b and Fig. 3.6b. Results from the Forcing computation are

3. Forcing shear flows – 3.2. Planar jet

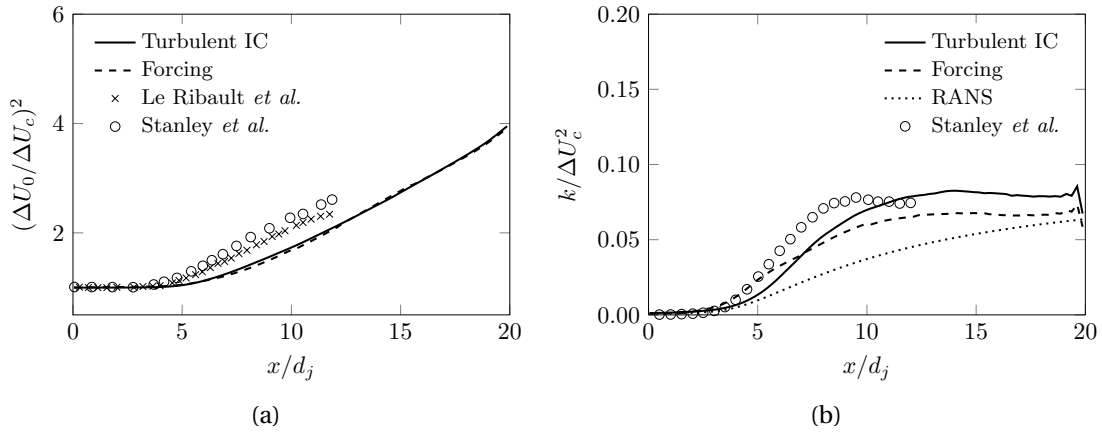


Figure 3.5. – (a) Axial evolution of the mean velocity at the center of the jet U_c . Comparison between the forcing method, the Turbulent IC simulation and the DNS results and LES results, (b) Axial evolution of the turbulent kinetic energy. Comparison between the forcing method, the Turbulent IC simulation, the RANS computation and the DNS results.

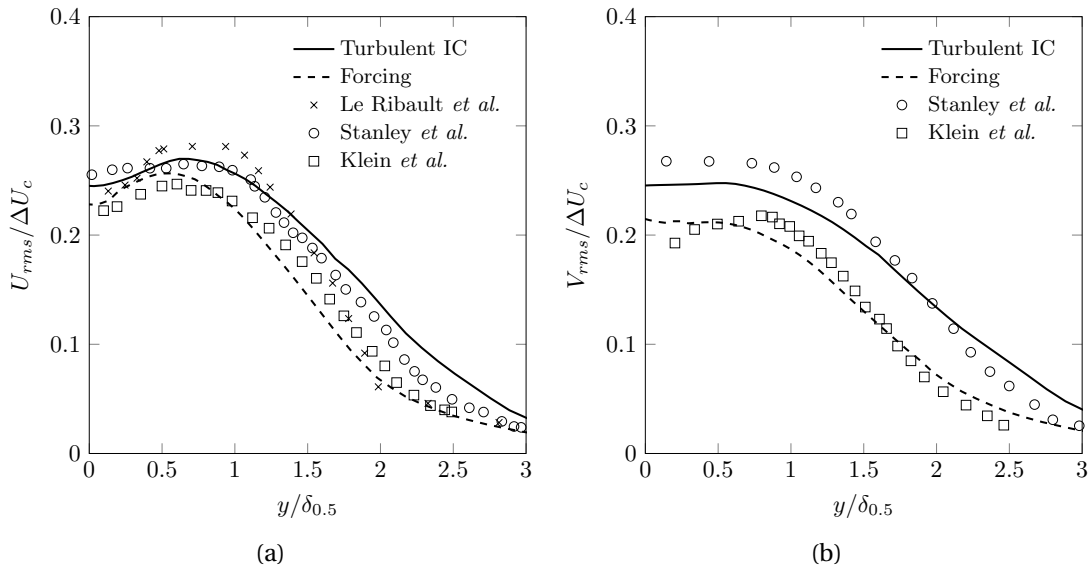


Figure 3.6. – Radial profiles in the self-similar region at $x = 11d_j$. (a) Streamwise velocity fluctuations U_{rms} , (b) Normalwise velocity fluctuations V_{rms} .

underestimated compared to the computation with turbulent inlet condition. This is in line with the previous results (axial evolution of the turbulent kinetic energy). However, the results are consistent with references.

There are some differences between simulations with Turbulent IC and the forcing

method, but the overall outcome remains largely unchanged.

3.2.4. Mimicking a zonal method

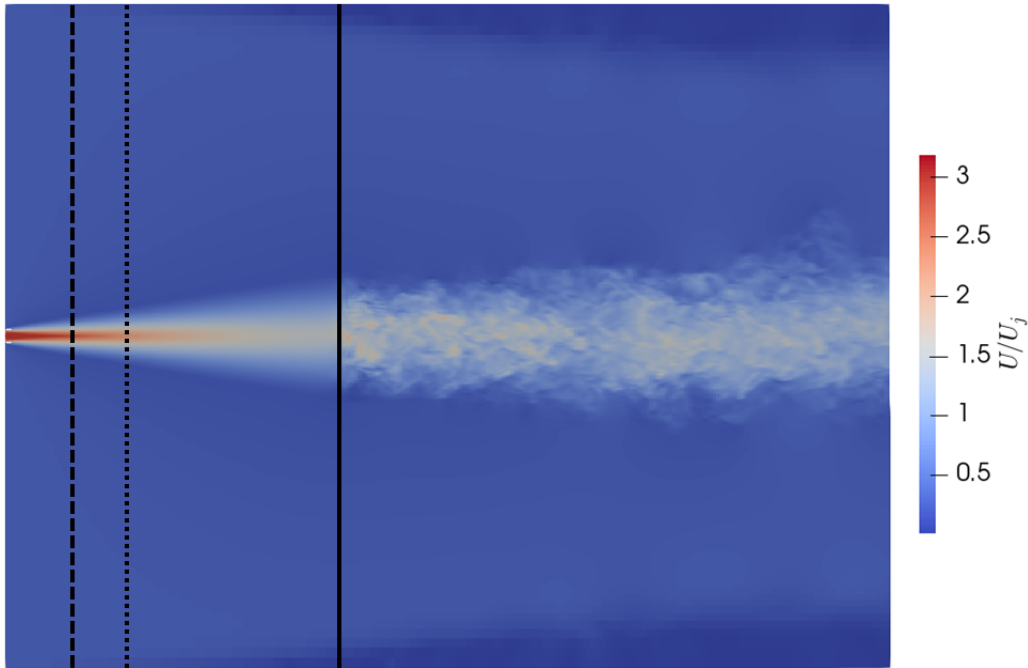


Figure 3.7. – Instantaneous snapshot of the velocity magnitude. The black plain line delimits the upstream RANS domain from the downstream E-DES at the axial position $x = 30d_j$. Dashed and dotted lines represent schematically the delimitation for zonal cases $x = 6d_j$ and $x = 11d_j$.

The aim of this section is to assess the reconstruction procedure in the framework of zonal hybrid RANS/LES. Three different zonal configurations are tested for which the RANS mode is enforced over:

- i) $6d_j$, referred to as $x_T = 6d_j$ **case**, this relates to a position where there is an increase of turbulent kinetic energy within the RANS zone (approximately at the end of the potential core),
- ii) $11d_j$, referred to as $x_T = 11d_j$ **case**, placing the interface at a position close to the peak of turbulent kinetic energy,
- iii) $30d_j$, referred to as $x_T = 30d_j$ **case**, putting the interface in the self-similar zone with a decrease in turbulent kinetic energy.

The influence of the reconstruction method is investigated by focusing on several quantities of interest such as the mean and root mean square values of the velocity in the self-similar region as well as the axial evolution of the turbulent kinetic energy.

Simulations	K1	K2	C1	C2
$x = 6d_j$	0.053	14.88	0.163	1.631
$x = 11d_j$	0.055	8.96	0.163	-2.92
$x = 30d_j$	0.0325	28.62	0.097	28.6
Turbulent IC	0.0545	19.05	0.169	4.73
RANS	0.0735	5.57	0.23	-6.352

Table 3.6. – Summary of the resulting coefficients K1, K2, C1 and C2 for the region $[50d_j; 65d_j]$.

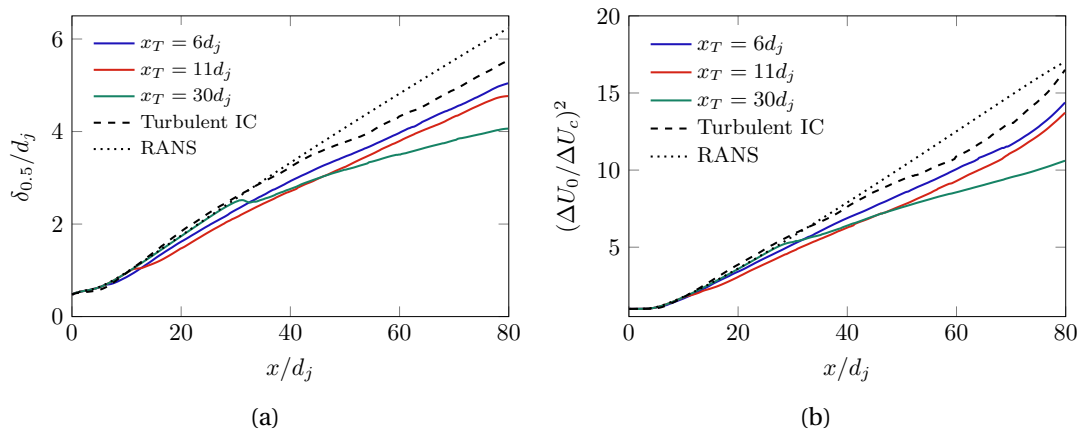


Figure 3.8. – (a) Axial evolution of the jet half width defined by Eq. 3.5. Comparison between the forcing method, Turbulent IC and RANS simulations, (b) Axial evolution of the mean velocity excess defined by Eq. 3.6.

The slope coefficients of the jet half-width evolution and the decrease of the axial mean velocity excess are also compared with the results from the literature. This emulation of a zonal hybrid RANS/LES model implies a transition area in between the two domains. Hence, it is interesting to evaluate the size of this transition region for the three cases.

This transition zone is highlighted on the snapshot of the instantaneous velocity displayed in Fig. 3.7. The black lines represent the interface between the upstream RANS domain ($r_k = 1$) and the zone where the E-DES model behaves in a self-adaptive way. Black dashed and dotted lines indicate respectively the position of the interface for the zonal $x_T = 6d_j$ and $x_T = 11d_j$ cases. As expected, no velocity fluctuations are observed upstream of the plain black line while the forcing enables the generation of fluctuations downstream. The transition area takes place just downstream the RANS domain. In this transition region, it appears that the jet half width evolution is reduced.

In order to discuss quantitative results, the effect of the proposed approach on

3. Forcing shear flows – 3.2. Planar jet

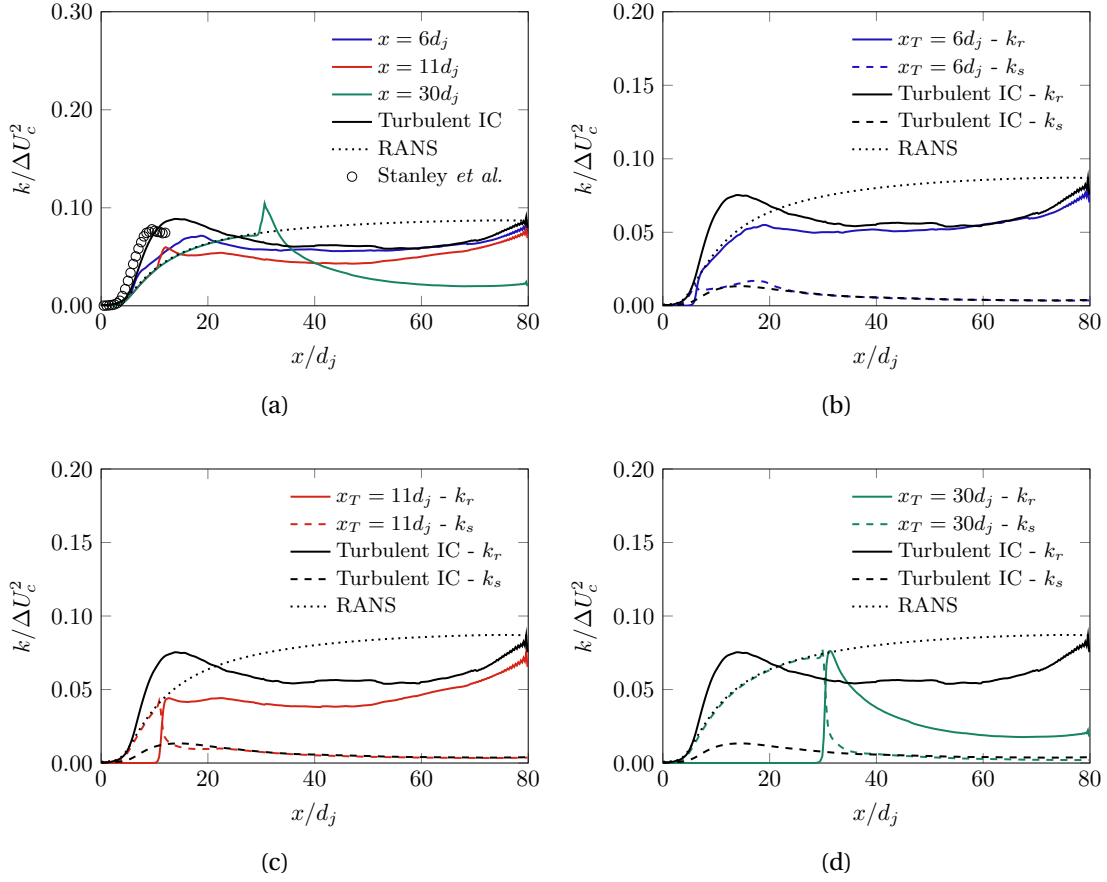


Figure 3.9. – Axial evolution of the turbulent kinetic energy for the three different zonal computations. (a) total turbulent kinetic energy, (b) $x_T = 6d_j$ case, (c) $x_T = 11d_j$ case and (d) $x_T = 30d_j$ case.

statistical quantities needs to be assessed. All statistical quantities presented hereafter are averaged over $15T_t$. First of all, the results of the jet half width $\delta_{0.5}$ evolution and the mean axial velocity are presented in Fig. 3.8 and are compared to the simulation using turbulent inlet condition and a RANS computation. The corresponding slope coefficients are displayed in Tab. 3.6. In all three cases, the RANS zone fits with the RANS computation, which was expected. For cases $x_T = 6d_j$ and $x_T = 11d_j$, slope coefficients K_1 and C_1 agree well with the Turbulent IC computation. However, for the $x_T = 30d_j$ case, a clear decrease of 40% for both slope coefficients K_1 and C_1 , is observed. This drop appears clearly in Fig. 3.8.

Fig. 3.9a displays the total turbulent kinetic energy for the three cases. As expected, the turbulent kinetic energy fits the RANS computation upstream of the transition regions. Even though the RANS computation underestimates the peak of energy, the turbulent kinetic energy of computations $x_T = 6d_j$ and $x_T = 11d_j$ nearly reach the slope of the Turbulent IC simulation in the self-similar region. In the case $x = 30d_j$, a

3. Forcing shear flows – 3.2. Planar jet

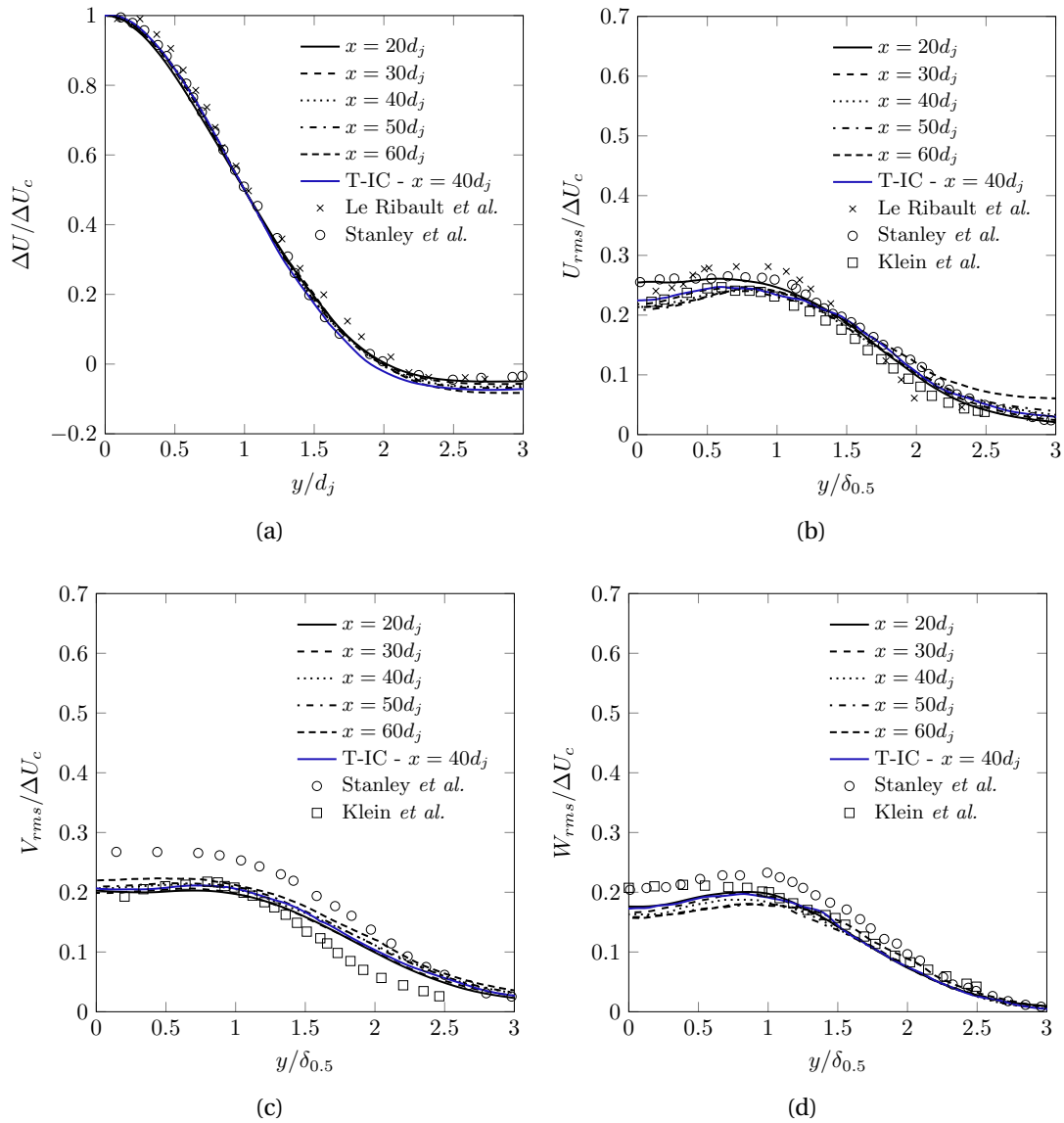


Figure 3.10. – RANS mode enforced for $x < 6d_j$. Radial profiles in the self-similarity region compared with the Turbulent IC simulation at $x = 40d_j$. (a) Mean streamwise velocity, (b) Streamwise velocity fluctuations U_{rms} , (c) Normalwise velocity fluctuations V_{rms} and (d) Spanwise velocity fluctuations W_{rms} .

strong energy peak is observed immediately downstream of the RANS region. This spike is followed by a drop in energy. For the sake of comprehension, it is necessary to look at the energy distribution between the resolved and the modeled parts. Fig. 3.9b, Fig. 3.9c and Fig. 3.9d represent energy distribution for the resolved and subgrid parts, respectively for simulations $x_T = 6d_j$, $x_T = 11d_j$ and $x_T = 30d_j$. In the first

3. Forcing shear flows – 3.2. Planar jet

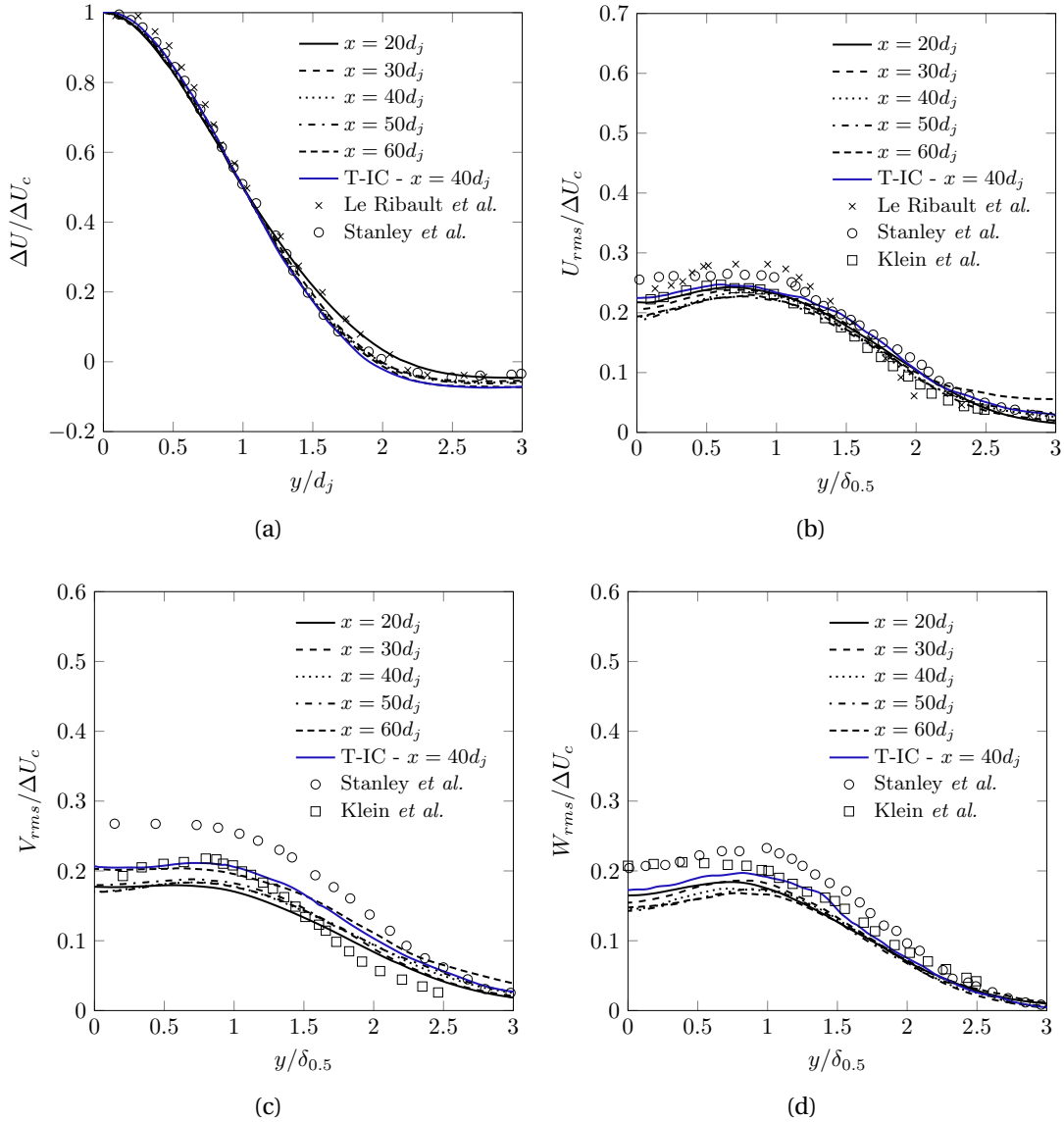


Figure 3.11. – RANS mode enforced for $x < 11d_j$. Radial profiles in the self-similarity region compared to the Turbulent IC simulation at $x = 40d_j$. (a) Mean streamwise velocity, (b) Streamwise velocity fluctuations U_{rms} , (c) Normalwise velocity fluctuations V_{rms} and (d) Spanwise velocity fluctuations W_{rms} .

case, $x_T = 6d_j$, the increase of the resolved part starts from $x = 6d_j$ for the zonal configuration. At the same location, the subgrid kinetic energy decays due to the sharp decrease of the kinetic energy ratio and the production term which is subtracted from the right hand side of the subgrid turbulent kinetic transport equation. The same observations are made for $x_T = 11d_j$ and $x_T = 30d_j$ simulations. In the $x_T = 30d_j$ case,

3. Forcing shear flows – 3.2. Planar jet

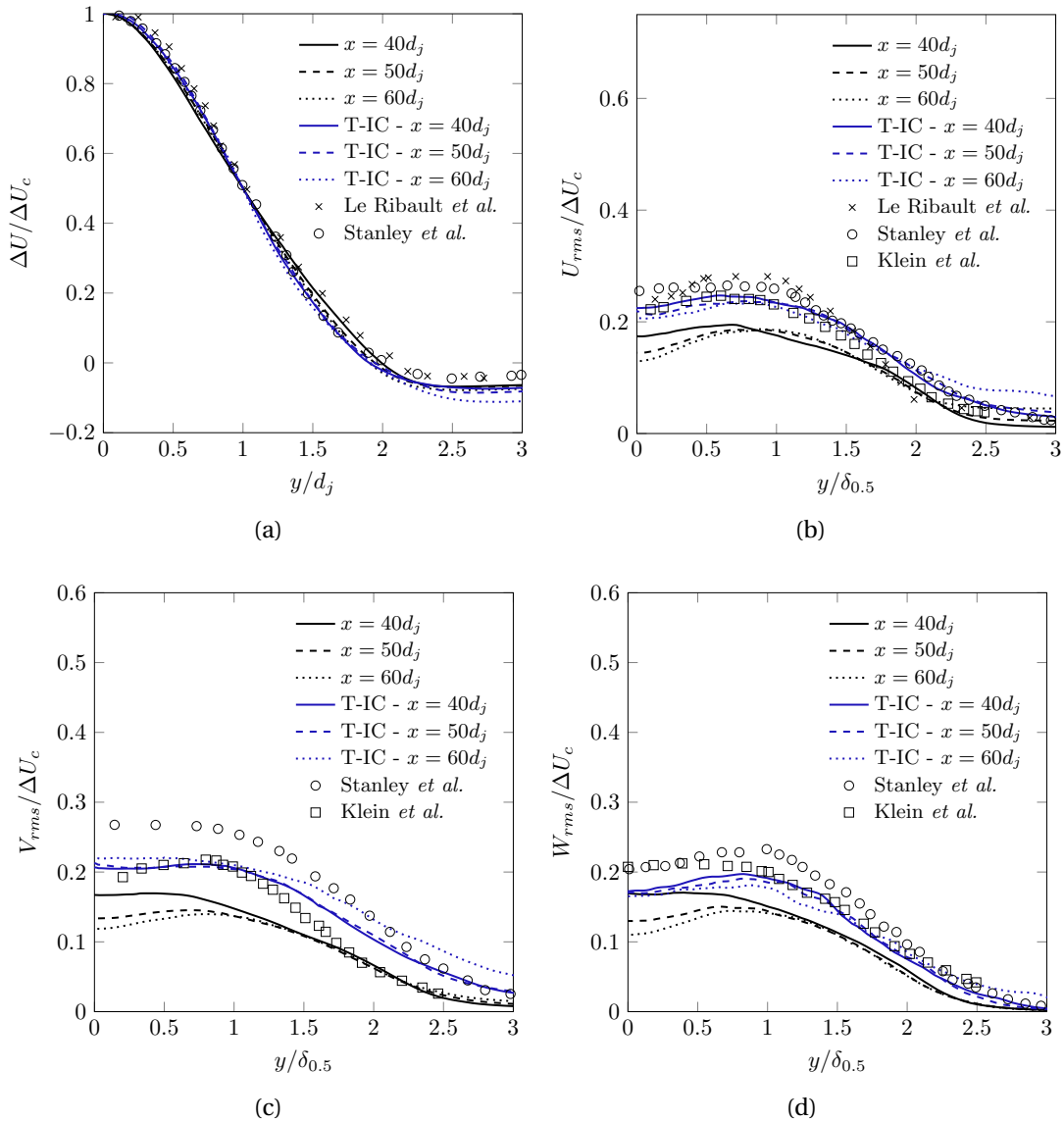


Figure 3.12. – RANS mode enforced for $x < 30d_j$. Radial profiles in the self-similarity region compared to the Turbulent IC simulation at $x = 40d_j$. (a) Mean streamwise velocity, (b) Streamwise velocity fluctuations U_{rms} , (c) Normalwise velocity fluctuations V_{rms} and (d) Spanwise velocity fluctuations W_{rms} .

it appears that the resolved turbulent kinetic energy overshoots the resolved turbulent kinetic energy from the Turbulent IC computation. Then, there is a decrease of the resolved turbulent kinetic energy.

For the $x_T = 6d_j$ case, radial profiles of the mean velocity excess and diagonal Reynolds stresses are presented in Fig. 3.10 for five different axial locations between

3. Forcing shear flows – 3.2. Planar jet

$x = 20d_j$ and $x = 60d_j$. Fig. 3.10a shows the normalwise evolution of the mean axial velocity for different axial positions. Results are in good agreement with results from the literature and the Turbulent IC simulation. Mean velocity profiles collapse well to a self-similar state. Radial profiles of the streamwise velocity fluctuations shown in Fig. 3.10b exhibit the same trends, namely that the jet is self-similar in the region $20d_j < x < 60d_j$. Profile at $x = 20d_j$ is not in agreement with profiles taken further downstream, near the center line before merging for $y/\delta_{0.5} > 1.25$. Additionally, the tail of profile at $x = 60d_j$ does not converge to the other profiles. Nevertheless, there seems to be a convergence between profiles at position $x = 30d_j$, $x = 40d_j$ and $x = 50d_j$. The results are in good agreement with the Turbulent IC simulation and references. The V_{rms} and W_{rms} radial profiles are shown respectively in Fig. 3.10c and Fig. 3.10d. Profiles collapse roughly to a self-similar behavior and fits well the Turbulent IC simulation. Regarding W_{rms} , profiles are underestimated, in comparison to the literature.

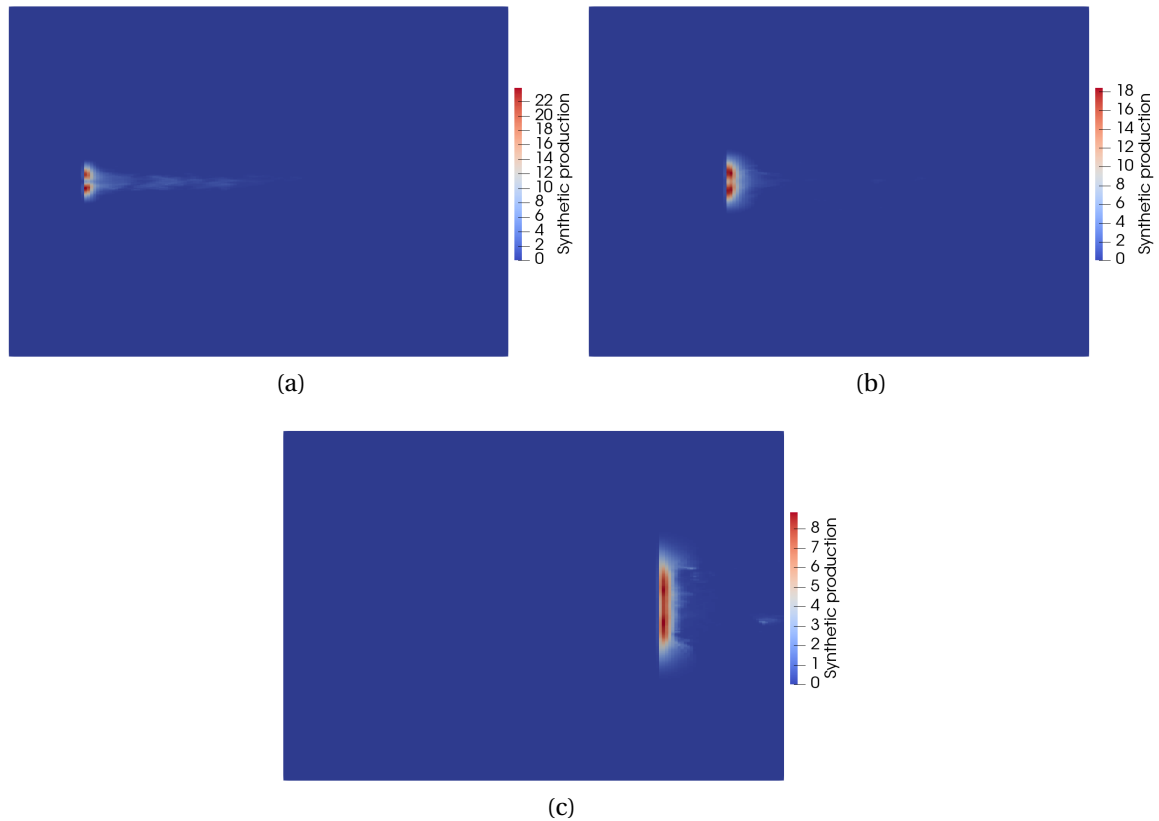


Figure 3.13. – Map color of the synthetic production. The domain ranges from $x = 0$ to $x = 40d_j$. (a) $x = 6d_j$ case, (b) $x = 11d_j$ case and (c) $x = 30d_j$ case.

Similar conclusions can be drawn for the $x_T = 11d_j$ case (Fig. 3.11). Mean velocity profiles, shown in Fig. 3.11a, collapse to a self-similar state except the profile at

$x = 20d_j$ meaning that the self-similarity region is not yet fully reached at this location. This is most likely because the transition zone is closer in this case. The same behaviour as in case $x = 6d_j$ is found for the root mean square velocities regarding self-similarity. However, in this case, the three root mean square velocities are underestimated. This is consistent with the underestimation of the axial turbulent kinetic energy observed in Fig. 3.9a.

In the case $x_T = 30d_j$, the axial turbulent kinetic energy decreases drastically downstream of the RANS region. This is reflected on the radial root mean square velocities displayed in Fig. 3.12 at $x = 40d_j$, $x = 50d_j$ and $x = 60d_j$. V_{rms} and W_{rms} profiles are not in agreement near the center line before merging from $y/\delta_{0.5} = 1.25$. Profiles of the streamwise root mean square velocity exhibit discrepancy near the center line and at the tail end of profiles. Nevertheless, mean streamwise velocity profiles show a self-similarity behavior. It should be highlighted in Fig. 3.12 that profiles of the Turbulent IC case are not perfectly self-similar.

It must be noticed that the reconstruction method has no influence on the ability of mean and fluctuating velocity profiles to converge towards self-similarity. The turbulent kinetic energy at the jet center line, is underestimated. For the two first cases, $x_T = 6d_j$ and $x_T = 11d_j$, this is mainly due to the fact that the upstream RANS statistics are not reliable. In the case $x = 30d_j$, the sudden decrease of the turbulent kinetic energy downstream of the RANS region is not fully understood yet. Several lines of research are envisaged for the prospects of this thesis:

- i) improving the quality of the synthetic signal,
- ii) improving the control of the synthetic production term,
- iii) finding a term to subtract to the subgrid dissipation transport equation.

Finally, to illustrate where the forcing takes place, Fig. 3.11a displays the map color of the synthetic production term (Eq. 3.4). The forcing occurs directly after the RANS region. The streamwise length of the forcing region seems to be similar in all three cases. However, the normalwise width of the forcing area increases with x_T . This is in line with the linear growth of the jet half width in the x direction.

3.2.5. Interest of the forcing for VLES

The focus is now on assessing the forcing method when increasing mesh sizes. Coarsening the mesh leads to filtering a larger part of the turbulent fluctuations. This sort of simulation is often called Very Large Eddy Simulation (VLES). These simulations require a richer subgrid model than the Smagorinsky model. As a hybrid RANS/LES method, E-DES is a good candidate. In this section, two new meshes are used:

- i) **Coarse8** - all space steps in Tab. 3.3 ($\Delta_x, \Delta_y, \Delta_z$) are multiplied by 2. The number of cells is equal to 495 444. This is equivalent to dividing the number of cells in the reference mesh by 8. Simulations on this mesh will be referred to as Coarse8,

3. Forcing shear flows – 3.2. Planar jet

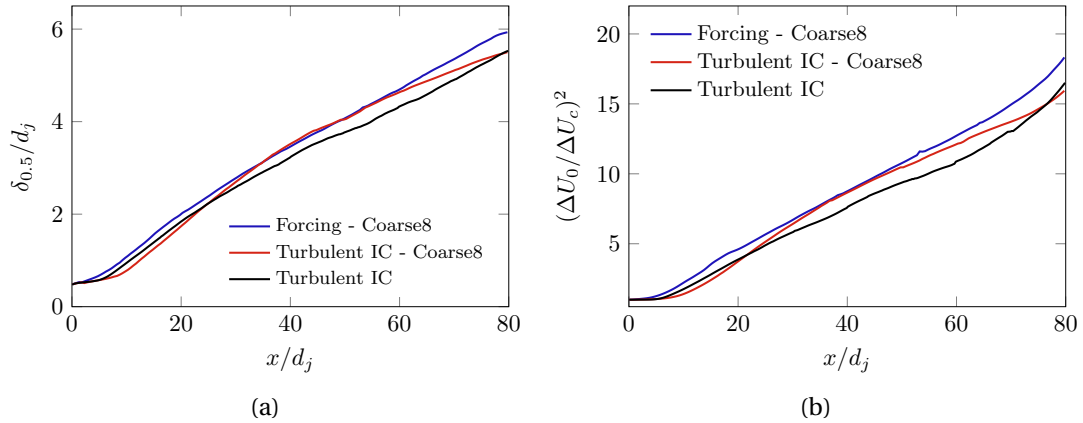


Figure 3.14. – Comparison between the Forcing and the Turbulent IC simulation on the Coarse8 mesh grid and also compared to the Turbulent IC simulation on the reference grid. (a) Growth of the jet half-width, (b) Decay of the streamwise mean velocity excess.

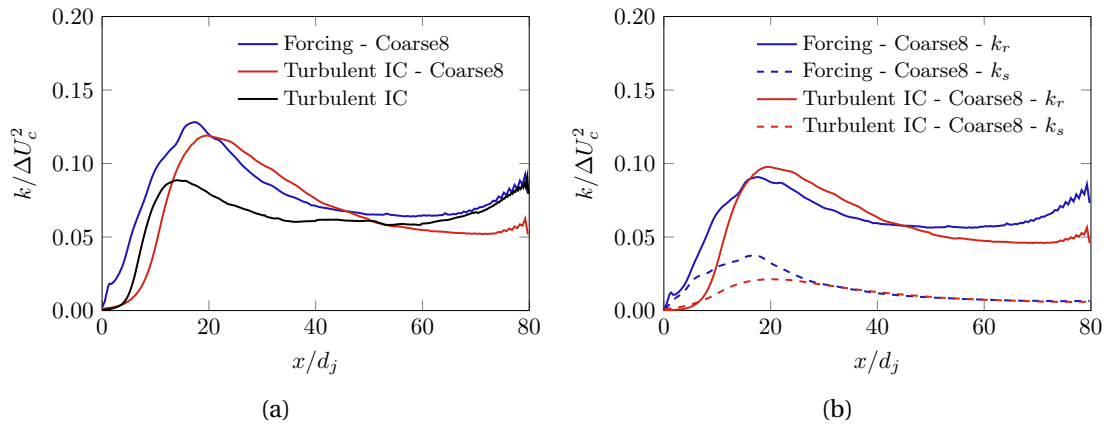


Figure 3.15. – Comparison between the Forcing and the Turbulent IC simulation on the Coarse8 mesh grid and also compared to the Turbulent IC simulation on the reference grid. (a) Total turbulent kinetic energy, (b) distribution of the total energy between the resolved part k_r and the sub grid part k_s .

- ii) **Coarse20** - all space steps in Tab. 3.3 are multiplied by 2.7. The number of cells is equal to 198 198. This is equivalent to dividing the number of cells in the reference mesh by 20. Simulations on this mesh will be referred to as Coarse20.

Results are compared with simulations with turbulent inlet condition on same meshes. For meshes Coarse8 and Coarse20, the turbulent kinetic energy ratio at the boundary condition is respectively equal to $r_k = 0.93$ and $r_k = 0.97$. As previously, the RFM method is employed to generate fluctuations at the boundary condition.

Simulations	K1	K2	C1	C2
Forcing	0.0645	13.08	0.199	4.12
Turbulent IC - Coarse	0.0551	24.05	0.171	10.78
Turbulent IC	0.0545	19.05	0.169	4.73

Table 3.7. – Computations on the Coarse8 grid. Summary of the resulting coefficients K1, K2, C1 and C2 for the region $x \in [50d_j; 65d_j]$.

Simulations	K1	K2	C1	C2
Forcing	0.0593	22.4	0.199	10.79
Turbulent IC - Coarse	0.0586	17.37	0.190	4.83
Turbulent IC	0.0545	19.05	0.169	4.73

Table 3.8. – Computations on the Coarse20 grid. Summary of the resulting coefficients K1, K2, C1 and C2 for the region $x \in [50d_j; 65d_j]$.

Firstly, the coarse8 grid case is considered. Fig. 3.14a displays the jet half width evolution for the forcing simulation compared to the Turbulent IC simulation on the same grid (Coarse) and the Turbulent IC computation on the reference grid (Tab. 3.3). It appears that the spread of the jet in the case of the Forcing simulation starts upstream of the reference simulation. In contrast, for the Turbulent IC (Coarse grid) computation, the spread of the jet starts downstream of the reference simulation. This difference in potential core length can also be observed in Fig. 3.14b, which represents the decay of the streamwise mean velocity excess. Despite this difference in the potential core length, the slopes of both growth of the jet half-width and the velocity excess decay are roughly the same, as shown in Tab. 3.7.

Fig. 3.15a shows the axial evolution of the total turbulent kinetic energy. For the forcing case, it is clear that the forcing alters the development of the total energy before its peak. The turbulent kinetic energy for both Forcing and Turbulent IC (Coarse) simulations overshoot the reference computation near the peak. For the Forcing simulation, this might be due to the overestimation of center line mean velocity decay. Fig. 3.15b displays the resolved and subgrid kinetic energy for the Forcing and the Turbulent IC (Coarse) simulations. As expected, the increase in resolved and subgrid turbulent kinetic energies begins directly at the nozzle outlet for the forcing simulation. The subgrid energy converges from $x = 26d_j$ between the two simulations while a discrepancy is observed for the resolved part.

Fig. 3.16a and Fig. 3.16b show the radial profiles of the streamwise velocity, respectively for the Forcing and the Turbulent IC (Coarse) simulations. In both cases, profiles collapse well towards self-similarity. The longitudinal Reynolds stress profiles are plotted in Fig. 3.16c and Fig. 3.16d. For both cases, profiles at $x = 20d_j$ and $x = 30d_j$ are not in agreement with the other downstream profiles. This is in line with the

3. Forcing shear flows – 3.2. Planar jet

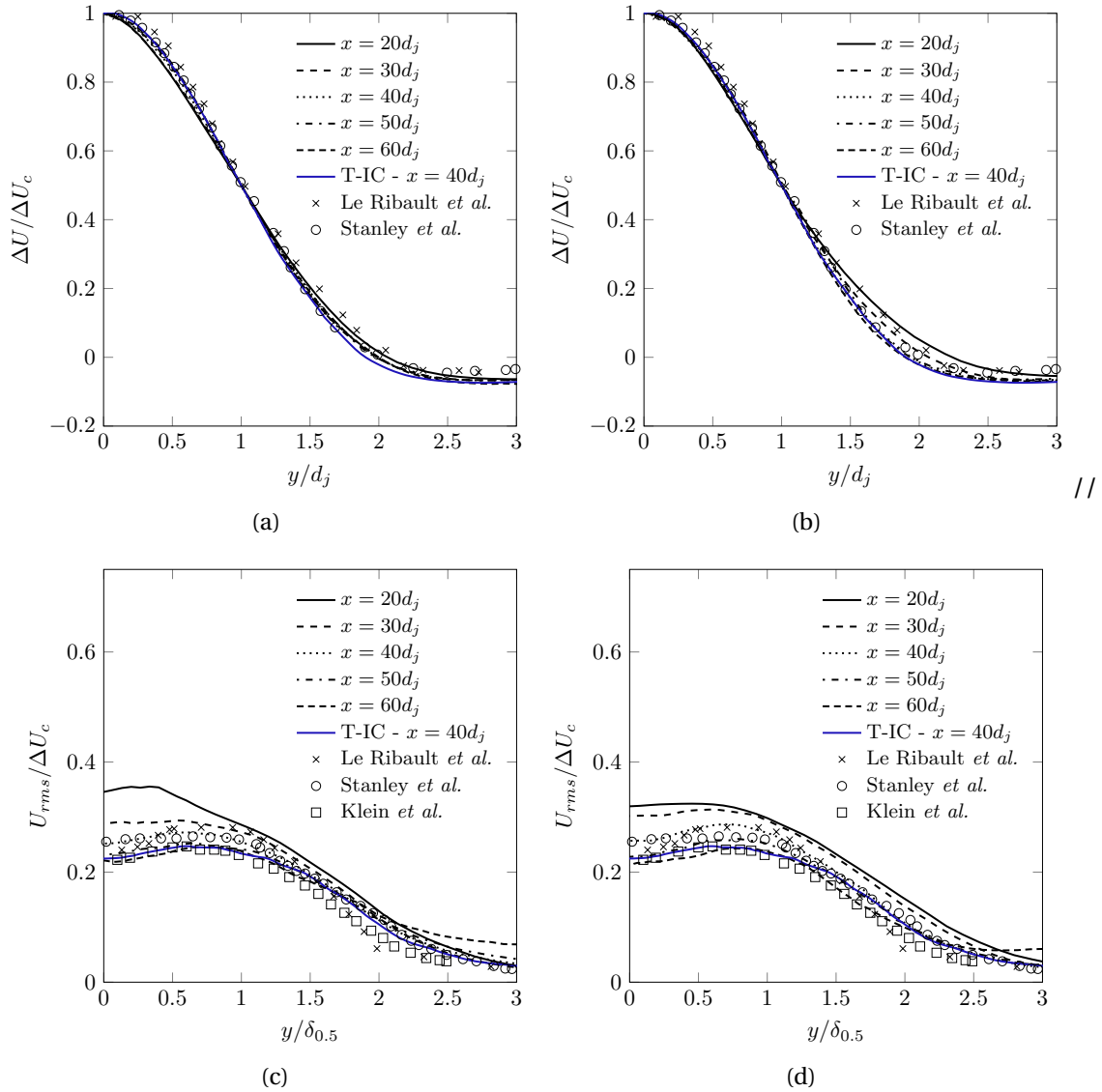


Figure 3.16. – Comparison between the Forcing and the Turbulent IC simulation on the Coarse8 mesh grid and also compared to the Turbulent IC simulation on the reference grid. Mean longitudinal velocity profiles (a) Forcing, (b) Turbulent IC - Coarse8 and longitudinal Reynolds stress profiles (c) Forcing, (d) Turbulent IC - Coarse8.

axial evolution of turbulent kinetic energy (Fig. 3.15a) since for both simulations the turbulent kinetic energy is largely overestimated before $x = 40d_j$.

Having presented the results for the mesh reduced by a factor 8 compared to the reference mesh, simulations with a factor 20 are now introduced. As in case Coarse8, a simulation with turbulent inlet condition has been performed. First, jet half-width

3. Forcing shear flows – 3.2. Planar jet

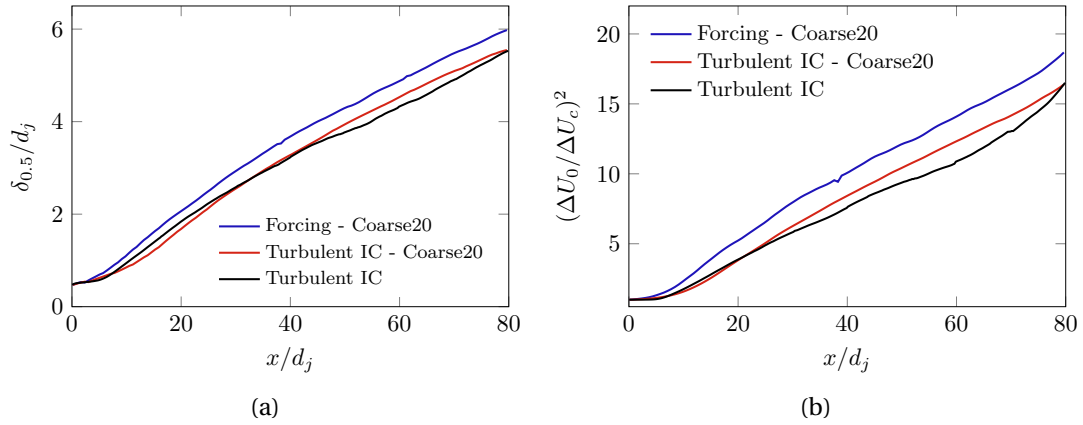


Figure 3.17. – Comparison between the Forcing and the Turbulent IC simulation on the Coarse20 mesh grid and also compared to the Turbulent IC simulation on the reference grid. (a) Growth of the jet half-width, (b) decay of the streamwise mean velocity excess.

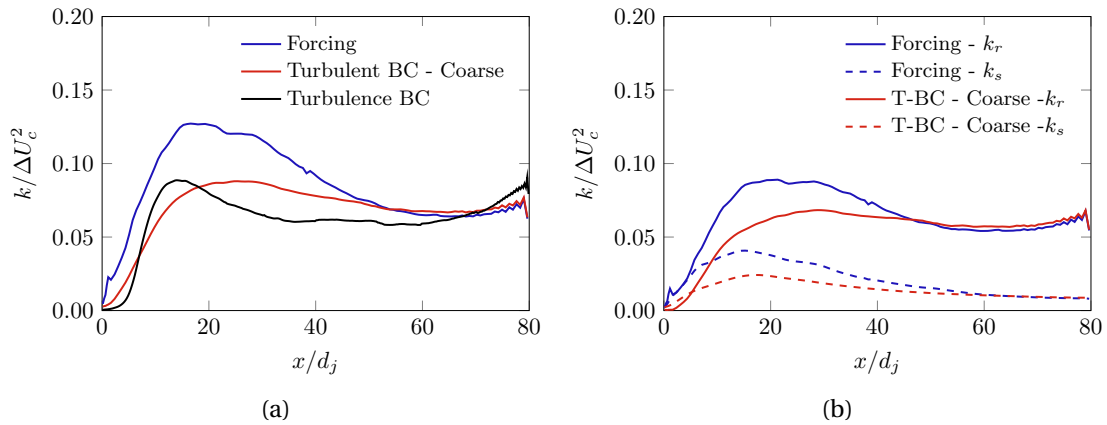


Figure 3.18. – Comparison between the Forcing and the Turbulent IC simulation on the Coarse20 mesh grid and also compared to the Turbulent IC simulation on the reference grid. (a) total turbulent kinetic energy, (b) distribution of the total energy between the resolved part k_r and the sub-grid part k_s .

evolution and velocity excess decay are plotted in Fig. 3.17a and Fig. 3.17b. In the case of the forcing, the jet half-width growth starts upstream of the reference simulation (Turbulent IC) as well as the Turbulence IC simulation on the Coarse20 mesh. In accordance with this, the length of the potential core, for the forcing case, is shorter compared to the reference simulation. This is shown by the decay of the mean axial velocity excess. This decay starts before in the case of the forcing simulation. Nevertheless, the slope of jet half-width growth K_1 (Tab. 3.8) of the forcing case is in good

3. Forcing shear flows – 3.2. Planar jet

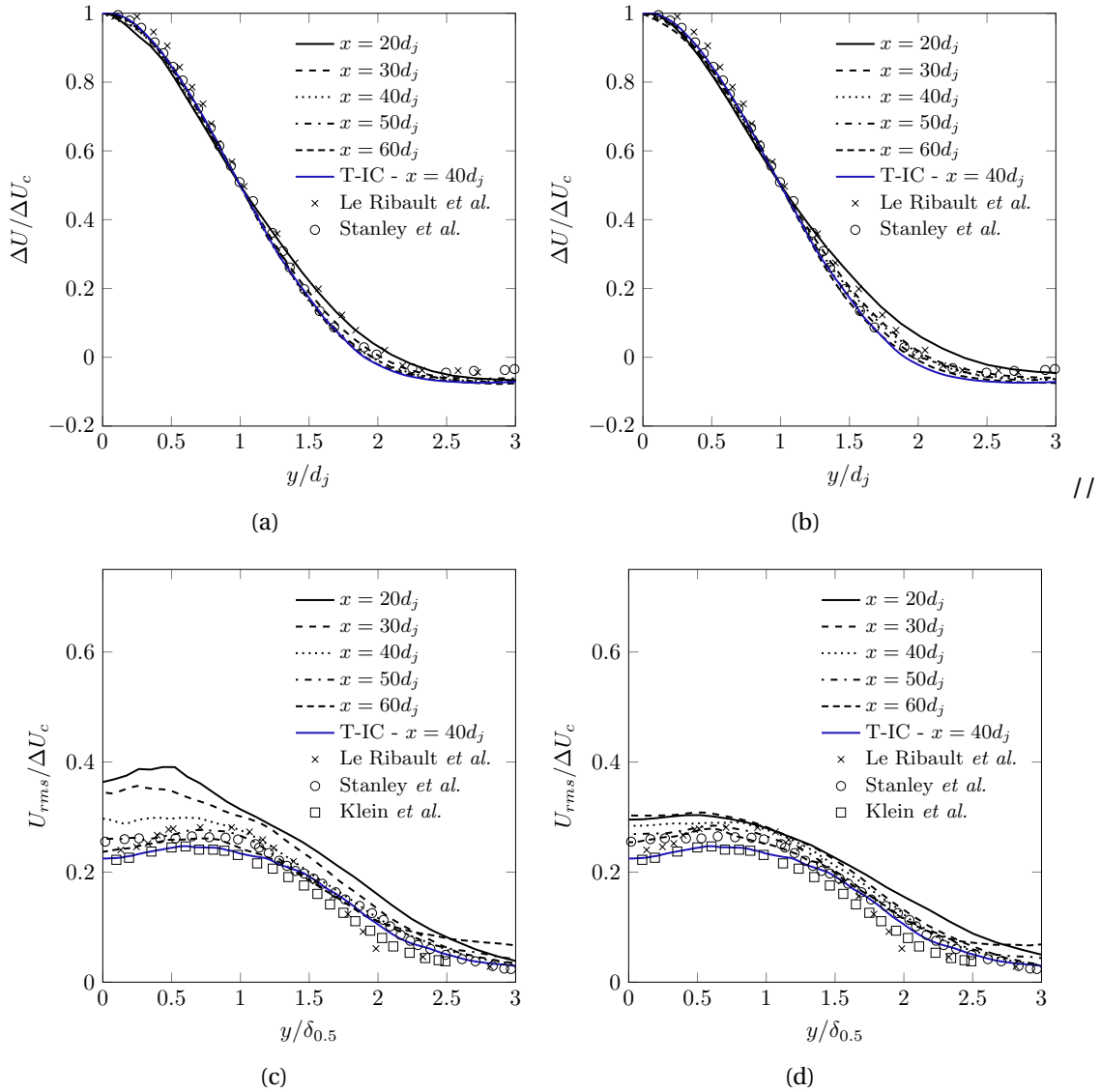


Figure 3.19. – Comparison between the Forcing and the Turbulent IC simulation on the Coarse20 mesh grid and also compared to the Turbulent IC simulation on the reference grid. Mean longitudinal velocity profiles (a) Forcing, (b) Turbulent IC - Coarse20 and longitudinal Reynolds stress profiles (c) Forcing, (d) Turbulent IC - Coarse20.

agreement with the reference simulation. The slope of the axial mean velocity excess C_1 is overestimated for the Forcing and the Turbulent IC (Coarse) cases.

The axial evolution of the turbulent kinetic energy is displayed in Fig. 3.18a. For the Forcing case, it is observed that the turbulent kinetic energy overshoots largely the reference curve. As previously, this can be attributed to the underestimation of the

axial mean velocity excess (Fig. 3.17b). The energy distribution for the Forcing and Turbulent IC (Coarse) cases are shown in Fig. 3.18b. The resolved and subgrid parts converge towards the same values after $x = 50d_j$ while there is a discrepancy after the jet inlet.

Fig. 3.19 displays radial profiles of the mean axial velocity excess (Fig. 3.19a and Fig. 3.19b) and longitudinal Reynolds stress profiles (Fig. 3.19c and Fig. 3.19d) for the Forcing (left) and the Turbulent IC Coarse (right) cases. The mean velocity profiles collapse well towards self-similarity for both cases. Regarding the root mean square value U_{rms} velocity profiles, it appears that the forcing disturbs the self-similarity region when compared to the Turbulent IC (Coarse) case.

The purpose of this section was to show the value of the reconstruction method in VLES. It was expected that forcing would improve the results. It has been observed that the forcing does at best as well as turbulent inlet conditions. The evolution of the mean axial velocity appears to be significantly influenced by the forcing. This might be due to the fact that the convective-like term of the forcing arising in the non-homogeneous case (see Eq. 3.4) has a non-zero average. This issue requires further investigation.

3.3. Conclusion

In this chapter, planar jet test case has been studied to assess the reconstruction method in the frame of non-homogeneous turbulent flows. First, the new formulation of the forcing, for non-homogeneous turbulent flow, has been derived. Two points in particular are worth noticing:

- i) an additional term in the transport equation of the mean velocity is implied by the enrichment of the convective term responsible for the turbulent production,
- ii) the synthetic velocity is no longer divergence-free.

The consideration of these two points is left for future perspectives.

The forcing was first used without solving the momentum and turbulent model equations. The synthetic velocity was just updated at each time step, using a precursor RANS simulation to determine the target quantities. The aim of this test was to show whether the desired synthetic energy can be recovered from a RANS solution. The synthetic turbulent kinetic energy was well recovered; discrepancies being only due to the prescribed energy spectrum model (PP or VKP). It has been shown that the use of space-dependent frequency results in changes in the energy field. This energy field produced by the synthetic signal was no longer consistent with RANS solution. The cosine term of the synthetic velocity should be space dependent to avoid decorrelation.

The forcing has then been tested on zonal configuration of the planar jet test case. The kinetic energy ratio was enforced to $r_k = 1$ ("RANS" mode) over a certain length

downstream of the jet inlet. Further downstream, at a position x_T , the flow transitioned from RANS to “free” E-DES description. Three different configurations were tested, $x_T = 6d_j$, $x_T = 11d_j$ and $x_T = 30d_j$. The first configuration is in the region of increased turbulent kinetic energy, at the exit of the potential core. The second configuration, $x_T = 11d_j$, was chosen because it is very close to the peak of turbulent kinetic energy and the beginning of self-similar region. For the last configuration, the transition region is located far into the self-similar region. The forcing method provided encouraging results for the first two configurations ($x_T = 6d_j$ and $x_T = 11d_j$). For both of these configurations, the forcing recovered good levels of resolved turbulent kinetic energy in the self-similar region. It was also shown that radial profiles (mean velocity, root mean square velocity) showed that they were self-similar. At the transition region, the jet half-width growth is reduced over a diameter ($\sim d_j$) before recovering correct slopes. For the configuration where the ratio is forced to $r_k = 1$ over 30 diameters, outcomes are different. It turns out that the force is too strong in this situation. The resolved turbulent kinetic energy is overestimated at the beginning of the transition region ($30d_j < x < 32d_j$). This leads to a sharp drop in kinetic energy downstream of the forcing zone. Average quantities such as the jet half-width are affected. This forcing dysfunction in this configuration can be due to various factors:

- i) quality of the synthetic signal,
- ii) control of the injected synthetic energy,
- iii) lack of an additional dissipation term related to the forcing in the transport equation of the subgrid dissipation.

These points are also part of the perspectives of this work.

Finally, the reconstruction method has been tested in the framework of Very Large Eddy Simulation. The contribution of forcing was demonstrated using two coarse meshes. Results were compared with simulations with turbulent inlet condition. The forcing has been shown to perform at most as well as simulations with turbulent inlet conditions.

4. Evaluation of E-DES with forcing for flows in ventilated room

Table of contents

4.1	The CARDAMOMETTE experimental program	117
4.1.1	Objectives	117
4.1.2	Description of the facility	118
4.2	Numerical simulations of the air transfer jet	119
4.2.1	Numerical set-up	119
4.2.2	Inlet precursor simulations	119
4.2.2.1	Fully developed flow in a square duct	119
4.2.2.2	Flow in the rectangular duct	123
4.2.3	Air transfer jet simulation results	124
4.3	Conclusion	131

While the previous chapters focused on dedicated academic cases, this chapter deals with the application of the synthetic forcing methodology to a more realistic configuration involving turbulent wall-bounded flows. The configuration corresponds to a ventilated room for which experimental measurements are available at IRSN. The validity and the predictive capabilities of the hybrid approach with synthetic forcing are discussed by comparing numerical predictions with measurement data together with RANS and LES simulations. The emphasis is on the proposed forcing methodology rather than on the hybrid approach as the moderate Reynolds number studied case can be addressed by properly resolved LES without too much computational resources.

4.1. The CARDAMOMETTE experimental program

4.1.1. Objectives

The experimental program CARDAMOMETTE conducted at IRSN is dedicated to the study of the dispersion of helium, which is a surrogate of hydrogen, in a ventilated room. This experimental program aims at reproducing similar dispersion studies carried out in the larger facility CARDAMOME with the addition of PIV measurements in various locations, in order to provide quantitative measurements for the validation of simulation tools used to assess explosion hazard. The main three steps of the program are:

- i) Prior to helium release experiments, the first step focuses on the aerodynamic characterization of the ventilated room,
- ii) The second step is concerned with helium distribution in the ventilated room for various release configurations (impinging helium jet, ...),
- iii) The third step extends the previous one by considering a congested ventilated room.

Throughout this chapter, focus will be put on the first step that features turbulent wall bounded flow without buoyancy effects.



Figure 4.1. – General view of the CARDAMOMETTE facility at IRSN Saclay

4.1.2. Description of the facility

The facility shown in Fig. 4.1 consists of a parallelepipedic enclosure, made of six walls of transparent plastic (PMMA) with an extraction vent located in an upper position and two possible locations of a supply vent in either a middle or an upper position. The dimensions of the room are 2 m length, 1.7 m width and 1.2 m high. The air vents consist of simple openings whose dimensions are 0.13 m width and 0.2 m height. Upstream of the supply vent, a supply duct of length 0.8 m allows to generate nearly fully developed turbulent flow at the entrance of the room. Various locations of helium release are envisaged in order to cover different situations as for instance the case of a strong interaction between air and helium jets or the case of a helium jet impacting a wall of the room with a limited interaction with the air jet coming from the supply vent.

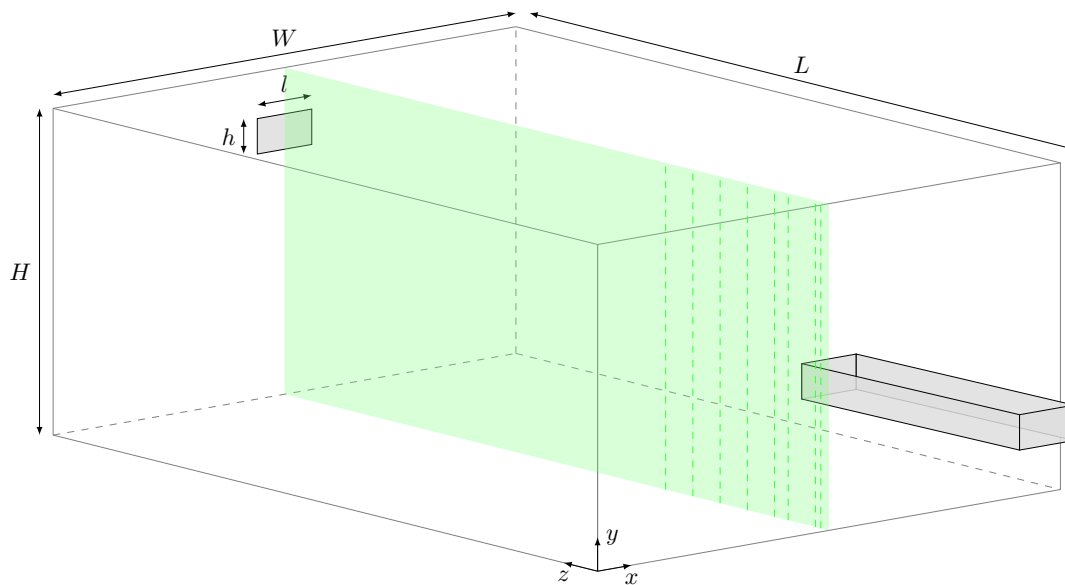


Figure 4.2. – Sketch of the CARDAMOMETTE facility

The velocity measurements are performed using Particle Image Velocimetry (PIV) within the duct and downstream the supply vent. The flow is seeded with tracer oil droplets and is illuminated by a laser sheet, generated by a continuous green laser (532 nm), along either a vertical or a horizontal plane. The dimensions of the interrogation windows are $0.25 \times 0.25 \text{ m}^2$ in the vicinity of the supply vent, either upstream within the duct or downstream within the room, or $0.95 \times 0.25 \text{ m}^2$ for more distant measurements of the jet within the enclosure. In both cases, the resolution corresponds to 2048×2048 pixels. The set-up of the facility together with PIV measurements in the large horizontal plane downstream air supply is sketched in Fig. 4.2.

4.2. Numerical simulations of the air transfer jet

4.2.1. Numerical set-up

The present work aims at assessing the validity and the interest in using hybrid RANS/LES approaches by focusing on the first step of the experimental program that corresponds to the air transfer jet coming from the supply vent. In this frame, three flow cases that remain statistically stationary are addressed:

- i) The first case corresponds to a fully developed flow in a *square* duct for which DNS data are available. This allows to evaluate the predictive capabilities of the hybrid approach at a Reynolds number close to that of the rectangular duct upstream of the supply vent.
- ii) The second case moves on the rectangular duct upstream of the supply vent. It is assumed that the flow is fully turbulent and numerical predictions are compared with available measurements in the duct. Moreover, this case serves as a precursor simulation to generate realistic inlet boundary conditions from the numerical predictions in a cross-section of the duct.
- iii) The third case deals with the aerodynamic characterization of the ventilated room using precursor simulations as inlet boundary conditions at air supply. The numerical predictions are compared with experimental measurements that consist of longitudinal and vertical profiles of the mean streamwise velocity and kinetic energy at various locations downstream to air supply.

In each case, RANS and LES simulations are also performed in order to discuss the validity and the interest of using hybrid approaches. RANS simulations are based on the $k-\omega$ SST (F. Menter 1994) and $k-\omega$ EARSM (Krishnan 2019) models while LES is based on the dynamic Smagorinsky model (Germano, Piomelli, Moin, et al. 1991). For both RANS and LES simulations, the mesh is sufficiently refined near the walls to avoid the use of wall functions. The hybrid approach is summarized in the Appendix B and is based on the EAHSM model (Krishnan 2019) with the introduction of elliptic blending as proposed in Fadai-Ghotbi, Christophe Friess, Rémi Manceau, and Borée 2010 to enforce the RANS mode in the near-wall region. The predictive capabilities of the hybrid approach are here assessed using either EAHSM or EARSM precursor simulations as inlet boundary conditions. In the latter case, synthetic forcing is employed either in the full domain or restricted to a downstream region mimicking a hybrid RANS/LES zonal approach. All the above mentioned models together with their acronym are listed in Table 4.1 for convenience.

4.2.2. Inlet precursor simulations

4.2.2.1. Fully developed flow in a square duct

Before moving to the precursor simulations in the rectangular duct, numerical simulations are first performed in a square duct in order to validate the proposed

4. Evaluation of E-DES with forcing for flows in ventilated room – 4.2. Numerical simulations of the air transfer jet

SST	k - ω Shear-Shear-Transport (F. Menter 1994)
EARSM	Explicit Algebraic Reynolds-Stress k - ω Model (Krishnan 2019)
LES	Dynamic Smagorinsky model (Germano, Piomelli, Moin, et al. 1991)
EAHSM	Explicit Algebraic Hybrid Stress Model k_s - ω_s model (Krishnan 2019) using elliptic blending for the energy ratio parameter
EAHSM-F	EAHSM model with synthetic forcing
EAHSM-FZ	EAHSM model with synthetic forcing mimicking zonal approach

Table 4.1. – RANS, LES and hybrid RANS/LES modes used for the calculations

approach against available DNS data at a similar bulk Reynolds number.

Compared to the rectangular duct, only the geometry is modified by considering a square duct whose side corresponds to the hydraulic diameter $D_h = 4A/P$ where A is the cross section area of the rectangular duct and P the corresponding perimeter. Introducing the bulk Reynolds number as $Re_b = W_b D_h / \nu$, this leads to $Re_b = 6770$ which is close to the DNS case $Re_b = 7000$ investigated by Pirozzoli, Modesti, Orlandi, et al. 2018. The corresponding friction Reynolds number based on the duct half width is given by $Re_\tau = 227$ leading to a friction velocity close to the usual estimate given by $0.05W_b$.

Numerical simulations are performed on the duct whose dimensions are $[0; D_h] \times [0; D_h] \times [0; 2\pi D_h]$. The streamwise flow is sustained by prescribing a constant mass flow rate at a cross-section, given by $Q = \rho W_b D_h^2$. Along the streamwise z -direction, the meshing is uniform with N_z number of grid points whereas a non-uniform meshing is used in the wall-normal directions for which the transformation reads:

$$\forall k \in [1, N], x_k, y_k = \frac{D_h}{2} \left[1 + \frac{1}{a} \tanh \left[\left(-1 + \frac{2(k-1)}{N-1} \right) \tanh^{-1}(a) \right] \right]$$

The parameter a is set to $a = 0.988$ so that the first dimensionless grid point location $\delta^+ = 2\delta Re_\tau / D_h$ is $\delta^+ = 0.5$ with $N = 60$. As the flow is statistically homogeneous in the streamwise direction, RANS simulations use $N_z = 3$ whereas LES use $N_z = 43$ in such a way that $\Delta z^+ = 50$. Simulations are run during a physical time of 70 convective times T_0 with $T_0 = L_z / W_b$. Regarding LES and hybrid simulations, time averaging is performed during $50T_0$ after removing a first period of $20T_0$ for flow establishment. The initial conditions for the resolved velocity correspond to a steady RANS solution with the superimposition of a synthetic velocity signal while subfilter quantities are

4. Evaluation of E-DES with forcing for flows in ventilated room – 4.2. Numerical simulations of the air transfer jet

prescribed arbitrarily as $k_s = 0.1k$ for the subfilter kinetic energy along with a subfilter viscosity ratio $\nu_s/\nu = 10$.

Case	$N_x \times N_y \times N_z$	Δt	Re_τ
SST	$60 \times 60 \times 5$	$0.01 T_0$	219
EARSM	$60 \times 60 \times 5$	$0.01 T_0$	220
LES	$60 \times 60 \times 43$	$0.25 \Delta z / W_b$	217
EAHSM	$60 \times 60 \times 43$	$0.25 \Delta z / W_b$	216
EAHSM-F	$60 \times 60 \times 43$	$0.25 \Delta z / W_b$	218

Table 4.2. – Square duct parameters and simulation results

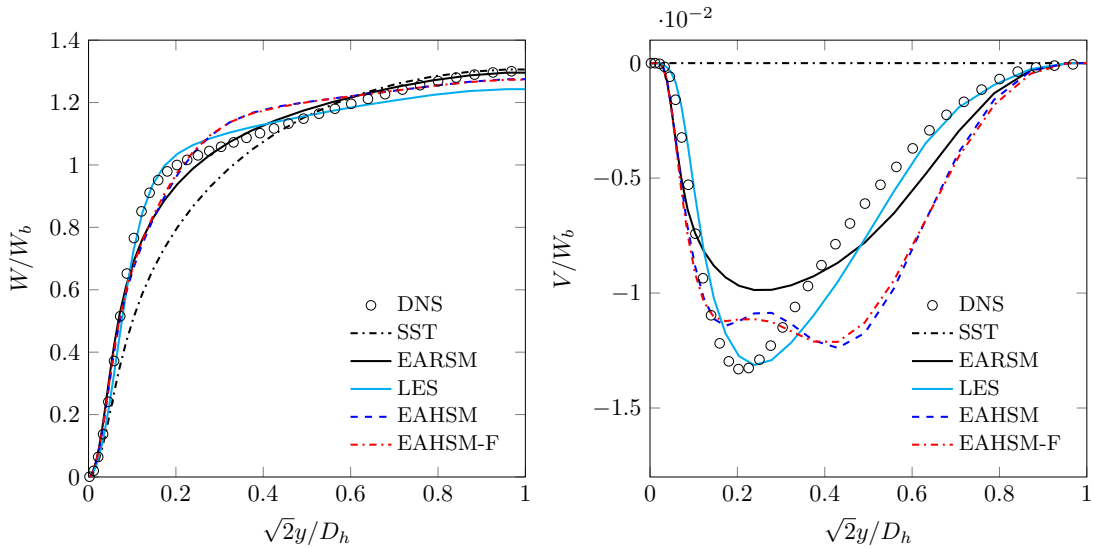


Figure 4.3. – Square duct flow: mean streamwise velocity (left) and secondary motion (right) along the corner bisector

The results are displayed on the corner bisector $x = y$ where, due to symmetry, $U = V$ for the mean flow quantities while $U_{rms} = V_{rms}$ and $\overline{uw} = \overline{vw}$ for the turbulent quantities. The statistics are spatially averaged along the homogeneous streamwise direction together with an average on the four quadrants, taking into account symmetry properties. It is worth noticing that the results displayed for hybrid simulations account for both resolved and sub-filter parts while LES results are restricted to the resolved part as the sub-filter contribution remains difficult to evaluate. As expected for such a flow, the $k-\omega$ SST model, which is based on the Boussinesq closure for the Reynolds stresses, is unable to predict the secondary motion caused by the anisotropy between the Reynolds stress components. This contrasts with explicit algebraic modeling of the Reynolds stresses which is able to predict the most important features of

4. Evaluation of E-DES with forcing for flows in ventilated room – 4.2. Numerical simulations of the air transfer jet

such a flow as illustrated in Fig. 4.3. Moving to the EAHSM model, similar conclusions as in Krishnan 2019 at higher Reynolds numbers without enforcing RANS mode in the near wall region, can be drawn in comparison with the dynamic Smagorinsky model, here referred to as LES. However, the benefits of using a hybrid RANS/LES approach appear here less pronounced. This may be due to (i) the low Reynolds number and (ii) enforcing RANS mode in the near-wall region probably requires further modifications of the hybrid approach (as suggested e.g. by Duffal, De Laage de Meux, and R. Manceau 2022). Regarding the latter issue, it is worth keeping in mind that enforcing RANS mode near the wall demands a reliable wall treatment.

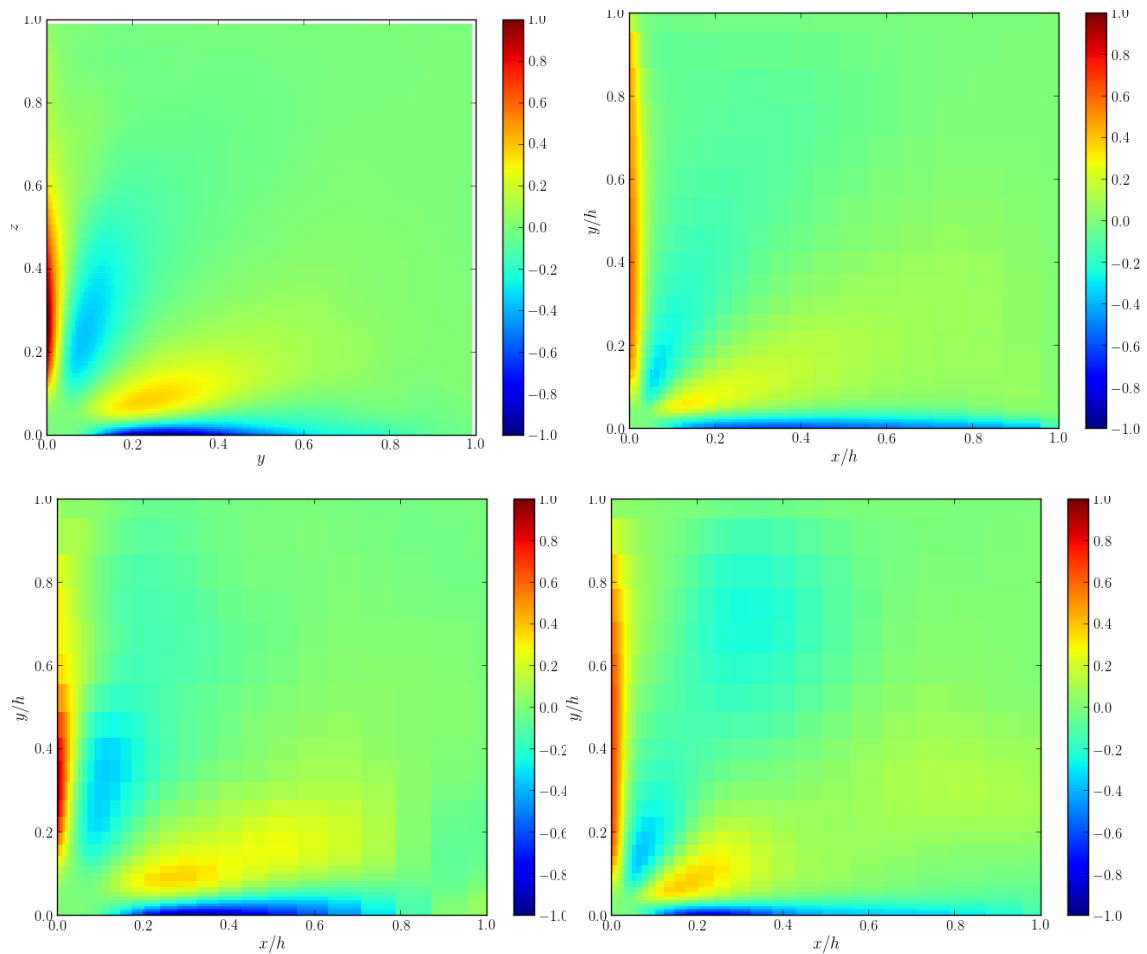


Figure 4.4. – Square duct flow: mean streamwise dimensionless vorticity $\bar{\omega}_z h / W_b$ for DNS (top left), EARSIM (top right), LES (bottom left) and EAHSM (bottom right)

The predicted mean flow shown in Fig. 4.3 and the turbulent kinetic energy shown in Fig. 4.5 along the corner bisector together with the mean streamwise vorticity shown in Fig. 4.4, which is non-zero owing to the secondary motion, are correctly predicted using the hybrid methodology. Moreover, contrary to the first results ob-

4. Evaluation of E-DES with forcing for flows in ventilated room – 4.2. Numerical simulations of the air transfer jet

tained in Krishnan 2019 with the EAHSM model, enforcing RANS mode near the wall¹ allows the kinetic energy ratio to tend rapidly to unity in the near-wall region and thus enforcing the RANS mode in this region. The use of synthetic forcing, which is denoted as EAHSM-F, leads to nearly the same results as the hybrid approach without forcing denoted as EAHSM. Some minor differences appear mainly on the turbulent quantities, as shown in Fig. 4.5, that could be attributed to insufficiently converged statistics. Hence, as a preliminary conclusion about the use of the proposed synthetic forcing for the simulation of fully developed turbulent flows in ducts, self-adaptivity performs relatively well, provided that the resolved dissipation is accounted for in the definition of the kinetic energy ratio², but it seems that there is no clear improvement on the RANS/LES transition region.

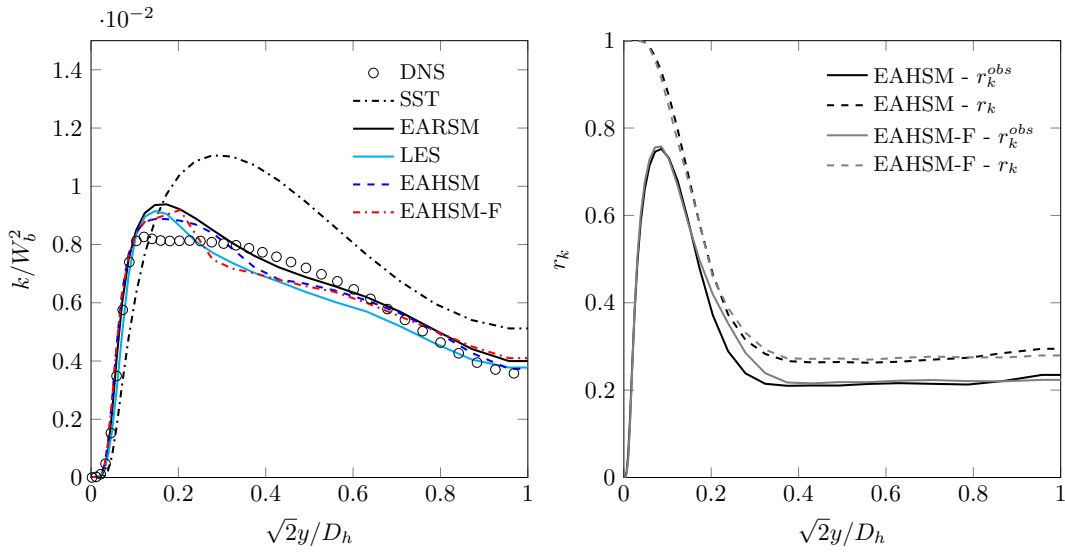


Figure 4.5. – Square duct flow: turbulent kinetic energy along the corner bisector (left) and average along the streamwise direction of the target, r_k , and observed, r_k^{obs} , kinetic energy ratio (right)

4.2.2.2. Flow in the rectangular duct

Moving to the precursor simulations in the rectangular duct with dimensions $[0; l] \times [0; h] \times [0; 2\pi l]$ upstream from the supply vent, the numerical set-up is similar to the previous one. The mesh distribution in the wall-normal directions uses the same transformation but with D_h replaced either by the vent width $l = 0.2$ m or the vent height $h = 0.13$ m. The coefficient $a = 0.988$ remains the same in both directions but the number of grid points is set to $N = 75$ and 50 respectively in the x - and y -directions.

1. Using elliptic blending, as explained in Appendix B

2. Preliminary simulations, not shown here, without the resolved dissipation, strongly overestimate the resolved kinetic energy using the same duration to compute statistics

4. Evaluation of E-DES with forcing for flows in ventilated room – 4.2. Numerical simulations of the air transfer jet

As previously, the simulations are performed using periodic boundary conditions in the streamwise direction together with an adaptive body force allowing to enforce a prescribed flow rate. As a result, the flow corresponds to a fully developed turbulent flow and one expects some discrepancies when comparing with experimental results.

The simulation results are compared with experimental measurements that are available upstream of the blowing vent along vertical and horizontal cut planes. Overall, a good agreement is observed between numerical predictions and measurement data. The results shown in Fig. 4.6-4.7 exhibit similar tendencies as observed previously for the square duct case. More specifically, the use of synthetic forcing leads to nearly the same mean streamwise velocity profiles compared with the hybrid approach without forcing. Here again, some differences appear regarding turbulent quantities that are slower to achieve statistical convergence. While it is difficult to distinguish the most accurate prediction of the mean streamwise velocity, the streamwise root mean square (rms) velocity is clearly underestimated using RANS approaches, especially near the walls. However, it has to be noticed that neither the SST nor the EARSM model employ a dedicated near wall modeling and this probably explains the underestimation of turbulence intensity near the walls.

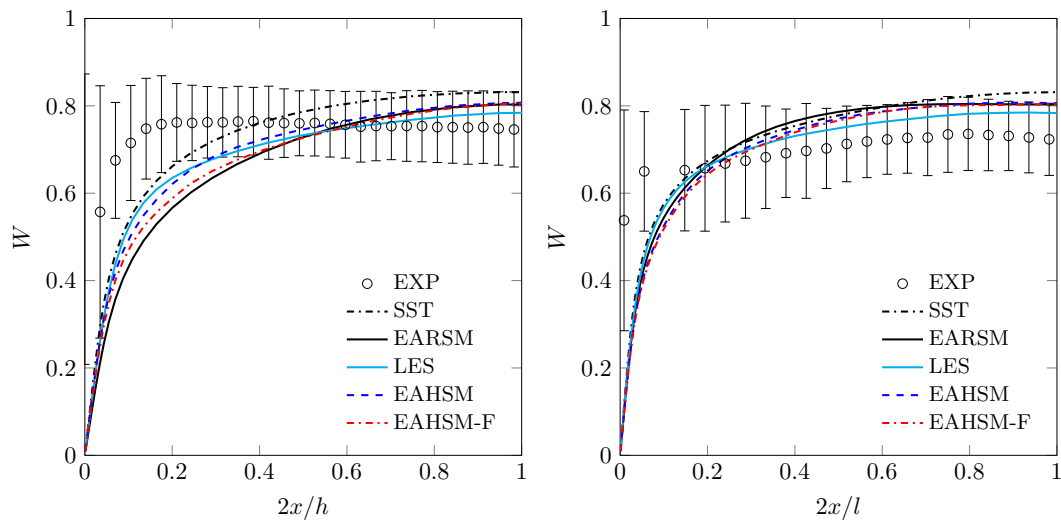


Figure 4.6. – Rectangular duct flow: mean streamwise velocity along the vertical (left) and horizontal (right) cut planes at the center of the duct

4.2.3. Air transfer jet simulation results

The numerical simulations of the air transfer jet in the ventilated room are performed in the enclosure $[0; W] \times [0; H] \times [0; L]$ with $W = 1.7$ m, $H = 1.2$ m and $L = 2$ m. The enclosure is supplemented by inlet and outlet rectangular ducts of length $l = 0.2$ m at the supply and the extraction vents. The length of the ducts has been set arbitrarily

4. Evaluation of E-DES with forcing for flows in ventilated room – 4.2. Numerical simulations of the air transfer jet

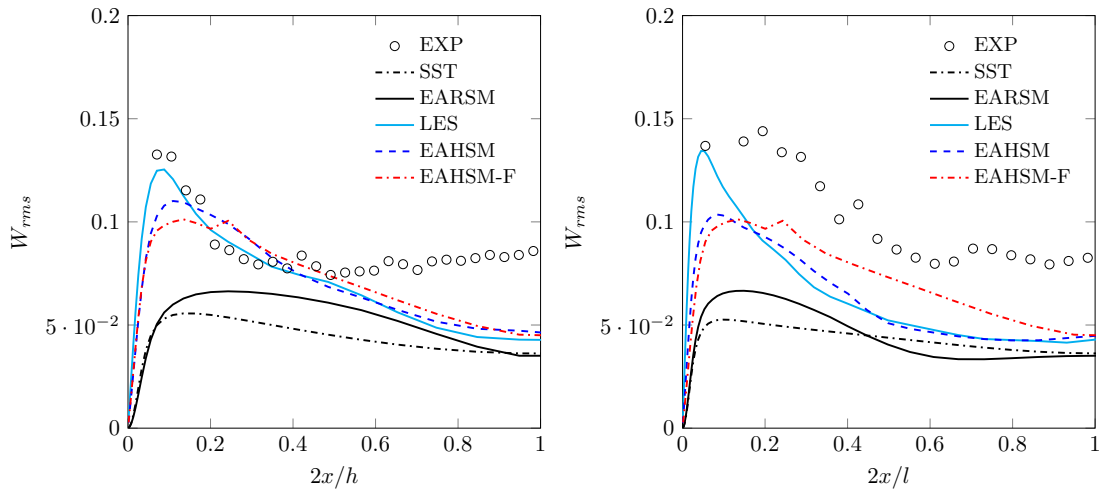


Figure 4.7. – Rectangular duct flow: mean streamwise rms velocity along the vertical (left) and horizontal (right) cut planes at the center of the duct

to avoid possible interactions between boundary conditions and the computed flow within the enclosure. The mesh of the rectangular duct corresponds to the mesh used for the previous precursor simulations, except in the streamwise z -direction for which the mesh is refined in the vicinity of the enclosure, leading to a mesh size Δz ranging from 0.025 to 0.0025 m. The structured mesh of the enclosure follows similar transformations as used in the precursor simulation and results in 3.25 million hexahedral cells. In addition, in order to have reference results and to investigate the influence of the resolution level, a finer mesh is also employed for LES composed of 26 million hexahedral cells.

The computations carried out using the open-source CFD solver library CALIF³S use different strategies for the discretization of the convective terms for the Navier-Stokes equations depending on whether RANS or scale-resolving methods are employed. The numerical schemes summarized in Table 4.3 corresponds to a centered second-order spatial discretization of both convective and diffusive fluxes together with the semi-implicit Crank-Nicolson time scheme for scale-resolving methods whereas a hybrid spatial discretization together with the Euler BDF1 time scheme for RANS methods.

The initial conditions correspond to air at rest within the enclosure. The inlet boundary conditions for RANS simulations are obtained from the previous precursor simulations using stored values at the plane $z = z_0$. The same process is adopted for LES simulations except that the resolved velocity has been stored during 2 convective times $T_{c,d} = 2\pi l / W_b$ at the end of the precursor simulation. In this case, this results in periodic time-dependent boundary conditions with $2T_{c,d}$ being the signal period. Regarding hybrid RANS/LES simulations, three different approaches to introduce turbulent fluctuations are investigated:

- i) The first one consists in using the same recycling method as used for LES simu-

4. Evaluation of E-DES with forcing for flows in ventilated room – 4.2. Numerical simulations of the air transfer jet

Case	Number of cells ($\times 10^6$)	Δt ($\times 10^{-2}$ s)	NS convective scheme
SST	3.25	1	hybrid
EARSM	3.25	1	hybrid
LES	26	0.2	centered
EAHSM	3.25	0.2	centered
EAHSM-F	3.25	0.2	centered
EAHSM-FZ	3.25	0.2	centered

Table 4.3. – Air transfer jet simulation parameters

- lations and thus introduces fluctuations through inlet boundary conditions.
- ii) The second approach uses also the recycling method but only for the mean velocity and subfilter quantities from an EARSM precursor simulation. The generation of fluctuations is then managed using the synthetic forcing methodology in the whole computational domain.
 - iii) Finally, the last approach is similar to the second one but enforces the RANS mode in a restricted region of the computational domain near the supply vent. In this case, the generation of fluctuations through synthetic forcing is carried out downstream air supply mimicking in this way a hybrid RANS/LES zonal approach. Here, the zonal approach is imitated by enforcing the RANS mode $r_k = 1$ in the near field region of air supply corresponding to $z \leq 0.2$ m which is the delimitation between reduced and large PIV planes. It has to be noticed that this location has been selected arbitrarily on the basis of available PIV plane measurements rather than on physical arguments.

The steady flow is computed during a physical time of 80s which corresponds roughly to 25 convective times T_0 with $T_0 = L/W_b$. The flow is established during a first transient period of $5T_0$ and then time averaging is performed during $20T_0$ to compute statistics for LES and hybrid simulations. The PIV measurements provide the mean and rms values for the streamwise velocity component in both vertical and horizontal planes downstream to the supply vent at distances $z = 0.03, 0.05, 0.15, 0.2, 0.3, 0.4, 0.5$ and 0.6 m. The PIV measurements performed at the first four locations use an interrogation window of 0.25×0.25 m² while the more distant locations use a larger window of 0.95×0.25 m².

In order to get an overview of the qualitative behavior of RANS, LES and hybrid approaches, Fig. 4.9 and 4.10 address first the dimensionless mean and rms for the streamwise velocity component in the vertical cut plane passing through the middle of the vents $x = 0.85$ m. The velocities are made dimensionless using the bulk velocity in the upstream duct. The turbulent jet coming from the rectangular slot exhibits three main regions: (i) the potential core region into which the turbulent mixing spreads from the edges to the core of the jet, (ii) the region of jet development into which the velocity decay closely looks like a free round jet and (iii) the impingement region into which both the mean and rms streamwise velocities decay rapidly to zero at the wall.

4. Evaluation of E-DES with forcing for flows in ventilated room – 4.2. Numerical simulations of the air transfer jet

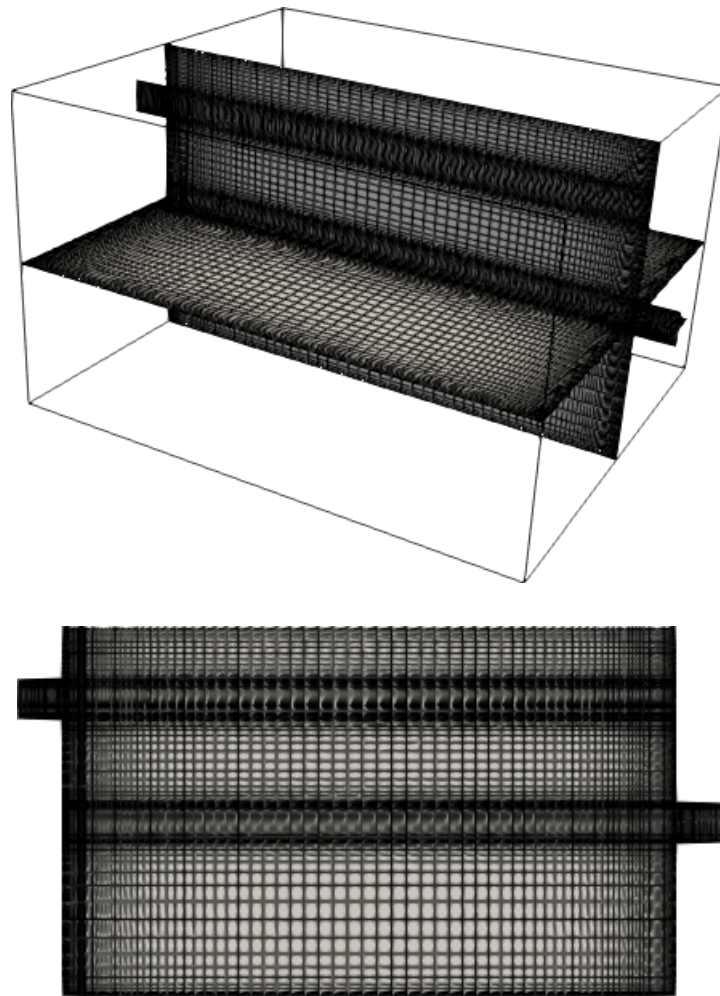


Figure 4.8. – Perspective view of vertical and horizontal cut planes (top) and side view of the vertical cut plane (bottom) of the meshing composed of 3.415 million hexahedral cells

Further downstream, the jet becomes wall-parallel causing back flows that possibly interact with the jet itself. The three main regions may be roughly delimited from the usual estimates $z \approx 2.5D_e$ (Quinn 1992) for the potential core length, where D_e is the equivalent diameter having the same area as a round jet, and $z \approx 0.86L$ (Beltaos and Rajaratnam 1974). These estimates lead respectively to the values $z \approx 0.45$ m and $z \approx 1.72$ m. RANS, LES and hybrid simulations globally predict the same qualitative flow behavior. However, differences appear regarding the spreading rate and the direction of the jet together with the magnitude of the back flow that appears at the bottom of the facility. These differences will be examined in more detail through the profiles in the vertical and horizontal planes. It has also to be noticed that turbulence intensity in the impinging near wall region is strongly overestimated by RANS models compared with either LES or hybrid approaches. This well-known behavior of RANS

4. Evaluation of E-DES with forcing for flows in ventilated room – 4.2. Numerical simulations of the air transfer jet

models refers to the stagnation point anomaly (Durbin 1996) and has probably an impact on the back flow.

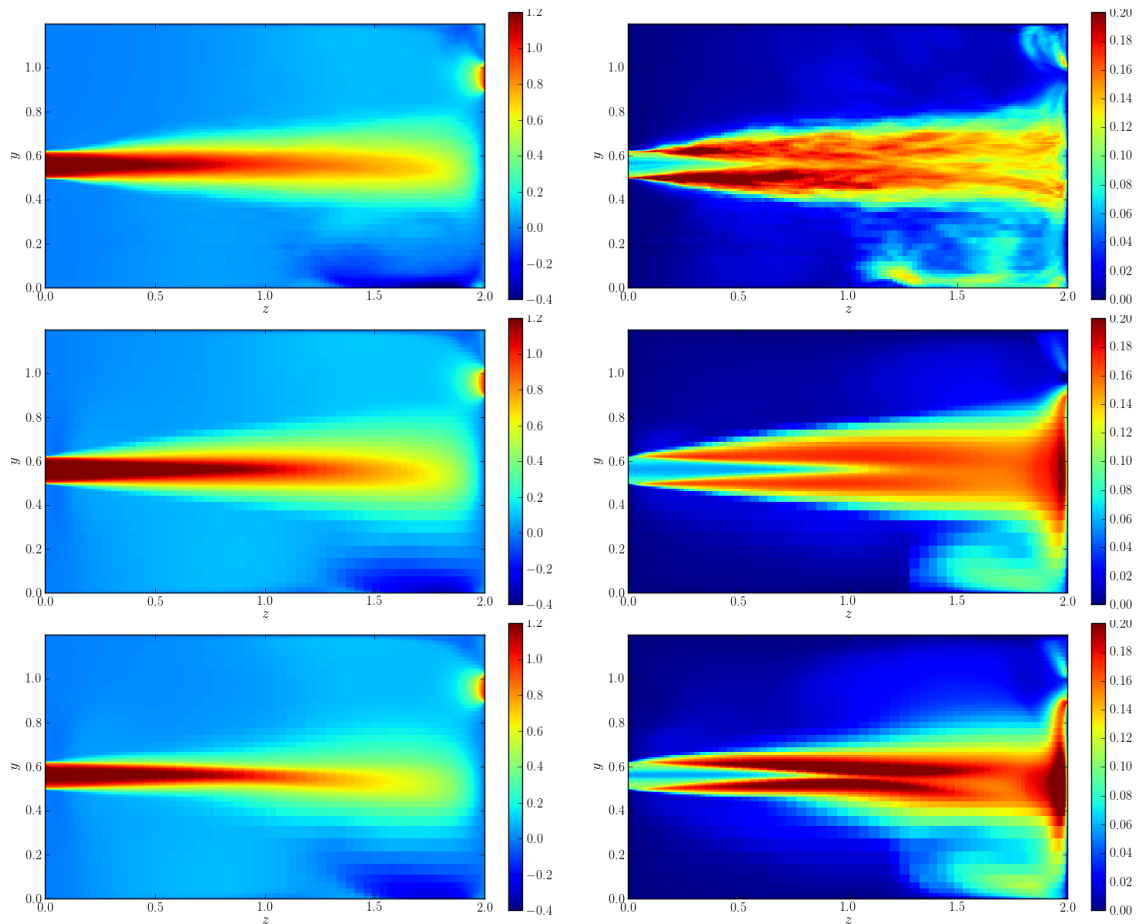


Figure 4.9. – Vertical cut plane passing through the middle of the vents $x = 0.85$ of the dimensionless mean (left) and rms (right) streamwise velocities for LES, SST, and EARSIM (from top to bottom) models.

Before moving to a quantitative comparison of model predictions, Tab. 4.4 first gives some details regarding the mean CPU time required to perform one time step. The CPU times corresponding to hybrid simulations with forcing remain indicative as reducing the cost of the forcing method did not give rise to a dedicated work. These times are given for EAHSM, EAHSM-F and EAHSM-FZ simulations that use the same mesh and the same time step. In addition, CPU time for LES using the same mesh, referred as LES-coarse³, is also reported for comparison. CPU times for RANS calculations (SST, EARSIM) are also displayed but should not be directly compared with CPU times for hybrid and LES simulations as they did not use the same time step and

3. LES results on the same coarse mesh as used for hybrid and RANS simulations are not shown in order to simplify the figures. The results are nearly identical to EAHSM predictions

4. Evaluation of E-DES with forcing for flows in ventilated room – 4.2. Numerical simulations of the air transfer jet

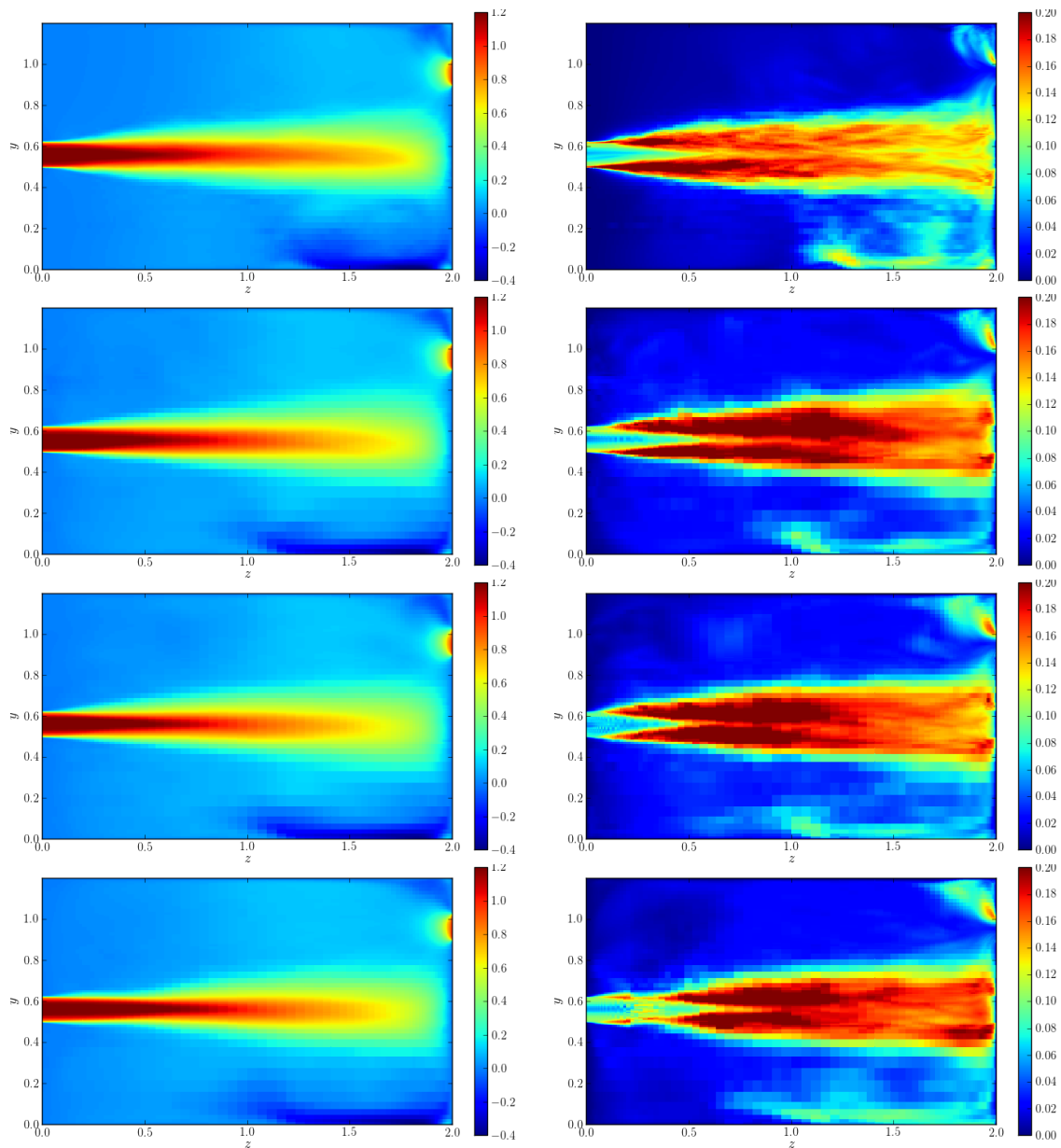


Figure 4.10. – Vertical cut plane passing through the middle of the vents $x = 0.85$ of the dimensionless mean (left) and rms (right) streamwise velocities for LES, EAHSM, EAHSM-F and EAHSM-FZ (from top to bottom) models.

mesh distribution. In Tab. 4.4, a partition of this CPU time is also reported among the Navier-Stokes (NS) equations and the turbulence model (dynamic procedure for LES, subfilter transport equations, ...). As can be shown, LES is the one with the lowest CPU time thanks to the low computation cost of the dynamic filtering procedure. The EAHSM CPU time is 36% higher than the one of the LES simulation. This increase is mainly caused by the additional subfilter equations that have to be solved. Focusing

4. Evaluation of E-DES with forcing for flows in ventilated room – 4.2. Numerical simulations of the air transfer jet

now on hybrid simulations with forcing, the zonal-like simulation exhibits shorter CPU time compared with the full continuous EAHSM-F simulation. This was expected as the forcing is activated in a smaller region in the zonal-like case. However, in both cases, forcing introduces an additional cost of at least 40% compared with EAHSM. This additional cost is directly related to the building of the synthetic velocity which is carried out nearly everywhere, independently of the required synthetic level meaning that the geometric criterion (related to κ_{min}) derived for the planar jet case to avoid forcing these low energy regions seems to not be effective here.

CPU (s)	Total	NS	Other
SST	13.03	10.10	2.34
EARSM	13.22	10.74	1.62
LES-coarse	2.09	1.73	0.22
EAHSM	2.85	1.91	0.60
EAHSM-F	4.16	2.03	1.58
EAHSM-FZ	3.99	1.88	1.55

Table 4.4. – Cost of the calculations for RANS, LES-coarse and hybrid simulations on the same mesh employing 3.25 million cells. The time step and the mesh distribution corresponds respectively to 0.002 s and 200 cores for LES and hybrid simulations whereas, for RANS simulations, these correspond to 0.02 s and 36 cores.

Moving to the comparisons with PIV measurements, the mean and rms streamwise velocity profiles in the vertical and horizontal planes shown respectively in Fig. 4.11-4.12 and 4.14-4.15 are fairly well predicted by the simulations despite small discrepancies observed in precursor simulations. Here again, it is worth noting that the results displayed for hybrid simulations take into account both the resolved and the sub-filter parts while LES results are restricted to the resolved part as the sub-filter contribution remains difficult to evaluate⁴. As previously observed in precursor simulations, the rms streamwise velocity is underpredicted by RANS models while both LES and hybrid approaches predict more accurately the level of streamwise turbulent intensity. Nevertheless, this seems to have a limited impact on the jet spreading, except for the EARSM model which clearly underestimates it. This contrasts with the good model performances in the previous flow cases within duct geometries and calls for further studies regarding the model calibration in such flow configurations.

Regarding hybrid simulations, the mean and rms streamwise velocity profiles are relatively close to those obtained from LES on a finer grid and, as already observed, numerical predictions from EAHSM without forcing and EAHSM-F employing forcing in the whole domain are nearly identical. On the other hand, the numerical predictions

4. Its is however assumed negligible.

4. Evaluation of E-DES with forcing for flows in ventilated room – 4.3. Conclusion

obtained from EAHSM-FZ based on a synthetic forcing mimicking a zonal approach with a sharp transition located at $z = 0.2\text{m}$ behave between EARSM and EAHSM predictions. As a result, the EAHSM-FZ model predictions are degraded compared with EAHSM or EAHSM-F predictions, highlighting again the need of a predictive underlying RANS model near transition regions. However, while Fig. 4.12 shows that the rms streamwise velocity profiles remain fairly well predicted near the transition region, this is obtained with completely different energy partition levels as shown in Fig. 4.13. This illustrates the validity and the potentialities of the proposed approach as the transition between the RANS mode and the scale-resolving mode remains smooth, and behaves properly regarding turbulence intensity levels. It has to be noticed that, owing to the back flows and to turbulence triggering, slight resolved fluctuations appear upstream to the location of RANS/LES transition but these remain much lower than the modeled subfilter stresses.

While the previous comparisons were restricted to the PIV plane locations, Fig. 4.16 show similar profiles in both the vertical and horizontal planes but at different locations in order to cover the overall mean flow as previously shown in Figs. 4.9-4.10. It is observed that far downstream from the zonal-like transition location, scale-resolving model predictions, including the EAHSM-FZ model predictions, are indistinguishable from each other. This is observed for both jet spreading and back flow, the latter remaining difficult to predict correctly using RANS approaches, probably owing to the excessive production of turbulence intensity in the impinging region. In the same way, the statistical average of the kinetic energy ratio in the vertical plane shown in Fig. 4.17 corresponding to the EAHSM, EAHSM-F and EAHSM-FZ model predictions are almost identical far enough downstream from air supply, illustrating the ability of the proposed approach to deal with different RANS/LES transition strategies. It is interesting to notice from Fig. 4.16 that in the spanwise horizontal cut plane, contrary to the vertical cut plane, EARSM numerical predictions are in a better agreement with LES or hybrid simulation results compared with SST predictions. However, the slight saddle-shaped mean streamwise velocity obtained using EARSM is much less pronounced or absent from LES or hybrid numerical predictions. This seems to be in accordance with experimental results that report such a saddle-shaped but for higher slot aspect ratio Quinn 1992.

4.3. Conclusion

The main objective of this chapter was to assess the validity and the predictive capabilities of the hybrid approach with synthetic forcing in a realistic situation that corresponds to a ventilated room for which experimental measurements are available at IRSN. While it remains difficult in the studied low-Reynolds number case to put forward the interest of using hybrid approaches, the simulation results clearly demonstrate the validity and the potentialities of the proposed approach. However, it has to be noticed that a strategy to avoid forcing regions with residual synthetic kinetic

4. Evaluation of E-DES with forcing for flows in ventilated room – 4.3. Conclusion

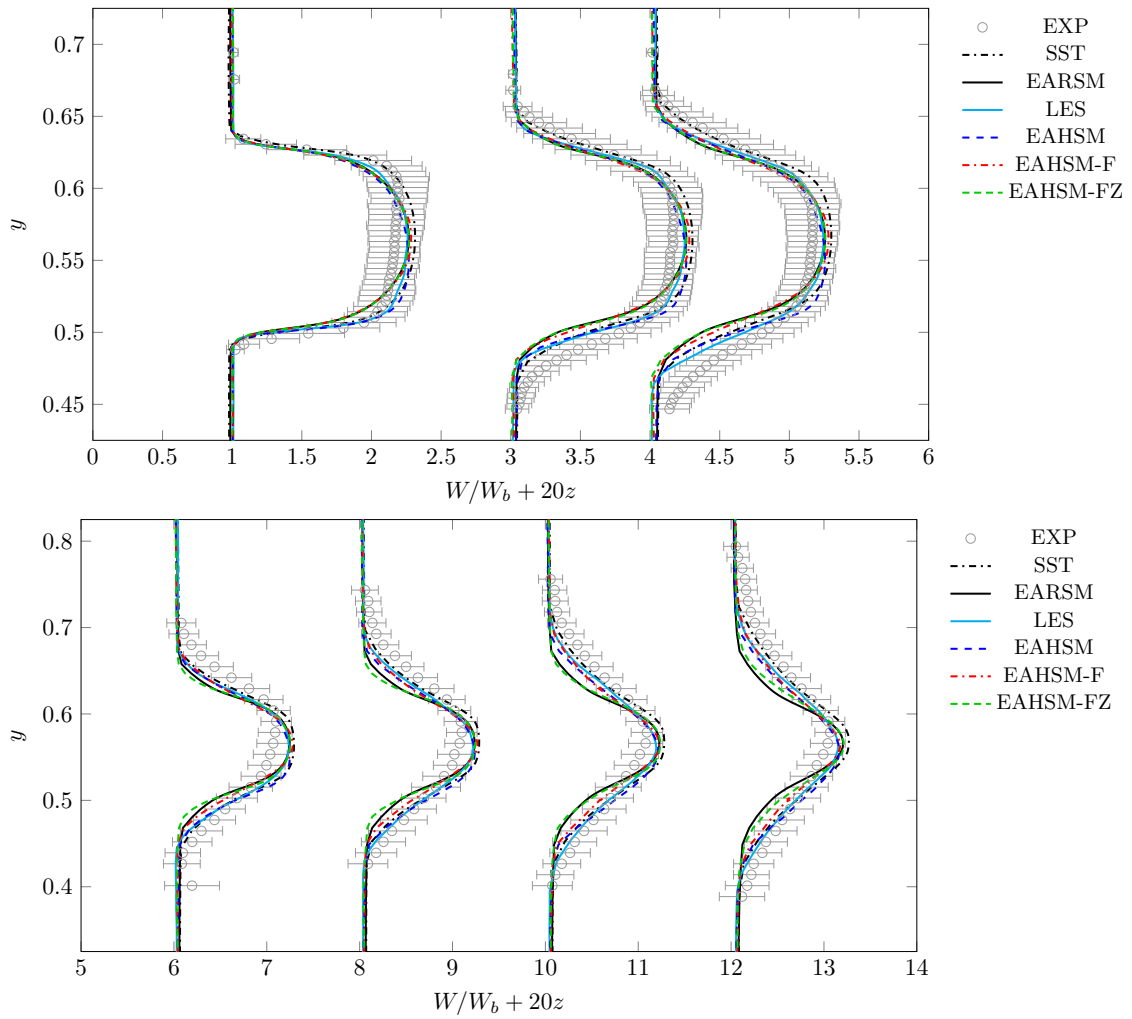


Figure 4.11. – Mean streamwise velocity profiles in the vertical plane at $z = 0.05, 0.15$ and 0.2 m (top) and $z = 0.3, 0.4, 0.5$ and 0.6 m (bottom)

energy, and thus to reduce its cost, remains to be implemented. The overall mean flow is correctly predicted by comparing with LES predictions on a finer grid and the comparisons with experimental measurements show that the proposed adaptive forcing ensures a continuous transition between RANS and LES behaviors in the framework of a zonal-like approach. The results obtained when enforcing the RANS mode in the near wall region or when using a zonal-like approach in the near-field region of jet development, emphasize the need of a reliable underlying RANS model.

4. Evaluation of E-DES with forcing for flows in ventilated room – 4.3. Conclusion

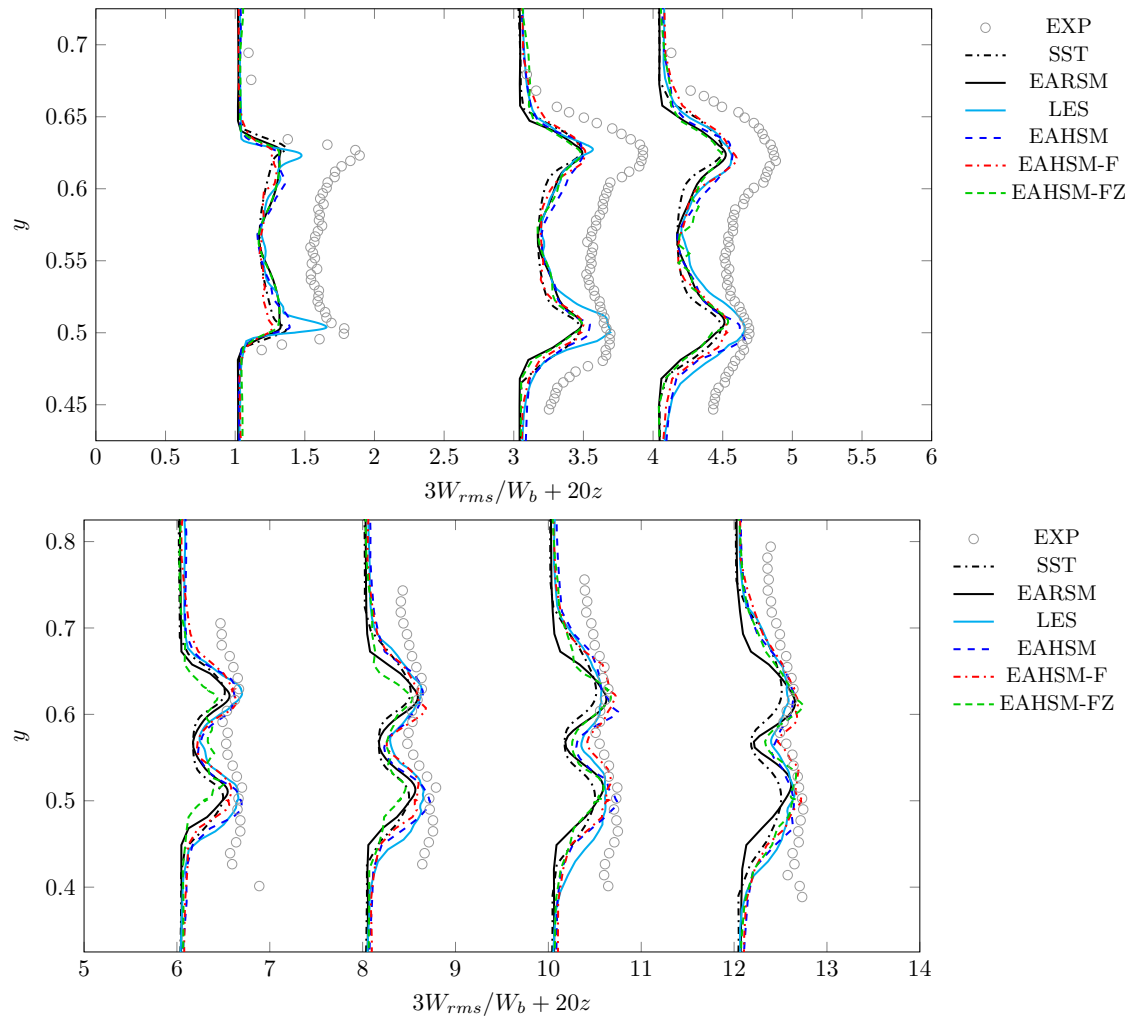


Figure 4.12. – Rms velocity profiles in the vertical plane at $z = 0.05, 0.15$ and 0.2 m (top) and $z = 0.3, 0.4, 0.5$ and 0.6 m (bottom)

4. Evaluation of E-DES with forcing for flows in ventilated room – 4.3. Conclusion

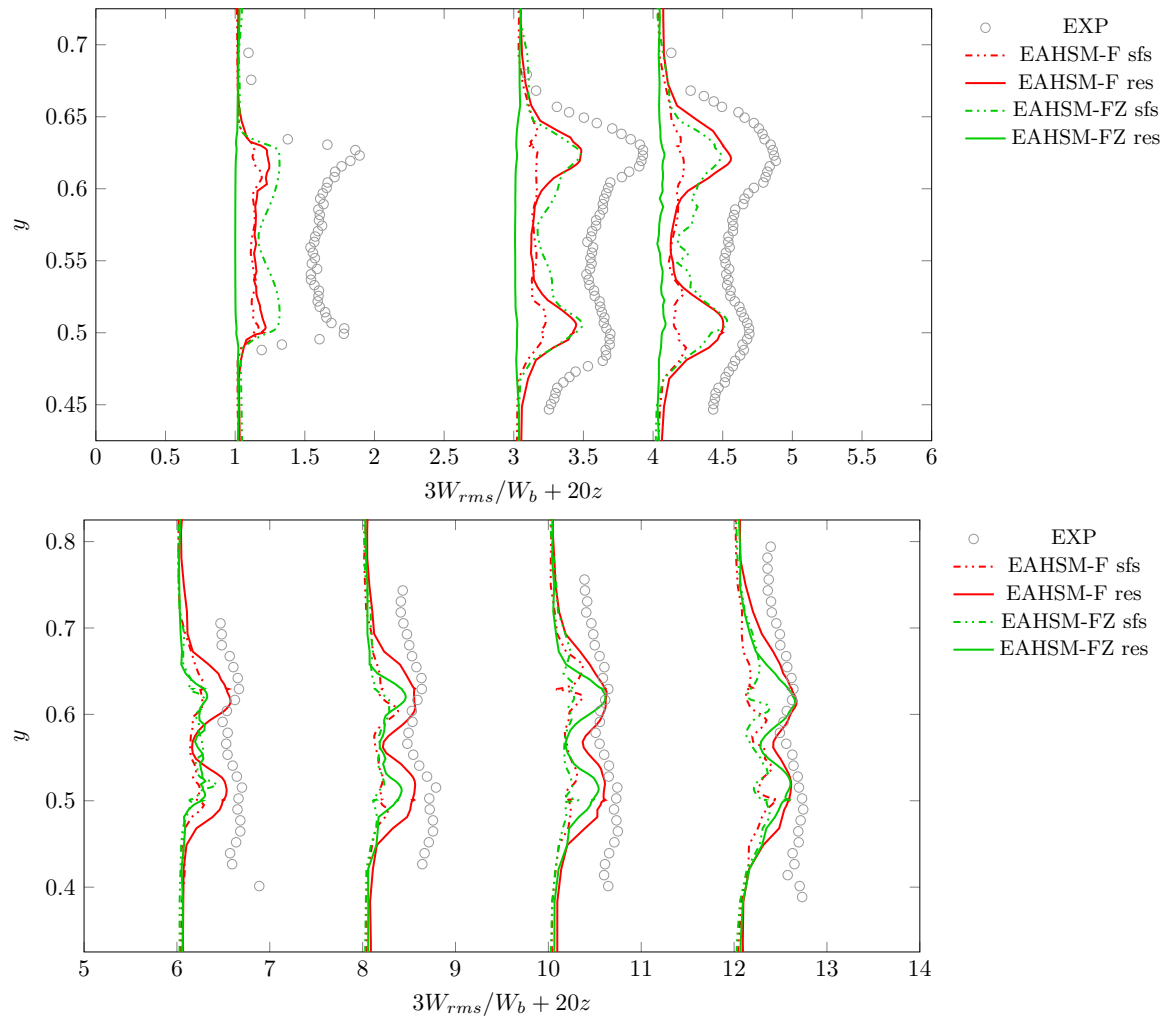


Figure 4.13. – Rms velocity profiles in the vertical plane at $z = 0.05, 0.15$ and 0.2 m (top) and $z = 0.3, 0.4, 0.5$ and 0.6 m (bottom)

4. Evaluation of E-DES with forcing for flows in ventilated room – 4.3. Conclusion

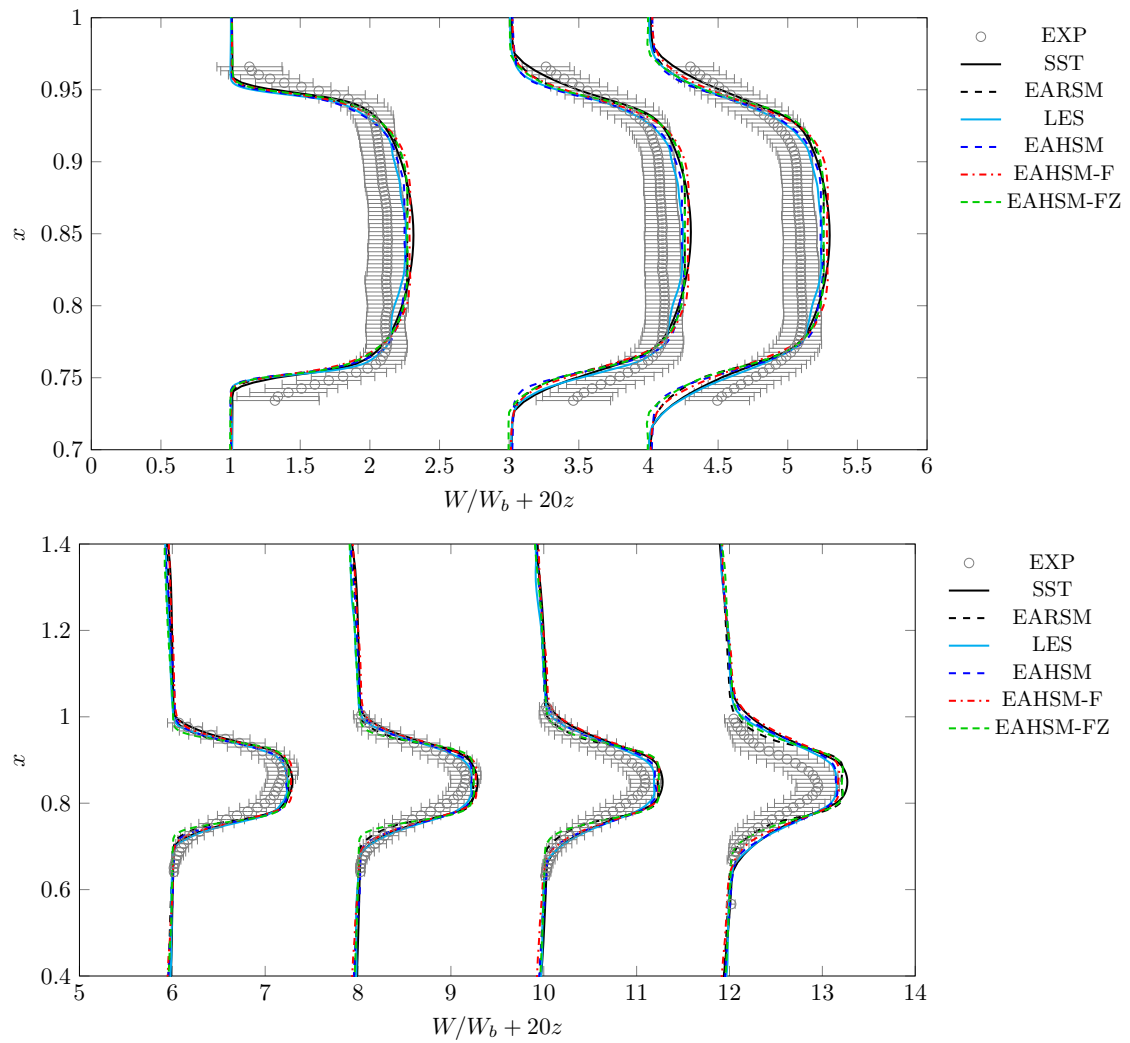


Figure 4.14. – Mean streamwise velocity profiles in the horizontal plane at $z = 0.05$, 0.15 and 0.2 m (top) and $z = 0.3$, 0.4 , 0.5 and 0.6 m (bottom)

4. Evaluation of E-DES with forcing for flows in ventilated room – 4.3. Conclusion

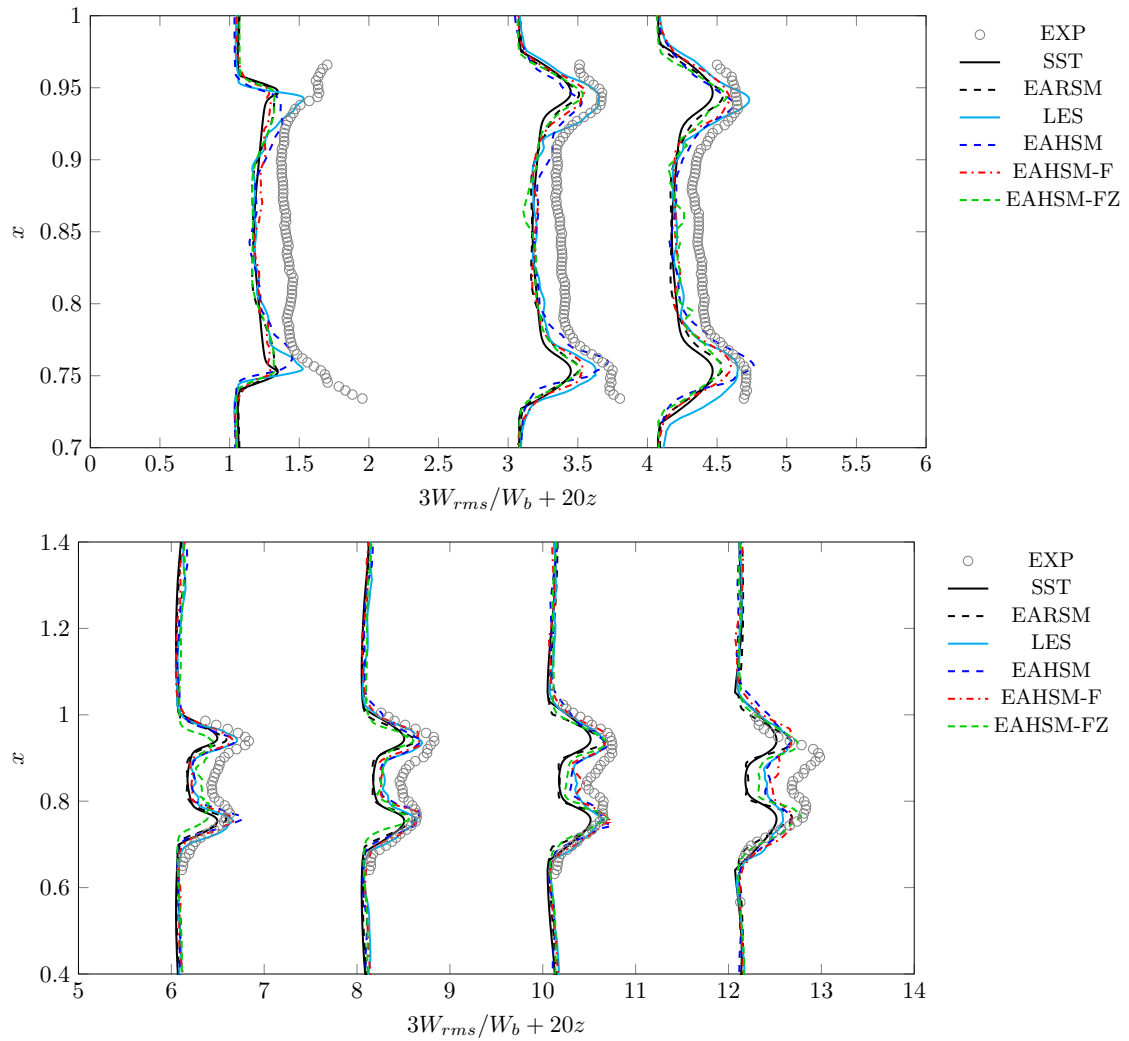


Figure 4.15. – Rms velocity profiles in the horizontal plane at $z = 0.05, 0.15$ and 0.2 m (top) and $z = 0.3, 0.4, 0.5$ and 0.6 m (bottom)

4. Evaluation of E-DES with forcing for flows in ventilated room – 4.3. Conclusion

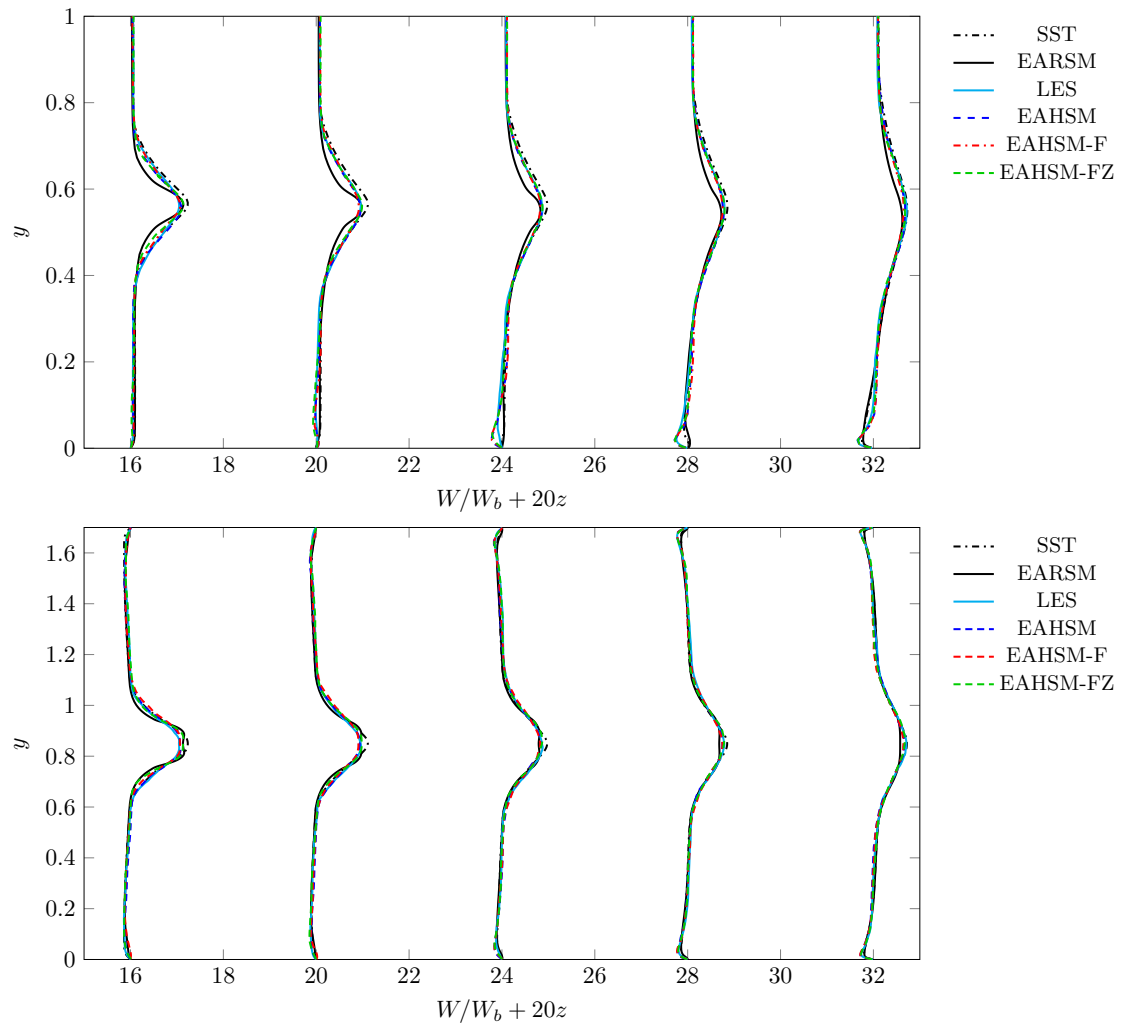


Figure 4.16. – Mean streamwise velocity profiles in the vertical (top) and horizontal (bottom) plane at $z = 0.8, 1, 1.2, 1.4$ and 1.6 m

4. Evaluation of E-DES with forcing for flows in ventilated room – 4.3. Conclusion

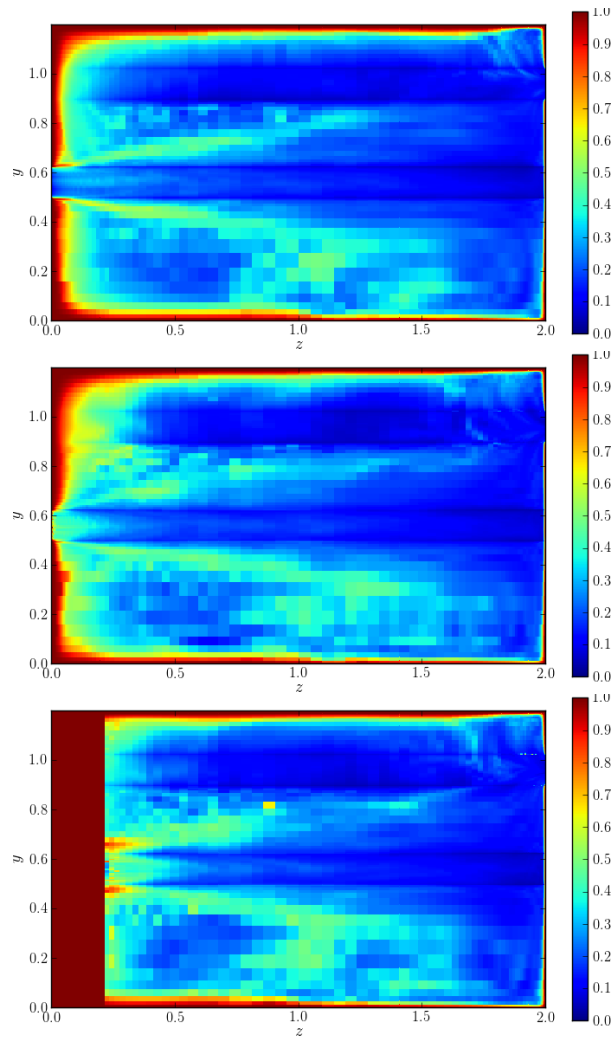


Figure 4.17. – Statistical (temporal) average of the energy ratio in the vertical plane corresponding to EAHSM (top) EAHSM-F (middle) and EAHSM-FZ (bottom) model predictions

Conclusions and perspectives

Conclusions This thesis work focused on the development and implementation of a forcing method based on resolved-scale enrichment for hybrid RANS/LES simulations. This study's methodology was organized around three main axes.

First, the method was developed and assessed in the framework of sustaining fluctuations for Homogeneous Isotropic Turbulence (HIT). In the frame of HIT, the proposed forcing method reads formally as the usual linear forcing method of Lundgren. However, the proposed approach is based on a reconstruction procedure for the resolved fluctuations and as a result, the resolved velocity of the usual linear forcing term is substituted here by a synthetic velocity. There are two downsides to the Lundgren's approach: a constrained resulting integral length scale and strong oscillations on the turbulent kinetic energy temporal evolution. Since the development of Lundgren's forcing, several methods have been proposed to address these two drawbacks. In this work, the proposed forcing method has shown to be a good alternative to overcome Lundgren's method limitations. An efficient method to control the turbulent kinetic energy, mimicking spectral forcing methods, has been developed. With this control method, forcing at low or high wavenumbers is achievable. Finally, Cholesky decomposition restores anisotropic turbulence, though it does not comply with the imposed value.

After demonstrating that the reconstruction-like method could sustain HIT and recover good statistical features, the method has been assessed to balance turbulent kinetic energy between the resolved and subgrid parts. The idea was to start from a RANS simulation, *i.e.* the kinetic energy ratio is equal to one, and to evaluate the capability of the forcing to drive the solution towards the desired unsteady state. This test was performed under the context of decaying HIT. By assuming conservation of the total turbulent kinetic energy, the subgrid forcing term was recovered. The kinetic energy ratio is a key point to this method since it allows to determine the targeted resolved turbulent kinetic energy.

In a second stage, the reconstruction-like approach has been extended to non-homogeneous turbulence. The forcing was assessed on the planar jet test case. The following steps were undertaken in order to pay attention to the many adjustments linked to the non-homogeneous turbulence framework. The synthetic velocity was first temporally updated to assess its capability to reproduce statistical quantities. The targeted statistical properties came from a RANS precursor simulation. The need of space-independent frequency was highlighted. In non-homogeneous turbulence, the synthetic velocity loses the divergence-free property. However, results remain satisfac-

tory despite the synthetic velocity not being divergence-free. As a result, no further effort has been put to guarantee a divergence-free synthetic velocity. Additionally, based on arguments proposed by Lundgren, the convective term that is responsible of turbulent production, has been enriched. Therefore, for this case, two forcing terms were considered. The new forcing term has the particularity of being non-zero in average, and thus has a potential effect on the mean flow. No strong negative effects were noticed and therefore the choice has been made not to take into account the mean part of the forcing terms. The forcing was then tested on zonal configurations of the planar jet. The RANS mode was enforced over a length of six, eleven and thirty jet nozzle diameters. These locations have been chosen to have transition region respectively at the end of the potential core, at the beginning of the self-similar region and right in the self-similar region. The reconstruction-like approach allowed a fast transition with a clear increase of the resolved turbulent kinetic energy. For the two first zonal cases ($x_T = 6d_j$ and $x_T = 11d_j$) the solutions tend towards the reference case (turbulent inlet condition) while this was not observed in the third case. Finally, the method was assessed to quantify its contribution in the framework of very large eddy simulation. The number of meshes in the reference mesh has been divided by eight and by twenty. It appears that forcing does not bring any improvement compared to turbulent inflow conditions.

Finally, the proposed forcing method has been assessed on a configuration of the CARDAMOMETTE program that corresponds to air flow within a ventilated room for which experimental measurements are available at IRSN. In order to provide air supply inlet conditions, preliminary calculations in duct geometries have also been carried out. These precursor simulations show that enforcing the RANS mode in the near-wall region through the use of elliptic blending to evaluate the energy ratio emphasizes the need of a reliable underlying RANS model in this region. In particular, the use of forcing leaves unchanged the behavior of the transition region where the kinetic energy ratio experiences large variations. Moving to the air transfer jet simulations, the overall mean flow is well predicted by applying the forcing to the whole computational domain or by restricting it downstream to air supply mimicking a zonal RANS/LES approach. Here again, this demonstrates the validity and the potentialities of the proposed approach.

Perspectives The developments conducted in this work provide a wide range of opportunities for further research. One way for improving results would consist in introducing a synthetic velocity that better replicates the turbulence of the considered flow. For instance, one could use a synthetic velocity that better represents anisotropy effects. In this context, it could be interesting to adopt a more general formulation in the Craya-Hearing reference frame as followed in Cambon, F. S. Godefert, and Favier 2012; Favier 2009 to build the synthetic velocity. On the other hand, it could also be interesting to measure and to remove artificial helicity introduced through the

proposed forcing following for instance similar arguments proposed in Alvelius 1999. Finally, enhancing the synthetic velocity through learning based methods could also be interesting to link the forcing characteristics to a particular flow situation (near-wall flow, jet, ...).

Regarding the reconstruction-like method, even though there was no apparent detrimental effects on the simulations, it could be worthwhile to take into account the average force term in the equations of motion. The forcing method has shown limitations for strong kinetic energy ratio gradients. As proposed by Zhang 2021, the reconstruction of the four convective-like terms in the filtered momentum equations, might improve results in the near wall region (*i.e.*, where strong gradients of the kinetic energy ratio occur). In these near-wall regions, it would be interesting to consider progress made by Duffal 2020. Additionally, the self-adaptivity of the forcing allows to operate only on regions of interest, which is crucial for reducing the computational cost of the method. However, the employed criterion (comparison of length scales) may not be the most suitable. This issue deserves further investigation to establish less case-dependant criterion. Furthermore, the forcing strongly relies on the energy ratio and the sub-filter quantities, which demand good estimations of these quantities for the forcing to be effective and accurate. The more accurate the RANS model, the better the forcing will perform. For instance, it could be beneficial to use an explicit algebraic Reynolds-stress model based on Elliptic blending that would improve the prediction of near-wall turbulence.

In the framework of the studies conducted on the CARDAMOMETTE configuration, simulation of the release of helium in the room will be the next step. In such a case, the proposed strategy offers the possibility to compute the near-field of helium release using a RANS mode and then the far-field where buoyancy effect becomes significant using a scale-resolving mode. The proposed forcing approach would ensure a smooth transition. In the framework of buoyancy-generated turbulence, the forcing could also be of great interest. Typically, the situation of interest consists in a buoyant turbulent plume with zero streamwise mean velocity. In this case, buoyancy is the only mechanism generating fluctuations and it could be interesting to extend the proposed resolved-scale velocity enrichment to a resolved-scale scalar (temperature or composition) enrichment approach.

Bibliography

- [Alv99] K. Alvelius. “Random forcing of three-dimensional homogeneous turbulence”. In: *Physics of Fluids* 11.7 (1999), pp. 1880–1889 (cit. on pp. [50](#), [51](#), [141](#)).
- [Arm+19] J. M. Armengol, R. Vicquelin, A. Coussement, et al. “Scaling of heated plane jets with moderate radiative heat transfer in coupled DNS”. In: *Int. J. Heat and Mass Transfer* 139 (2019), pp. 456–474 (cit. on pp. [92](#), [95](#)).
- [AC82] B. Aupoix and J. Cousteix. “Modèles simples de tensions de sous-maille en turbulence homogène isotrope (in french)”. In: *Rech. Aéro.* 4 (1982), pp. 273–283 (cit. on pp. [39](#), [40](#)).
- [BJ99] C. Bailly and D. Juvé. “A stochastic approach to compute subsonic noise using linearized Euler’s equations”. In: *5th AIAA/CEAS Aeroacoustics Conference, AIAA Paper* (1999), pp. 99–1872 (cit. on p. [89](#)).
- [BLC95] C. Bailly, P. Lafon, and S. Candel. “A stochastic approach to compute noise generation and radiation of free turbulent flows”. In: *AIAA Paper* (1995), pp. 95–092 (cit. on pp. [54](#), [59](#)).
- [Ban+07] S. Banerjee, R. Krahl, F. Durst, et al. “Presentation of anisotropy properties of turbulence, invariants versus eigenvalue approaches”. In: *J. Turbul.* 8 (2007), pp. 1–27 (cit. on p. [75](#)).
- [Bas+16] M. Bassenne, J. Urzay, G.I. Park, et al. “Constant-energetics physical-space forcing methods for improved convergence to homogeneous-isotropic turbulence with application to particle-laden flows”. In: *Phys. Fluids* 28 (2016), p. 035114 (cit. on pp. [52](#), [54](#), [56](#), [65](#)).
- [BGC04] P. Batten, U. Golberg, and S. Chakravarthy. “Interfacing statistical turbulence closures with large-eddy simulation”. In: *AIAA J.* 42 (2004), pp. 485–492 (cit. on pp. [41](#), [96](#)).
- [BBL94] W. Béchara, C. Bailly, and P. Lafon. “Stochastic approach to noise modeling for free turbulent flows.” In: *AIAA Journal* 32(3) (1994), pp. 281–318 (cit. on p. [58](#)).
- [BR74] S. Beltaos and N. Rajaratnam. “Impinging circular turbulent jets”. In: *Journal of the hydraulics division* 100.10 (1974), pp. 1313–1328 (cit. on p. [127](#)).

- [BMB15] A. Bentaib, N. Meynet, and A. Bleyer. “Overview on hydrogen risk research and development activities: methodology and open issues”. In: *Nuclear Engineering and Technology* 47.1 (2015), pp. 26–32 (cit. on p. 24).
- [Bis+17] M. Bisoi, M. K. Das, S. Roy, et al. “Large eddy simulation of three-dimensional plane turbulent free jet flow”. In: *European J. of Mechanics B/Fluids* 65 (2017), pp. 423–439 (cit. on pp. 92, 95).
- [Boy+14] F. Boyer, F. Dardalhon, C. Lapuerta, et al. “Stability of a Crank-Nicolson pressure correction scheme based on staggered discretizations”. In: *International Journal for Numerical Methods in Fluids* 74 (2014), pp. 34–58 (cit. on p. 48).
- [BBM06] M. Breuer, H. T. Baytekin, and E. A. Matida. “Prediction of aerosol deposition in 90° bends using LES and an efficient Lagrangian tracking method”. In: *Journal of Aerosol Science* 37 (2006), pp. 1407–1428 (cit. on p. 23).
- [CGF12] C. Cambon, F. S. Godeferd, and B. Favier. “Incorporating linear dynamics and strong anisotropy in KS. application to diffusion in rotating, stratified, MHD turbulence, and to aeroacoustics”. In: *New Approaches in Modeling Multiphase Flows and Dispersion in Turbulence, Fractal Methods and Synthetic Turbulence* 24 (2012), (ERCOFTAC Series 18), ISBN 978-94-007-2505-8 (cit. on p. 140).
- [CGM95] D. Carati, S. Ghosal, and P. Moin. “On the representation of backscatter in dynamic localization models”. In: *Phys. Fluids* 7 (1995), p. 606 (cit. on p. 51).
- [CB13] P.L. Carroll and G. Blanquart. “A proposed modification to Lundgren’s physical space velocity forcing method for isotropic turbulence”. In: *Phys. Fluids* 25 (2013), p. 105114 (cit. on pp. 52, 54, 55, 65).
- [Cas+20] E. Cascioli, S. Buckingham, S. Keijers, et al. “Numerical and experimental analysis of a planar jet with heated co-flow at medium and low Prandtl-number values”. In: *Nuclear Engineering and Design* 361 (2020), p. 110570 (cit. on p. 92).
- [CM00] V. K. Chakravarthy and S. Menon. “Subgrid Modeling of Turbulent Premixed Flames in the Flamelet Regime”. In: *Flow, Turbulence and Combustion* 65 (2000), pp. 133–161 (cit. on p. 40).
- [Cha17] B. Chaouat. “The State of the Art of Hybrid RANS/LES Modeling for the Simulation of Turbulent Flows”. In: *Flow Turb. Combust.* 99 (2017), pp. 279–327 (cit. on pp. 41, 43).
- [CS05] B. Chaouat and R. Schiestel. “A new partially integrated transport model for subgrid-scale stresses and dissipation rate for turbulent developing flows”. In: *Phys. Fluids* 17 (2005), p. 065106 (cit. on p. 43).

- [CS07] B. Chaouat and R. Schiestel. “From single-scale turbulence models to multiple-scale and subgrid-scale models by Fourier transform”. In: *Theor. Comput. Fluid Dyn.* 21 (2007), pp. 201–229 (cit. on pp. 43, 44).
- [CS09] B. Chaouat and R. Schiestel. “Progress in subgrid-scale transport modelling for continuous hybrid non-zonal RANS/LES simulations”. In: *Int. J. Heat Fluid Flow* 30 (2009), pp. 602–616 (cit. on p. 27).
- [Cha91] J. R. Chasnov. “Simulation of the Kolmogorov inertial subrange using an improved subgrid model”. In: *Phys. Fluids* 3 (1991), p. 188 (cit. on p. 50).
- [CS88] S. Chen and X. Shan. “High-resolution turbulent simulations in direct numerical simulations of turbulence”. In: *Comput. Fluids* 16 (1988), p. 257 (cit. on p. 51).
- [CL01] K. Choi and J. Lumley. “The return to isotropy of homogeneous turbulence”. In: *J. Fluid Mech.* 436 (2001), pp. 59–84 (cit. on p. 75).
- [CC71] G. Comte-Bellot and S. Corrsin. “Simple eulerian time correlation of full- and narrow-band velocity signals in grid-generated "isotropic" turbulence”. In: *Journal of Fluid Mechanics* 48(2) (1971), pp. 273–337 (cit. on p. 81).
- [DB06] L. Davidson and M. Billson. “Hybrid LES-RANS using synthesized turbulent fluctuations for forcing in the interface region”. In: *Int. J. Heat Fluid Flow* 27 (2006), pp. 1028–1042 (cit. on p. 91).
- [DP03] L. Davidson and S. H. Peng. “Hybrid LES-RANS modelling: A one-equation SGS model combined with a $k\omega$ model for predicting recirculating flows”. In: *Int. J. Numer. Meth. Fluid.* 43 (2003), pp. 1003–1018 (cit. on p. 41).
- [De +15] B. De Laage de Meux, B. Audebert, R. Manceau, et al. “Anisotropic linear forcing for synthetic turbulence generation in large eddy simulation and hybrid RANS/LES modeling”. In: *Phys. Fluids* 27 (2015), p. 035115 (cit. on pp. 52, 76, 87, 90).
- [De +18] G. De Nayer, S. Schmidt, J.N. Wood, et al. “Enhanced Injection Method for Synthetically Generated Turbulence within the Flow Domain of Eddy-Resolving Simulations”. In: *Computers & Mathematics with Applications* 75 (7) (2018), pp. 2338–2355 (cit. on pp. 45, 53).
- [Dea80] J. W. Deardorff. “Stratocumulus-capped mixed layers derived from a three-dimensional model”. In: *Boundary-Layer Meteorology* 18.4 (1980), pp. 495–527 (cit. on p. 38).
- [DBL18] N. S. Dhamankar, G. A. Blaisdell, and A. S. Lyrintzi. “Overview of Turbulent Inflow Boundary Conditions for Large-Eddy Simulations”. In: *AIAA J.* 56 (2018), pp. 1317–1334 (cit. on p. 41).

- [Duf20] V. Duffal. “Développement d’un modèle hybride RANS-LES pour l’étude des efforts instationnaires en paroi”. In: *Thesis (in french) - Mécanique des fluides [physics.class-ph]. Université de Pau et des Pays de l’Adour* (2020), NNT : 2020PAUU3015ff. fftel-03038837 (cit. on p. 141).
- [DDM22] V. Duffal, B. De Laage de Meux, and R. Manceau. “Development and Validation of a New Formulation of Hybrid Temporal Large Eddy Simulation”. In: *Flow, Turbulence and Combustion* 108 (2022), pp. 1–42 (cit. on pp. 45, 122).
- [Dur91] P.A. Durbin. “Near-wall turbulent closure modeling without "damping functions"”. In: *Theoretical and Computational Fluid Dynamics* 3 (1991), pp. 1–13 (cit. on p. 160).
- [Dur96] P.A. Durbin. “On the k - ϵ stagnation point anomaly”. In: *International Journal of Heat and Fluid Flow* 17.1 (1996), pp. 89–90 (cit. on p. 128).
- [EI14] M. Emory and G. Iaccarino. “Visualizing turbulence anisotropy in the spatial domain with componentality contours”. In: *Center for Turbulence Research - Annual Research Briefs* (2014), pp. 161–178 (cit. on p. 75).
- [EKK21] L. Engelmann, M. Klein, and A.M. Kempf. “A-posteriori LES assessment of subgrid-scale closures for bounded passive scalars”. In: *Comput. Fluids* 218 (2021), p. 104840 (cit. on pp. 92, 93).
- [EP88] V. Eswaran and S. B. Pope. “An examination of forcing in direct numerical simulations of turbulence”. In: *Computers & Fluids* 16 (1988), pp. 257–278 (cit. on pp. 50, 51).
- [Fad+10a] Atabak Fadai-Ghotbi, Christophe Friess, Rémi Manceau, and Jacques Borée. “A seamless hybrid RANS-LES model based on transport equations for the subgrid stresses and elliptic blending”. In: *Physics of Fluids* 22.5 (2010), p. 055104 (cit. on pp. 119, 160).
- [Fad+10b] Atabak Fadai-Ghotbi, Christophe Friess, Rémi Manceau, Thomas B Gatski, et al. “Temporal filtering: A consistent formalism for seamless hybrid RANS–LES modeling in inhomogeneous turbulence”. In: *International Journal of Heat and Fluid Flow* 31.3 (2010), pp. 378–389 (cit. on p. 41).
- [Fav09] B. Favier. “Modélisation et simulations en turbulence homogène anisotrope : effets de rotation et magnétohydrodynamique”. PhD thesis. École Centrale de Lyon, 2009 (cit. on p. 140).
- [FGC10] B. Favier, FS. Godeferd, and C. Cambon. “On space and time correlations of isotropic and rotating turbulence”. In: *Phys. Fluids* 22 (2010), p. 015101 (cit. on pp. 54, 59).
- [FV00] P. Flohr and J.C. Vassilicos. “A scalar subgrid model with flow structure for large-eddy simulations of scalar variances”. In: *Journal of Fluid Mechanics* 407 (2000), pp. 315–349 (cit. on p. 58).

- [Fri10] C. Friess. “Modélisation hybride RANS/LES temporelle des écoulements turbulents”. PhD thesis. Université de Poitiers, 2010 (cit. on p. 160).
- [FMG15] C. Friess, R. Manceau, and T.B. Gatski. “Toward an equivalence criterion for hybrid RANS/LES methods”. In: *Computers & Fluids* 122 (2015), pp. 233–246 (cit. on pp. 42, 45, 78).
- [Fun+92] J.C.H. Fung, J.C.R. Hunt, N.A. Malik, et al. “Kinematic simulation of homogeneous turbulence by unsteady random Fourier modes”. In: *J. Fluid Mech* 236 (1992), pp. 281–318 (cit. on pp. 54, 57).
- [Ger+91] M. Germano, U. Piomelli, P. Moin, et al. “A dynamic subgrid-scale eddy viscosity model”. In: *Physics of Fluids A: Fluid Dynamics* 3.7 (1991), pp. 1760–1765 (cit. on pp. 65, 119, 120).
- [Gos+95] S. Goshal, T. Lund, P. Moin, et al. “A dynamic localization model for large-eddy simulations of turbulent flows”. In: *J. FLuid Mech.* 286 (1995), p. 229 (cit. on p. 51).
- [GO77] D. Gottlieb and S. A. Orszag. “Numerical analysis of spectral methods: theory and application”. In: *CBMS-NSF Reg. Conf. Ser. Appl. Math.* 26 (1977), SIAM, Philadelphia (cit. on p. 50).
- [GL16] I. Grigoriev and W. M. J. Lazeroms. “Direct solution for the anisotropy tensor in explicit algebraic Reynolds stress models”. In: *Methodological note* (2016), pp. 1–10 (cit. on p. 34).
- [Ham01] F. Hamba. “An attempt to combine large eddy simulation with the $k - \epsilon$ model in a channel-flow calculation”. In: *Theor. Comput. Fluid Dyn.* 14 (2001), pp. 323–336 (cit. on p. 41).
- [Ham03] F. Hamba. “A hybrid RANS/LES simulation of turbulent channel flow”. In: *Theor. Comput. Fluid Dyn.* 03 (2003), pp. 387–403 (cit. on p. 41).
- [Ham09] F. Hamba. “Log-layer mismatch and commutation error in hybrid RANS/LES simulation of channel flow”. In: *Int. J. Heat Fluid Flow* 30 (2009), pp. 20–31 (cit. on p. 41).
- [Han70] K. Hanjalic. “Two-dimensional asymmetric turbulent flow in ducts”. In: *PhD thesis, University of London* (1970) (cit. on p. 29).
- [HLS80] K. Hanjalic, B. E. Launder, and R. Schiestel. “Multiple-time scale concepts in turbulent transport modelling”. In: *Springer Verlag (ed) Proceedings of the 2th Symposium on Turbulence Shear Flow* 30 (1980), pp. 36–49 (cit. on p. 41).
- [HN68] F. H. Harlow and P. I. Nakayama. “Transport of turbulence energy decay rate”. In: *Report LA-3854, Los Alamos Sci. Lab., univ. of California* (1968) (cit. on p. 29).

- [Hel98] Antti Hellsten. “Some improvements in Menter’s k-omega SST turbulence model”. In: *29th AIAA, Fluid Dynamics Conference*. 1998, p. 2554 (cit. on p. 31).
- [Hin75] J. O. Hinze. *Turbulence*. McGraw-Hill, 1975 (cit. on pp. 38, 39, 67, 69).
- [HWX20] X. Huang, L. Wang, and J. Xu. “Numerical Study on Dynamical Structures and the Destratification of Vertical Turbulent Jets in Stratified Environment”. In: *water* 12 (2020), p. 2085 (cit. on p. 95).
- [IK02] T; Ishihara and Y. Kaneda. “High resolution DNS of incompressible homogeneous forced turbulence - Time dependence of the statistics”. In: *Statistical Theories and Computational Approaches to Turbulence* (2002), pp. 177–188 (cit. on p. 51).
- [JB08] B. Jaffrézic and M. Breuer. “Application of an explicit algebraic Reynolds stress model within a hybrid LES-RANS method”. In: *Flow Turbul. Combust.* 81 (2008), pp. 415–448 (cit. on p. 41).
- [Jim+93] A. Jiménez, A. Wray, P Saffman, et al. “The structure of intense vorticity in isotropic turbulence”. In: *J. FLuid Mech.* 255 (1993), p. 65 (cit. on p. 51).
- [JL72] W. P. Jones and B. E. Launder. “The prediction of laminarization with of turbulence”. In: *Int. J. Heat Mass Transfer* 15 (1972), pp. 301–314 (cit. on p. 29).
- [Ker84] Robert M. Kerr. “Higher-order derivative correlations and the alignment of small-scale structures in isotropic numerical turbulence”. In: *J. FLuid Mech.* 153 (1984), pp. 31–58 (cit. on p. 50).
- [KSJ03a] M. Klein, A. Sadiki, and J. Janicka. “A digital filter based generation of inflow data for spatially developing direct numerical or large eddy simulations”. In: *J. of Comp. Physics* 186 (2003), pp. 652–665 (cit. on pp. 92, 94, 95).
- [KSJ03b] M. Klein, A. Sadiki, and J. Janicka. “A digital filter based generation of inflow data for spatially-developing direct numerical or large-eddy simulations”. In: *J. Comput. Phys.* 186 (2003), pp. 652–665 (cit. on p. 53).
- [KSJ03c] M. Klein, A. Sadiki, and J. Janicka. “Investigation of the influence of the Reynolds number on a plane jet using direct numerical simulation”. In: *Int. J. Heat and Mass Transfer* 24 (2003), pp. 785–794 (cit. on p. 92).
- [Kra70] R.H. Kraichnan. “Diffusion by a random velocity field”. In: *Phys. Fluids* 13 (1970), p. 22 (cit. on pp. 53, 54, 57).
- [Kri19] Adithya Ramanathan Krishnan. “Explicit algebraic subfilter scale modeling for DES-like methods and extension to variable density flows”. PhD thesis. Université Aix-Marseille, 2019 (cit. on pp. 119, 120, 122, 123, 158).

- [Laf+14] A. Lafitte, T. Le Garrec, C. Bailly, et al. “Turbulence Generation from a Sweeping-Based Stochastic Model”. In: *AIAA Journal* 52 (2014), n°2 (cit. on pp. 61, 96).
- [LCP05] A. G. Lamorgese, D. A. Cauhey, and S. B. Pope. “Direct numerical simulation of homogeneous isotropic turbulence with hyperviscosity”. In: *Phys. Fluids* 17 (2005), p. 015106 (cit. on p. 51).
- [LDS11] R. Laraufie, S. Deck, and P. Sagaut. “A dynamic forcing method for unsteady turbulent inflow condition”. In: *Journal of Comput. Phys.* 230 (2011), pp. 8647–8663 (cit. on p. 54).
- [Lau+72] B. E. Launder, A. P. Morse, W. Rodi, et al. “The Prediction of Free Shear Flows - A comparison of Six Turbulence Models”. In: *NASA SP-322* (1972) (cit. on p. 26).
- [LRR75] B. E. Launder, G. J. Reece, and W. Rodi. “Progress in the development of a Reynolds-stress turbulence closure”. In: *Journal of Fluid Mechanics* 68 (1975), pp. 537–566 (cit. on p. 32).
- [LSS99] C. Le Ribault, S. Sarkar, and S.A. Stanley. “A-posteriori LES assessment of subgrid-scale closures for bounded passive scalars”. In: *Phys. Fluids* 11 (1999), p. 3069 (cit. on pp. 92, 95).
- [Li+19] H. Li, N. K. Anand, Y. A. Hassan, et al. “Large eddy simulations of the turbulent flows of twin parallel jets”. In: *Int. J. Heat and Mass Transfer* 129 (2019), pp. 1263–1273 (cit. on p. 92).
- [LDL19] Q. Liu, Y. H. Dong, and H. Lai. “Large Eddy Simulation of Compressible Parallel Jet Flow and Comparison of Four Subgrid-Scale Models”. In: *Journal of Applied Fluid Mechanics* 12 (2019), pp. 1599–1614 (cit. on p. 92).
- [LN77] J. Lumley and G. Newman. “The return to isotropy of homogenous turbulence”. In: *J. Fluid Mech.* 82 (1977), pp. 161–178 (cit. on p. 75).
- [Lun03] T.S. Lundgren. “Linearly forced isotropic turbulence”. In: *Annual Research Brief (Center for Turbulence Research, Stanford)* (2003), pp. 461–473 (cit. on pp. 47, 50, 52, 54, 55, 63, 69, 91).
- [MGW13] G. Mallouppas, W. K. George, and B. G. M. van Wachem. “New forcing scheme to sustain particle-laden homogeneous and isotropic turbulence”. In: *Phys. Fluids* 25 (2013), p. 083304 (cit. on p. 54).
- [Man18] R. Manceau. “Progress in Hybrid Temporal LES”. In: *In the 6th Symp. Hybrid RANS-LES Methods, 26–28 September 2016, Strasbourg, France* 137 (2018), pp. 9–25 (cit. on p. 45).
- [Man+79] N. N. Mansour, P. Moin, W. C. Reynolds, et al. “Improved methods for large eddy simulations of turbulence”. In: *Turbulence Shear Flows* 1 (1979), p. 386 (cit. on p. 50).

- [Men94] F.R. Menter. “Two-equation eddy-viscosity turbulence models for engineering applications”. In: *AIAA Journal* 32.8 (1994) (cit. on pp. 31, 119, 120).
- [Men92] Florian R Menter. “Influence of freestream values on k-omega turbulence model predictions”. In: *AIAA journal* 30.6 (1992), pp. 1657–1659 (cit. on p. 30).
- [Men93] Florian R Menter. “Zonal two equation kw turbulence models for aerodynamic flows”. In: *23rd fluid dynamics, plasma dynamics, and lasers conference*. 1993, p. 2906 (cit. on p. 30).
- [Mos+03] K. Mosheni, B. Kosovic, S. Shkoller, et al. “Numerical simulations of the Lagrangian averaged Navier-Stokes equations for homogeneous isotropic turbulence”. In: *Phys. Fluids* 15 (2003), p. 524 (cit. on p. 51).
- [PD18] John A. Palmore Jr. and O. Desjardins. “Technique for forcing high Reynolds number isotropic turbulence in physical space”. In: *Physical Review Letters* 3 (2018), p. 034605 (cit. on p. 52).
- [Pam+09] M Pamier, P. E. Weiss, E Garnier, et al. “Generation of synthetic turbulent inflow data for large eddy simulation of spatially evolving wall-bounded flows”. In: *Phys. Fluids* 21 (2009), p. 045103 (cit. on p. 90).
- [Pan04] C. Pantano. “Direct simulation of non-premixed flame extinction in a methane-air jet with reduced chemistry”. In: *J. Fluid Mech.* 514 (2004), pp. 231–270 (cit. on p. 95).
- [PR18] L. Patruno and M. Ricci. “A systematic approach to the generation of synthetic turbulence using spectral methods”. In: *Computer methods in applied mechanics and engineering* 340 (2018), pp. 881–904 (cit. on p. 58).
- [Pir+18] S. Pirozzoli, D. Modesti, P. Orlandi, et al. “Turbulence and secondary motions in square duct flow”. In: *Journal of Fluid Mechanics* 840 (2018), pp. 631–655 (cit. on p. 120).
- [PCR13] R. Poletto, T. Craft, and A. Revell. “A New Divergence Free Synthetic Eddy Method for the Reproduction of Inlet Flow Conditions for LES”. In: *Flow Turbulence Combust* 91 (2013), pp. 519–539 (cit. on p. 58).
- [Qui92] W.R. Quinn. “Turbulent free jet flows issuing from sharp-edged rectangular slots: the influence of slot aspect ratio”. In: *Experimental Thermal and Fluid Science* 5.2 (1992), pp. 203–215 (cit. on pp. 127, 131).
- [Rey95] O. Reynolds. “On the dynamical theory of incompressible viscous fluids and the determination of the criterion”. In: *Philos. Trans. R. Soc.* 186 (1895), pp. 123–164 (cit. on p. 28).
- [RM05] C. Rosales and C. Meneveau. “Linear forcing in numerical simulations of isotropic turbulence: Physical space implementations and convergence properties”. In: *Phys. Fluids* 17 (2005), p. 095106 (cit. on pp. 52, 55, 65).

- [Rot51] J. C. Rotta. “Statistische Theorie nichthomogener Turbulenz”. In: *Zeitschrift für Physik* 129 (1951), pp. 547–572 (cit. on p. 32).
- [Saa+17] T. Saad, D. Cline, R. Stoll, et al. “Scalable Tools for Generating Synthetic Isotropic Turbulence with Arbitrary Spectra”. In: *AIAA Journal* 55 (2017), pp. 327–331 (cit. on p. 58).
- [Sag04] P. Sagaut. *Large Eddy Simulation for Incompressible Flows*. Springer-Verlag, Berlin/New York, 2004 (cit. on pp. 36, 39, 52, 55, 71, 156).
- [SC18] P. Sagaut and C. Cambon. *Homogeneous Turbulence Dynamics*. Springer International Publishing AG, 2018 (cit. on pp. 67, 69).
- [Sch87] R. Schiestel. “Multiple-time scale modeling of turbulent flows in one point closures”. In: *Phys. Fluids* 30 (1987), pp. 722–731 (cit. on p. 41).
- [SD05] R. Schiestel and A. Dejoan. “Towards a new partially integrated transport model for coarse grid and unsteady turbulent flow simulations”. In: *Theor. Comput. Fluid Dyn.* 18 (2005), pp. 443–468 (cit. on pp. 43, 44).
- [SB14] S. Schmidt and M. Breuer. “Hybrid LES-URANS methodology for the prediction of non-equilibrium wall-bounded internal and external flows”. In: *Comput. Fluids* 96 (2014), pp. 226–252 (cit. on p. 41).
- [SB17a] S. Schmidt and M. Breuer. “Source term based synthetic turbulence inflow generator for Eddy-Resolving predictions of an airfoil flow including a laminar separation bubble”. In: *Compt & Fluids* 146 (2017), pp. 1–22 (cit. on pp. 53, 55).
- [SB17b] S. Schmidt and M. Breuer. “Source term based synthetic turbulence inflow generator for Eddy-Resolving predictions of an airfoil flow including a laminar separation bubble”. In: *Comput. Fluids* 146 (2017), pp. 1–22 (cit. on p. 91).
- [Ser+01] C. Seror, P. Sagaut, C. Bailly, et al. “On the radiated noise computed by large-eddy simulation”. In: *Phys. Fluids* 13 (2001), p. 476 (cit. on p. 51).
- [Shu+14] M. L. Shur, P. R. Spalart, M. K. Strelets, et al. “Synthetic turbulence generators for RANS-LES interfaces in zonal simulations of aerodynamic and aeroacoustic problems”. In: *Flow Turbul. Combust* 93 (2014), pp. 63–92 (cit. on p. 41).
- [Sig81] E. D. Siggia. “Numerical study of small-scale intermittency in three-dimensional turbulence”. In: *J. Fluid Mech.* 107 (1981), pp. 375–406 (cit. on p. 50).
- [SP78] E. D. Siggia and G. S. Patterson. “Intermittency effects in a numerical simulation of stationary three-dimensional turbulence”. In: *J. Fluid Mech.* 86.3 (1978), pp. 567–592 (cit. on p. 50).
- [SLR15] C. B. da Silva, D. C. Lopes, and V. Raman. “The effect of subgrid-scale models on the entrainment of a passive scalar in a turbulent planar jet”. In: *Journal of Turbulence* 16 (2015), pp. 342–366 (cit. on pp. 92, 95).

- [SM03] K. Sone and S. Menon. “Effect of Subgrid Modeling on the In-Cylinder Unsteady Mixing Process in a Direct Injection Engine”. In: *Journal of Engineering for Gas Turbines and Power* 125 (2003), pp. 435–443 (cit. on p. 40).
- [Spa97] Philippe R Spalart. “Comments on the feasibility of LES for wings, and on a hybrid RANS/LES approach”. In: *Proceedings of first AFOSR international conference on DNS/LES*. Greyden Press. 1997 (cit. on p. 42).
- [SK01] A. Spille-Kohoff and H.-J. Kaltenbach. “Generation of turbulent inflow data with a prescribed shear-stress profile, Third AFOSR International Conference on DNS/LES Arlington, TX”. In: *DNS/LES Progress and Challenges* (2001) (cit. on pp. 50, 54).
- [SSM02] S. A. Stanley, S. Sarkar, and J.P Mellado. “A study of the flow-field evolution and mixing in a planar turbulent jet using direct numerical simulation”. In: *J. Fluid Mech* 450 (2002), pp. 377–407 (cit. on pp. 92, 94, 95, 98, 99).
- [SMK94] N. Sullivan, S. Mahalingam, and R. Kerr. “Deterministic forcing of homogeneous, isotropic turbulence”. In: *Phys. Fluids* 6 (1994), p. 1612 (cit. on p. 51).
- [TR18] J. Taghinia and M. Md. Rahman. “Large eddy simulation of round impinging jet with one-equation subgrid scale model”. In: *International Journal of Heat and Mass Transfer* 116 (2018), pp. 1250–1259 (cit. on p. 40).
- [Tav11] J. Taveau. “Explosion hazards related to hydrogen releases in nuclear facilities”. In: *Journal of loss prevention in the process industries* 24.1 (2011), pp. 8–18 (cit. on p. 24).
- [Tem+05] L. Temmerman, M. Haziabdic, M. A. Leschziner, et al. “A hybrid two-layer URANS-LES approach for large eddy simulation at high Reynolds numbers”. In: *Int. J. Heat Fluid Flow* 26 (2005), pp. 173–190 (cit. on p. 41).
- [TTL06] F. Tessicini, L. Temmerman, and M. A. Leschziner. “Approximate near-wall treatments based on zonal and hybrid RANS,-LES methods for LES at high Reynolds numbers”. In: *Int. J. Heat Fluid Flow* 27 (2006), pp. 789–799 (cit. on p. 41).
- [TS13] Y. Tominaga and T. Stathopoulos. “CFD simulation of near-field pollutant dispersion in the urban environment: A review of current modeling techniques”. In: *Atmospheric Environment* 79 (2013), pp. 716–730 (cit. on p. 23).
- [WJ00] S. Wallin and A. V. Johansson. “An explicit algebraic Reynolds stress model for incompressible and compressible turbulent flows”. In: *Journal of Fluid Mechanics* 403 (2000), pp. 89–132 (cit. on p. 34).
- [Wan+96] L. Wang, S. Chen, J. Basseur, et al. “Examination of hypotheses in the Kolmogorov refined turbulence theory through high-resolution simulations. Part 1: velocity fields”. In: *J. Fluid Mech.* 309 (1996), p. 113 (cit. on p. 51).

- [Wil88] David C Wilcox. “Reassessment of the scale-determining equation for advanced turbulence models”. In: *AIAA journal* 26.11 (1988), pp. 1299–1310 (cit. on p. 30).
- [Wu17] X. Wu. “Inflow Turbulence Generation Methods”. In: *Annu. Rev. Fluid Mech.* 49 (2017), pp. 23–49 (cit. on p. 41).
- [YH85] A. Yoshizawa and K. Horiuti. “A Statistically-Derived Subgrid-Scale Kinetic Energy Model for the Large-Eddy Simulation of Turbulent Flows”. In: *Journal of the Physical Society of Japan* 54 (1985), pp. 2834–2839 (cit. on p. 40).
- [Zha21] J. Zhang. “Significance of generating synthetic turbulence for zonal detached eddy simulation of shallow water flows”. In: *Ocean Engineering* 237 (2021), p. 109418 (cit. on pp. 91, 141).

APPENDICES

A. Synthetic velocity

A.1. Isotropy

In order to obtain a random point on the surface of a sphere, we cannot use a uniform distribution on the interval $[0; 2\pi]$ for θ and φ . This would lead to a concentrated distribution around the poles. Let a point s be on a sphere of radius $\kappa_n = |\boldsymbol{\kappa}^n|$.

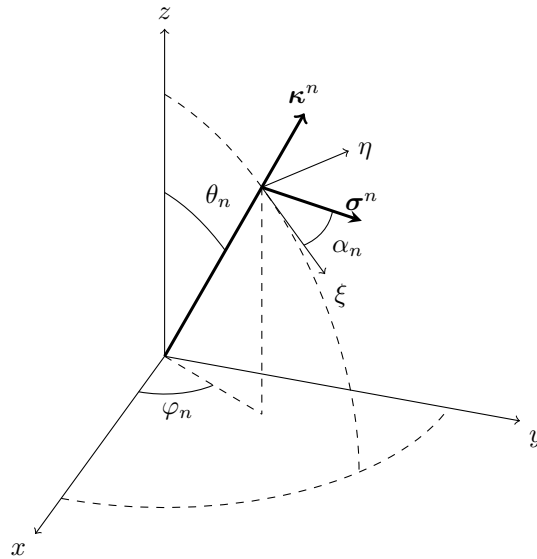


Figure .1. – Wave vector geometry of the n^{th} Fourier mode.

The probability that the point s lies on an elementary surface dA of the sphere is written:

$$P(s)dA \quad (.1)$$

After normalization, we get:

$$\iint_S P(s)dA = 1 \quad (.2)$$

with

$$dA = \kappa_n^2 \sin\theta_n d\varphi_n d\theta_n \quad (.3)$$

and as

$$\int_{\varphi_n} \int_{\theta_n} \kappa_n^2 \sin\theta_n d\varphi_n d\theta_n = 4\pi\kappa_n^2 \quad (.4)$$

The probability density on the surface of a sphere is given by:

$$P(s) = \frac{1}{4\pi\kappa_n^2} \quad (.5)$$

The probability can also be defined as:

$$P(s)dA = P(\varphi_n, \theta_n)d\varphi_n d\theta_n \quad (.6)$$

$$\frac{1}{4\pi} \sin\theta_n d\theta_n d\varphi_n = P(\varphi_n, \theta_n)d\varphi_n d\theta_n \quad (.7)$$

The probability density is then written:

$$P(\varphi_n, \theta_n) = \frac{\sin\theta_n}{4\pi} \quad (.8)$$

Finally, the probability densities of the random variables θ_n and φ_n are determined by:

$$P(\varphi_n) = \int_0^\pi P(\varphi_n, \theta_n)d\theta_n = \frac{1}{2\pi} \quad (.9)$$

$$P(\theta_n) = \int_0^{2\pi} P(\varphi_n, \theta_n)d\varphi_n = \frac{\sin\theta_n}{2} \quad (.10)$$

A.2. Statistical homogeneity

The random variables θ and φ are distributed in such a way as to obtain a uniform distribution on a sphere (see Appendix A.1). In order to determine the probability density of the random variable ψ , two-point correlations are used:

$$\mathbf{R}(\mathbf{x}, r) = \overline{\mathbf{u}^s(\mathbf{x})\mathbf{u}^s(\mathbf{x} + r)} \quad (.11)$$

where $\overline{\quad}$ represents the mean operator like the previously used operator, $\langle \cdot \rangle$.

$$\mathbf{R}(\mathbf{x}, r) = 4 \overline{\sum_{n=1}^N \hat{u}_n \cos(\boldsymbol{\kappa}^n \cdot \mathbf{x} + \psi_n) \boldsymbol{\sigma}^n \sum_{m=1}^M \hat{u}_m \cos(\boldsymbol{\kappa}^m \cdot (\mathbf{x} + r) + \psi_m) \boldsymbol{\sigma}^m} \quad (.12)$$

Since modes are two by two independent, the correlations at two points are null for two different modes. Therefore,

$$\mathbf{R}(\mathbf{x}, r) = 4 \overline{\sum_{n=1}^N \hat{u}_n^2 \cos(\boldsymbol{\kappa}^n \cdot \mathbf{x} + \psi_n) \cdot \cos(\boldsymbol{\kappa}^n \cdot \mathbf{x} + \boldsymbol{\kappa}^n \cdot r + \psi_n)} \quad (.13)$$

Equation Eq. .13 can be written as

$$\mathbf{R}(\mathbf{x}, r) = 2 \sum_{n=1}^N \hat{u}_n^2 [\overline{\cos(\boldsymbol{\kappa}^n \cdot r)} + \overline{\cos(\boldsymbol{\kappa}^n \cdot r + 2\boldsymbol{\kappa}^n \cdot \mathbf{x} + 2\psi_n)}] \quad (.14)$$

In order to respect the homogeneity, the following condition must be satisfied:

$$\overline{\cos(\boldsymbol{\kappa}^n \cdot r + 2\boldsymbol{\kappa}^n \cdot \mathbf{x} + 2\psi_n)} = 0 \quad (.15)$$

The random variable ψ is determined to satisfy equation Eq. .15. By expanding we get:

$$\frac{\overline{\cos(\boldsymbol{\kappa}^n \cdot \mathbf{r} + 2\boldsymbol{\kappa}^n \cdot \mathbf{x} + 2\psi_n)}}}{\overline{(\cos(\boldsymbol{\kappa}^n \cdot \mathbf{r} + 2\boldsymbol{\kappa}^n \cdot \mathbf{x}))(\cos(2\psi_n)) - \sin(\boldsymbol{\kappa}^n \cdot \mathbf{r} + 2\boldsymbol{\kappa}^n \cdot \mathbf{x})(\sin(2\psi_n))}} = \quad (.16)$$

Since the variables $\boldsymbol{\kappa}^n$, ω_n and ψ_n are independent, the mean of the product of different random variables can be written as the product of the means.

$$\frac{\overline{\cos(\boldsymbol{\kappa}^n \cdot \mathbf{r} + 2\boldsymbol{\kappa}^n \cdot \mathbf{x} + 2\psi_n)}}}{\overline{\sin(\boldsymbol{\kappa}^n \cdot \mathbf{r} + 2\boldsymbol{\kappa}^n \cdot \mathbf{x})\sin(2\psi_n)}} = \frac{\overline{\cos(\boldsymbol{\kappa}^n \cdot \mathbf{r} + 2\boldsymbol{\kappa}^n \cdot \mathbf{x})}\overline{\cos(2\psi_n)}}}{\overline{\sin(\boldsymbol{\kappa}^n \cdot \mathbf{r} + 2\boldsymbol{\kappa}^n \cdot \mathbf{x})}\overline{\sin(2\psi_n)}} \quad (.17)$$

The mean in space can be considered as a mean on the modes, they are indeed independent realizations Sagaut 2004. Considering that the random variable ψ_n follows a uniform distribution with probability density $P(\psi_n) = \frac{1}{2\pi}$ and that the space average is transformed into an average over the modes:

$$\overline{\cos(2\psi_n)} = \int_0^{2\pi} \cos(2\psi_n)P(\psi_n)d\psi_n = \frac{1}{4\pi}(\sin(4\pi) - \sin(0)) = 0 \quad (.18)$$

$$\overline{\sin(2\psi_n)} = \int_0^{2\pi} \sin(2\psi_n)P(\psi_n)d\psi_n = \frac{-1}{4\pi}(\cos(4\pi) - \cos(0)) = 0 \quad (.19)$$

Injecting equations Eq. .18 and Eq. .19 into Eq. ?? and substituting the latter two equations into Eq. .15, we obtain:

$$\overline{\cos(\boldsymbol{\kappa}^n \cdot \mathbf{r} + 2\boldsymbol{\kappa}^n \cdot \mathbf{x} + 2\psi_n)} = 0 \quad (.20)$$

Consequently, to satisfy the condition of homogeneity, the random variable ψ_n , $0 \leq \psi_n \leq 2\pi$, follows a uniform distribution with a probability density :

$$P(\psi_n) = \frac{1}{2\pi} \quad (.21)$$

A.3. Moments of the synthetic velocity

In this section, we propose to calculate the first four statistical moments of the synthetic velocity:

i) Mean :

$$\overline{u_i^s} = 2 \sum_{n=1}^N \overline{\hat{u}_n \cos(\boldsymbol{\kappa}^n \cdot \mathbf{x} + \psi_n) \boldsymbol{\sigma}_i^n} \quad (.22)$$

and

$$\overline{\cos(\boldsymbol{\kappa}^n \cdot \mathbf{x} + \psi_n)} = \overline{\cos(\boldsymbol{\kappa}^n \cdot \mathbf{x}) \cos(\psi_n)} - \overline{\sin(\boldsymbol{\kappa}^n \cdot \mathbf{x}) \sin(\psi_n)} \quad (.23)$$

with

$$\overline{\cos(\boldsymbol{\kappa}^n \cdot \mathbf{x})} = \int \int_0^{2\pi} P(\boldsymbol{\kappa}) P(\psi_n) \cos(\boldsymbol{\kappa}^n \cdot \mathbf{x}) \cos(\psi_n) d\psi_n d\boldsymbol{\kappa} \quad (.24)$$

$$\int_0^{2\pi} \cos(\psi_n) P(\psi_n) d\psi_n = 0 \quad (.25)$$

$$\int_0^{2\pi} \sin(\psi_n) P(\psi_n) d\psi_n = 0 \quad (.26)$$

Therefore,

$$\overline{u_i^s} = 0 \quad (.27)$$

ii) Variance:

$$\begin{aligned} \overline{u_i^s u_i^s} &= \frac{4}{3} \sum_{n=1}^N \hat{u}_n^2 \overline{\cos^2(\boldsymbol{\kappa}^n \cdot \mathbf{x} + \psi_n)} = \frac{2}{3} \sum_{n=1}^N \hat{u}_n^2 \overline{(1 + \cos(2\boldsymbol{\kappa}^n \cdot \mathbf{x} + 2\psi_n))} \\ &= \frac{2}{3} \sum_{n=1}^N \hat{u}_n^2 = \frac{2}{3} k_{\text{synthetic}} \end{aligned} \quad (.28)$$

B. Hybridization of a RANS model

B.1. Overview

In seamless hybrid RANS/LES methods, a RANS closure is generally, the physical sense of the various variables, changes.

- i) The mean primary variables, such as momentum, become filtered variables:

$$\bar{A} \rightarrow \tilde{A}. \quad (.29)$$

- ii) Generally, the turbulent variables, from the closure model, transform as:

$$\phi \rightarrow \phi_s. \quad (.30)$$

To summarize, the “beauty” of seamless hybrid RANS/LES methods, is that the subfilter closure model is formally identical to its “parent RANS”, except for the partitioning functions, responsible for the hybridization (e.g. F_{E-DES} in Equivalent DES).

Hereafter, this is illustrated in the case of an explicit algebraic closure, based on $k-\omega$ as a platform model.

B.2. EAHSM $k-\omega$ model

The hybrid model follows the Equivalent-Detached Eddy Simulation (E-DES) methodology and is based on the Explicit Algebraic Hybrid Stress Model (EAHSM) proposed in Krishnan 2019. The model is based on the weak equilibrium assumption for the sub-filter stress anisotropy tensor that leads to a nonlinear relationship for the sub-filter stresses expressed as:

$$\boldsymbol{\tau} = \beta_1 \tilde{\mathbf{S}} + \beta_2 \delta \beta_3 \tilde{\boldsymbol{\Omega}}^2 + \beta_4 (\tilde{\mathbf{S}}\tilde{\boldsymbol{\Omega}} - \tilde{\boldsymbol{\Omega}}\tilde{\mathbf{S}}) + \beta_6 (\tilde{\mathbf{S}}\tilde{\boldsymbol{\Omega}}^2 - \tilde{\boldsymbol{\Omega}}^2\tilde{\mathbf{S}}) + \beta_9 (\tilde{\boldsymbol{\Omega}}\tilde{\mathbf{S}}\tilde{\boldsymbol{\Omega}}^2 - \tilde{\boldsymbol{\Omega}}^2\tilde{\mathbf{S}}\tilde{\boldsymbol{\Omega}}) \quad (.31)$$

where $\tilde{\mathbf{S}}$ and $\tilde{\boldsymbol{\Omega}}$ denote respectively the filtered strain tensor and the resolved rotation tensor normalized with the sub-filter turbulent time scale and where the β -coefficients are functions of the invariants of $\tilde{\mathbf{S}}$ and $\tilde{\boldsymbol{\Omega}}$. The interested reader may refer to Krishnan 2019 for a comprehensive presentation of the model derivation.

While an algebraic expression is used for the sub-filter anisotropy tensor, transport equations are solved for the sub-filter quantities that correspond to the E-DES

methodology applied to the k - ω BSL model:

$$\frac{dk_s}{dt} = \mathcal{P}_s - \psi' \beta^* \omega_s k_s + \frac{\partial}{\partial x_j} \left[\left(\nu + \sigma_k \frac{k_s}{\omega_s} \right) \frac{\partial k_s}{\partial x_j} \right] \quad (.32)$$

$$\begin{aligned} \frac{d\omega_s}{dt} = & \frac{\omega_s}{k_s} \gamma \mathcal{P}_s - \beta \omega_s^2 + \frac{\partial}{\partial x_j} \left[\left(\nu + \sigma_\omega \frac{k_s}{\omega_s} \right) \frac{\partial \omega_s}{\partial x_j} \right] \\ & + 2(1 - F_1) \sigma_{\omega_\epsilon} \frac{1}{\omega_s} \frac{\partial k_s}{\partial x_j} \frac{\partial \omega_s}{\partial x_j} \end{aligned} \quad (.33)$$

where F_1 is the blending function of the k - ω BSL model and where the coefficients are expressed as $\gamma = F_1 \gamma_\omega + (1 - F_1) \gamma_\epsilon$, $\beta = F_1 \beta_\omega + (1 - F_1) \beta_\epsilon$, $\sigma_\omega = F_1 \sigma_{\omega_\omega} + (1 - F_1) \sigma_{\omega_\epsilon}$, $\sigma_k = F_1 \sigma_{k_\omega} + (1 - F_1) \sigma_{k_\epsilon}$ and $C_{\epsilon 1\omega} = \gamma_\omega + 1$ and $C_{\epsilon 2\omega} = \beta_\omega / \beta^* + 1$ with

$$\gamma_\omega = \frac{5}{9}, \quad \beta_\omega = 0.075, \quad \sigma_{\omega_\omega} = 0.5, \quad \sigma_{k_\omega} = 0.5 \quad (.34)$$

$$\gamma_\epsilon = (C_{\epsilon 1} - 1), \quad \beta_\epsilon = \beta^* (C_{\epsilon 2} - \psi^{k_\epsilon}), \quad \sigma_{\omega_\epsilon} = 0.856, \quad \sigma_{k_\epsilon} = 1 \quad (.35)$$

The non-dimensional lengthscale ψ' is given by

$$\psi' = \max \left[1; \frac{l_s}{r^{3/2} L_t} (F_1 \Psi_\omega + (1 - F_1) \Psi_\epsilon) \right] \quad (.36)$$

with

$$l_s = \frac{k_s^{1/2}}{\beta^* \omega_s}, \quad L_t = \frac{(\overline{k_s} + k_r)^{3/2}}{\beta^* \overline{\omega_s} k_s} \quad (.37)$$

along with

$$\Psi_\omega = 1 + \left(\frac{C_{\epsilon 2\omega}}{C_{\epsilon 1\omega}} - 1 \right) \left(1 - r^{\frac{C_{\epsilon 1\omega}}{C_{\epsilon 2\omega}}} \right) \quad (.38)$$

$$\Psi_\epsilon = 1 + \left(\frac{C_{\epsilon 2\epsilon}}{C_{\epsilon 1\epsilon}} - 1 \right) \left(1 - r^{\frac{C_{\epsilon 1\epsilon}}{C_{\epsilon 2\epsilon}}} \right) \quad (.39)$$

In the above relations, the kinetic energy ratio r is defined as the ratio of the modeled sub-filter energy k_s to the total energy $k = k_r + k_s$.

B.3. Enforcing near-wall RANS mode using elliptic blending

The kinetic energy ratio entering in the formulation of PITM or E-DES models is determined by integrating a prescribed analytical energy spectrum. In practice, regardless of the chosen spectrum, the energy ratio increases in the near wall region but remains lower than the RANS limit. This is in contradiction with the objectives of hybrid approaches that intent to tend to a RANS modeling in the near wall region in

order to reduce the cost of the simulation.

In order to enforce the RANS mode in the near-wall region regardless of the mesh size, the energy ratio is sensitized to the wall distance by using the elliptic blending coefficient as proposed in Fadai-Ghotbi, Christophe Friess, Rémi Manceau, and Borée 2010:

$$r'_k = (1 - \alpha^2) + \alpha^2 r_k \quad (.40)$$

The elliptic blending coefficient α which takes values between zero at the wall and one far from the wall is determined from the elliptic blending equation:

$$\alpha - L_s^2 \nabla^2 \alpha = 1 \quad (.41)$$

The sub-filter turbulent length scale follows a similar expression as in RANS modeling with the limitation procedure proposed by Durbin 1991, and reads in hybrid RANS/LES (Fadai-Ghotbi, Christophe Friess, Rémi Manceau, and Borée 2010):

$$L_s = C_L \max \left(\frac{k_s^{3/2}}{\varepsilon_s}, r'^{3/2} C_\eta \left(\frac{v^3}{\varepsilon_s} \right)^{1/4} \right) \quad (.42)$$

with $C_L = 0.18$ and $C_\eta = 80$. Following similar arguments, the sub-filter turbulent time scale is expressed as C. Friess 2010:

$$\tau_s = \max \left(\frac{k_s}{\varepsilon_s}, r'_k C_\tau \sqrt{\frac{v}{\varepsilon_s}} \right) \quad (.43)$$

with the usual value $C_\tau = 6$.